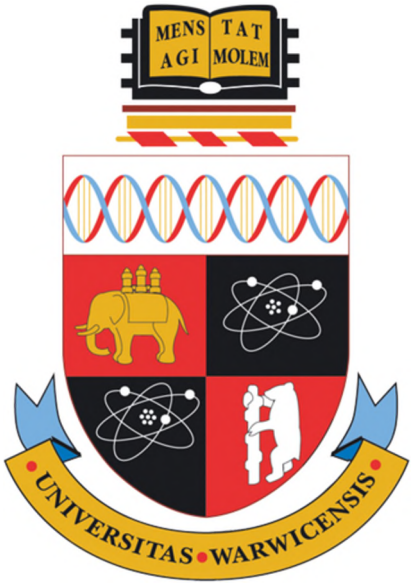

Exploring Electrochemical Deposition in Aqueous and Non-Aqueous Solvents Using Boron Doped Diamond Electrodes

By

Haytham E. M. A. I. Hussein

A thesis submitted in partial fulfilment of the requirements for the degree of

Doctor of Philosophy in Chemistry

University of Warwick, Department of Chemistry

November 2018

For my Mom and Dad

Contents

List of Figures

List of Tables

Abbreviations

2D	Two Dimensional
3D	Three Dimensional
AFM	Atomic Force Microscopy
BDD	Boron Doped Diamond
CE	Counter Electrode
CV	Cyclic Voltammetry
CVD	Chemical Vapour Deposition
DI	Deionised Water
DPS	Double Potential Step
EDL	Electrical Double Layer
FCC	Face Centred Cubic
FE-SEM	Field Emission Scanning Electron Microscopy
G-C	Gouy-Chapman
HFCVD	Hot Filament Chemical Vapour Deposition
HPHT	High Pressure High Temperature
IHP	Inner Helmholtz Plane
IL	Identical Location
IR	Infrared
MPCVD	Microwave Plasma Chemical Vapour Deposition
NP	Nanoparticle
OCP	Open Circuit Potential
OHP	Outer Helmholtz Plane
RE	Reference Electrode
SAED	Selected Area Electron Diffraction
SCE	Saturated Calomel Electrode

SECM	Scanning Electrochemical Microscopy
SEM	Scanning Electron Microscopy
SERS	Surface Enhanced Raman Spectroscopy
SIMS	Secondary Ion Mass Spectrometry
SPS	Single Potential Step
STEM	Scanning Transmission Electron Microscopy
STM	Scanning Tunnelling Microscopy
TEM	Transmission Electron Microscopy
TPV	Temperature Pulsed Voltammetry
UV	Ultraviolet
XEDS	X-Ray Energy-Dispersive Spectroscopy
XPS	X-Ray Photoelectron Spectroscopy
XRD	X-ray Diffraction
WE	Working Electrode

Glossary of terms

α	Bond angle
η	Overpotential
ρ	Density
β	Temperature coefficient or non-dimensional factor
θ	Contact angle
[B]	Boron concentration
D	Diffusion coefficient
E	Electrode potential
$E_{1/2}$	Half wave potential
E^0	Standard electrode potential
E_a	Impurity acceptor level
E_F	Fermi level
F	Faradaic constant
i	Faradic current
i_{lim}	Limiting current
j	Current density of diffusional flux
k_B	Boltzmann constant
n	Number of electrons transferred
p	Pressure
P_d	Laser power density
R	Gas constant
T	Temperature
ΔT	Temperature change
ν	Scan rate

Acknowledgments

First and foremost, I would like to thank my supervisor Prof. Julie V. Macpherson for granting me the chance to do my PhD at the University of Warwick. In particular, her advice, providing me the freedom to do what I like to study, patience, teaching me how to write journal articles, and encouragement throughout the course of my Ph.D, have played the major role in achieving many milestones. Her enthusiasm, be it for research, outreach, teaching, coffee, or diamond, has provided a constant source of inspiration over the last four years.

I would like to acknowledge EPSRC, the University of Warwick, department of chemistry, and AstraZeneca for both funding and supporting my Ph.D. studies. I would like to thank Prof. Mark Newton, Dr. Richard Beanland, Dr. Reinhard Maurer, Dr. Houari Amari, and Dr. Jon Peters for their help, advice, encouragement, and for teaching me about diamond science, TEM and DFT simulations. I am grateful to all of you. I also thank ElementSix for the provision of the boron doped diamond samples. I would like to thank Dr. Andrew Ray from AstraZeneca for his help, advice, guidance and encouragement. I have always felt welcome in Macclesfield.

Many thanks go to past and present members of the Warwick Electrochemistry and Interfaces Group. It has been a pleasure to work with and learn from Dr. Max Joseph, Dr. Ashley Page, Dr. David Perry, Dr. Lingcong Meng, Dr. Tania Read, Dr. Rob Johnson, and Dr. Cameron Bentley. I appreciate your help and advice. I thank Mareike Herrmann for preparing many samples for my Ph.D. work. I am constantly learning; hence I enjoy the scientific discussions with Dr. Lijiang Song, Dr. Jon Ustarroz, Sam Cobb, Alex Borrill, Binglin Tao, and Dr. Slava Shkirskiy. I would like to thank Rod Wesson, Lee Butcher, Marcus Grant, Lee Simcox and Josh Tully.

Before, I started my Ph.D. studies, there are people whose work and efforts have shaped my scientific background. In particular, I would like to thank Prof. Hoda El Diwani, who spent long time teaching me basics laboratory skills and elements of research. I owe her much and I hope my accomplishment during my Ph.D. can reward her support. I also thank my teachers Mr. Hassan Ragab, Mr. Ahmad Amer and Mr. Hussain Shokre for teaching me basics and fundamentals of different subjects and disciplines. Many thanks go to Sherif Gomaa, P&G plant manager for his kind help and support.

Finally, I thank my family, specifically my Mom and Dad were the fuel behind my success. I owe much to my mom, whose contributions stand behind my achievements. So, thank you and I hope this work makes you proud.

Declaration

I declare that the work contained in this thesis is entirely my own work, except where carried out in collaboration, as outlined below. I confirm that this thesis has not been submitted for a degree at another university.

Chapter 3, TEM images and SAED data were collected by myself with the help of Dr. Houari Amari (Scientific officer, Electron microscopy RTP, University of Warwick). *Chapter 4*, TEM, STEM images and data analysis were carried out by myself, Dr. Houari Amari, Dr. Jon Peters, and Dr. Richard Beanland (Electron microscopy RTP, University of Warwick). In *Chapter 4*, Dr. Reinhard Maurer performed the DFT simulations (Chemistry, University of Warwick). *Chapter 5*, NMR data were collected by Robert Perry, and Dr. Ivan Prokes (Chemistry, University of Warwick), and analysed by myself. ICP and mass spectrometry data were collected by Philip Broad, and Dr. Lijiang Song (Chemistry, University of Warwick), and analysed by both of them and myself. XRD data were collected by Dr. David Walker, and analysed by him and myself.

Parts of this thesis have been published or to be submitted, as detailed below:

Chapter 3 was published as:

Electrochemical Synthesis of Nanoporous Platinum Nanoparticles Using Laser Pulse Heating: Application to Methanol Oxidation.

Haytham E. M. Hussein, Houari Amari, and Julie V. Macpherson. ACS Catalysis, 7 (2017): 7388-7398.

Chapter 4 was published as:

Tracking Metal Electrodeposition Dynamics from Nucleation and Growth of a Single Atom to a Crystalline Nanoparticle

Haytham E. M. Hussein, Reinhard J. Maurer, Houari Amari, Jonathan J. P. Peters, Lingcong Meng, Richard Beanland, Mark E. Newton, and Julie V. Macpherson. ACS Nano, 12 (2018): 7388-7396.

Chapter 5 is under preparation:

Water Addition Switches Pd Electrochemical Deposition On

Haytham E. M. Hussein, Andrew Ray, and Julie V. Macpherson. *In preparation.*

Abstract

In this thesis, we use boron doped diamond (BDD) because of its unique properties such as: a high thermal conductivity, a good resistance to chemical and electrochemical attack, a very large potential window, and low background currents to investigate electrochemical deposition of the platinum group metals. We first explore the effects of deposition potential and time, in tandem with temperature control, on the morphology of Pt nanostructures created. In this way, we managed to make porous Pt nanoparticles (NPs) via a one-step deposition. We then further use electrochemistry as a diagnostic and analytical technique for characterisation of their electrocatalytic properties, using Pt NPs for studying methanol oxidation for energy conversion applications.

Having realised the power of the transmission electron microscope (TEM) as an analytical and a quantitative tool. We made thin BDD (few nm thickness), to provide an electrode, which is electron transparent. Using this dual function BDD in combination with complimentary high-resolution electron microscopy techniques, it was possible to investigate the nucleation and growth of Au at the atomic level. By taking time snapshots, we can provide information about the mechanisms of early stage phase formation and the transition of amorphous nanostructures to crystalline NPs.

Finally, we carry out spectroscopic, analytical and electrochemical studies to understand ion-ion, ion-solvent and solvent-solvent interactions, which then aid the utilisation of electrodeposition for the recovery of Pd from industrial-like solutions. We show that the addition of water to acetonitrile switches on the Pd electrodeposition from its Pd-acetate compound. Moreover, we provide proof of concept measurements for the electrochemical recovery of Pd from an organic synthesis solution, without impacting the organic molecules or the active pharmaceutical ingredients.

In general, BDD holds a great avenue for nucleation and growth studies, provides features that allow controlling the metal electrodeposition and can be used to make specific nanostructures and catalysers.

Chapter 1
Introduction

1.1 Electrochemistry, electricity and chemistry

Electrochemistry is a corner stone technology in the development of materials for energy conversion and storage, as well as for testing the electrocatalytic performance of different materials. Additionally, electrochemical technologies are constantly evolving with the aim of solving global problems and challenges, including the green production of ammonia, conversion of carbon dioxide to bring accelerated climate change under control, and the recovery and recycling of metals for reuse. Electrochemical approaches are especially attractive, being simple to operate, and relatively low-cost. Electrochemical synthesis (deposition) contends to be the tool of choice to make nanostructures, thin films and layers with unique properties, tailored for applications such as metal recovery from complex solutions, batteries and fuel cell catalysts. In principal electrochemistry investigates the relationship between the passage of electricity (flow of electrons) and chemical changes (chemistry).[1] Efforts underpinning the understanding of electricity date back to the work of Luigi Galvani and Alessandro Volta,[2, 3] which paved the way for Nicholson and Carlisle in 1800 to study water splitting into hydrogen and oxygen by electrolysis.[4] In 1801, Ritter discovered electrodeposition[5] and in 1833, Faraday carried out quantitative studies of electrolysis and developed the nomenclature "electrochemistry".[6]

Electrochemistry describes charge transfer at an interface (*e.g.* electron transfer) and the subsequent physico-chemical reactions.[7] An alternative description is structure and physico-chemical processes occurring at the interface between a substrate (an electrode, electronic conductor) and electrolyte (ionic conductor) or at the interface between two electrolytes.[8] Two common interfaces are represented in Figure 1.1, (a) a solid-liquid interface[9, 10] and (b) an immiscible liquid-liquid interface.[11]

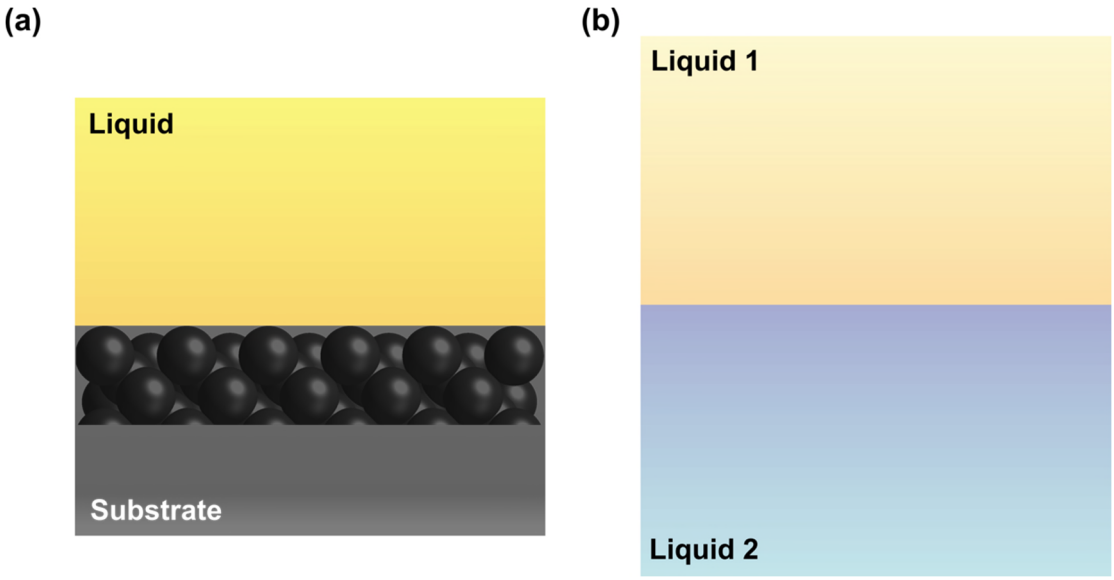

Figure 1.1: The exemplar electrochemical interfaces, (a) solid-liquid interface and (b) liquid-liquid interface.

1.2 Electrochemical deposition or electrodeposition

Electrochemical deposition is a method to form a new solid phase on an electrode (substrate) surface from ions in a solution.[10, 12] The method is relatively simple,[13] but the mechanistic processes governing phase formation are complex, involving physical, chemical and material science phenomena.[14-18] At its simplest, electrodeposition is the reduction of metal ions (cations, M^{n+}_{liquid},) from aqueous, organic, or mixed electrolytes to a solid metal (M_{solid}), as described by Equation 1.1.[10, 19-21]

$$M^{n+}_{liquid} + n\,e^- \rightarrow M_{solid} \qquad \text{Equation 1.1}$$

Practically, one way to achieve this is via external supply of a number of electrons ($n\ e^-$) via an applied potential (voltage) at the electrode-solution interface,[10] where charged particles (metal ion and electron) cross in both directions, as depicted in Figure 1.2.[22]

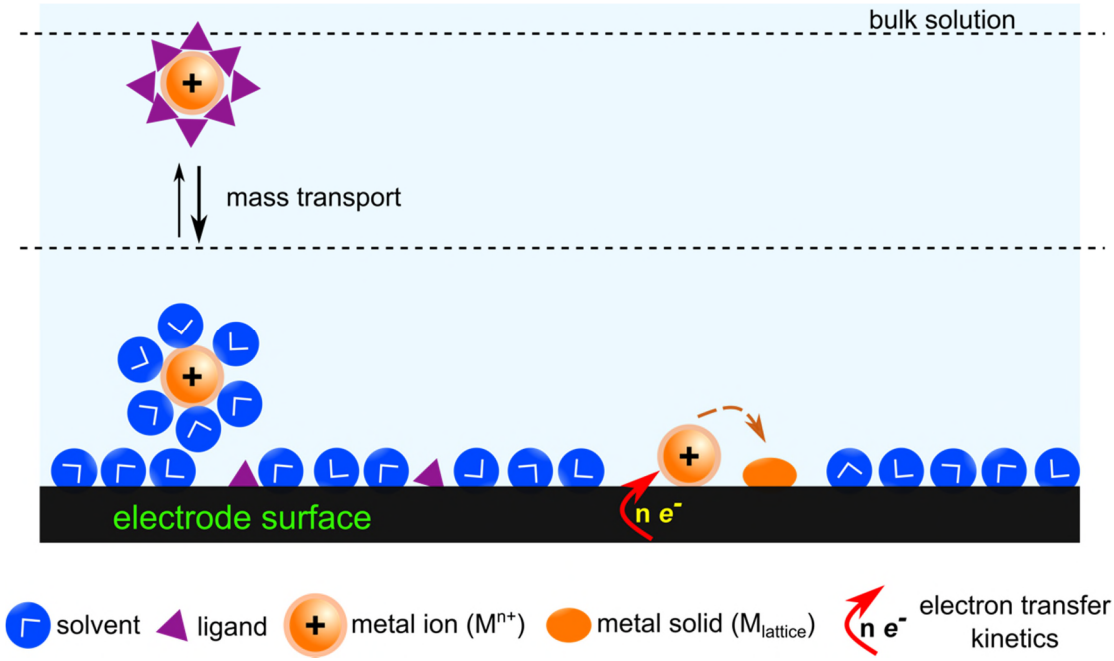

Figure 1.2: Demonstration of an electrode heterogeneous processes.

Electrodeposition requires knowledge of the following four factors, (1) electrode-solution interface,[23] (2) kinetics and mechanism of metal ion reduction (electrodeposition),[24, 25] (3) nucleation and growth,[18, 26] and (4) structure and properties of the growing crystal.[27, 28] The interface is the location of the electrochemical process, consequently, the relevant properties of the individual components of the interface are first discussed.[10] To construct an electrode-solution interface, we build an electrochemical cell, as shown in Figure 1.3.[29] The basic components of an electrochemical cell are; a substrate (or a working electrode), which can be a metal, a carbon material (*e.g.* boron doped diamond (BDD), glassy carbon), or a conducting polymer, and an electrolyte such as salt containing water (aqueous) or an organic (non-aqueous).[30-33] In this thesis, both water and acetonitrile (MeCN) are employed as the solvent. Other liquids can be used such as ionic liquids, molten salts etc.,[34] but they do not fall under the scope of this work. The electrochemical cell can be adapted and built in different designs to fit with the different experimental aims, which are discussed in *Chapters 3, 4* and *5* as well as using electrodeposition to create unique nanostructures and how nucleation and growth occur.

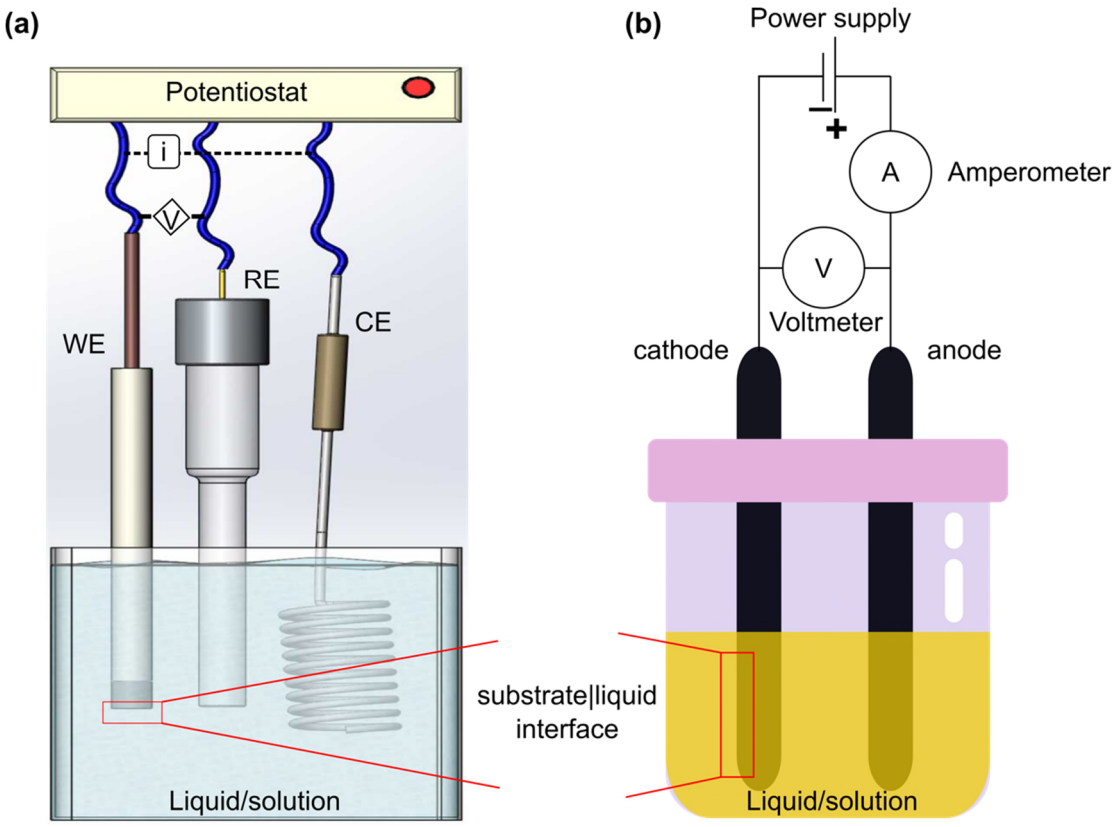

Figure 1.3: (a) three electrode setup. (b) two electrode setup (Galvanostatic). WE: working electrode, RE: reference electrode, and CE: counter electrode.

1.2.1 The structure of the liquid

The solvent is the medium for solute dissolution and supply of ions to the electrode surface.[35, 36] The nature of the solvent can dictate the electrochemical processes.[1] Thus, its properties such as the acid-base character (protic or aprotic), polarity, anodic and cathodic voltage limit (*i.e.* the solvent window), the mutual solubility of a solute in a solvent or solvent-solvent solubility in mixed systems, and the physico-chemical properties of the solvent (dielectric constant, viscosity, donor number or solvating properties) play a major role in electrochemical studies.[1, 37] Hence, understanding solvent structure is important.

The most common solvent for electrochemical deposition is water, it is also described as a green and environmentally friendly solvent.[38, 39] A water molecule is hetero-nuclear, due to differences in electron affinities of the oxygen and the hydrogen atoms, this leads to an unequal electron charge distribution in the bond.[40, 41] Consequently, the O–H bond is polarized; *i.e.* the oxygen atom carries a small partial negative charge

(δ-), while the hydrogen atom carries a small partial positive charge (δ+).[10, 42, 43] The water structure is shown in Figure 1.4.

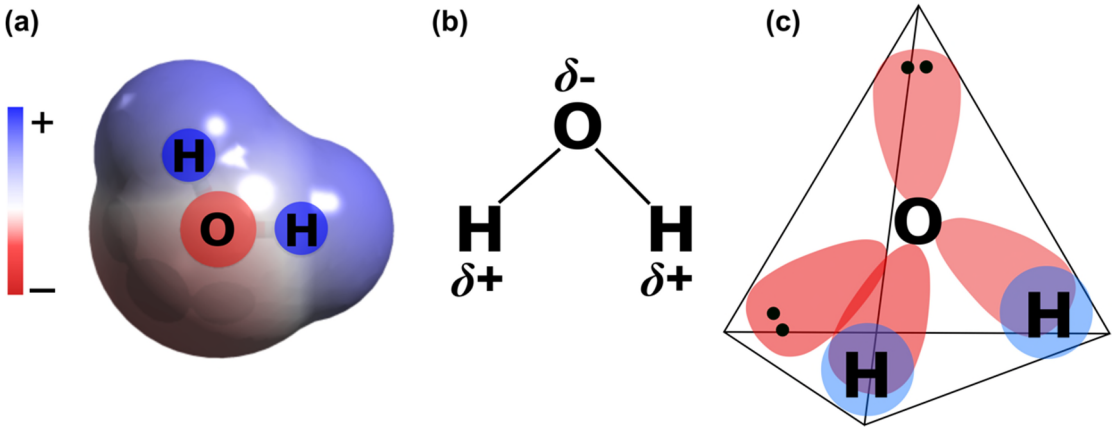

Figure 1.4: (a and b) Approximate shape and electrostatic charge distribution of water. (c) The electronic structure of water molecule, sp^3 model.[10]

Water is a very reactive molecule.[1, 44] However, its reactivity is moderated by forming hydrogen bonds in bulk liquid at room temperature.[10] The hydrogen bonds result from the electrostatic interaction between O–H bond dipole of one water molecule and the unshared lone pair of electrons on the oxygen of another water molecule.[10, 40, 45] The existence of H-bonds in liquid water leads to formulation of the flickering water cluster model,[10] which describes the degree of association between water molecules.[40] In this model, liquid water is suggested to consist of structured and unstructured regions.[40] Large numbers of hydrogen-bonded water molecules are clustering together (approx. 50 to 100 water molecules), which make up the structured regions.[10] Regions of monomeric single water molecules are known as the unstructured regions.[10] The flickering cluster model structures is shown schematically in Figure 1.5.

Water will also exist partially dissociated, forming protons (H^+) and hydroxyl ions (HO^-), Equation 1.2, which are hydrated in aqueous media.[10, 42, 43]

$$H_2O \rightleftharpoons H^+ + HO^- \quad \text{Equation 1.2}$$

The concentration of H^+ or HO^- ions in pure water at 25°C is 1.0×10^{-14} mol/L.[1, 10, 46] Despite the important properties of water, for example its strong ability to solvate both the anions and the cations via hydrolysis,[47] organic solvents such as MeCN, have gained increasing attention due to their widespread use in industry and chemical synthesis.[48, 49] MeCN can dissolve many salts including those with hydrophobic or

hydrophilic characteristics.[48] MeCN and its interaction with water in MeCN-water mixed solvent systems is the subject of interest and discussion in *Chapter 5*.

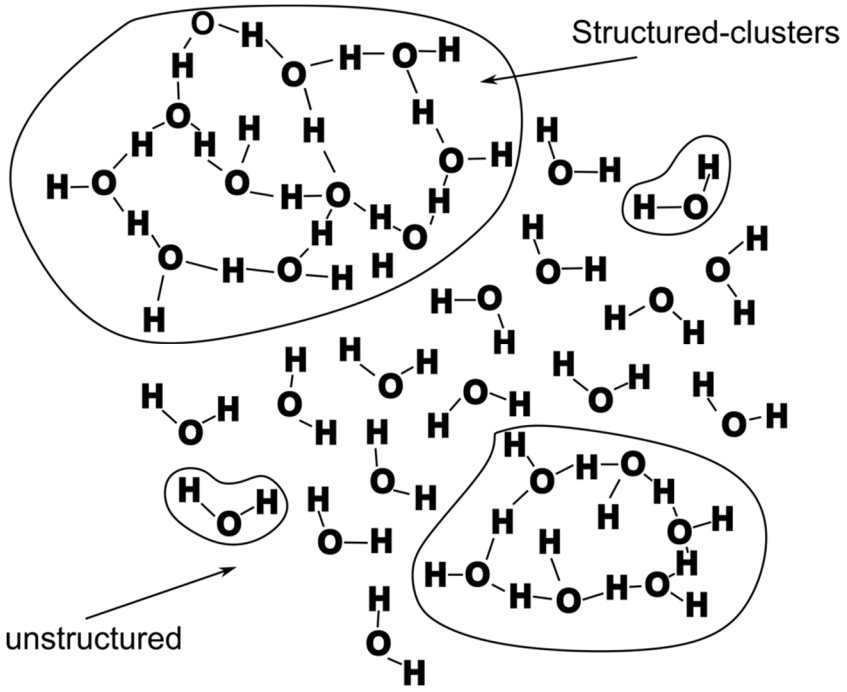

Figure 1.5: Cluster model of water showing regions of structured and unstructured water molecules.[40]

MeCN is a polar aprotic solvent, unlike water, MeCN molecules are unable to form hydrogen bonds between themselves.[50-60] The structure of MeCN is shown in Figure 1.6, it contains molecules with an antiparallel molecular orientation, and consequently the charges of the dipoles are located at the ends of the molecule (*i.e.* on the methyl group and the N atom).[61-64]

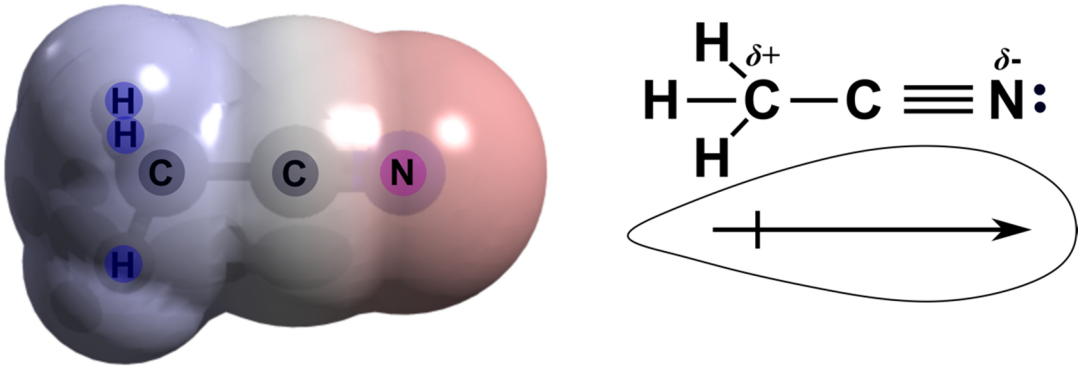

Figure 1.6: Approximate shape and electrostatic charge distribution of acetonitrile.

1.2.2 Ion solvation

When solutes dissolve in a solvent, an ion-solvent interaction occurs.[10, 36, 65, 66] There are five major ion-solvent interactions, which are dependent on the nature of the solvent. Examples include (1) Born-type electrostatic interaction, in which the solvent works as a dipole and hence ion-dipole interactions are dominant,[67] (2) H-bond formation, this is linked to the H donor or acceptor ability of solvents,[45] (3) the different degree of Lewis-acidity or Lewis-basicity,[68-70] (4) the different coordination capability,[66, 71] and (5) the dispersion force interaction.[50-54, 72-76]

The dissolution process of a solute leads to a structure modification.[30, 53] In water, Figure 1.7(a), the solute's ions are hydrated upon dissolution (*i.e.* hydrolysis) by water molecules, which orient themselves in the immediate vicinity of the ion (ion-dipole model).[10, 52] This occurs when one end of the water dipole is attached electrostatically to the oppositely charged ion.[52] Consequently, a primary hydration shell (region 1) is formed by a number of preferentially oriented water molecules in the immediate vicinity of the solute ion. As a result, the ion and its primary water shell form a single entity that move together.[10, 52]

Water is a strong H-bond donor and acceptor, this results in the formation of the secondary water sheath (region 2) next to the primary water hydration shell.[52] Both the solute ion and its water primary shell induce orienting forces on the water molecules in the secondary shell.[52] Thus, water molecules in the secondary water shell are partially oriented.[52] In region 3, water molecules are disordered and beyond this region is the bulk water (region 4).[52] The importance of all four regions depends very much on the individual solvating ion.[52]

In aprotic polar solvent such as MeCN (Figure 1.7(b)), similar behavior to water is established in the first MeCN shell around the ion (region 1), where MeCN dipoles orient themselves so that the N atom (negatively charged and carrying a lone pair) is attracted to the cation.[52] Conversely, an anion (negatively charged ion) attracts MeCN so that the positively charged methyl group points towards it.[52] However, region 2 (as found for water) does not exist.[52] The poor properties of MeCN as H donor, lead directly to the establishment of the third region (region 3), where MeCN molecules are disordered, and region 4 represents the bulk of the MeCN solvent.[52]

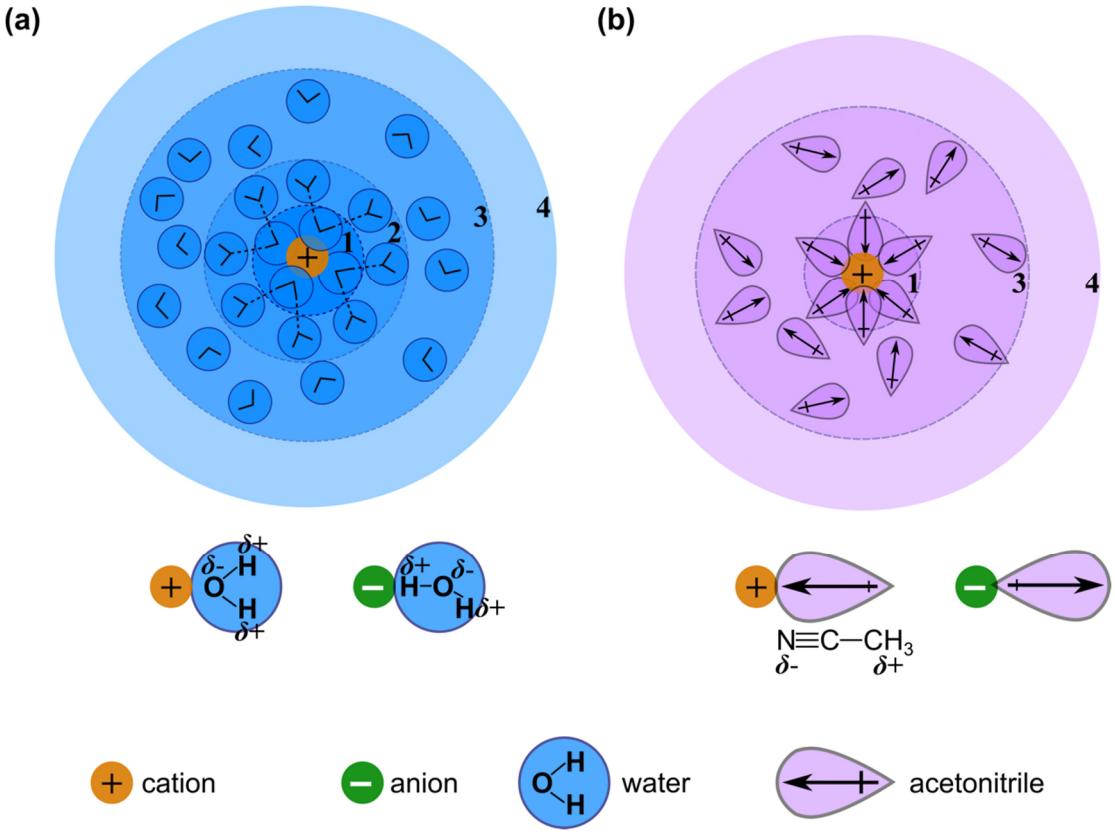

Figure 1.7: Schematic illustration of the molecular environment of the solvation shell around a particular cation (a) in water and (b) in aprotic solvent (MeCN). Orientation of the water and MeCN molecules with respect to the cation and anion are shown.[52]

Finally, solvents have different properties, Table 1.1., such as DN, dielectric constant (ϵ), viscosity, dipole moment (μ_s), specific electrical conductivity, boiling point, melting point, etc. From the industrial point of view, the best solvents are those that have a high boiling point, a high specific electrical conductivity, a low melting point, a low viscosity and a low toxicity. Additionally, solvents with a high dipole moment and a high DN are assumed to form strong bonds with metal ions in the solution.

Metal ion solvation in water and mixed solvents is under continuous study.[47, 77] Metal ions are expected to have greater tendency to coordinate with H_2O (*i.e.* dissolve) because of its higher dielectric constant (ϵ), and DN.[78-80] Additionally, owing to these high constant values of H_2O, the degree of dissociation will be high.[79] As a result in aqueous medium, the solution structure will be made up with metal ions, which have dissociated and are now surrounded by H_2O molecules (*i.e.* hydrolysis).[81, 82] Conversely, ligands and more specifically, ones containing oxygen (O), will stay ligated to the metal centre in non-aqueous medium.[83-85] In both cases, the bonding

strength will largely rely on the DN and the μ_s of the solvent.[86] However, the solvation process is dependent on the nature of the solvent's molecules, and the metal properties, for example if the d-orbital has electron vacancies in the case of transition metals. [53, 87]

1.2.3 The electrode material/structure (or the substrate)

The electrode material can influence both the electrochemical processes occurring at the interface and the structure of the liquid.[31, 32, 88-97] Metal electrodes (*e.g.* Pt, Au, etc.) and liquid metal, hanging mercury electrode, received great attention in the early days of electrochemical studies.[32, 90, 98-118] Nevertheless, the emergence of carbon (the fourth most abundant element) as an electrode material and specifically, conductive BDD, has received rapidly increasing attention due to favourable properties such as good electrical conductivity, chemical inertness and a wide solvent window.[119-127]

1.2.3.1 Diamond and BDD

Diamond is known as a valuable natural gem stone, which has gained its importance from its unique physical and chemical properties as well as rarity.[128-130] A multitude of extraordinary properties include a broad wavelength transparency, the hardest known material (85-100 GPa), and high thermal conductivity (2200 $Wm^{-1}K^{-1}$), hence diamond material works as a heat sink in many applications such as electronics.[131] These properties, besides the high cost of diamond mining and processing, have driven the exploration of methods to make diamond in the laboratory.[129, 132, 133]

Table 1.1: Properties of MeCN and water solvents used in this chapter studies.[61, 134-136]

Solvent							Indexes of solvent solvation ability				
	bp (°C)	***D* (m^2 S^{-1})**	***ρs* (*Kg* m^{-3})**	**V_m (cm^3 mol^{-1})**	***η* (*mPa s*)**	***k* (*S* m^{-1})**	**DN**	**AN**	**ϵ**	**μ_s**	**E_T^N**
MeCN	81.6	4.85×10^9	776.0	52.9	0.96	0.06×10^6	14.1	18.9	37.5	3.9	0.460
H_2O	100	2.27×10^9	997.045	18.07	0.8903	5.89×10^6	18.0	54.8	78.3	1.8	1

1.2.3.2 Synthesis of diamond and BDD

Diamond grows deep in the planet, specifically in the earth's upper mantle, where both temperature and pressure are high.[137] To make diamond artificially, it is not surprising that attempts in 1950s required using high pressures and high temperature (HPHT) methods.[132, 133] Using this thermodynamically driven method, it is possible to obtain single crystal diamond of microns to millimetre dimensions.[122, 123, 129, 132, 133] Soon thereafter, progress in the solid synthesis technology resulted in growth of diamond using chemical vapour deposition (CVD) technique at low pressures.[138, 139] Since CVD techniques can produce high quality diamond (poly and single crystals) with properties matching those found in the natural ones, it is now the most widely used for many commercial applications.[138-142]

Briefly, CVD is kinetically driven and it is achieved by deposition of carbon from its gas phase species (*e.g.* methane, 0.5-5%)) in the presence of excess hydrogen.[122, 140, 143-145] Such a reaction is induced by either thermal energy *e.g.* hot filament or microwave activation (MW-CVD) of gas-phase reactants generating a plasma to create reactive radical species ($CH_3^{\bullet}$), which then deposit as a solid on the substrate surface.[122, 140, 143-145] The temperature of the reaction is usually maintained in excess of 1000 K.[122, 123, 129, 140, 143-145]

The excess hydrogen present in the gas-phase is essential for diamond growth using CVD techniques.[129, 130, 142, 146-149] It acts as a stabilising agent via combination with the nucleation and growth sites of the sp^3 lattice.[129, 130, 142, 146-149] Hydrogen atoms are generated during gas-phase activation, they then react with both carbon containing molecules in the gas-phase and C-H bonds on the substrate.[129, 130, 142, 146-149] In this way the diamond lattice is stabilised by forming surface radical sites, which are able to react with carbon-containing radicals, adding to the diamond lattice.[129, 130, 142, 146-149] Additionally, rearrangement of carbon atoms that build the sp^3 structure to the more thermodynamically stable graphitic sp^2 carbon is inhibited.[129, 130, 142, 146-149] Hence, the reactive atomic hydrogen drives the conversion of any non-carbon sp or sp^2 bonded carbon to diamond sp^3 bonded carbon.[129, 130, 142, 146-149]

Diamond can be grown as a single crystal, which is achieved using a single-crystal diamond as the growth substrate, where carbon atoms deposited onto the single crystal substrate adopt the orientation of the parent substrate. Polycrystalline diamond, where

multiple crystallites with different crystal orientations are present is achieved when the substrate used is itself polycrystalline in nature *e.g.* tungsten, titanium, silicon or contains diamond seeds. Thin film growth across the parent substrate occurs by the nucleation of crystallites of diamond or continuous growth from the seed diamond particles.[129, 146, 148, 150-155]

Growth proceeds in all directions, hence crystallites of different lattice orientation form. These different grains grow at different rates and are dependent on the preferential facets and crystal orientations, with some orientations growing at faster rates than others. Once a film is formed, the grains continue to grow, increasing in size as the film grows thicker. The growth process for diamond is depicted in Figure 1.8.[129, 146, 148, 150-155] Though CVD growth results in high-quality diamond films/plates with minimum incorporation of non-diamond carbon, it is regarded as a slow growth method, where the constant "turn-over" at the diamond surface is about 0.1 – 10 μm hr^{-1}.[129, 142, 147-149] For further information and in-depth reviews about diamond synthesis, growth and processing, see references131, 139, 142.

1.2.3.3 Diamond and BDD surface termination

After removal from a CVD synthesis oven, the diamond surface is hydrogen (H-) terminated and hydrophobic. Oxygen (O-) termination, leading to hydrophilic surfaces, can be achieved by oxygen plasmas, oxidative acid treatment (chemical process) and via anodic polarisation in acidic media. Contact angle measurements can help distinguish between the two surface terminations, Figure 1.9. These surface terminations can impact electrochemical measurements and must therefore be taken into account. The contact angle of H-terminated diamond with water in air is around 90°. However, H-terminated surfaces are thought to oxidise over time to a more stable O-terminated surface in air. Consequently, O-terminated surfaces are normally preferred for electrochemical applications. Using X-ray photoelectron spectroscopy (XPS); the functional groups of O-terminated surfaces have been determined as hydroxyl (C-OH), ether (C-O-C) as well as carbonyl groups such as ketones (C=O) and carboxylic groups (-COOH). The crystallography of the diamond surface plays a role in which groups are present at the surface.[156, 157]

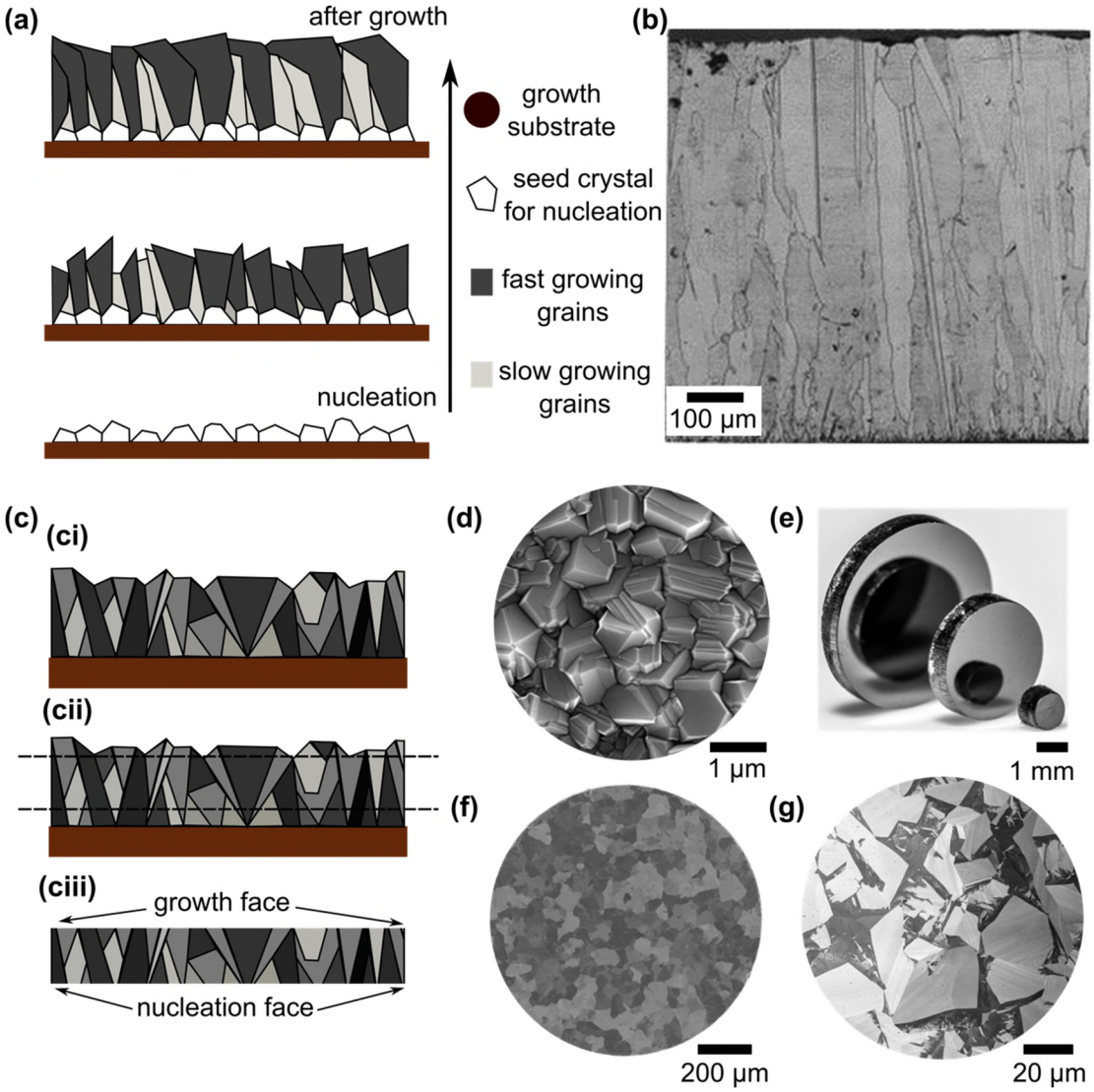

Figure 1.8: Schematic presentation of polycrystalline diamond growth and synthesis. (a) Illustration of the nucleation and growth stages. (b) SEM side face image of diamond at the end of the growth process. (c) Diamond film grow to a certain thickness (ci), which then cut and polished both sides (cii), and the resultant free standing BDD is ready for use (ciii). (d) SEM image of as grown MW-CVD BDD. (e) Image of the free-standing BDD plates. (f and g) FE-SEM image of the BDD surface after lapping and polishing, which is then used for the electrochemical studies.[122, 123, 129, 130, 158]

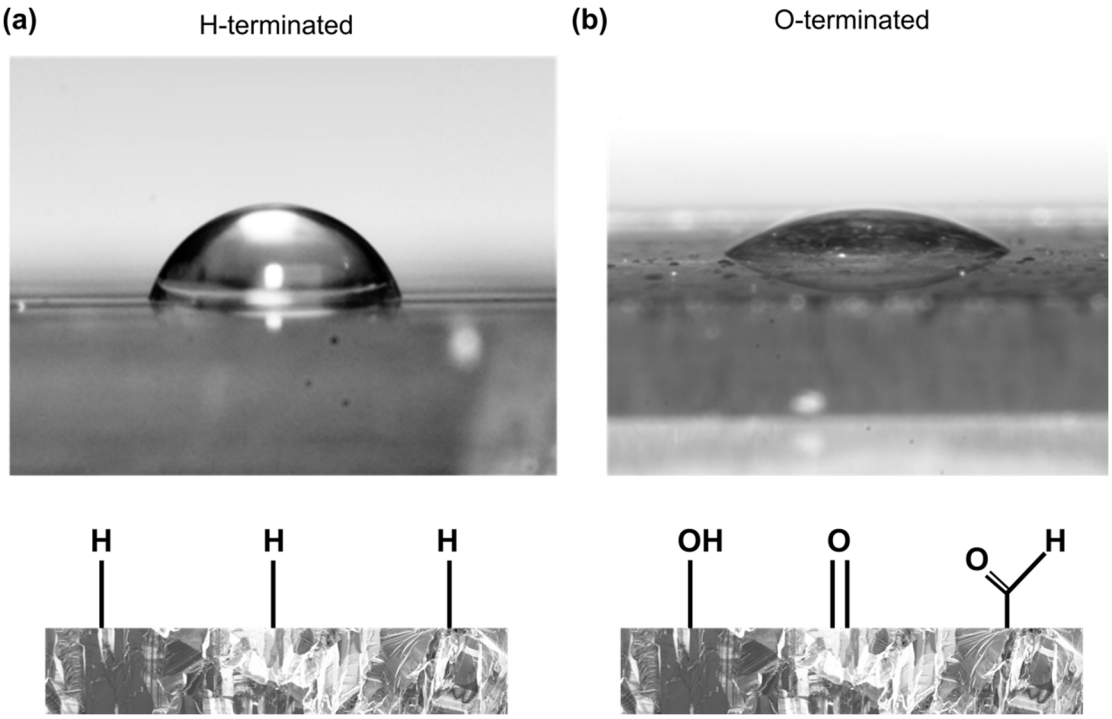

Figure 1.9: Surface termination of diamond or BDD. (a) Hydrogen terminated surface shows a wide contact angle between water droplet and the hydrophobic surface in air, where (b) O-terminated diamond exhibits a small contact angle. Note: H-terminated surface contains only hydrogen, whereas O-terminated surface features different functional groups such as hydroxyl, ketone and carboxylic groups as shown in the schematics.[122, 129, 130]

Given the ability to control the synthesis and growth conditions, various diamond properties can be tailored.[159] The most prominent feature is the electrical conductivity. Diamond is carbon; however, incorporation of other elements, such a nitrogen (N) and boron (B), either side of carbon in the periodic table, occurs in nature and thus is also possible during laboratory synthesis. Diamond manufacturers introduce boron containing gas (*e.g.* boron hydride B_2H_6) to the carbon gas feedstock to grow electrically conductive BDD, while retaining many of the intrinsic diamond properties. Further information about the properties of BDD are discussed in the next section.[132, 133, 139-142, 147-149, 160]

1.2.3.4 Structure, doping and properties of diamond

Diamond is an allotrope of carbon, its structure is made of tetrahedral, sp^3 bonded carbon atoms, which create a face centred cubic lattice (fcc) as presented in Figure 1.10, where each C atom is surrounded by four carbon atoms.[130, 161]

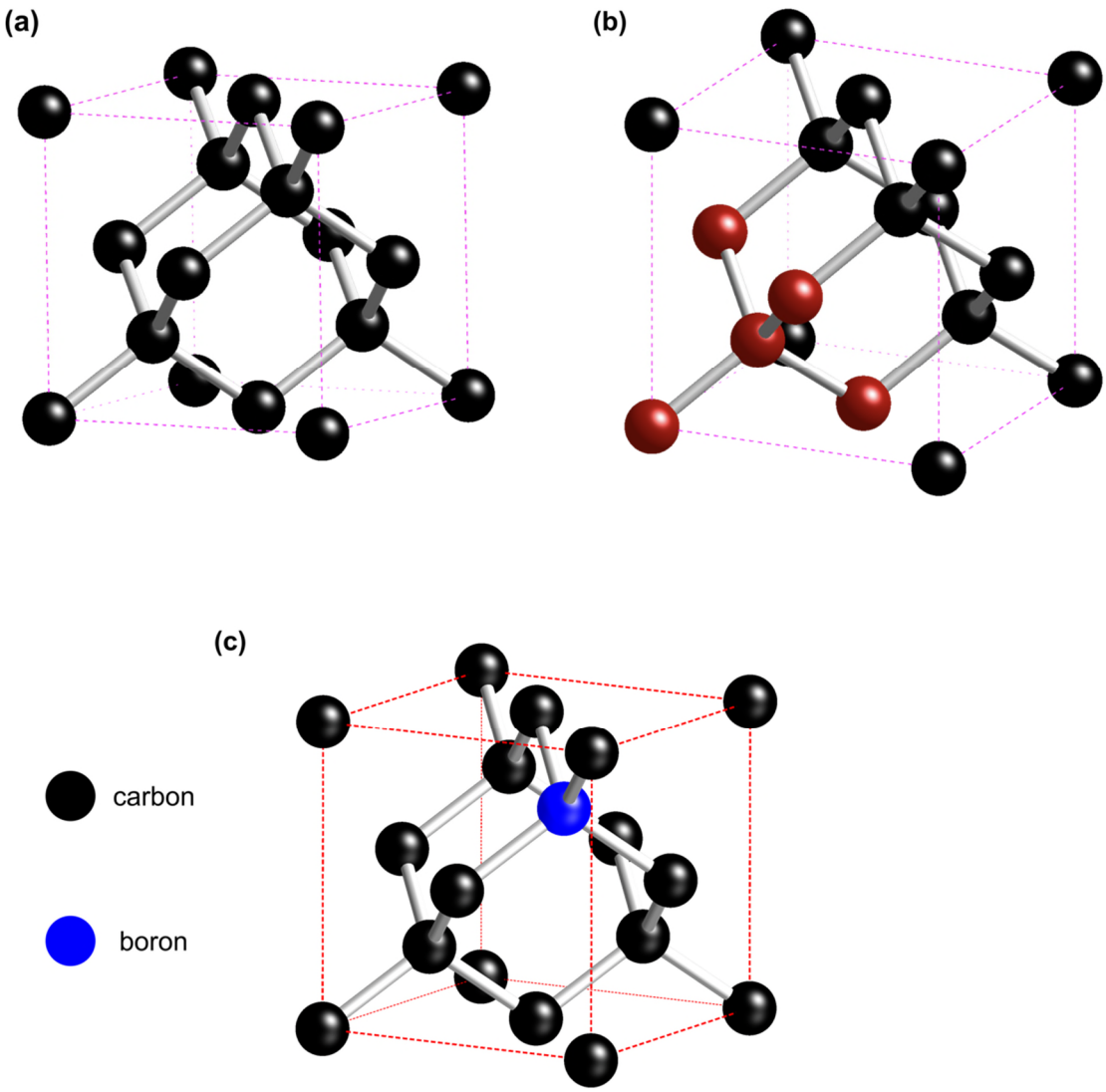

Figure 1.10: Diamond structure (a and b) sp^3 carbon atoms form the tetrahedral structure of diamond, the highlighted red carbon atoms represent the tetrahedral unit within the structure. (c) boron doped diamond structure is formed by replacing one carbon with a boron atom.

All bonds between carbon atoms are single σ bonds (covalent) with no π bonding as found in other allotropes of carbon such as graphite. The C-C bond length is 0.154 nm with a C-C-C angle, α, of 109.5°. This unique structure gives diamond its well-known characteristics and properties, which are listed in Table 1.2.[130, 131, 161]

Intrinsic or un-doped diamond is an insulator (wide band gap semiconductor). By virtue of its sp^3 structure, where all electrons of each C atom are involved in the bonding, the energy gap between the valence and the conduction band is wide with a value of 5.47 eV at 300 K, Figure 1.11(a). As a result, intrinsic diamond features two properties;

firstly, it is visually colourless due to its wide spectral transmission range (226 nm – 500 μm); secondly, it has extremely high electrical resistivity (10^{16} Ω cm).[125, 131, 139, 150, 162-174]

Table 1.2: Properties of diamond

Property[150, 175, 176]	**Value**
Thermal conductivity	2200 W m^{-1} K^{-1}
Hardness	85-102 GPa
Thermal expansion coefficient	1.0 ± 0.1 ppm K^{-1} at 300 K
Spectral Transparency	226 nm – 500 μm
Electronic Band-gap	5.47 eV

Diamond doping is achieved by replacing a small number of carbon atoms in the lattice with N or boron (B) (the dopant), thus diamond acquires a new property "electrical conductivity". For 3.5 g cm^{-3} there are around 3×10^{23} C atoms cm^{-3} in a diamond lattice. When doped with B, an electron hole is introduced into the lattice resulting in an acceptor level, E_a at 0.37 eV above the valence band; see Figure 1.11(a). For a very low doped diamond lattice $<10^{17}$ [B] atoms cm^{-3}, the activation energy required to excite electrons from the valence band to the acceptor level is still quite high and the diamond material possesses large resistance. In the case of medium doping concentrations, in the range of $10^{18} – 10^{19}$ [B] atoms cm^{-3}, the boron atom-atom spacing becomes small enough so that wave-function overlap between boron atoms leads to the formation of an impurity band and thus a lowering of the activation energy; see Figure 1.11(b). Diamond that has such doping level exhibits resistivity of ~ 2×10^3 Ω cm and is considered a semiconductor. By increasing boron concentrations to around ~ 1.5×10^{19} [B] atoms cm^{-3}, hopping conduction is assumed to occur and the resistivity of the material falls sharply.[125, 131, 139, 150, 162-174]

Once boron concentrations reach > 10^{20} [B] atoms cm^{-3} (1 in 1000 carbon atoms replaced with boron), the activation energy reaches zero for electron excitation from the valence band to the acceptor band and the transition to metallic conductivity occurs. The resulting diamond material is considered semi-metallic *i.e.* the number of charge

carriers (holes) is high enough that the material behaves like a metal (resistivity of ≤ 0.1 Ω cm). In this case, high doping densities of boron cause an overlap of the wave-functions in acceptor atoms creating a continuum of states between the acceptor level at 0.37 eV and the valence band, see Figure 1.11(c). The doping density of a material is typically measured using secondary ion mass spectrometry.[125, 131, 139, 150, 162-174]

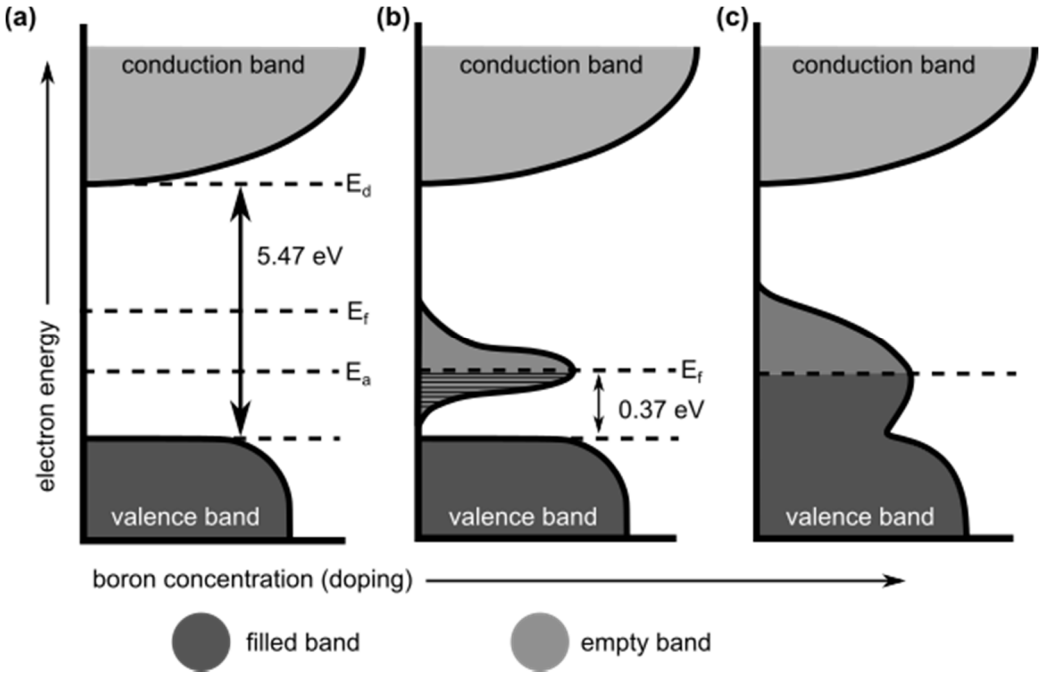

Figure 1.11: Schematic representation of the band structure for (a) intrinsic diamond, (b) moderately doped and (c) and highly doped diamond with boron. E_a and E_d are the energy associated with the acceptor and donor levels and E_f is the fermi level.[168]

The relationship between electrical resistivity and boron concentration in synthetic diamond has been studied and is shown in Figure 1.12. This demonstrates the transition between conduction modes with varying boron doping density. The concentration of boron incorporated into the diamond lattice has a near linear dependency on the boron concentration of the gas mixture of the reactor and is very much dependent on the crystal face undergoing growth. Boron up-take into the crystal face (111) is 10 times higher than for a (100) crystal surface. Thus, BDD, unless grown in the single crystal form, is described as a heterogeneously doped material.[125, 131, 139, 150, 162-174]

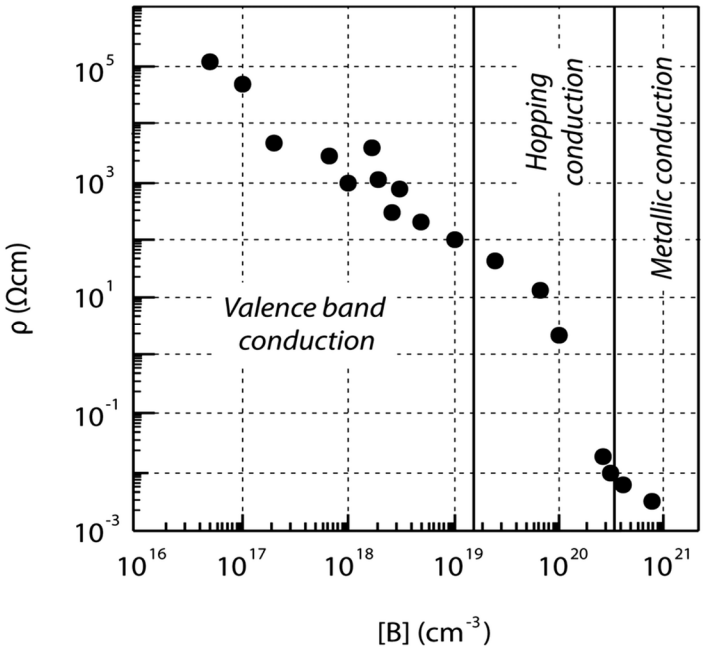

Figure 1.12: Room temperature electrical resistivity of BDD as function of the concentration of boron (the dopant).[165]

1.2.3.5 BDD as an electrode material

The electrode material type also represents a major factor influencing the process of metal reduction and phase formation at the surface.[119, 122, 177] Metal electrodes made of Au, Pt can be used, however their narrow solvent window, poor deposit adhesion to the surface, high cost and possible physicochemical reactions such as surface corrosion, and adsorption, can limit their use. For this reason, carbon materials are typically used as a support for metal recovery electrochemically in aqueous solution.[178-181]

In the first report of diamond based material use as a substrate for electrochemical studies, Iwaki highlighted the wide potential window and low background currents associated with these materials electrochemistry.[173] Swain et al. also, reported the wide featureless solvent window and low capacitance of BDD.[125, 174] Additionally, BDD is more mechanically strong, resistive to harsh environment and corrosion and exhibit high durability.[123] BDD shows very high thermal conductivity and conductivity.[122] Due to its unique electrochemical characteristics, BDD electrodes have been used in many applications such as waste water treatment, electroanalysis and detection of neurotransmitters, organic compounds (hydrazine for example) and environmental sensors.[182-185] Use of BDD in fundamental physico-chemical studies or in energy application such as electrodes in fuel cells or batteries remain relatively unexplored.[186]

For many of these application, the BDD surface can be modified with metal nano-structures or conductive polymer layers to add additional features and access properties such hydrogen adsorption and catalysis of alcohols.[187] Consequently, BDD is used in this work to explore electrochemical deposition in aqueous, organic and mixed solvents.

1.3 Electrode-solution interface formation

We have discussed earlier each component of the interface separately (*i.e.* the electrolyte and the electrode) so, what happens when both of them come in contactv? In general, surfaces carry excess electric charge, when two dissimilar phases meet, an electrified interface is established and perturbation of the solution composition near the electrode occurs.[23, 188, 189] At the interface, the forces experienced by ions and solvent molecules are anisotropic.[23, 190] Thus, a new solvent structure, which is different from that of the bulk develops.[191] There will be a net orientation of solvent dipoles and a net excess charge in any volume of the solution adjacent to the electrode surface.[7]

As the interface is now electrified *i.e.* acquired a net/excess charge, an electric field is developed.[192] For a metallic electrode, free electrons will move away or towards the interface depending on the direction of the electric field.[193] As a result, a net charge will be induced on the electrode surface, which will be equal in magnitude and opposite in sign to that of the electrolyte (*i.e.* this is known as the electrical double layer (EDL), which can be described simply as a sheet of negative charges (electrode) next to a sheet of positive charges (solution) or vice versa).[194] Consequently, charge separation occurs across the boundary between the solid (electrode) and the liquid phase (solution or electrolyte).[194] This gives rise to an interfacial potential difference (Galvani potential difference, $\Delta\phi$).[194, 195] Models have been developed to provide insights about the EDL, these are (1) Helmhotz model; (2) Gouy–Chapman model (G-C); (3) Stern model, and (4) Esin and Markov, Grahame, and Bockris, Devanathan, Müller model, shown in Figure 1.13.[10, 23, 88, 188, 196-198]

In the Helmholtz model of the interface the solvated ions arrange themselves along the surface of the electrode but are held away from it by their hydration spheres (Figure 1.13(a)).[23, 188, 195, 199, 200] The outer Helmholtz plane (OHP) is established and is known as the plane running through the solvated ions. The Helmholtz model represents a simple model of the EDL, where the electrical potential changes linearly within the

layer bounded between the electrode surface and the OHP plane (Figure 1.13(a)).[23, 188, 195, 199, 200] In an enhancement of the Helmholtz model, the inner Helmholtz plane (IHP) was suggested to form when ions lose their solvating molecules and become attached to the electrode surface by chemical bonds.[23, 188, 195, 199, 200] However, the Helmholtz model ignores the disrupting effect of thermal motion, which tends to break up and scatter the rigid outer plane of charge. Figure 1.13(b) depicts the G-C model of the diffuse EDL, where the disordering effect of thermal motion is considered. The G-C model shows how the interfacial region concentrations of anions and cations differ in the G–C model from the bulk concentrations *i.e.* ions of opposite charge cluster close to the electrode and ions of the same charge are repelled from it.[23, 32, 188, 195, 196, 199-203]

In other terms, it is supposed that the disordering forces arising from the thermal energy of the ions should oppose the ordering tendency induced in the interphase region by electrostatic forces. Consequently instead of considering a simple compact layer (the Helmholtz layer), these thermal and electrostatic forces are assumed to result in an equilibrium, in which the excess surface charge density, σ_S, counter balancing the surface charge density, ϕ_M, on the metal, is at a maximum close to the electrode surface. This diminishes in an approximately exponential way with increasing distance from the electrode surface, thereby giving rise to a diffuse layer adjacent to the electrode. Detailed analysis indicates that the thickness of the latter region will depend on the potential applied to the electrode and on the concentration of ions in the electrolyte.[23, 32, 188, 190, 196, 199-203]

The Helmholtz model overemphasises the rigidity of the local (interface) solution, whereas the G–C model underemphasises the structure of the interface, [23, 32, 188, 190, 196, 198-203] see references 184-189. In a refinement of both models, the ions, which are close to the electrode are constrained into a rigid Helmholtz plane, while the ions that are located outside that plane, are spread in a similar fashion to the G–C model, [23, 32, 188, 190, 196, 198-203] see references 32, 41, 174, 176, 182 as well. This model is known as the Stern model and is shown in Figure 1.13(c).[198] Stern considered ion sizes and avoided treating ions as point charges only, where solvated ions can approach the electrode surface to a distance equal to its solvated radius. At the electrode surface, there is a region of high electric field and low dielectric constant (ε_r) with a row of firmly held counter ions (Figure 1.13(c), cation at OHP in this case as the electrode is negatively charged).

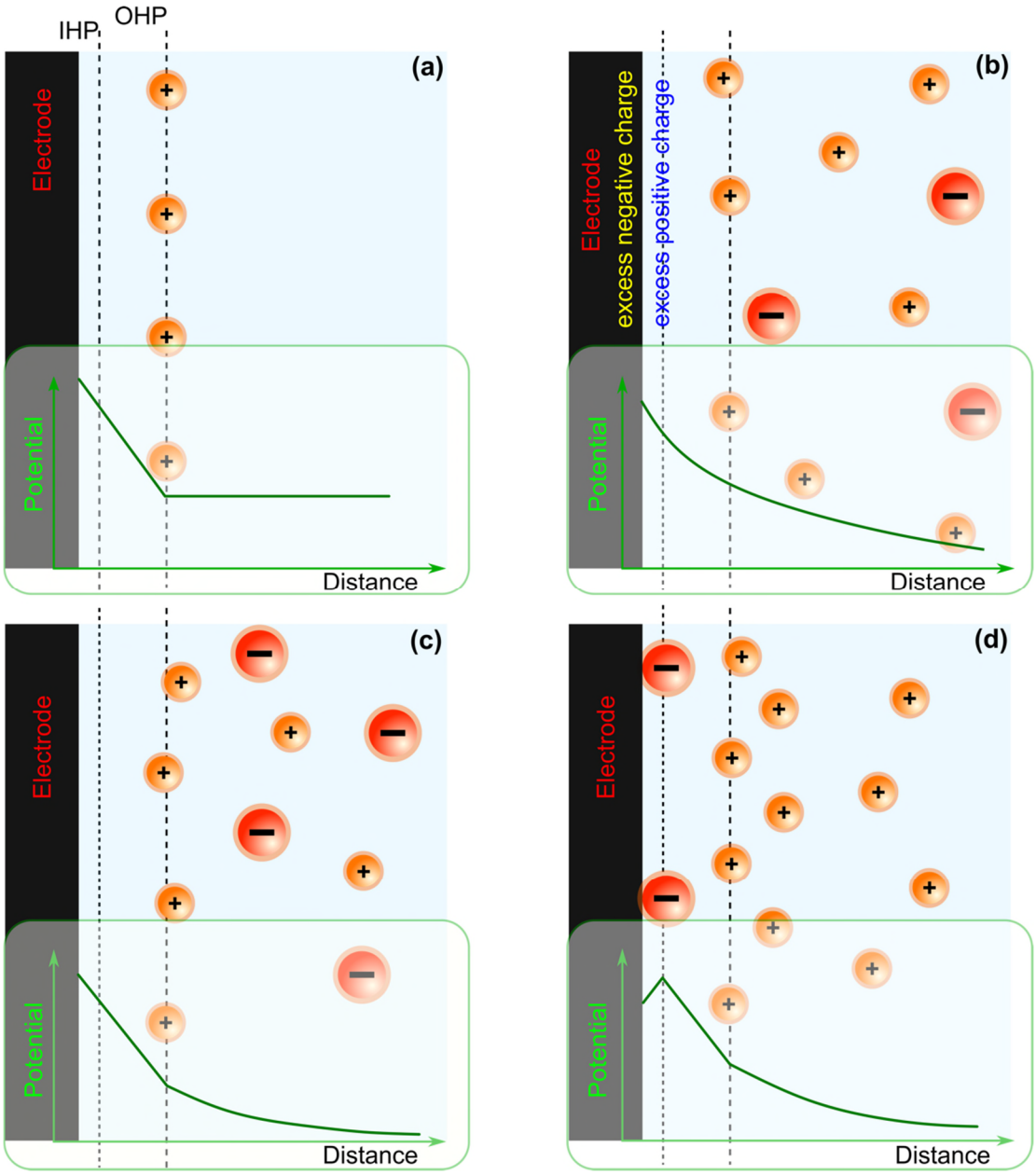

Figure 1.13: Schematics of the different models for the EDL at electrode|electrolyte interface, for ion distribution and potential versus distance from the metal surface. (a) Helmhotz model; (b) Gouy–Chapman model; (c) Stern model, and (d) composite of models from Esin-Markov-Grahame, and Bockris-Devanathan-Müller model.[194] Schematic potential change is superimposed.[195]

Beyond that there is the diffuse layer, where a balance between the ordering electrostatic force and disordering thermal motions exists. The dielectric constant increases rapidly with distance in this region. The line of demarcation between the

compact and diffuse regions is the OHP. Electrical potential drops linearly with distance within the inner compact region (IHP+OHP) after which it decreases in an approximate exponential manner with distance within the diffuse region, and approaching to zero in the bulk solution.[23, 32, 188, 190, 196, 198-203]

Further improvement to these models, led to the development of the Grahame model, which adds an IHP to the Stern model.[32, 191, 199, 204] In the IHP, de-solvated ions that had been adsorbed specifically to the surface are considered because they would be able to be within the immediate proximity of the surface. The potential difference between points in the bulk metal and the bulk solution is the Galvani potential difference, $\Delta\phi$.[23, 32, 188, 190, 196, 198-203] Yet another level of sophistication is found in the triple layer model displayed in Figures 1.13(d) and 1.14, [23, 31, 32, 36, 88, 91, 191, 199, 204-213] see references 32, 40, 41, 45, 86, 89, 177, 185 for further discussions. In this model, the IHP is introduced and regarded as the location of the electrical centres of specifically adsorbed ions. These ions are strongly adsorbed onto the electrode surface and are partially de-solvated. Thus, a reversal of electrostatic potential in the region between the IHP and the OHP establishes. Primary and secondary water layers are introduced with differing dielectric properties. The primary water layer is located immediately adjacent to the electrode surface. The secondary water layer is located as a hydration sphere around a solvated cation and anion. This model accounts for the solvent interactions with the electric field at the electrode, assigning orientations to dipoles of the solvent molecules which are dependent on the relative charge, for more information consult 32, 40, 41, 45, 86, 89, 129, 177, 185.[23, 31, 32, 36, 88, 91, 129, 191, 199, 204-213]

Efforts are undergoing to further develop better understanding of the electrified interface.[203, 214-220] For example, in a recent work by Crumlin et al., ambient pressure X-ray photoelectron spectroscopy (AXPS) and electrochemical modelling were used to probe the interface of a single crystal gold electrode. Using this method, information about the potential distribution in the EDL was extracted. The study showed that there is a potential drop over the compact layer and the structure within the double layer region is dependent on both the applied potential and the electrolyte solution.[219]

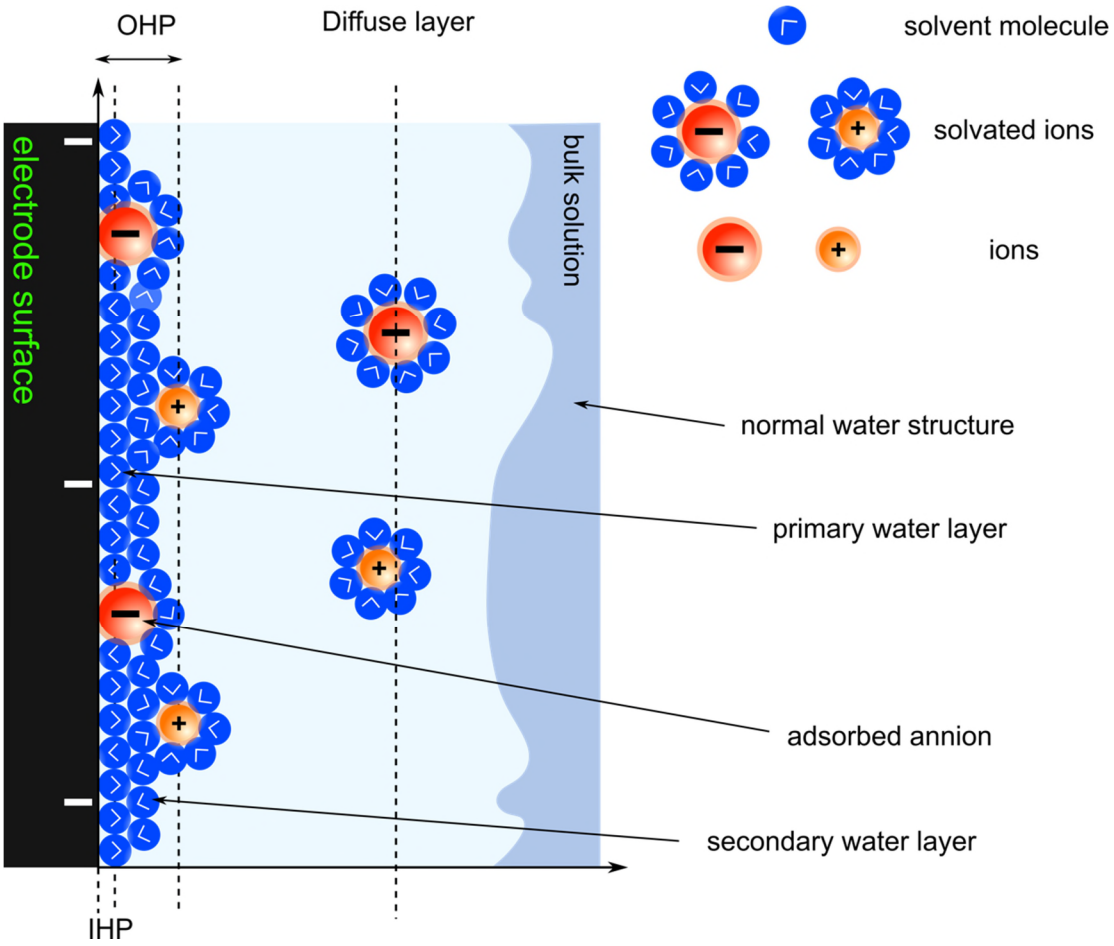

Figure 1.14: A representation of the Bockris-Devanathan-Müller model for the electrical double layer at the electrode|electrolyte interface.[23, 88, 96]

1.4 Kinetics and mechanism of electro-deposition (or electro-reduction)

All electrochemical experiments carried out in this work use a three electrode cell set-up (Figure 1.3(a)), where the potential of working electrode is measured with respect to a reference electrode and current flows between the working and the counter electrode.[7-28, 29, 221] Ideally, no current passes through the cell, until the potential reaches or exceeds the equilibrium potential, E_{eq} of the redox process of interest.[7, 10, 28, 222, 223] When a cathodic potential (E_{app}) greater than the equilibrium potential (E_{eq}) is applied, the metal ion reduction process begins, Equation 1.1.[22, 223-225] This process is known as electrodeposition and the difference between E_{app} and E_{eq} equates to the overpotential (η) (*i.e.* departure from the equilibrium), Equation 1.3.[13, 226-230]

$$\eta = E_{app} - E_{eq} \qquad \text{Equation 1.3}$$

Consequently, the magnitude of η can be controlled and the resulting cathodic current or current density provides a measure of electrodeposition.[26] During electrodeposition, there are three possible deposition regimes; (1) a charge transfer or activation controlled, (2) competition between charge transfer and diffusion *i.e.* mixed control, and (3) diffusion controlled or mass transport region.[7, 10, 28] Charge-transfer between the electrode and an ion or a molecule, involves transfer of charge carriers, these can be electrons or ions, across the double layer at the solid-electrolyte interface.[10, 28] Charge-transfer can be the rate limiting factor when it is slow compared to mass transport.[10, 28] During electrodeposition, under conditions where excess inert salt is present, a concentration gradient, for the ion of interest, is established, thus mass transport process is an essential component of electrodeposition.[10, 28] The electrodeposition potential can be considered diffusion-limited (mass transport controlled) and hence rate-determining, when the charge transfer is very fast (*e.g.* high η) and no other reactions take place.[10, 28] If both charge transfer and mass transport are competing, then the overall electrode reaction can be described as a mixed kinetic-diffusion controlled process.[10, 28]

1.5 Electro-nucleation and phase formation and growth

1.5.1 Atomistic view of electro-nucleation and growth

As stated, earlier metal electrodeposition occurs as a result of Equation 1.1, shown in more detail in Figure 1.15, which illustrates the steps involved in electrodeposition at the atomistic level.[14-16, 28, 231-234] Specifically, deposition (in aqueous solution) involves (1) transport of the solvated metal ion (for example, $[M(H_2O)_x]^{n+}$) to the electrode surface crossing the interfacial solvent and double layer; (2) at the surface, electro-reduction via charge transfer (electron) takes places, followed by (3) de-solvation (dehydration for aqueous) *i.e.* partial or complete loss of the solvation shell and ad-atom formation, then (4) surface diffusion of ad-atoms; (5) grouping of ad-atoms (clustering) to form a stable nucleus, and finally (6) growth of the nucleus to a crystal by incorporating ad-atoms at preferential sites in the lattice structure of the metal crystal (note: in literature this process is also called irreversible ad-atom incorporation).[14-16, 28, 225, 231-234]

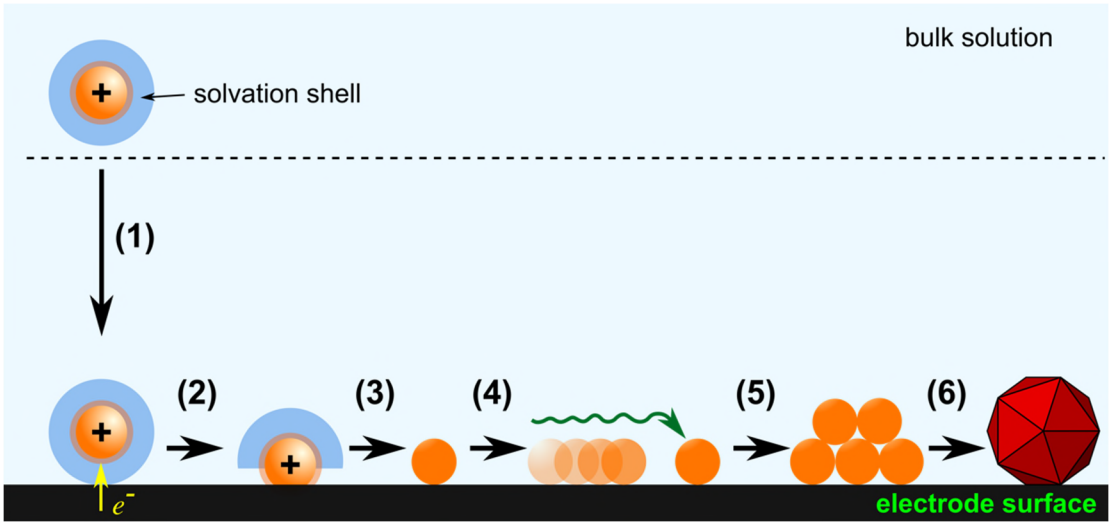

Figure 1.15: Steps involved in the formation of stable nucleus and its growth on an electrode comprised of a different material.

1.5.2 Thermodynamics, kinetics, and theory of nucleation and growth

Nucleation and growth are a general scientific concept,[235-237] which covers and applies to phase formation in many scientific research fields such as nanoparticle synthesis in colloidal solution, thin film growth, atomic layer deposition, electrodeposition and many more.[9, 18, 238] Generally, it can be divided into homogeneous and heterogeneous processes and both describe the nucleation and growth of a crystal via atomic addition to form a growing thermodynamically stable crystal up to a point where the reaction is halted (*i.e.* irreversible growth).[9, 18, 238]

Homogeneous nucleation takes place in a uniform media *i.e.* there are no different phases involved in the process, hence there are no specific sites to catalyse reactions, for example particle formation in liquid (colloidal synthesis).[239-241] On the other hand, when nucleation occurs at preferential sites between two physically different phases (*e.g.* liquid and solid, etc.), then such processes are known as heterogeneous nucleation.[9, 12, 14, 237, 242-248] Electrodeposition on a foreign electrode surface is regarded as heterogeneous nucleation process.[249, 250]

The theoretical interpretation of electrodeposition was first described for metal crystal nucleation and growth on a perfect defect free metal surface by Erdey-Gruz and Volmer in 1930.[242, 251] However, real surfaces suffer from defects and imperfections, discussed by Frank and Burton et al..[252] Understanding nucleation and growth has been classically interpreted based on thermodynamic and dynamic data extracted from current-time (*i*-

t) or potential-time (*E-t*) or current-potential (*i-E*) plots, as discussed in more detail below. Such information is used to infer as to what is happening on the surface at an atomistic or microscopic level.[16, 231, 253, 254] Progress in developing surface imaging and characterisation techniques, to directly visualise the surface, has led to the development of *ex-situ* and *in-situ* microscopy and spectroscopy methods, such as SEM, AFM, SERS, and SECM, which provide greater insight about nucleation and growth.[94, 104, 245, 248, 255-279] However, resolution of many of these techniques is limited to nm dimensions and long capture times, limiting information capture in the early stages. Consequently, improved spatio-temporal data collection and capturing is required, ultimately at the atomic level dimension and pico to nano-second capture times. Recently, using TEM, more information about electrodeposition at the sub-nm level was extracted and further understanding of growth kinetics developed.[280, 281] see Section 1.7 for more details.

The electrochemical reduction of M^{n+} to M^0 ($M^{n+}_{(sol)} + ne^- = M_{(ads)}$) is described using the Nernst equation assuming reversibility, Equation 1.4, which defines the electrode potential by defining the activity of the metal ad-ions (ad-atom) adhered to the surface.[26, 28]

$$E_{rev} = E^o + \frac{RT}{nF}\ln\left(\frac{a_{M_{eq}^{ads}}}{a_{M^{n+},sol}}\right) \qquad \text{Equation 1.4}$$

Where E^o is the standard potential of the redox equilibrium between bulk metal and a solution of M^{n+}, $a_{M_{eq}^{ads}}$ is the equilibrium surface activity of ad-atoms, and $a_{M^{n+},sol}$ is the activity of M^{n+} in solution, R is the gas constant, T is the temperature and F is the Faraday constant. As discussed in section 1.4, for electrodeposition to take place, η is required for the system to move away from a position of equilibrium. This process is referred to as overpotential deposition (OPD). As a consequence of applying η, a current flow (seen as an increase of charge and current *vs.* time for chronoamperometric methods) and the activity of atoms adhered to the surface ($a^*_{ad\text{-}atom}$) will change. The, Nernst equation can be re-written to include the dependency of the change of a metal ad-ion's activity on η, in other words this quantity may be modified at will varying the electrode potential to a new value $E = E_{rev} + \eta$, where η is the overpotential at which the surface activity of M satisfies the relation in Equation 1.5.[26, 225, 238]

$$\frac{a_{M^{ads}}}{a_{M^{ads}_{eq}}} = \exp\left(\frac{-n\,F\,\eta}{RT}\right) \qquad \text{Equation 1.5}$$

Solvation and the arrival of ions to the surface, as well as ad-atom formation and diffusion on the surface prior to cluster formation and growth are fundamentally important, but they are yet to be understood. A stable nucleus made of number of atoms (cluster) is referred to as a new interface, which requires an excess of free energy ($\Delta G_{nucleation}$) (N_{at}) to compensate for its creation at the boundary of the new nucleus or nuclei centre and the surface.[26, 225, 238] Thus, to activate such process and overcome the thermodynamic barrier, a supersaturation must be achieved. In electrodeposition, η is the driving force for supersaturation.[10, 26, 225, 238]

The free energy of formation of cluster of N_{at} atoms, $\Delta G_{nucleation}$ (N_{at}), has two terms, the first component is a negative term, ΔG_v (N_{at}), which accounts for the transfer of N ions to the nucleating and growing phase.[10, 26, 225, 238] Hence the thermodynamic energy decreases by the phase transformation of N_{at} atoms to a particle as the volume of the cluster increases.[10, 26, 225, 238] The second component is a positive term, ΔG_s (N_{at}), associated with the increase in surface energy due to the creation of the cluster surface assuming a growing sphere, as shown in Equations 1.6, 1.7 and Figure 1.16. [10, 26, 225, 238]

$$\Delta G_{nucleation}(N_{at}) = -\Delta G_v\,(N_{at}) + \Delta G_s(N_{at}) \qquad \text{Equation 1.6}$$

$$\Delta G_{nucleation}(N_{at}) = -N\,n\,e\,|\eta| + \Delta G_s(N_{at}) \qquad \text{Equation 1.7}$$

For a spherical nucleus formation, Equation 1.7 can be modified to Equation 1.8.

$$\Delta G_{nucleation} = -\frac{4}{3}\pi r^3\left(\frac{n\,e\,F\,\rho}{MW}\right)|\eta| + 4\,\pi r^2\sigma_t \qquad \text{Equation 1.8}$$

Nucleation and growth can be treated from two points of views, either the classical nucleation theory or the atomistic theory, both theories are based on the Becker-Doering approach describing the formation of nucleus as a sequence of bimolecular chemical reactions where each cluster of size N_{at} (*i.e.* critical nuclei that contains specific number of atoms or have a specific size) can gain or lose an atom leading to size transformation events. At equilibrium, the rate of atom incorporation into the nucleating nucleus or atom detachment is equal, Equation 1.9.[10, 26, 225, 238, 248, 282]

$$Nc(1n) \overset{atom}{\Longleftrightarrow} Nc(2n) \overset{atom}{\Longleftrightarrow} Nc(3n) \overset{atom}{\Longleftrightarrow} Nc(4n) \ldots\ldots\ldots Nc(xn)$$ Equation 1.9

From the classical viewpoint, N_{at} has a relatively large size (of nm dimensions) and can be treated as a continuous variable. The quantity ΔG_s (N_{at}) can be expressed in terms of specific surface energy($4\pi r^2\sigma$), where σ is the surface tension or free energy of formation of the surface related to the appearance and disappearance of nucleus. η is related to ΔG_v (N_{at}) by, ΔG_v (N_{at})= F|η|/V_m, where V_m is the molar volume and it is equal to MW (molecular weight) / ρ (mass density), Equation 1.10. The relationship between the free energy of nucleus formation and the size of nucleus and the dependence of the nucleus size on η is presented in Figure 1.16, where the formation of critical nucleus represents the maximum work of formation.[10, 12, 26, 225, 238, 248]

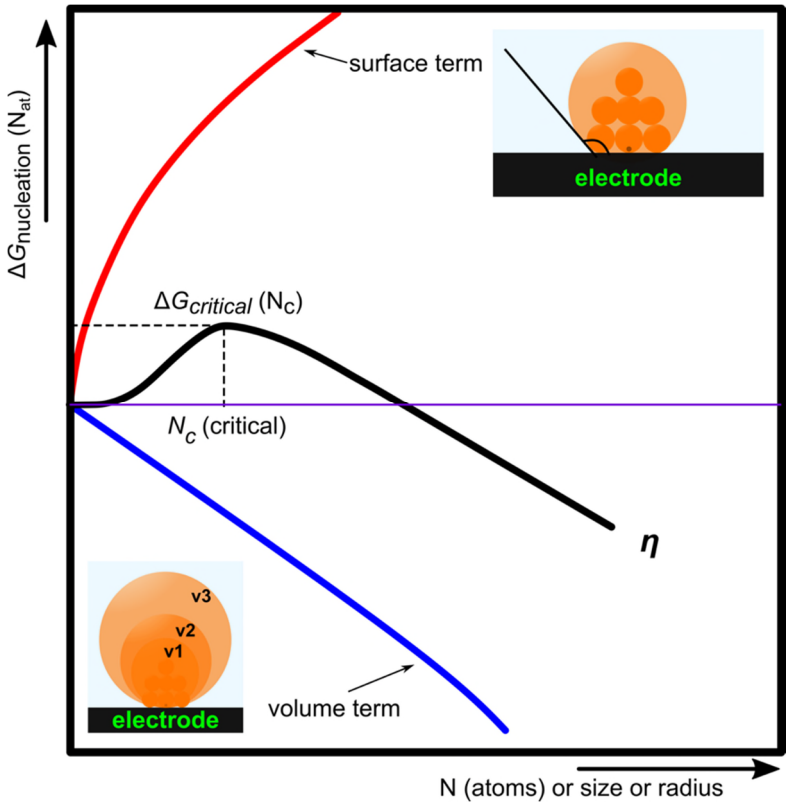

Figure 1.16: Illustration of the change of the free energy of cluster formation (nucleus) as function of size (*i.e.* number of atoms or radius) or the nucleation work for forming a nucleus of a specific size, which is the sum of its crystal volume free energy and surface free energy, ($\Delta G_{nucleation}$) (N_{at}) . N_c is the critical size.

From Figure 1.16, a given nucleus will only prosper if the addition of another atom to its lattice results in a negative change of free energy as its volume increases, otherwise

the newly formed nucleus will disappear. Therefore, only nucleus/nuclei larger than a critical size will grow.[10, 12, 26, 225, 238, 248, 279]

The size of a critical nucleus, N_c (Equations 1.10 and 1.11) according to the classical approach can be derived by differentiating Equation 1.7 or Equation 1.8 with respect to N_{at}. [10, 12, 26, 225, 238, 248, 279]

$$\frac{\partial \Delta G}{\partial N_{at}} = 0 \implies N_c = \frac{8\,B\,V_m^2\sigma^3}{27\,(n\,e\,\eta)^3} \qquad \text{Equation 1.10}$$

$$\Delta G_{critical} = \frac{4\,B\,V_m^2\,\sigma^3}{27(n\,e\,\eta)^2} \qquad \text{Equation 1.11}$$

Where B is a geometric factor related to the size of a 3D particle (volume and size), *i.e.* B = 36 π for a sphere and 18 π for a hemisphere and the critical size can then be expressed in terms of radius (r_c) assuming a sphere or hemisphere 3D growth, Equation 1.14.[10, 12, 26, 225, 238, 248, 279]

$$r_c = \frac{2\,\sigma\,M}{\rho\,n\,F\,|\eta|} \qquad \text{Equation 1.12}$$

Equation 1.12 shows the dependence of the size (expressed in terms of r_c and assuming the growth of a sphere or hemisphere 3D object holds) on η, where an increase of η leads to a decrease in the size, a basic assumption derived from macroscopic data. The formation of stable nuclei is thought to follow first order kinetics. The nucleation rate, J (number of nuclei cm^{-2} s^{-1}), Equation 1.13, according to the classical view is a probability process associated with the free energy of formation of critical clusters. Therefore,

$$J = A_{3D} \exp\left(\frac{-\Delta G_c}{k\,T}\right) = A_{3D} \exp\left(\frac{-4\,B\,V_m^2\sigma^3}{27\,k\,T\,(n\,e\,\eta)^2}\right) \qquad \text{Equation 1.13}$$

where A_{3D} is a pre-exponential constant and equal unity, and k is the Boltzmann constant, and n is the number of electrons. The evolution of the number of nuclei on a surface or the number density, $N(t)$, is given by Equation 1.14 in the case of single step (pulse) potentiometry after applying η for a specific time.[9, 12, 14, 16, 232, 237, 243, 247, 248]

$$N(t) = N_0\,[1 - \exp(-At)] \quad \text{Equation 1.14}$$

Where N_0 is the total number of sites where nuclei can be created, A is the nucleation rate constant; and then the nucleation rate can be expressed as $J = AN_0$. Consequently,

two cases of nucleation and growth kinetic mechanisms emerge. First when $A\ t >>> 1$ (also can be expressed as $A \rightarrow \infty$), then Equation 1.14 becomes $N(t) = N_0$, in which all nucleation sites are transformed into nuclei immediately (N_0 nuclei are instantaneously formed at $t = 0$).[9, 12, 14, 16, 232, 237, 243, 247, 248] Hence, nucleation and growth are assumed to follow an instantaneous nucleation mechanism and nuclei centres would be expected to have the same size. If $A\ t <<< 1$, then $N(t) = N_0\ A\ t$, and the nuclei are created gradually *i.e.* not all nucleation sites are converted into nuclei after the application of η. In this case, the nucleation and growth mechanism is described as progressive, and a broad size distribution of nuclei will be obtained. Both limiting conditions have been the subject of mechanisms to describe long time metal deposition, which can be deduced from analysing and fitting *i-t* curves to the Scharifker and Hills model and the models developed afterwards or by statistical analysis of microscopy images and data.[9, 12, 14, 16, 232, 237, 243, 247, 248]

Previously, we discussed that a nucleus has to reach a specific size (to be supercritical) and to be able to grow, because small nuclei will have a high ratio of surface area to volume. However, nuclei can be one or few atoms (discrete variable), hence the macroscopic treatment by classical theory isn't appropriate as specific surface energy or surface adhesion and tension and volume lose their physical meanings and $\Delta G_{nucleation}(N_{at})$ and $\Delta G_s\ (N_{at})$ can only be represented as discrete values. Hence, for the formation of an entity containing n atoms, N_{at}, an estimation of the surface energy associated with the formation process can be carried out using the bond energy between the atom and the substrate ($\Psi a\text{-}s$) and the atoms themselves ($\Psi a\text{-}a$). The values of these energies are restricted to the nearest neighbour and are equal to the bond energies in vacuum. Therefore, the surface energy $\Delta G_s\ (N_{at})$ follows, Equation 1.15.[9, 12, 14, 16, 232, 237, 238, 243, 247, 248]

$$\Delta G_s\ (N_{at}) = N\ \Psi_{kink} - \sum_N \Psi_x \qquad \text{Equation 1.15}$$

And Equation 1.7 can be re-written as

$$\Delta G_{nucleation}(N) = N\left(\frac{-4}{3}\right)\pi r^3\ \frac{F|\eta|}{V_m} + N\ \Psi_{kink} - \sum_N \Psi_x \qquad \text{Equation 1.16}$$

Where Ψ_{kink} is the bond energy of an atom in a kink position and $\sum \Psi x$ is the sum of the bond energies of atom(s) in all other position in an entity (cluster). Consequently, the relationship of the free energy of nucleus formation and the size of nucleus $\Delta G_{nucleation}$

(N_{at}) *vs.* N is represented as a minima and maxima, where the highest maximum at a given η corresponds to the critical nucleus size. The relationship between η and N_c is as shown in Figure 1.17.[9, 12, 14, 16, 232, 237, 243, 247, 248]

So, one can control the size of a critical nucleus by changing η, hence the equilibrium can be shifted towards conditions where the critical nucleus contains one or only few atoms or in some cases the active sites will be the critical nucleus and one atom can be considered as a supercritical nucleus over a large range of η.[9, 12, 14, 16, 232, 237, 243, 247, 248] However, the mechanism of nuclei formation is not fully understood and further investigation and experiments as well as theoretical treatment are required. In *Chapter 4*, we investigate whether experimentally we can electrodeposit a single atom by careful choice of η.

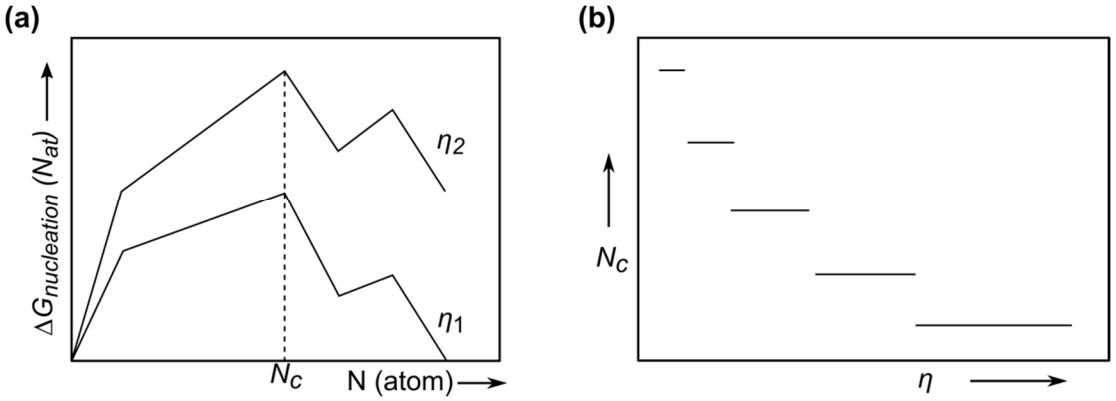

Figure 1.17: (a) The free energy of nucleation takes discrete values and is dependent on η and the nuclei can be one atom or more. (b) Variation of the number of atoms that build up the critical nucleus as function of η.[9, 12, 14, 16, 232, 237, 243, 247, 248]

1.5.3 Growth modes

The new nuclei appearing on the surface will further grow.[26, 238] General aspects of growth are illustrated in Figure 1.18. These are (1) formation of many nuclei on the surface Figure 1.18(a), (2) growth of newly formed nuclei and the formation of new ones, Figure 1.18(b), (3) further nucleation and growth of existing ones Figure 1.18(c), (4) commencement of overlap, Figure 1.18(d), and (5) overlap of all particles and formation of a film, Figure 1.18(e).[88, 225] It is important to note that the aforementioned growth is three dimensional (3D), commonly known in the case of nanoparticles growth.[10, 225, 238] Indeed, monolayer or atomic layer is a possibility since further

nucleation does not occur. In such case, the growth is described as two dimensional (2D), though the layer itself is three dimensional.[10, 225, 238]

The extent of the binding energy between the electrode (foreign) and the metal ions ($M_{ads\text{-}S}$) and the crystallographic misfit between the growing 3D metal particle and the electrode governs the mechanism during OPD, Figure 1.19.[9, 10, 12] In general, in the absence of any kinetic influences, the growth mechanism can be described in three ways. First, Volmer-Weber 3D island growth is achieved when the deposited metal atoms are more tightly bound to each other than to the substrate.[9, 10, 12] Nuclei form hemispherical islands, which then grow radially, and more ad-atoms are added by direct attachment to the growing island or particle.[9, 10, 12]

Second, Stranski-Kastanov growth mode, where both layer and 3D islands grow simultaneously due to the intrinsic existence of lattice misfits between the electrode and metal undergoing deposition.[9, 10, 12] Third, Frank Van Der Merwe layer-by-layer growth occurs when the metal deposit atoms are more tightly bound to the substrate than between themselves, which are featured during under potential deposition.[9, 10, 12] Nanoparticle electrodeposition and growth is usually described by the Volmer-Weber mechanism, however recent work *e.g.* references 272, 273, 278, 281, 283, 284 has postulated new mechanisms such as coalescence of the growing centre and fusion of neighbouring particles.

Irrespective of the growth mode, the concentration of ad-atoms in the interfacial region is a function of η with most depletion at or around the growing nuclei, for more details see references 26, 35, 217, 228, 234, 237, 238.[17, 26, 233, 244, 250, 253, 254, 285-287] Hence the rate of the growth is determined by the rate of metal ion conversion to ad-atoms and incorporation into the growing centre.[238, 278, 284] Furthermore, the rate of electroreduction of metal ions and thus the metal deposition rate can however depend either on the rate of mass transport of ions from bulk to the electrode (diffusion limited scenario) or the rate of electron transfer (kinetic limited scenario).[17, 26, 233, 244, 250, 253, 254, 285-287] Diffusion can be enhanced using rotating disc electrodes as an example, additionally the diffusion around the growing centres will be spherical and thus enhanced just at the perimeter of the growing islands, see references 269-271.[7, 17, 26, 233, 244, 250, 253, 254, 285-287] Finally, in all cases the nuclei and their growth are treated as occurring at fixed locations (*i.e.* nuclei are pinned to their primary location), and only ad-atoms can diffuse on the surface. Electro-reduction of ions is assumed to happen at

the growing nuclei where the metal ion in solution is reduced, leading to direct incorporation into the crystal of the growing islands (*i.e.* direct attachment). Changes of the surface during growth and formation of defects, that may influence further growth, are either neglected or not fully addressed.[238, 278]

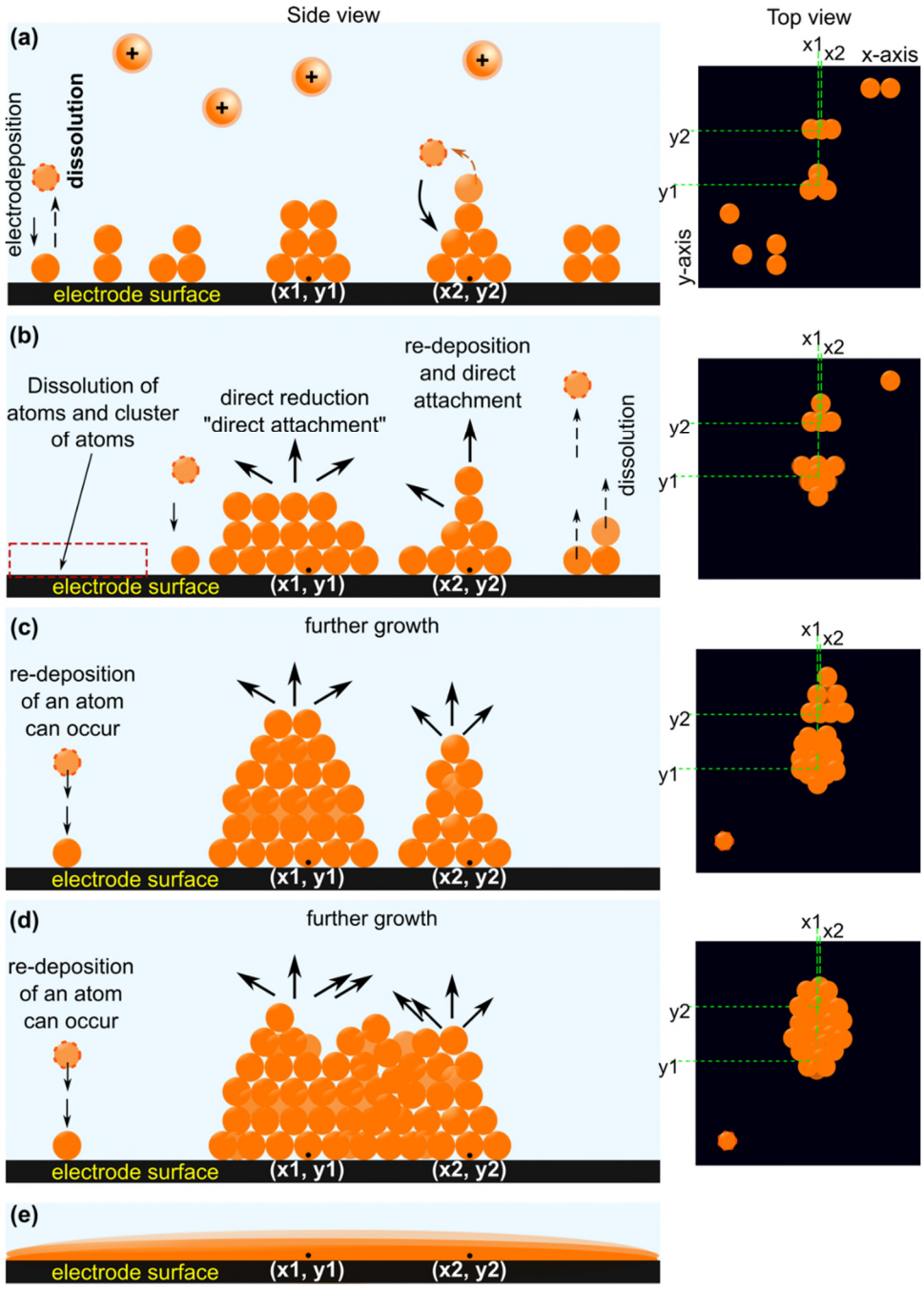

Figure 1.18: The various steps of the metal electro-nucleation and growth. (a) Formation of stable nuclei. (b) Simultaneous growth of the stable nuclei, dissolution of some nuclei and formation of new ones. (c) Further nucleation and growth also overlap may commence. (d) Complete overlap of neighbouring growing crystals/particles. (e) thickening and layer growth.

In *Chapter 4*, we provide further insights about the mechanistic aspects of metal nucleation and growth.

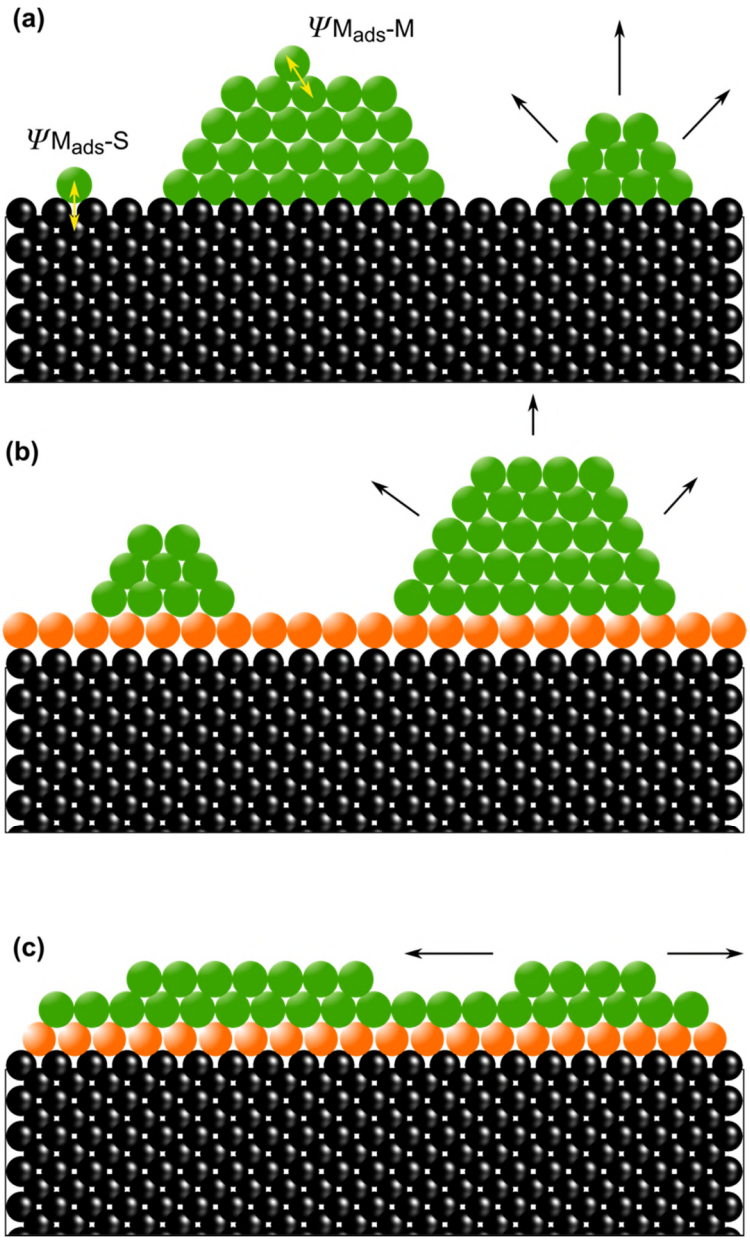

Figure 1.19: Illustration of the different growth modes. Black solid spheres represent the electrode, green solid spheres are the electrodeposited metal atoms and the orange ones represent one layer atomic deposition. (a) Volmer-Weber (growth of nanoparticles), (b) Stranski-Kastanov, and (c) Frank Van Der Merwe.[12, 243]

1.6 Potentiostatic current-time profile

On way to achieve electrodeposition is by applying a potential and recording the resulting *i-t* profile. This method can be considered as an *in-situ* measurement of

nucleation and growth and much work was devoted by many researchers to link the kinetics and mechanisms of electrodeposition that take place at the surface to changes of i as function of η and t.[17, 26, 233, 237, 238, 243, 244, 247, 253, 254, 285, 288, 289] For example, how mass transport (diffusional flux) or electron transfer enhancement can impact the electrodeposition.[228, 267, 270, 271, 273, 290-302] For a homogeneous surface such as amorphous carbon, when a specific η is applied, nuclei are expected to form at random locations over the electrode according to Equation 1.14.[253]

Nuclei are expected to grow since their size exceed the critical size, so they will grow irreversibly until the potential pulse terminates or the concentration of active species in the vicinity of the growing nuclei diminishes (under diffusion limited case).[238] Electrodeposition on foreign substrate then follows "mostly" Volmer-Weber growth mechanism by reducing metal ions directly on the 3D nuclei (hemispherical or spherical), which already have grown beyond their critical size (*i.e.* this mechanism can be called direct attachment). The chronoamperometric profile is used to relate the $i(t)$ response to the nucleation rate and the number of active sites (Equation 1.14).[233, 253, 254, 285, 286, 289, 303-306]

Indeed, many nuclei grow randomly on the surface and during this process both the concentration of active species and the η distribution in the vicinity of the growing nuclei change. This creates zones of reduced concentration and η, and hence the nucleation rate is reduced. Then, by considering the growth of multiple neighbour nuclei, their local zones of reduced nucleation rate spread and gradually overlap. This is a very complex problem, and may be solved by approximating the areas of reduced nucleation rate by the overlapping planar diffusion zones in which nucleation is fully hindered, see Figure 1.20.

Subsequently by assuming that these nuclei (also known as the growth centres), which are randomly distributed on the electrode surface, grow under hemispherical diffusion regime, then the total electrochemical current can be expressed by either progressive nucleation (Equation 1.17) or instantaneous nucleation (Equation 1.18):

$$i(t) = S_{electrode}\, j\,(t) = S_{electrode}\, \beta\, n\, F\, c\, \left(\frac{D}{\pi t}\right)^{1/2} \times \left[1 - \exp\left(-\frac{1}{2} A\, N_0 \pi \gamma \left(\frac{8\pi c M}{\rho}\right)^{1/2} D t^2\right)\right] \qquad \text{Equation 1.17}$$

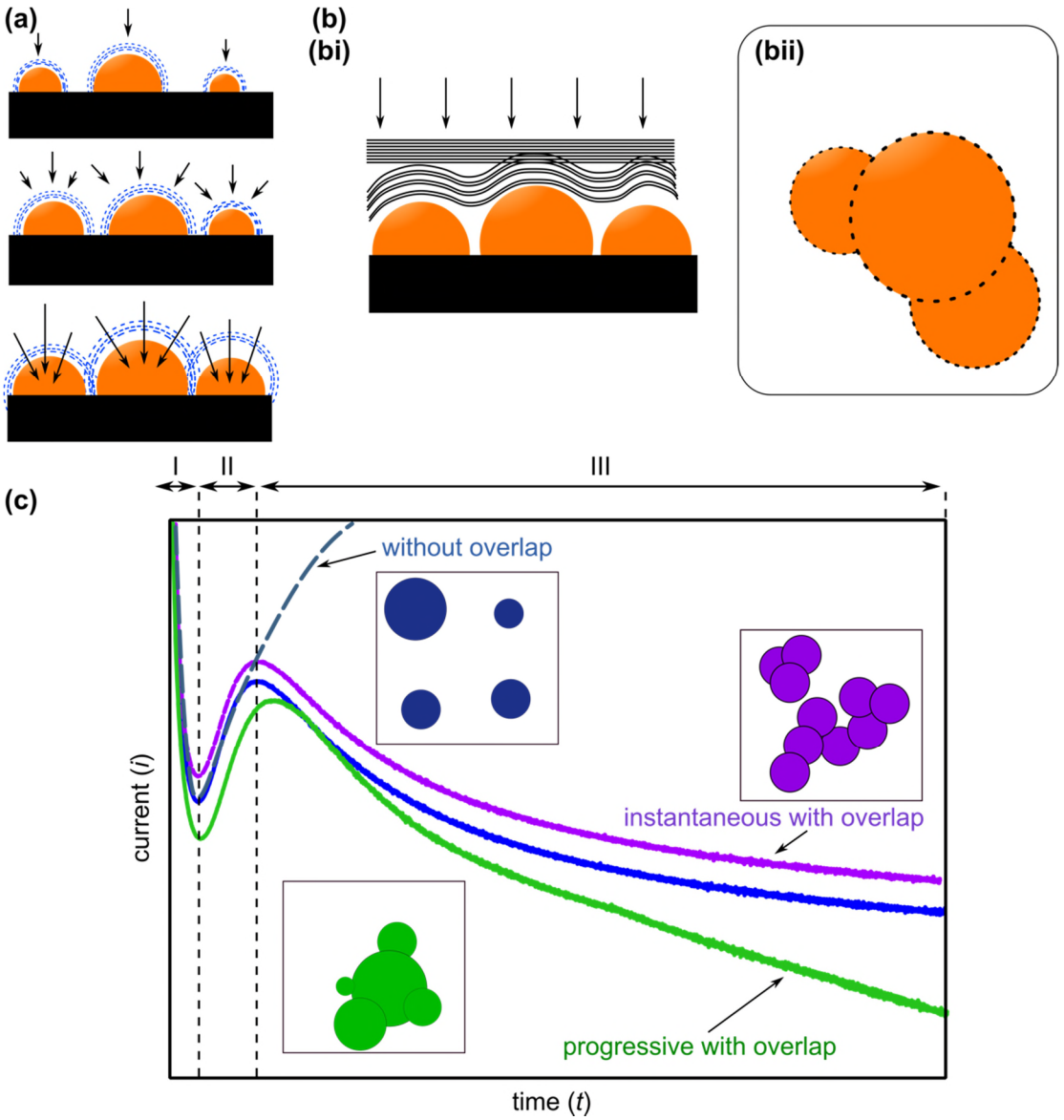

Figure 1.20: (a) Side view of the diffusional domains at short time scale are planar within the vicinity of the nuclei (region I in c) then become hemispherical as nuclei grow but they are still isolated hence they show independent convergent diffusion (region II in c). Nuclei can be thought then as a growing nanostructure (*e.g.* NPs), hence as these structures grow more and more, surface coverage is expected to increase and partial overlap of diffusion zones happen (intermediate case off convergent and planar diffusion). (b) Side and top projection to the electrode surface. Nuclei are large enough and within the vicinity of each other, complete overlap of diffusional domains occurs and the diffusion is now planar (region III in c). (c) *i-t* profiles illustrating the different 3D nucleation and growth modes under diffusion-controlled electrodeposition (blue is experimental, grey, green and violet are theoretical fitting to SH).

$$i(t) = S_{electrode}\, j\,(t) = S_{electrode}\; n\,F\,c\,\left(\frac{D}{\pi t}\right)^{1/2} \times \left[1 - \exp\left(-N_0\pi\left(\frac{8\pi cM}{\rho}\right)^{1/2} Dt\right)\right] \qquad \text{Equation 1.18}$$

Where $S_{electrode}$ is the electrode surface area, $i(t)$ is the current or the equation can be expressed in terms of current density $j(t)$, c is the concentration of the electrolyte, D is the diffusion coefficient, ρ is the density, M is the molar mass, β a non-dimensional factor, which equals 1 (see references 253, 254) or 4/3 according to references 286, 305, and γ equals 1 or 4/3 (see references 22, 253, 307).[10, 22, 28, 238] These equations are known as Scharifker-Hills models (SH) for 3D nucleation and diffusion limited growth.

In principal, both the progressive and the instantaneous equations (1.17 and 1.18) should lead to *i-t* transients similar to the ones shown in Figure 1.20(c), which are expected to display a peak just after the charging current (*i.e.* the initial high current at $t = 0$, which decays quickly, traditionally attributed to double-layer charging).[253, 288, 296, 308] Beyond the charging region, the current increases due to the increasing number of growing nuclei of the new phase on the electrode surface, which leads to an increase of the active surface area, where electrochemical reduction is happening.[238, 278] During this time, nuclei undergo uncoupled hemispherical growth and $i \propto t^3$ when nucleation is progressive and $i \propto t^2$ when the process is instantaneous.[238, 278] The current reaches a maximum then decreases as the diffusion zones at the vicinity of the growing nanostructures coalesce.[238, 253, 278, 303] These curves are thought to be associated with 3D nucleation and are characteristic of diffusion limited growth processes.[303]

SH models and equations have been the subject of much research work, and were further improved by *e.g.* accounting for adsorption processes prior to nucleation, multiple nucleation and growth events in the absence of any overlap.[233, 309, 310] An example of such a modification is found in the Scharifker and Mostany model (SM), which simply joined both the progressive and the instantaneous assumptions in one equation, see Equation 1.19.[233] Other examples of SH reformulations include work by Mirkin and Nilov, Heerman and Tarallo, and Sluyter-Rehbach, see references 9, 14-16, 232, 286, 289, 304-306, 310-312 for more information.

$$i(t) = S_{electrode}\, j\,(t) = S_{electrode}\; n\,F\,c\,\left(\frac{D}{\pi t}\right)^{1/2} \times \left[1 - \exp\left(-N_0\pi k_{SM} D\left[t - \frac{1}{A}(1 - \exp(-At))\right]\right)\right] \qquad \text{Equation 1.19}$$

Despite the mathematical modifications to SH and any consideration such as the changes of the behaviour of the diffusional fields around the NPs, all models are based on two major factors. First, nuclei are treated as fixed points (*i.e.* once a nuclei forms at a specific site, it is pinned there), and second, only the Volmer-Weber mechanism is considered for 3D growth.[10, 18, 243] Developing theoretical models or modifying the existing ones for nucleation and growth do not fall under the remit of this thesis. However, we attempt to study and extract information about nucleation and growth of Pt on BDD in *Chapter 3* from the *i-t* profiles using SH models and SM model, when comparing growth modes under room temperature and laser pulse heating conditions (see *Chapter 3*, section 3.4.1, Figure 3.5).

The usual practice to analyse *i-t* curves involves, (1) fitting the chronoamperometry data obtained at different η to one of the models referred in section 1.6. This way, if we consider using Equation 1.17 as an example, D and AN_0 can be obtained by a standard least-squares algorithm. Similar parameters can be acquired from the fits of equations 1.18 and 1.19. Conversely, (2) morphological characterization is carried out to estimate the number of particles/nanostructures at different deposition times in order to get $N(t)$. (3) The nucleation rate constant (A) and N_0 can be inferred from equation 1.14 in order to compare the values with those obtained with the model fit and hence test the validity of the models for different experimental systems. If nucleation rates are derived for different η, the size of the critical nucleus can be deduced by using the theory described in section 1.5.2.

The values of the nucleation rate constant and number of active sites extracted from the *i-t* curves can differ significantly from those calculated from the AFM images (*e.g.* results in *Chapter 3*). Nevertheless, some reports claim a good agreement between experimental and theoretical data.[313] However, generally, morphological characterization provides larger number densities of NPs than predicted from fitting *i-t* profiles to SH or SM models.[283] Several hypotheses suggested that the inconsistencies presented may arise from the presence of nucleation exclusion zones.[238] These are considered in the SH model as areas, where the probability to find a new nucleus is reduced, but not completely halted.[253] Hence, the measured current density does not describe the overlap of diffusion zones of single nuclei appropriately.[287, 314-317] On the other hand, discrepancies could stem from electrochemical deposition under mixed control, instead of either diffusion controlled or kinetically controlled deposition.[288, 318]

Also, physical coalescence of nuclei may take place and may lead to miscalculation of nucleation densities.[238, 278, 319] Moreover, the formation of sub-nm NPs (clusters) or the adsorption of metal atoms followed by surface diffusion may affect the interpretation of the *i-t* transients.[268, 280, 320-322] Finally, the nature of the chemical and electrochemical reactions or complexation of metal ions have been suggested to cause experimental deviations from the theoretical models.[268]

1.7 Visualisation of electrodeposition - experimental study of nucleation and growth using microscopy techniques

Obviously, determination of N_0 and N_t accurately is not that simple. These values depend on finding precisely the dimensions of nuclei, which rely very much on the resolving power of the imaging technique.[238] Because of the presence of the nanostructures (*e.g.* NPs) on a solid plate then the techniques available to characterise the substrates were first limited to *ex-situ* surface analytical tools such as SEM, AFM and STM.[7, 244, 267, 323-326] Practically, SEM can resolve NPs that have dimensions within 5-6 nm at best.[327] AFM/STM resolution can approach sub-nm provided a very flat low roughness electrode surface is used, however the lateral resolution is limited by the geometry of the scanning tip.[328] Additionally, *in-situ* methods *e.g.* using AFM have been used to explore nucleation and growth mechanism but its operation is not trivial and the presence of a liquid layer may impact the resolution negatively.[329, 330]

Ex-situ TEM offers better resolution, ultimately at the atomic level,[331] with *in-situ* TEM technology having been developed over the past few years.[332] It is then not surprising that TEM finds wide spread use by material scientists to study phase formation.[281, 321, 332] However, because the electron beam has to transmit through the sample, *ex-situ* TEM is limited to electron transparent materials.[333] *In-situ* TEM suffers from reduced resolution capability because the liquid scatters the electron beam.[334] Also, the high power electron beam may induce surface changes, and hence account for its effect is mandatory.

Nonetheless, using microscopy techniques such as SEM, STM, AFM and recently TEM to image the surface and extract information about nucleation and growth shows that theoretical and experimental treatment of *i-t* curves may not precisely account for what is actually happening at the interface.[270, 278, 280, 284, 335] This is because the *i-t*

transient represents a collection of responses of many processes and lacks the spatio-temporal resolution required to investigate metal electrodeposition at the atomic level and over a short time.[278, 332, 336, 337] Hence, extracting information about metal deposition and crystallisation solely using information based on *i-t* behaviour is non-trivial. However, surface analysis techniques are yet to provide enough evidence about the size of the critical nuclei and nucleation and growth mechanisms.

1.8 Thermo-electrochemistry

Thermo-electrochemistry involves the investigation of the effect of temperature on an electrochemical experiment.[338] The variation of the temperature in general allows for kinetics and thermodynamics measurements and may influence one or more parameters such as diffusion, and electron transfer kinetics.[339, 340] Thermo-electrochemistry can be achieved via two routes, (1) isothermal and (2) non-isothermal.[130] The former, is achieved by heating the electrolyte and hence all the electrodes immersed in the solution (the interfacial regions) using a water jacket.[341] Though it is the most widely used method, it suffers from few drawbacks such as (i) uncontrolled or uneven temperature regimes within the electrochemical cell and (ii) fluctuation of the potential reading due to imposing high temperature at the RE.[338] In the non-isothermal approach, the temperature of the surface of the WE only changes in a controlled fashion.[338] Furthermore, the WE can be heated continuously or heated and cooled simultaneously (pulse heating), thus only the temperature gradient is established at the WE-solution interface, while the temperature of both the RE and CE remains unchanged.[340]

In electrodeposition, enhanced mass transport deposition can be achieved by using *e.g.* a RDE or micro-electrode.[7, 342] Similarly, via increasing the temperature, the diffusional flux and electron transfer kinetics can increase, both of which can have an impact on electrodeposition.[338, 343, 344] Additionally, increasing the temperature leads to a shift of the onset of the electrodeposition of Ag to much lower η.[345] To achieve fast localised temperature change, scientists devised different techniques such as Joule heating and laser heating.[346] References 347-355, provide reviews on current thermo-electrochemical techniques. As an example, a focused laser beam was used to locally deposit Cu and Zn for applications in the field of microcircuit electroplating development.[356-359] Electrodeposition in conjunction with temperature control has mainly addressed kinetics, mechanisms of nucleation and growth, and production of

nanostructure that exhibit better electrocatalytic performance.[360-362] However, less efforts have been devoted to understanding how temperature variations may induce structural changes of the nanostructures and consequently their properties.

1.9 Electrodeposition from aqueous, non-aqueous and mixed solvents

There are a relatively large number of accounts of electrodeposition in aqueous solutions but less studies investigate such an important concept in non-aqueous (organic) solutions.[10, 363, 364] A mixture of both (*i.e.* mixed or binary solvents) was previously made to study thermodynamics of metal ion transfer between two phases as an example.[77] In recent studies, mixed solvents have gained further interest due to limiting water side effects (such as hydrolysis, which limits the solvent window range and prevent studying reactions that require η beyond water decomposition). Moreover, we can benefit from the capability of an organic solvent to dissolve many salts.[21, 365] For instance, electrodeposition of Ag from its cyanide organic solution has shown better deposition characteristics in comparison to deposition from $AgNO_3$ solutions.[21, 366] Conversely, the former is not a straight forward process and hence electroplating was carried in mixed solvents to find an alternative route to deposit Ag from such media.[21, 366] It is surprising to note that reports about electrodeposition or recovery of noble metals such as Pd from their catalyst compounds, which are used extensively in organic or inorganic synthesis are minimal. many industries use such reactions to produce many valuable products including but not limited to pharmaceuticals, fine chemicals and degradable polymers.[367, 368] Recovery of the precious metal in industry relying on using chemical compounds that are capable of binding to the metal centres in solution and can attach to insoluble porous solid materials such carbon.[369]

1.10 Thesis aims and objectives

This doctoral work is concerned with the development of understanding of metal electrodeposition on BDD electrodes from aqueous, non-aqueous (MeCN) and mixed solvent solutions. This thesis focuses on developing thermally driven electrodeposition as a synthesis technique for the production of catalytic nanostructures in a one-step

deposition and investigating the early stages of nucleation and growth of NPs. Both provide understanding for the fabrication of new materials for energy conversion at the atomic and nano level. We extend the electrodeposition work to explore the use of electrochemical techniques such as chronoamperometry as a recovery tool to remove precious metals from industrial solutions to meet stringent regulation's rules.

In particular, by utilising the physical properties of BDD as a very good heat conductor, *Chapter 3*, we aim to study the effect of temperature on the electrodeposition of Pt by using a single chronoamperometry step in tandem with laser pulse heating (non-isothermal method). Following this procedure, we avoid the disadvantages of iso-thermal and other non-isothermal techniques (section 1.8). The effect of laser pulses (*i.e.* periodic changes in temperature between hot and ambient) on the resulting structures, imaged using AFM, SEM and TEM techniques, is rationalised and their resulting electrocatalytic activity explored with respect to methanol oxidation.

In *Chapter 4*, we aim to provide dynamic information about the early stages of metal electrodeposition (Au) at the level of single atoms using scanning electron microscopy (STEM). Since many surface characterisation tools have limited capability to reveal nucleation and growth processes that are happening at the nano level only (Section 1.7), there is a need to visualise phase growth during the early stages of formation at the atomic level. We explore in detail the use of BDD as a dual functional electrode, where electrodeposition can be carried out and high resolution (atomic level) imaging can be acquired spontaneously using the STEM technique. The method is based on tracking Au nucleation and growth by recording electrodeposition at the same location, over different time intervals of deposition, then using *ex-situ* STEM for imaging and atom counting. The objective of this procedure is to provide mechanistic information on how nucleation takes place, *for example* what is the size of a critical nucleus. Moreover, we aim to examine how growth proceeds on the surface, *for example*, are there any processes happening on the surface or is electrodeposition only occuring between ions in the solution and the stable nuclei ?

Pd-acetate is widely used in the pharmaceutical industry, where the synthesis is usually carried out in MeCN media, therefore the aim of *Chapter 5*, is to investigate how ligands can hinder the electrochemical deposition of Pd from its Pd-acetate salt. We will study the influence of the ion-solvent interactions, and solvent composition on Pd electrodeposition. The solvent systems considered are pure organic (MeCN), pure

water and mixed compositions of both (MeCN-water binary system). A combination of electrochemical techniques, spectroscopy and high-resolution microscopy measurement will be carried out to elucidate the feasibility of electrodeposition and possible electroplating mechanisms. This will include understanding the role of the solvent in the process of ligand exchange and either bond formation or cleavage, which ultimately impact the deposition process. The second study will apply our learning from studies in pure and mixed solvents to test pre-concentration and electrochemical removal strategies in real pharmaceutical synthesis solutions, where Pd catalysts and other organic and inorganic compounds exist in the solution. Consequently, we aim to develop a proof of concept or a procedure discussing the possibility to electroplate Pd on BDD from industrial-like solutions to help pharmaceutical industries meeting the regulation limits of metals in the drug products.

The final Chapter summarises and contextualises the studies herein, providing an insight into the possible future studies using the newly developed electron transparent boron doped diamond and the developed electrodeposition techniques for materials synthesis and energy conversion applications.

Chapter 2

Experimental approaches and methods

2.1 Chemicals and Materials

2.1.1 Chemicals and solution preparation

Liquids used in this work are either aqueous, non-aqueous or mixed aqueous, non-aqueous solvents. All aqueous solutions used in *Chapters 3* and *4* were prepared from Milli-Q water (Millipore Corp.) with a resistivity of 18.2 MΩ cm at 25 °C. Water used to prepare solutions in *Chapter 5* is high purity de-ionised (DI) water (Purite, Select HP). For the non-aqueous experiments, far UV-Vis high purity MeCN was used, which was kept dry using molecular sieves. For NMR and IR analysis, deuterated water (D_2O) and MeCN-d3 (*i.e.* deuterated acetonitrile) were used. All chemicals were weighed using a four-figure analytical balance (Sartorius A2008), and are listed in Table 2.1.

Table 2.1: List of solvents and chemicals

Chemical	Formula	Purity	Supplier
Solvents			
Acetonitrile	C_2H_3N	99.9999%	Fisher Scientific UK Ltd.,UK
Deuterated acetonitrile	C_2D_3N	9.9999%	Acros Organics, UK
Methanol	CH_4O	9.9999%	Fisher Scientific UK Ltd.,UK
Ethanol	C_2H_5O	9.9999%	Sigma-Aldrich
Deuterated water	D_2O	9.9999%	Sigma-Aldrich
Chemicals for the electrochemical studies			
Palladium Acetate	$C_4H_6O_4Pd$	99.99%, trace metal basis	Merck and

			Sigma Aldrich
Tetrabutyl ammonium tetrafluoroborate	$C_{16}H_{36}BF_4N$	99.99%	Sigma Aldrich
Phenylboronic acid	$C_6H_7BO_2$	99%	Acros Organics
4'-Bromoacetophenone	C_8H_7BrO	99%	Acros Organics
Potassium carbonate	K_2CO_3	98%	Alfa Aesar
Potassium nitrate	KNO_3	99.99%, trace metal basis	Acros Organics
Nitric acid	HNO_3	99.99%	Sigma Aldrich
Perchloric acid	$ClHO_4$	99.99%, trace metal basis	Sigma Aldrich
Sulfuric acid	H_2O_4S	99%	Merck
Ruthenium (III) hexaamine chloride	$Ru(NH_3)_6Cl_3$	99%	Sigma Aldrich
Potassium chloride	KCl	99.99%	Sigma Aldrich
Hydrochloric acid	HCl	37%	Sigma Aldrich
Ferrocene	$C_{10}H_{10}Fe$	99.9 %	Sigma Aldrich
Ferrocene methanol	$C_{11}H_{12}FeO$	99.9 %	Sigma Aldrich

2.1.2 Electrode preparation and fabrication of boron doped diamond (BDD) TEM substrate

The BDD substrates/electrodes used in this work are provided by Element Six Ltd., Oxford, UK, and were synthesised using MW-CVD (section 1.3.3.2). The materials were suitably doped with boron (boron dopant level $>10^{20}$ B atoms cm^{-3}) such that all were above the metallic threshold.[370] The BDD was grown on a silicon wafer to a suitable thickness for it to be removed from the wafer as a freestanding BDD material.[176] The surface was polished using Scaife method,[371] to thin the material to a desired thickness. A minimum thickness of ~ 50 μm could be obtained this way, with a surface roughness of 1-3 nm.[129] The specific details of the BDD electrodes are outlined in Table 2.2.

Table 2.2: List of the BDD materials used in this work

Code	Type	[B] concentration (atom cm^{-3})	Thickness (μm)
MR 14	Polycrystalline BDD	3×10^{20}	630
MR 11	Polycrystalline BDD	3×10^{20}	200
MR 11	Polycrystalline BDD	3×10^{20}	50
MR 12	Polycrystalline as grown BDD	3×10^{20}	250

2.1.3 BDD disk preparation

1 mm diameter BDD disks (thickness = 450 μm, for the fabrication of glass sealed BDD electrode) and 9 mm diameter BDD disks (thickness = 200 μm, for pulse laser heating experiments) were cut from MR14 and MR11 BDD wafers, respectively using laser micromachining (wavelength: 355 nm, E- 55H-3-ATHI-O system, Oxford Lasers, UK) at 100 % power, 20 kHz.[129] The electrodes were cleaned by immersion in a bath

of boiling concentrated sulphuric acid supersaturated with KNO_3 for 30 minutes and then boiling concentrated sulphuric acid only for another 30 minutes to remove any remaining KNO_3 salt.[372] Finally the BDD was sonicated in DI water for 15 minutes. This ensured that the resulting surface of BDD is oxygen terminated and removed any amorphous carbon formed during the laser micromachining process. To make an ohmic contact, the back surface (nucleation side) of the BDD disks were sputtered using an E606 sputter/evaporator, Moorfields, UK, with Ti (10 nm)/Au (300 nm), followed by an annealing process at 500 °C for 4 hours in air, during which titanium carbide is formed to provide the Ohmic contact to the BDD.[129, 373, 374]

2.1.4 Glass sealed BDD electrode

Sputtered BDD disks were then sealed in a borosilicate glass capillary (i.d. 1.16 mm, o.d. 2 mm, Harvard Apparatus Ltd., UK) under vacuum. Electrical contact was made using a copper wire with silver epoxy (Chemtronics, RS Components Ltd., Northants, UK) in contact with the Au contact on the BDD surface. The end of the glass capillary was then polished using silicon carbide grinding papers to expose the BDD surface. Finally, epoxy resin (Araldite, Bostik Findley, UK) was used to cover the top of the capillary to fix the copper wire in place and ensure electrical isolation of the contact from solutions, Figure 2.1(a).[129, 130, 372, 375]

2.1.5 BDD electrode for atomic force microscopy measurement

For AFM data collection, BDD electrodes were prepared by placing directly a on a quartz slide that was sputtered with Ti/Au then silver epoxy was placed on the Au layer. After which 1 mm diameter back contacted BDD disk was placed directly on top of the conductive silver epoxy. This procedure ensures good electrical contact and a flat surface. Epoxy resin was employed to seal around the edges of the BDD disk to ensure all the exposed areas (sputtered quartz slide, edges of BDD disk) except the 1 mm diameter BDD electrode are insulated, Figure 2.1(b).[375-377]

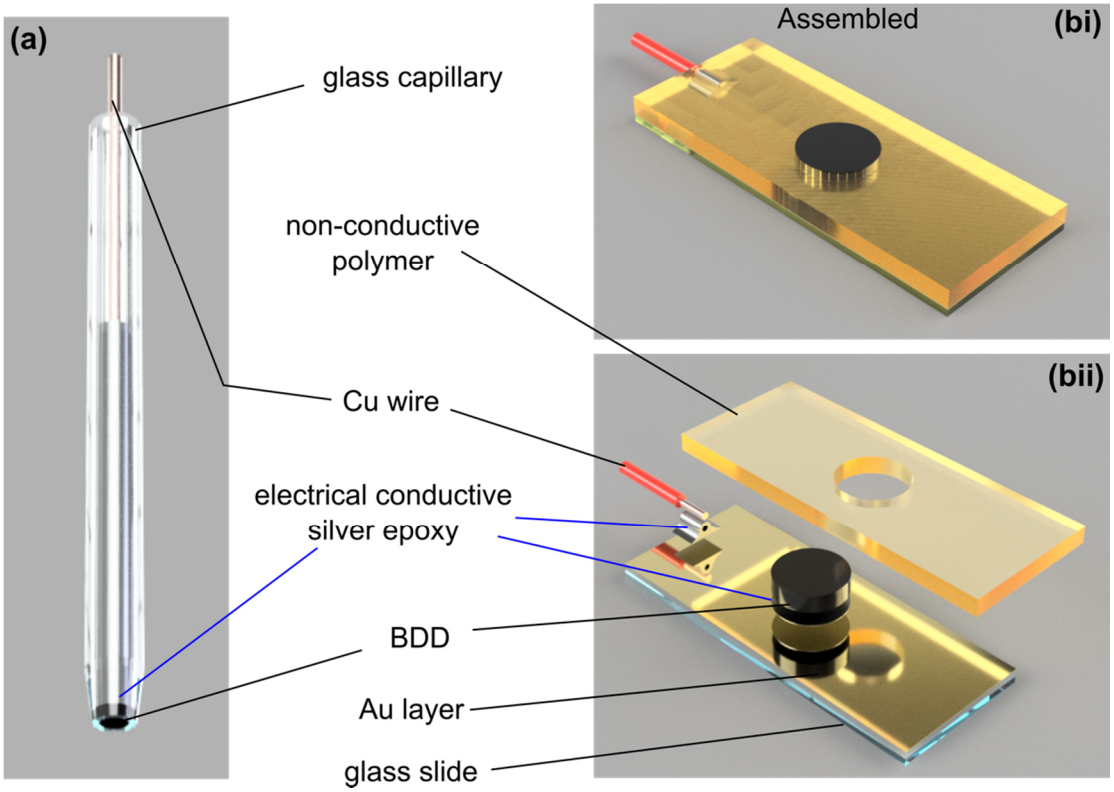

Figure 2.1: Schematic illustration of the different electrode designs used in this thesis, (a) glass sealed electrodes and (bi and bii) flat electrodes for AFM studies. (credit: Haytham Hussein and Joshua Tully)

2.1.6 Fabrication of BDD-TEM plate by ion milling

The fabrication of an electron transparent BDD TEM grid was performed using a freestanding polycrystalline BDD disk. The plate was mechanically polished to ~ 50 µm thickness, both sides showing a surface roughness finish of *ca.* 0.18 nm on the surface of a grain (2-8 µm). The plate was cut into disks of 3 mm diameter (suitable for insertion into the TEM holder) using laser micromachining and acid cleaned to remove machining debris. The plates were Ar^+ ion milled to electron transparency at an accelerating voltage of 6 kV and an angle of incidence of ~4° (Figure 2.2) using GATAN precision ion polishing system (PIPS). The sample was mounted on a post support using glycolphthalate bonding wax (Agar Scientific), allowing continuous milling as the sample rotated. Each side was milled in turn (approx. 2 hours each side) until a small hole (*ca.* 50 - 100 µm in diameter) was formed in the centre of the BDD disk. The disk was mounted in a clamp support for a final low energy ion mill of both sides of the disk at an accelerating voltage of 2 kV with a modulated ion beam to provide a smooth surface finish. The BDD TEM plate was subjected to an acid clean

process after the ion milling. The acid bath contains 0.1 M H_2SO_4, which was saturated with KNO_3 and a final cleaning step was run in 0.1 M HNO_3 to make sure the surface is free of any salt contamination and O-terminated.[378]

The roughness of the surface before and after ion milling was measured by AFM, which indicates that the surface roughness on a grain has increased from 0.18 nm (before ion milling) to 6.28 nm (after). To make an ohmic contact to the electrode the upper quarter of one of the edges was sputtered (Moorfield MiniLab 060 Platform) with Ti (20 nm)/Au (400 nm) and annealed in a tube furnace for 5 hr at 450 °C in air.

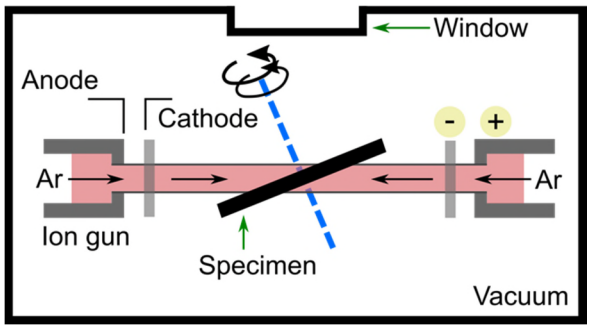

Figure 2.2: Schematic illustration of the ion milling set-up and the method employed to thin down BDD in the centre of the BDD disk to electron transparency.[379]

2.2 Experimental electrochemistry; measurements and setup

Electrochemical measurements were made using a commercial potentiostat either a CHI potentiostat (CH Instruments Inc., US) or an Ivium Compactstat (Ivium Technologies, Netherlands). For a review on basic function and operational procedure of a potentiostat, see references 7, 29, 221. The electrochemical cell is constructed of three electrodes, Figure 2.3, namely working (WE), reference (RE) and counter (CE) electrodes. The potentiostat is used to keep the WE at a desired potential with respect to the RE, which is carried out by passing the current from the WE to the CE, this arrangement is shown schematically in Figure 2.4.

Figure 2.3: Three electrode set-up. (credit: Joshua Tully)

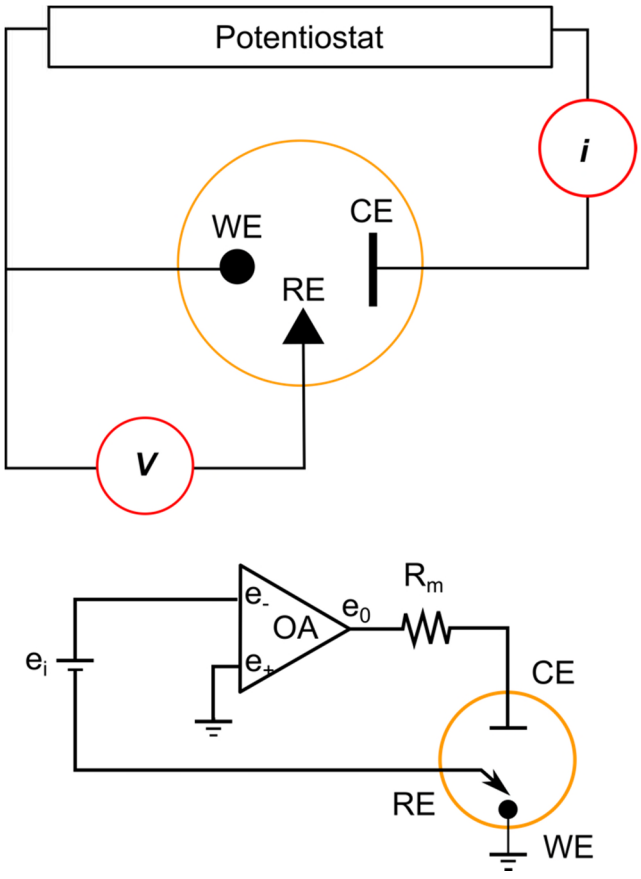

Figure 2.4: Typical three electrode electrochemical setup.[7]

The electrochemical cell was made either of glass, Teflon or PEEK. For controlled temperature measurements, the cell was surrounded by a jacket that allowed water

circulation, thus the temperature of the electrolyte was always controlled. BDD was used for all experiments as the WE. For aqueous experiments, saturated calomel electrode (SCE) was employed as a RE, and $Ag|Ag^+$ or $Pt|Fc^+|Fc$ systems were used for non-aqueous and mixed solvent experiments. A Pt gauze or carbon felt (very high surface area) were used as CE.

2.2.1 Cyclic voltammetry

Cyclic voltammetry (CV) represents, in many cases, the first choice to provide dynamic and thermodynamic information about the electrochemical system under study. It is a technique whereby the current response of a WE is excited by a triangular potential wave form.[380] The potential is swept linearly from a potential where ideally no faradaic reactions take place to a limiting potential value vs. a RE, where the rate of the linear variation can be controlled. The scan continues between two limiting potentials, anodic and cathodic, by repeating the excitation signal several times in both positive and negative directions.[7]

2.2.2 Chronoamperometry

In chronoamperometry (CA), a potential is applied to the WE, E_{app}, for a defined time, t, and the response of the electrode is recorded as current, i, which is presented as current-time plot. To achieve a single step potential chronoamperometry, the electrode is first held at a potential positive to the equilibrium potential, then a step is applied to a more negative potential.[7, 10, 310]

2.2.3 Thermo-electrochemistry: pulsed laser BDD heating set-up (non-isothermal) and Isothermal electrochemical set-up

In this thesis, non-isothermal heating is employed consisting of an IR diode laser (LM-D0296, LIMO, Germany) 914.7 nm, of maximum power density ~ 3.8 kW cm^{-2}, controlled by a laser diode controller (LDC1000, Laser Electronics Ltd., Lincolnshire, UK) and focused to a 1 mm diameter central circular spot on the back face of the BDD electrode by the delivery lens. A dual-channel function generator (AFG3022B, Tektronix, US) was used as a master controller to ensure that the potentiostat and laser were synchronised and start at the same time when the experiment begins. In this way, the temperature of the WE can be brought to values above the water (solvent) boiling

point. By using materials such as BDD, surface roughening and oxide formation are avoided, which are observed when metal electrodes are used. Also, heating the back face of the BDD, rather than the front surface that faces the solution, brings an additional advantage over conventional laser heating. Since the laser beam does not pass through the solution, therefore no photo-chemical reactions are induced prior to or during any electrochemical measurements.[340, 375]

To calibrate the temperature, open circuit potential (OCP) was acquired for an outer-sphere redox mediator (*e.g.* ferro/ferri-cyanide) to measure the temperature coefficient β, according to Equation 2.1

$$\beta = \frac{\partial\, OCP}{\partial T} \qquad \text{Equation 2.1}$$

OCP values were collected using two separate cells housing one BDD electrode each and connected using a salt bridge. Whilst one cell is kept at fixed temperature, the other cell experienced temperature changes. OCPs were then recorded as a function of the temperature difference, ΔT, between the two cell compartments.[130, 340]

2.2.4 Temperature pulsed voltammetry

For laser heated BDD experiments in *Chapter 3*, CV was performed in tandem with laser pulses *i.e.* temperature pulse voltammetry (TPV). The TPV experiments were accomplished by the imposition of a laser light of a specific power in a pulse fashion to heat the surface of the BDD electrode during the CV measurements. The laser was switched on for 10 ms and switched off for 90 ms while the CV is being recorded (Figure 2.5). This laser pulse method helps avoid building a strong heat profile that may dissipate into the solution and further complicate the measurements. Thus, it allows for the electrode temperature to cool down to room temperature.[130, 340, 381]

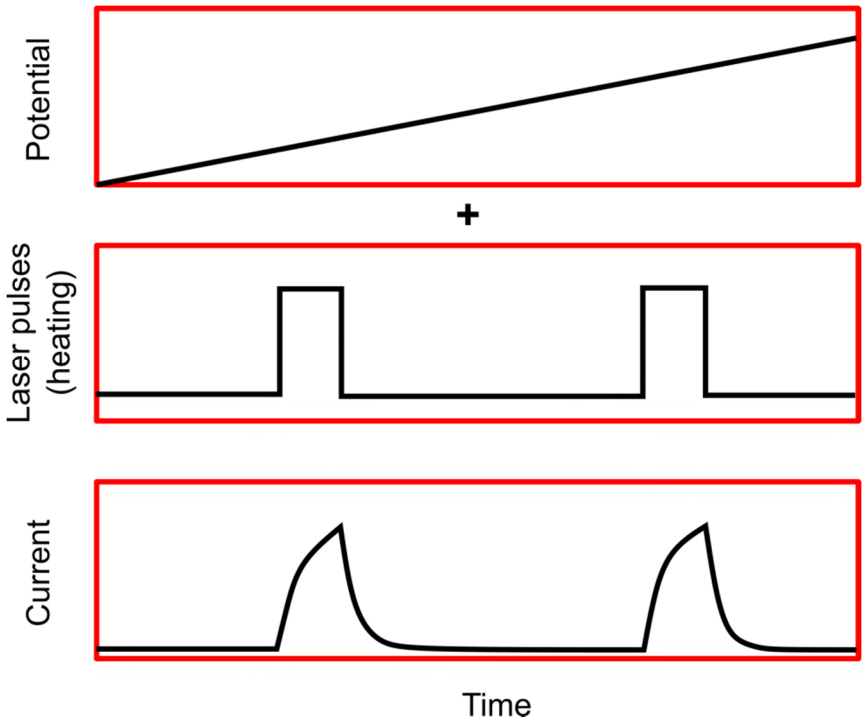

Figure 2.5: Schematic description of the current profile response of a BDD electrode heated using laser system during cyclic voltammetry experiments.

2.3 Instrumentation, analysis and characterisation techniques

2.3.1 Transmission electron microscopy (TEM) and scanning transmission electron microscopy (STEM)

Advances in material science nowadays rely very much on the amount of information that can be extracted using different characterisation tools. Among which, TEM represents an essential cornerstone, in which atomic resolution images hold a wealth of qualitative and quantitative data. In TEM, electrons from an electron source are made into a parallel beam by a condenser lens (*i.e.* magnetic lenses); this passes through the specimen (sample under study) and then the electron beam is focused as an enlarged image onto the fluorescent screen by the objective lens.[382] The image as well can be recorded using a charge-coupled device (CCD) camera. Two criteria are essential for TEM to operate, first the system has to be under vacuum and second, the sample has to be very thin *i.e.* less than 100 nm to allow electrons to travel through it (a challenging option and non-trivial to achieve).[382] In the scanning transmission electron microscopy (STEM) mode, the microscope lenses are adjusted to create a focused convergent electron beam (probe) at the surface of the specimen.[382] This focused probe is then

raster over the sample and various signals are collected point-by-point to form an image.[383]

In TEM, the image is formed by (1) mass thickness contrast mechanism (dark-field imaging), (2) phase contrast, or (3) diffraction contrast (bright-field imaging).[238, 383] The last two modes are the most frequently used to image crystalline specimens. Amplitude-contrast images are formed by inserting an objective aperture into the back focal plane of the objective lens, hence most of the diffraction pattern that lies outside of the aperture gets blocked.[331] When a small objective aperture is used to select only the directly transmitted beam of electrons, a bright-field image is formed.[383] Whereas, a dark-field image is formed. When the objective aperture is used to select electrons that have been scattered by the specimen.[382] In crystalline materials, diffraction contrast arises from coherent elastic scattering of electrons at special Bragg angles, for more information on image formation see references 258, 331, 382, 384-393. Diffraction contrast imaging is useful to study the nature of defects in crystals. Mass-thickness contrast can be imaged because areas of higher atomic number (Z) or greater thickness scatter electrons more strongly and thus appearing dark in bright in dark-field images and bright-field images.[384]

Phase contrast (high resolution) occurs by a phase modulation of the electron wave when it passes through the crystal structure of the sample. The electron wave is thought to be modulated in phase only and not in amplitude.[382, 383, 394] When electrons transmit through a crystal, their kinetic energy is perturbed by the variation of the potential field due to different atomic configurations. Consequently, the TEM image formed is the result of a thickness-projected crystal potential along the beam direction of a three-dimensional object. This means that the TEM image is a two-dimensional projection of a three-dimensional object. Such high-resolution images are then formed due to contribution from the transmitted and diffracted Bragg, which are interfering.[382]

Finally, in STEM mode, Z-contrast images are formed by mapping the intensity of high-angle scattered electrons as the electron probe is scanned in a rectangular raster over the sample. The images represent a direct map of the scattering power at atomic resolution. Also, a phase problem does not exist because Z-contrast images are incoherent, and do not reverse contrast with focus or specimen thickness. Additionally, the image is formed from high-angle scattering from the atomic nuclei, thereby the scattering cross section depends on atomic number (Z).[258, 384]

2.3.2 X-ray energy-dispersive spectroscopy (XEDS) and electron energy-loss spectroscopy

The X-ray energy dispersive spectroscopy (EDS) and electron energy-loss spectroscopy (EELS) signals are caused by inelastic scattering of electrons as they transmit through the sample.[382] The characteristic X-rays typically used in EDS are generated when high-energy electrons of the beam eject inner shell electrons from atoms in the specimen, and the ionized atoms return to their lowest energy states by replacing the missing inner shell electrons by electrons from the outer shells. This process results in either the emission of an X-ray or an Auger electron, whose energy of emission is characteristic of the difference in energy of the two electron shells involved, thereby providing a unique signature to identify the type of atoms present.[130, 382]

EELS is concerned with the energy distribution of the electrons that have been inelastically scattered while passing through the sample. Low energy losses (< 50 eV) correspond typically to electrons that have interacted with the weakly bound outer shell electrons of the atoms in the sample and provide information about the electronic properties of the material. High losses (> 50 eV) correspond to electrons that have been inelastically scattered by the inner electron shells and so contain information characteristic of the atoms in the sample. The fine structure of the ionization edges can provide information on chemical bonding and atomic configurations.[382, 385, 395, 396]

2.3.3 Scanning electron microscopy (SEM)

To investigate the surface of the specimen, rather than a projection through it, scanning electron microscope (SEM) is employed, which means thick materials can be imaged.[397] SEM is similar to STEM, whereby an accelerating voltage (0 - 30 kV) is employed to generate the high energy electron beam, the electron beam is focused and scanned across the surface of the sample.[398, 399] Interactions between the electron beam and sample result in several types of signals, including secondary electrons (SEs) and backscattered electrons. SEs are a good representation of the surface structure and provide topographical information. Images can be collected using an in-lens detector and a SE detector.[398, 399]

Backscattered electrons arise due to the elastic scattering of the incident electrons. Backscattered electrons are sensitive to the composition of the sample as the intensity of backscattering electron is associated with the atomic number of the atom. The in-lens detector is located in the column of the electron gun; thus SEs are collected with high efficiency and images can be obtained with high contrast. Therefore, an in-lens detector is regularly used to characterise grain structures, whereas the SE detector is employed to analyse surface topography (*e.g.* nanoparticles).[398, 399]

2.3.4 Atomic force microscopy (AFM)

Atomic force microscopy (AFM) is an imaging technique, which provides *x,y* topographical information with nm resolution, and *z* resolution < 1 nm.[400] A very sharp tip or probe scans across a surface with the feedback from interaction forces between the tip and the surface being recorded in order to provide the topography of the surface.[129] This is achieved by mounting the tip on a force sensitive cantilever, which is deflected by attractive and repulsive forces generated between the tip and surface. A laser focused onto the back surface of the cantilever is reflected on a photodiode detector and every change the cantilever undergoes is then detected precisely.[401] These changes arise from the cantilever movement, which is used to provide a feedback mechanism whereby the sample is repositioned during scanning in order to maintain a constant force (contact mode) or constant amplitude (tapping mode) between tip and sample. The basic principal of AFM is shown in Figure 2.4.[401, 402]

The two common modes of operation are (1) contact and (2) tapping mode. The first mode simply maintains contact between tip and surface, so the cantilever deflection (due to a repulsive force) is kept constant.[401-403] The tip is scanned over the surface in a raster like mode using a piezoelectric scanner. In order to maintain a constant force, a feedback mechanism is used so that the height of the tip relative to the sample surface is continually adjusted as a function of *x,y* position. The short-range decay of the repulsive forces gives contact mode a high level of sensitivity and thus resolution, however, forces in lateral directions can be large. Hence, contact mode is not recommended for soft samples and may cause tip damage.[129]

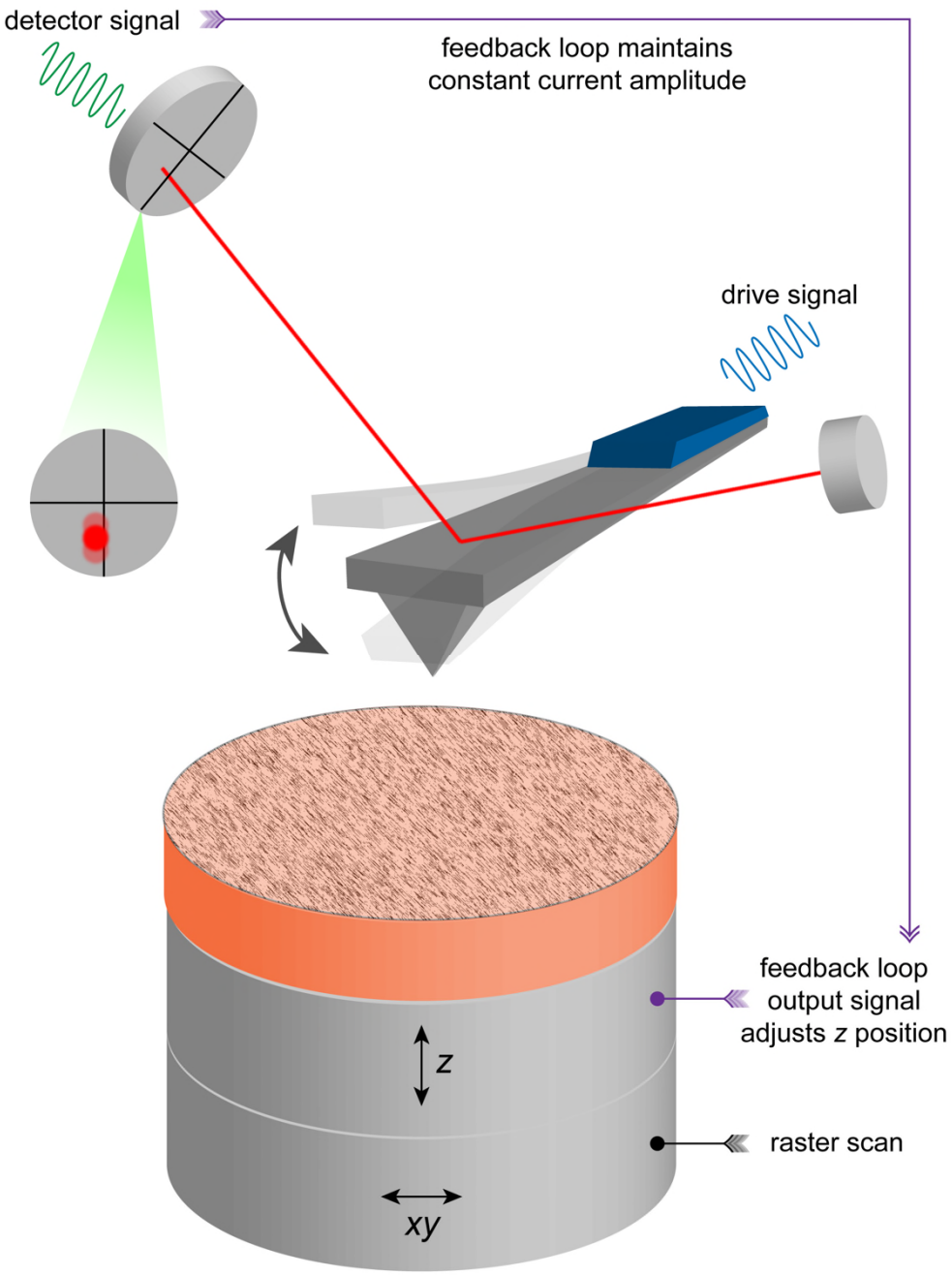

Figure 2.6: Illustration of the AFM system. The figure demonstrates the tapping mode. (credit: Lee Simcox)

In the tapping mode, the tip is oscillated at the resonant frequency of the cantilever whilst simultaneously scanning the surface. The oscillation amplitude of the cantilever is high enough so that the tip makes an intermittent contact with the surface to sample short-range repulsive forces, allowing high resolution imaging of surface topography. Tip contact with the surface generates a dampening in the oscillation amplitude, which

is used as a feedback mechanism, where the damping amplitude is kept constant in order to track the surface.[130]

The lateral resolution of an AFM is limited to the radius of curvature (Ra) of the tip apex. Typical Ra values are 30 ± 3 nm for silicon-based tips. Scan sizes are limited to the range of the lateral piezoelectric positioners, typically *ca.* 100 × 100 μm.

Chapter 3

Electrochemical Synthesis of Nanoporous Platinum Nanoparticles Using Laser Pulse Heating: Application to Methanol Oxidation

3.1 Abstract

Nanoporous platinum nanoparticles (NPs) have been proposed as promising electrocatalytic materials. Routes to produce them typically consist of chemical synthesis or selective dissolution of one component of a two-component mix. Here we show that by employing a pulsed laser heating approach during electrodeposition, whereby the electrode/electrolyte interface is continually heated and cooled, NPs with a nanoporous structure, can be grown directly on the electrode (boron doped diamond) surface. Transmission electron microscopy shows the NPs to be composed of loosely packed aggregates of much smaller crystalline particles of size 2-5 nm, with the porosity increasing with increasing deposition overpotential. In contrast electrodeposition at room temperature (RT) results in particles which show a considerably more compact morphology, and less higher index crystal facets, as revealed by electron diffraction techniques. Pulsed heating also offers a route towards controlling the monodispersity of the electrodeposited NPs. When applied to the oxidation of methanol, the laser heated NPs show considerably higher catalytic current densities compared to RT deposited particles. The highest catalytic activity is observed for the most porous NPs produced at the highest overpotential. Interestingly, the ratio of the forward oxidative current to the backward one is highest for those particles deposited under laser heated conditions but with the smallest overpotential. This suggests that the most catalytically active NPs may also encourage binding of residual adsorbed carbon monoxide and that a compromise must be reached.

3.2 Introduction

Nano-sized particles of platinum (Pt) supported on an electrode are pivotal for an array of electrocatalytic reactions, such as the oxidation-reduction reactions in direct methanol (MeOH) fuel cells, a subcategory of the proton exchange membrane fuel

cell.[404, 405] The electrocatalytic activity of the Pt nanostructure is governed by the morphology, size, loading level, and stability of the deposit, as well as any possible interactions between the support substrate and particle which facilitate electron transfer.[406, 407]

Electrodeposition is a versatile method for both fabricating the nanostructure and ensuring it remains in intimate electrical contact with the underlying electrode substrate.[7, 299, 408] The resulting morphology depends on the deposition parameters employed such as potential, time and choice of substrate.[409] Temperature may also have a significant impact on the structure,[409] although surprisingly this is often left unexplored, in the academic literature.

In practice, temperature can be controlled either isothermally or non-isothermally.[344] The former often involves heating the solution using a water jacket or bath but this approach can lead to uncontrolled mass transport, ill-defined thermal gradients and slow response to changes in temperature.[344] Conversely, a non-isothermal heating approach is attractive due to significantly greater control over mass transport in the system, faster heating times and the ability to heat beyond the boiling point of water without introducing unwanted bubbles or solvent evaporation.[338]

Non-isothermal heating has been achieved previously using a pulsed laser.[339, 410] Typically, the electrode surface is illuminated through solution,[356, 358] although this can result in unwanted photo-effects, such as electrolyte decomposition and formation of unknown compounds as side products, in addition to oxide formation.[339] There are only limited reports of laser heating via irradiation of the back surface of the electrode.[411-413] Dependent on the response of the electrode material to the inputted thermal energy,[343] both approaches, can result in unwanted damage to the electrode surface.

Over the past decade, boron doped diamond (BDD) has emerged as an interesting choice as a substrate for electrodeposition due to its sp^3 bonded structure, and consequently inert surface,[414] leading to low background currents and a wide solvent window, which are also attractive for electrocatalytic applications.[122] BDD also has a very high thermal diffusivity (600 W m^{-1} k^{-1} at 300 K) and extreme resistance to thermal ablation, being able to withstand laser power densities, P_d, of GW cm^{-2} (for nanosecond pulses)[415-417] and is thus an ideal material for thermoelectrochemical studies.[377] For BDD, absorption of optical energy from a laser occurs very quickly resulting in rapid

heating of the surface.[340] Thus the interface temperature can be changed elegantly without changing the temperature of the bulk solution. The BDD surface can also be either grown or prepared (by polishing) to nm-level roughness, allowing electrodeposited nanoparticles (NPs) to be probed with techniques such as atomic force microscopy (AFM) and field emission scanning electron microscopy (FE-SEM).[122]

Commonly in electrochemical deposition the resulting particle size and shape is often heterogeneous due to differing rates of nucleation and growth.[278] This situation is further complicated with BDD as the material is typically employed in the polycrystalline form which is heterogeneously doped.[122] Attempts to electrodeposit relatively monodisperse metal NPs have been demonstrated (on highly oriented pyrolytic graphite), using a double potential step (DPS) technique to separate growth and nucleation.[249] By combining DPS with tailored solution conditions, such as pH or electrolyte chemical composition, through *e.g.* the addition of capping agents and surfactants, it is also possible to control the shape of the electrodeposited particles.[418, 419]

Among the many shapes and structures possible for Pt NPs,[420] porous Pt has gained recent interest due to the high electrocatalytic activity,[420, 421] attributed primarily to the high surface area to volume ratio[421] and the creation of a confined reaction environment.[422] Methods to fabricate nanoporous Pt NPs have thus become an important topic of research. To date, porous Pt has been synthesized in solution, using transmetallation reactions, self-organization processes and templating methods.[240, 423-425] To achieve such structures electrochemically, the most common method is electrodeposition of bimetallic NPs, followed by preferential leaching of the least noble metal.[426] Recently, DPS electrodeposition has also been used to both control the size range of the deposited particles and induce porosity.[421]

In this study, we explore whether electrodeposition under controlled, elevated temperature conditions also offers a route towards the creation of nanoporous structures. BDD is used as the substrate electrode and a pulsed laser approach is utilized to non-isothermally heat the electrode, from the backside, during electrodeposition of Pt. We also examine the subsequent electroactivity of the resulting structures, produced under both room temperature (RT) and laser pulse heating, towards the electro-oxidation of MeOH.

3.3 Experimental

3.3.1 Solutions and chemicals

Pt electrodeposition solutions were prepared from potassium hexachloroplatinate (K_2PtCl_6, 99 %, Sigma-Aldrich) with sulfuric acid (H_2SO_4, 99.99%, Sigma Aldrich) as a supporting electrolyte in ultra-pure Milli-Q water (18.2 MΩ cm, Millipore Corp., U.S.) at 20 °C. All chemicals were used as received without further purification. Pt deposition solutions contained 500 μM $[PtCl_6]^{2-}$ in 0.5 M H_2SO_4 (pH = 0.65) which was deaerated with N_2 gas for 15 minutes before the experiment to exclude O_2. N_2 flow was maintained over the solution during the experiment.

3.3.2 Materials

The experiments were performed using a polycrystalline BDD plate, 9 mm in diameter and 200 μm thick, with a boron dopant level of ~3 $\times 10^{20}$ B atoms cm^{-3}, grown using microwave chemical vapour deposition by ElementSix (Harwell, Oxford).[340] To make an ohmic contact to the electrode the upper quarter of the back surface was sputtered (Moorfield MiniLab 060 Platform) with Ti (20 nm)/Au (400 nm) and annealed in a tube furnace for 5 hr at 450 °C.[372]

3.3.3 Electrochemical Set-Up

For the electrochemical measurements during pulsed heating and at RT, a custom-built electrochemical cell was designed and fabricated in-house. The cell is composed of two parts, a Teflon container and a Perspex® window, held together with Teflon screws. The Perspex window contained a hole in the centre, across which the BDD disk was mounted (inside face) and held in place with adhesive Kapton® tape (100 μm thickness, stable up to 1000 °C, R.S. Components Ltd.). The geometry of the electrode area exposed to solution was defined using Kapton® tape, which contained a laser-micromachined circular hole, 1 mm in diameter. A conductive track was made from the Au sputtered contact on the back face of the BDD electrode (not in contact with solution) using two parts silver conductive epoxy (R.S. Components Ltd.) to the top of the Perspex® window, where electrical contact was made with a crocodile clip. The set-up is shown in Figure 3.1.

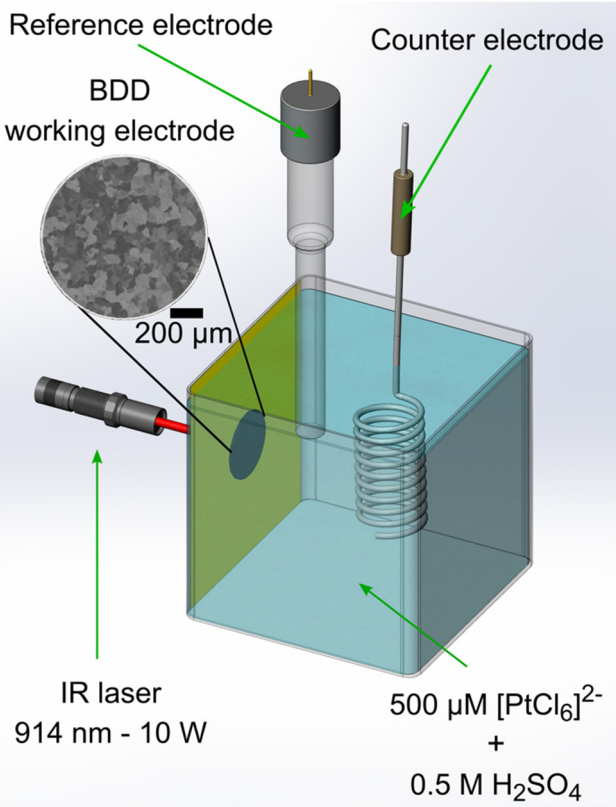

Figure 3.1: Schematic drawing of the pulsed laser heating experimental set-up. The laser beam is focused by the laser lens onto the back face of the BDD electrode held in the Perspex® cell with Kapton® tape which also defines the active electrode area (1 mm disc). The inset image is an FE-SEM image of the BDD electrode surface, where the different colours represent the differently doped grains.

For the non-isothermal experiments, cyclic voltammetry (CV) and chronoamperometry were performed simultaneously with pulsed laser heating, termed temperature pulse voltammetry (TPV). A diode IR laser (914.7 nm, 30 W, LM-D0296, LIMO) was used for all pulsed temperature experiments, controlled by a laser diode controller (LDC1000, Laser Electronics Ltd Lincolnshire, England). An optical fibre was used to deliver the irradiation of a 1 mm diameter central circular spot via a focusing lens onto the back face of the BDD electrode. A dual-channel function generator (AFG3022B, Tektronix) was employed as a master controller for TPV experiments to ensure that the potentiostat (CompactStat, Ivium Technologies, The Netherlands) and laser were synchronized when triggered by the start of the experiment. For these experiments, a fixed laser power (P_d) of 1.2 kW cm^{-2} was utilised (laser power = 10 W) and the laser was cycled with 10 ms on and 90 ms off, *i.e.* a heating period of 10 ms and a cooling period for 90 ms to ensure that heat does not dissipate to the bulk solution. This P_d

equated to an initial average local temperature at the electrode/electrolyte interface of 66.4 °C, determined via open circuit potential (OCP) measurements in a solution containing 0.5 mM potassium ferricyanide, $Fe(CN)_6^{3-}$ (Sigma-Aldrich, 99 %), and 0.5 mM potassium hexacyanoferrate trihydrate, $Fe(CN)_6^{4-}$ (Sigma-Aldrich, ≥ 98.5 %); the method for which has been described previously in detail.[340, 377]

All electrochemical experiments were carried out using a three-electrode set-up controlled by a potentiostat; CompactStat Ivium Technologies (The Netherlands) for TPV and CHI730A (CH Instruments, Inc. Austin, TX) for RT experiments. A commercial saturated calomel electrode (SCE: CHI150, CH Instruments Inc. TX) was used as the reference electrode and a helical Pt wire served as the counter electrode. For hydrogen adsorption/desorption studies in sulfuric acid, mercurous sulfate, MSE, ($Hg/HgSO_4/K_2SO_4$(sat.)) served as the reference electrode, to avoid any possible Cl^- contamination / adsorption affects.[427, 428]

For all experiments, to ensure a clean BDD surface, the electrode was first polished with alumina powder (0.05 μm sized particles, micro-polish, Buehler, Germany) then further polished on a water saturated polishing pad (micro-polish, Buehler, Germany). The electrode was then cycled in 0.5 M H_2SO_4 for 5 minutes to verify a clean surface CV response.

3.3.4 Surface characterization

The morphology of the electrodeposited Pt NPs was characterized *ex-situ* using AFM, FE-SEM and transmission electron microscopy (TEM). Before imaging, the surface of the sample was rinsed with deoxygenated ultra-pure water and left to dry in a desiccator under a N_2 atmosphere. For each experiment, at least three images (n = 3) were recorded in different areas of the surface. AFM images were acquired at a low scan rate (0.25 Hz) in tapping mode (TM) using a Bruker Enviroscope AFM with a Nanoscope IV controller. FE-SEM images were recorded using the secondary electron (SE2) detector on a Zeiss Supra 55-VP operating at 7 keV. Energy dispersive X-ray spectroscopy (XEDS) spectra were recorded using an Oxford Instruments Si–Li detector unit on the FE-SEM instrument, at a working distance of 8.5 mm and accelerating voltage of 10 keV. TEM measurements of particle shape, structure, size and composition were carried out using a JEOL-JEM 2100FX (LaB_6 filament) microscope operated at 200 keV.

The BDD electrode is approximately 200 μm thick, thus imaging the Pt NPs directly on the BDD using TEM is impractical as TEM requires a very thin and transparent substrate.[429] Hence a replication method[430] was used to transfer the Pt NPs to a Cu TEM grid suitable for imaging, as shown schematically in Figure 3.2. For TEM imaging, a positive replica technique was employed to transfer the Pt NPs to a Cu TEM grid (300 mesh, Agar Scientific).[430] This procedure is shown schematically in Figure 3.2 and consists of the following steps: (i) a drop of acetone was placed on the Pt NP electrodeposited BDD surface, followed immediately by the replica film (cellulose acetate sheet), pulled onto the surface by surface tension. The film was left to dry for 30 minutes, before (ii) being separated from the surface and placed on a microscope slide with the NPs facing upwards. The surface was then (iii) vacuum carbon coated (Emitech evaporator, Quorum technologies, UK), before (iv) the required area cut from the film and laid, carbon side up, on the TEM grid. The grid was subsequently (v) placed in acetone to dissolve the cellulose sheet, leaving the NPs supported on the carbon film attached to the Cu TEM grid. (vi) After one hour, the grid was removed from the mesh and dried in a desiccator under N_2 flow before being placed in the TEM for examination. In addition to imaging, XEDS was also carried out to determine the composition of the deposited material. In order to minimize electron beam damage, all images were acquired with one single scan fast exposure with a beam current of ~10 pA and an acquisition dwell time of 12 μs per pixel.

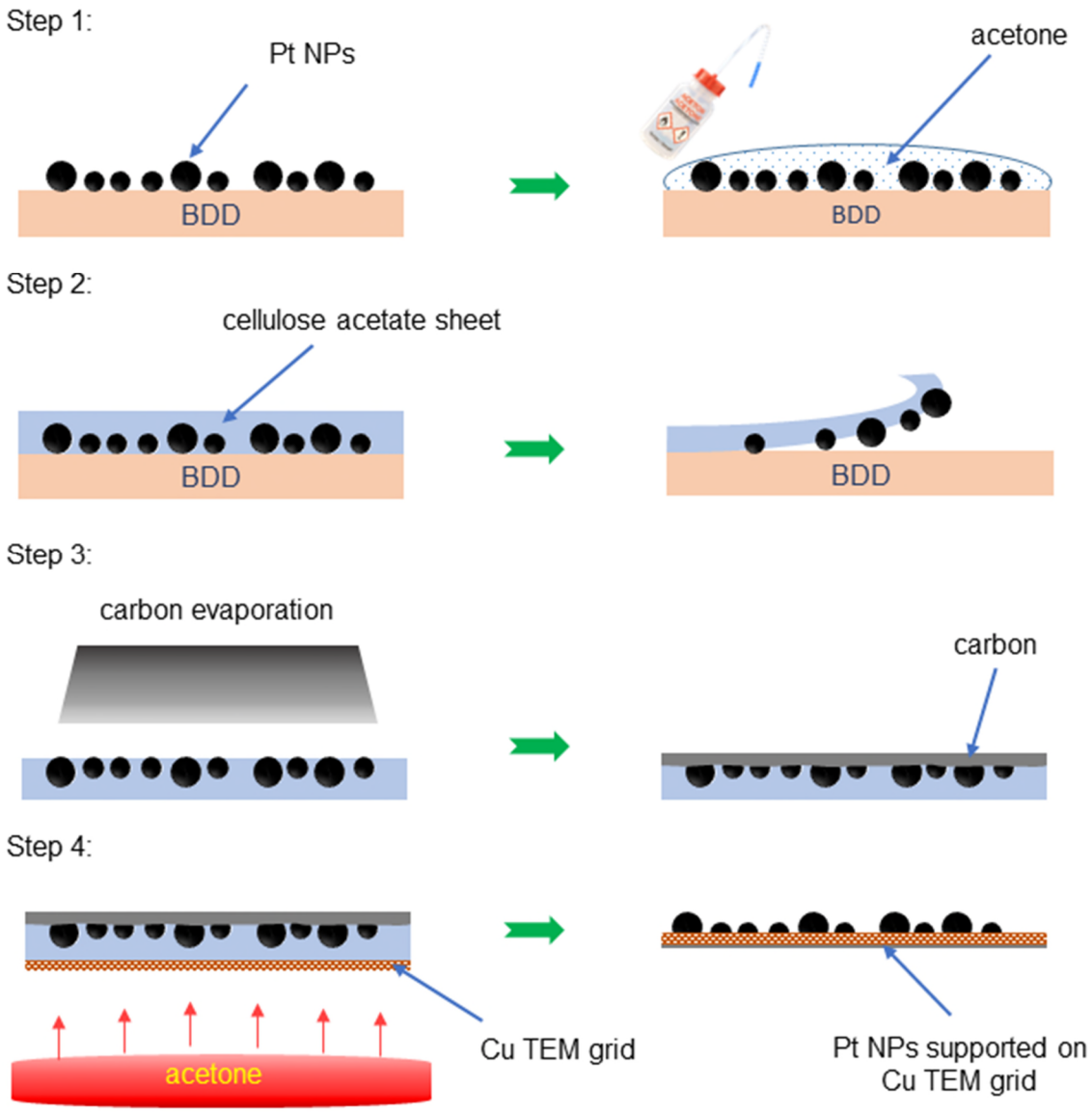

Figure 3.2: A schematic drawing of the replication method for transferring Pt NPs to a Cu TEM grid.

3.4 Results and discussion

3.4.1 CV Studies of Pt Electrodeposition in Acid Solution at Room and Elevated Temperature.

The speciation of Pt when dissolving Pt(IV) salts in aqueous media can be influential in the electrodeposition process.[431] A low pH was chosen to make hydrated Pt(IV) the major solution species.[432] In order to understand the characteristic electrochemical signature of $[PtCl_6]^{2-}$ in 0.5 M H_2SO_4 (at pH = 0.65) and the role of an increased interfacial temperature on Pt(IV) reduction, CVs were carried out at RT (T = 20.0 °C)

and under laser pulse heating (average *T* across the electrode / electrolyte interface = 66.4 °C), under de-aerated conditions, as shown in Figure 3.3. The CVs were run negatively at 0.1 V s^{-1} from +0.6 V (where no faradaic electron transfer reactions take place) to -0.25 V (where hydrogen evolution begins to dominate) and back to +0.6 V.

Figure 3.3(a) shows the response under RT conditions (blue line). In Figure 3.3(b), under laser heated conditions, the pulsed response of the laser (10 ms on, 90 ms off) generates a pulse-like current response (black line). During the heating period a temperature gradient extends out from the electrode surface into the solution nearby, which then readjusts during the cooling period. The red line in Figure 3.3(b) represents the maximum current achieved during each laser pulse.

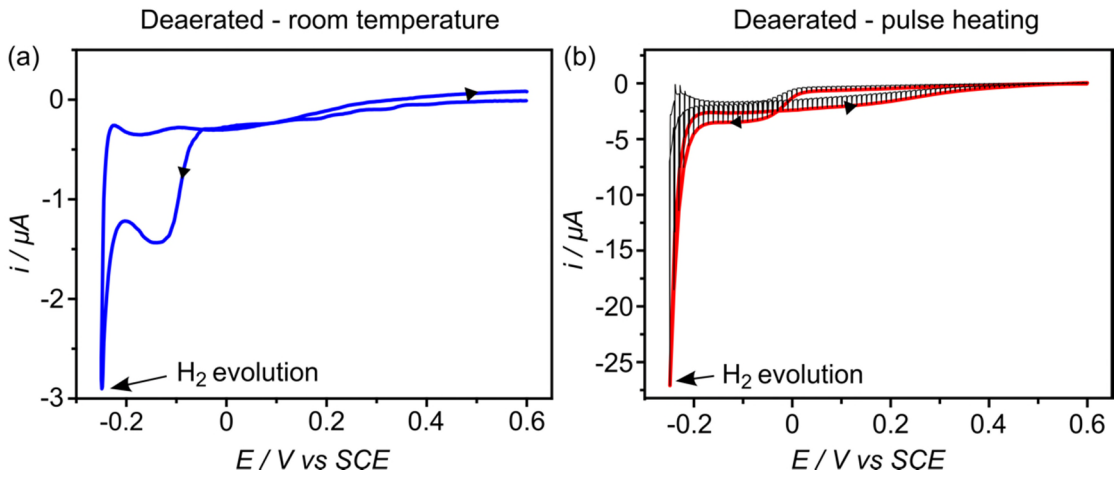

Figure 3.3: CVs for Pt electrodeposition recorded in a deaerated solution containing 500 μM $[PtCl_6]^{2-}$ in 0.5 M H_2SO_4 at 0.1 V s^{-1} under (a) RT and (b) laser heated conditions (1.2 kW cm^{-2}, pulsed laser on for 10 ms, and off for 90 ms).

Under RT conditions (Figure 3.3(a)), scanning negatively (forward scan) leads to an increase in current from *ca.* +0.5 V *vs.* SCE, due, most likely, to the onset of Pt reduction on the BDD (kinetically limited region). As the potential is made more negative, and Pt reduction moves into a diffusion-limited region, a current peak of -1.48 μA is seen at -0.11 V. At potentials, more negative than -0.21 V a large increase in current is seen due to the reduction of protons (H^+) and subsequent evolution of hydrogen (H_2). Upon reversing the scan direction, the current still flows in the negative direction due to further reduction of Pt on the freshly formed Pt phase.[433]

Under laser heated conditions (Figure 3.3(b)), scanning negatively produces similar features to those observed under RT, except the currents passed are larger. This may

be due to a combination of many factors, including: (i) the increased electron transfer kinetics for reduction of Pt(IV) and H^+;[339] (ii) an increase in diffusional flux due to both a reduction in local viscosity and increase in diffusion coefficient (in accordance with the Stokes-Einstein equation[339]) in the vicinity of the electrode/electrolyte interface, and (iii) convective effects arising from density changes due to the established thermal gradient.[340, 359, 377] The potential at which a current starts to flow in the diffusion-limited regime also occurs at a slightly more positive potential when compared with RT conditions (-0.07 V versus -0.11 V, Figure 3.3) suggesting increased ET kinetics and/or a negative temperature coefficient, for Pt deposition under high temperature conditions.[340, 377] When the scan direction is reversed, a negative current is again seen in the pulsed CV.

The result of repeated scanning, over a further four cycles, where Figure 3.3 represents cycle one, at 0.1 V s^{-1} at RT and with laser pulse heating in the acidic Pt electrodeposition solution, is shown in Figures 3.4(a) and 3.4(b), respectively. As Pt is continuously deposited on the surface during the additional four CV cycles (peak 1)[274, 434, 435] the expected CV response associated with the presence of polycrystalline Pt in acidic solution (peaks 2 and 3) emerges.[274, 436] In particular, Figure 3.4(a) shows clearly the H adsorption (H_{ads}) and H desorption (H_{des}) peaks, in the region between -0.01 V and -0.21 V. H_{ads} (peak 2) is associated with a negative current ($H^+ + e^- \rightarrow H_{ads}$), whilst H_{des} (peaks 3) with a positive current ($H_{des} \rightarrow H^+ + e^-$).[437]

As the potential is scanned positively, the Pt will oxidise to form PtO_x provided a sufficient positive potential is reached; no evidence of elemental Pt dissolution or oxide layer formation is observed in these CVs.[435] Similar features are observed under laser pulse heating, as shown in Figure 3(b), with the current registered for peaks 1, 2 and 3 increasing with further cycling. The charge transferred during either H_{ads} or H_{des} (peaks 2 and 3 respectively) from the electrodeposited Pt provides an estimate of the electroactive surface area (ESA), using a value of 210 μC cm^{-2} for monolayer hydrogen adsorption.[7]

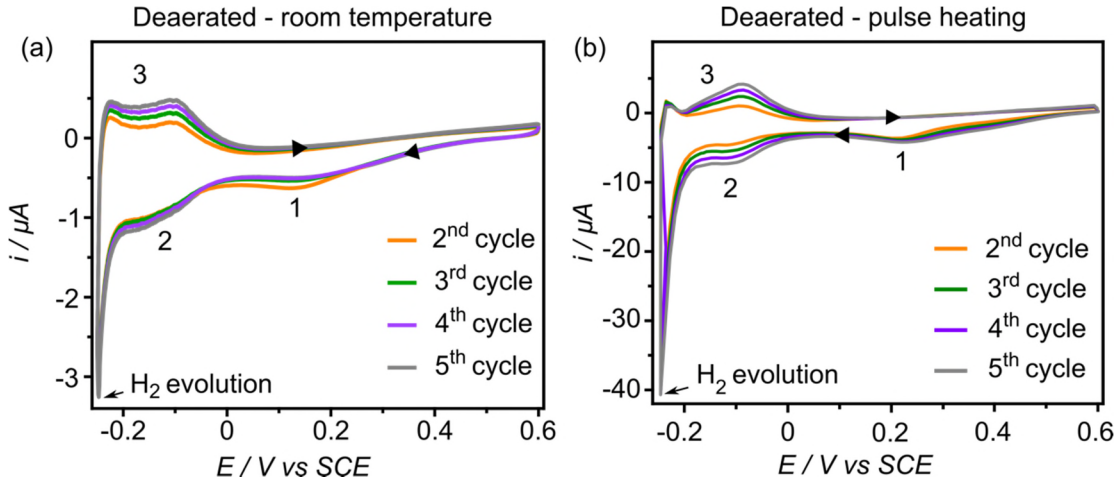

Figure 3.4: CVs of four subsequent cycles following the first cycle of $[PtCl_6]^{2-}$ electrochemistry (shown in Figure 3.3) under (a) RT and (b) heating by laser pulsing in a deaerated solution containing 500 μM $[PtCl_6]^{2-}$ in 0.5 M H_2SO_4 at 0.1 V s^{-1}. Note the CVs recorded under laser pulse heating represent the maximum current achieved during each current pulse.

The charge, Q, due to H_{des} is measured by integrating the area under the appropriate peaks, to obtain Q for Pt electrodeposition in a deaerated solution containing 500 μM $[PtCl_6]^{2-}$ in 0.5 M H_2SO_4 at 0.1 V s^{-1}. Table 3.1 shows the corresponding Q and ESA values as a function of CV cycle number, under both RT (blue) and laser heated (red) conditions. Note, under laser heating, where the laser is on for 10 ms and off for 90 ms, a pulsed current response is obtained, which we integrate under to account for metal nucleation during the cooling period as well as heating.

Table 3.1 shows H_{des} and the associated ESA's for consecutive scans under both RT and increased temperature conditions, quantitatively demonstrating the increased surface density of Pt in the presence of laser pulse heating.

Table 3.1: Experimental values of Q passed during CV cycling for Pt electrodeposition (taken from Figure 3.4) under RT and laser pulse heating and the corresponding ESA.

	Charge (Q) / µC		**ESA**	
	RT	Laser pulse heating	RT	Laser pulse heating
Cycle 2	0.0711 ± 0.0012	0.344 ± 0.0011	0.00033 ± 0.0011	0.0016 ± 0.0015
Cycle 3	0.0865 ± 0.0011	0.513 ± 0.0013	0.00041 ± 0.0012	0.0024 ± 0.0015
Cycle 4	0.0991 ± 0.0011	0.617 ± 0.0011	0.00047 ± 0.0012	0.0029 ± 0.0013
Cycle 5	0.111 ±0.0013	0.728 ± 0.0011	0.0005 ± 0.0013	0.0035 ± 0.0014

3.4.2 Chronoamperometric electrodeposition of Pt under room temperature and laser heated conditions.

To further investigate the Pt electrodeposition process, chronoamperometric current-time (*i*-*t*) plots were first recorded from a potential where no faradaic electron transfer takes place (+0.75 V) to different electrochemical driving forces (E_{dep} = +0.1 V, 0 V, -0.1 V and -0.2 V); within the Pt electrodeposition window (Figures 3.3 and 3.4), but before significant H_2 evolution. A fixed electrodeposition time (t_{dep} = 5 s) was employed for both RT (T = 20.0 °C) and laser pulse heating (T = 66.4 °C, 10 ms on and 90 ms off), as shown in Figure 3.5.

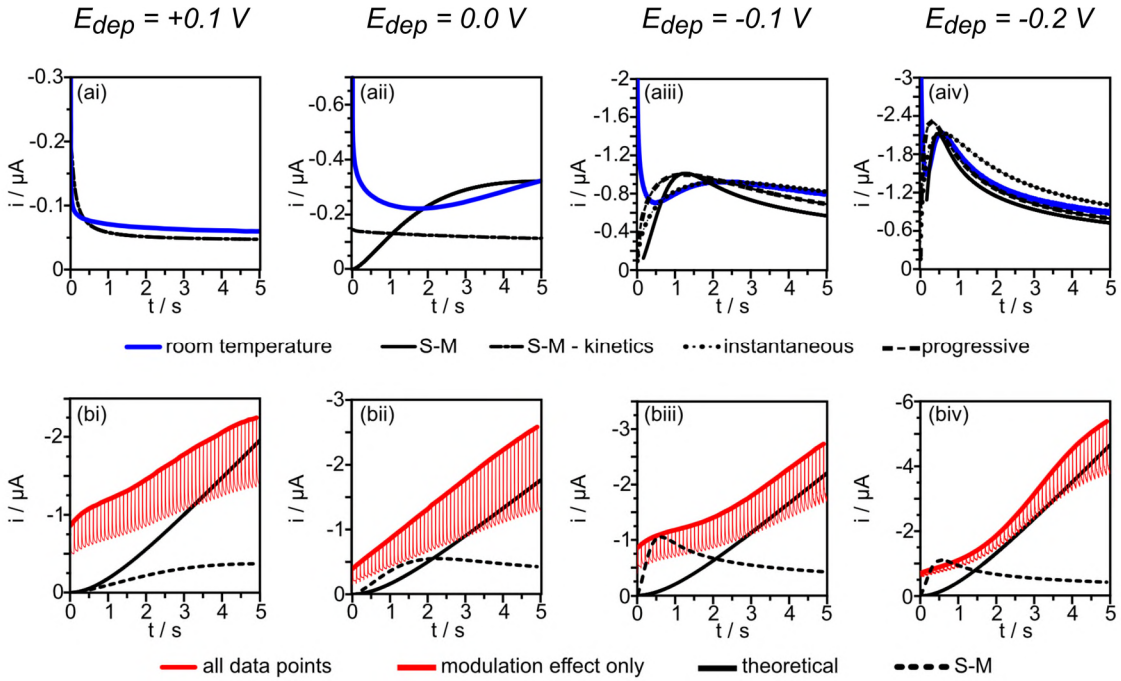

Figure 3.5: Current-time transients for Pt electrodeposition (a) RT (blue lines) and (b) laser pulse heating (red lines) at E_{dep} of (i) +0.1 V, (ii) 0 V, (iii) -0.1 V, (iv) -0.2 V for t_{dep} = 5 s. The bolded red line represents the maximum current passed during the laser pulse.

Under RT conditions, at the lowest driving potential (+0.1 V), after an initial decay in the charging current, the current appears almost Cottrellian in response, decreasing slightly with time. At E_{dep} = 0 V, after 1.5 s the current starts to rise with time, corresponding to the growth of Pt deposits which are initially sufficiently well separated to prevent individual diffusion fields overlapping.

This behaviour is also evident in the -0.1 V data; however, it rises to a maximum and then decreases with time. This is due to the overlap of diffusion fields of neighbouring particles, so that a predominantly linear diffusion field is established, resulting in the observed *i-t* characteristic. At the most negative potential, E_{dep} = -0.2 V, the current maxima is now occurring at a much shorter deposition time, due to the increased driving potential, with the *i-t* behavior approaching a Cottrellian response at longer times.[26]

Under laser pulse heating, *i* increases with *t* regardless of the value of the electrodeposition potential and the currents are greater than those observed under RT conditions. Due to the pulsed nature of the heating procedure it is difficult to interpret the *i-t* behaviour in the same way as it is for RT. Therefore, microscopy analysis was

employed to understand the nucleation and growth behavior in further detail under both temperature conditions. It is important to note that H_{ads} and H_2 evolution starts at slightly less negative potentials under high temperature conditions (H2 evolution onset = -0.19 V) compared to RT (H_2 evolution onset = -0.21 V), Figure 3.3. This further suggests that at the highest E_{dep}, the increase in current could be related to both Pt deposition and simultaneous H_2 evolution.

3.4.3 Microscopic analysis of Pt NPs electrodeposited under room and high temperatures

Representative AFM and FE-SEM images recorded for Pt electrodeposition on BDD under both (a) RT and (b) laser pulse heating conditions for a fixed t_{dep} of 5 s and E_{dep} of +0.1 V, 0 V, -0.1 V and -0.2 V are shown in Figure 3.6. The images provide statistical data (from 3 images) on NP height and diameter extracted from AFM and FE-SEM images respectively, as shown in the histogram analysis in Figure 3.7. FE-SEM was used to extract diameter information as AFM can slightly overestimate or underestimate the true diameter due to AFM tip convolution effects.[438]

AFM was used to provide information about the particle density, expressed as number of particles per μm^2 (density), under both RT (blue) and laser heated (red) conditions, respectively, as a function of E_{dep} for t_{dep} = 5 s (Number densities are given quantitatively in Figure 3.8). In general, number particle density increases with increasing E_{dep} as well as temperature (*i.e.* laser heating always leads to an increase in the NP number density (for the same E_{dep})). From Figures 3.6 and 3.8, it is immediately clear that irrespective of the temperature an increase in E_{dep} increases the particle number density, however, increasing temperature results in a higher number density compared to RT deposition, for all E_{dep} considered. Under elevated temperatures, it is also clear as E_{dep} becomes more negative, the particle size distribution moves away from being heterogeneous towards more homogeneous, which is also significant given the polycrystalline nature of the BDD surface. The more elevated grains in the AFM images (corresponding to the lighter grains in the FE-SEM images) represent the lower doped regions and vice versa.[439] Previous studies have found a difference in the boron doping levels of ~ four, for similar material.[171]

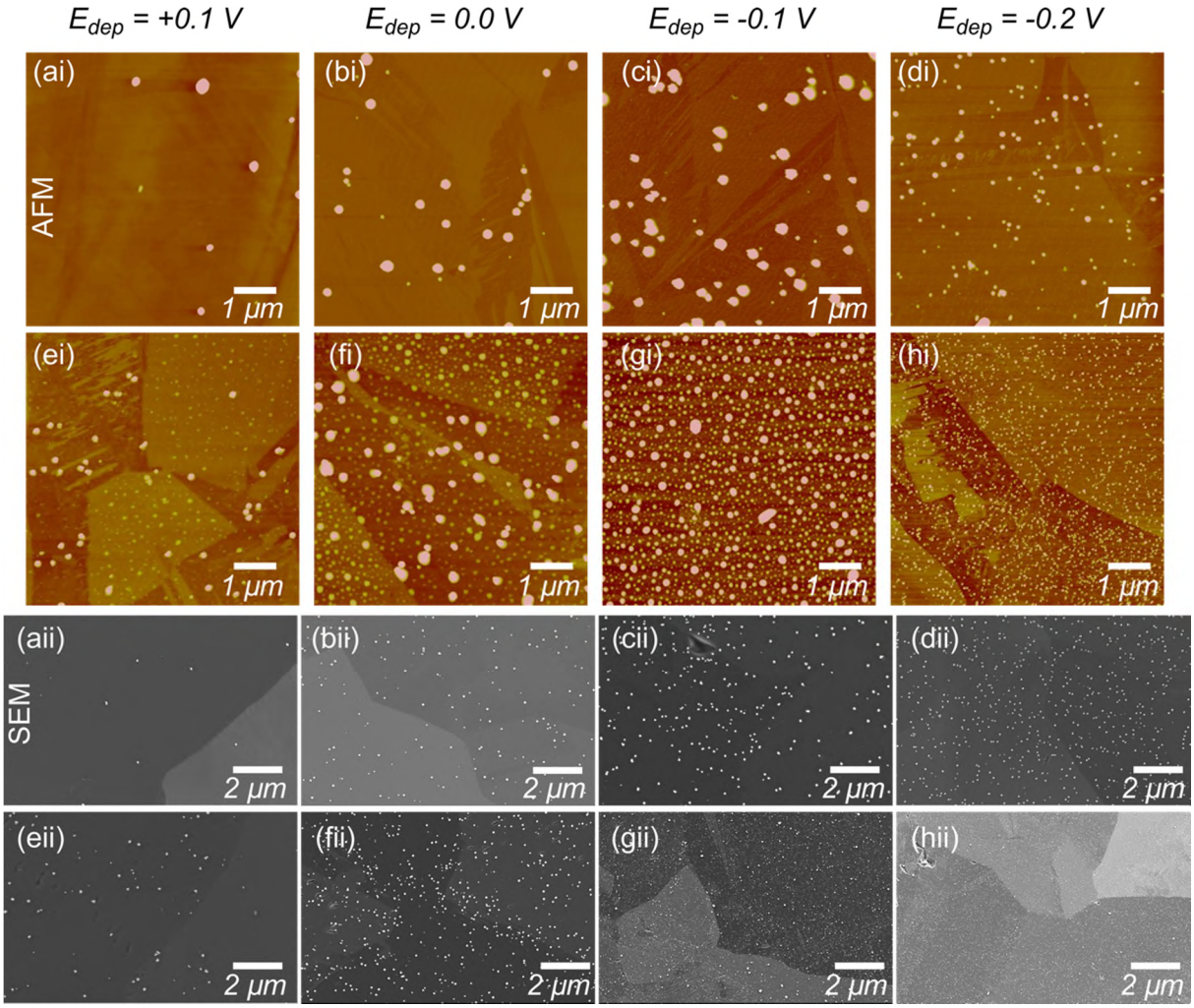

Figure 3.6: Representative (i) 5 µm × 5 µm AFM and (ii) FE-SEM images of a BDD electrode after electrodeposition of Pt NPs from a solution containing 500 µM $PtCl_6^{2-}$ and 0.5 M H_2SO_4 under (a - d) RT and (e - h) laser pulsed heating. Electrodeposition was carried out by applying E_{dep} = +0.1 V (a and e), 0 V (b and f), -0.1 V (c and g) and -0.2 V (d and h) for t_{dep} = 5 s.

Under laser pulsed heating temperature with the most negative E_{dep} (*i.e.* largest overpotential) the size of the Pt particles is the smallest of all, with the most homogeneous distribution (mean particle height of 13.3 ± 4.8 nm), Figure 3.7.

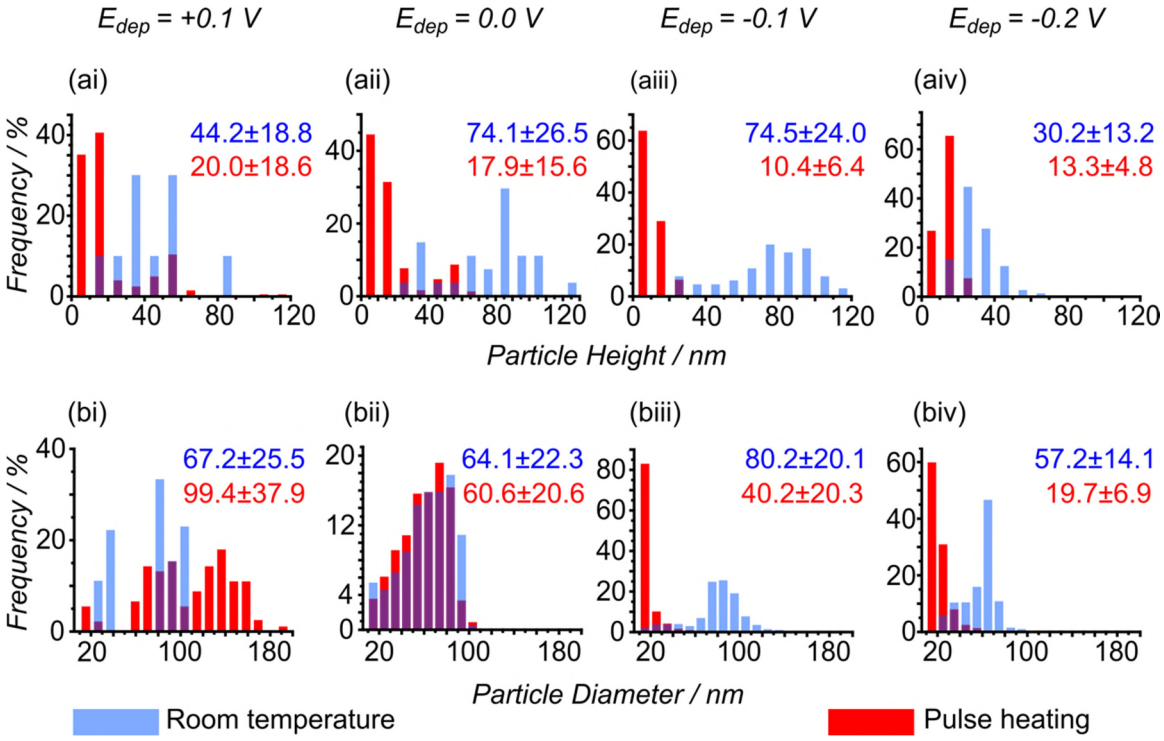

Figure 3.7: Histogram analysis of Pt NPs (a) height and (b) diameter for both RT (blue) and laser pulse heating (red) experiments extracted from AFM and FE-SEM images, respectively. Electrodeposition was carried out for t_{dep} = 5 s at E_{dep} of +0.1 V (ai and bi), 0 V (aii and bii), -0.1 V (aiii and biii) and -0.2 V (aiv and biv).

RT electrodeposition of Pt, using a single potential step (SPS), often shows a wide distribution of particle sizes; such growth is often referred to classically as "progressive" nucleation.[9] More recently, the term aggregation has also been used to describe this process thought to be due to the physical coalescence of growing clusters and the overlapping of diffusion fields of neighbouring NPs.[278] DPS chronoamperometry has proven effective as a means of controlling the mono-dispersity in the size distribution for Pt NPs on HOPG or GC electrodes.[267, 421, 440, 441] However, given the inherent surface heterogeneity in polycrystalline BDD, more extreme procedures were thought to be necessary to achieve monodispersity, for example, the use of a combination of wet chemical seeding of Pt NPs on the surface, followed by electrodeposition.[442, 443]

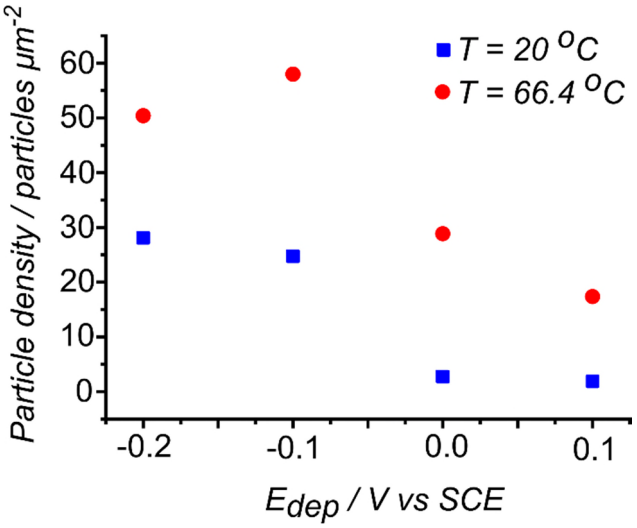

Figure 3.8: Variation of particle number density with temperature and E_{dep} of Pt NPs electrodeposited on BDD under room (blue) and high (red) temperatures.

In contrast, our data shows that by implementing laser pulse heating during the electrodeposition process, SPS chronoamperometry, at the highest overpotential, is sufficient to significantly reduce the variation in particle size, and overcome variations in dopant density in the underlying BDD. We attribute this, in part, to the large overpotential and the rapid heating / cooling of the electrode interface acting to separate the nucleation and growth processes sufficiently over the time scale of electrodeposition. Note, at this potential simultaneous H_{ads} and H_2 evolution is also occurring to the greatest degree, which could also play a role. For example, recently, Moffat et al. electrodeposited a single monolayer of Pt by using these processes to quench subsequent growth.[444]

By fitting the chronoamperometric data to Scharifker-Mostany (SM) models, we noticed that the number of density and nucleation rate constant extracted from the AFM images for both RT and laser pulse heating condition are higher by five orders of magnitude in comparison to values calculated using the SM models. This suggests that further theoretical development is required to be able to link *i-t* curves to the nucleation and growth of NPs.

3.4.4 Investigation of the structure of Pt NPs using TEM imaging

Even though AFM and FE-SEM provide high resolution topographical information, they do not have the resolving power to extract details on NP structure and crystallinity. Further insight was thus obtained by imaging the Pt NPs using TEM as shown in Figure

3.9, where particle morphology was investigated to examine the nature of atomic cluster aggregation/agglomeration and their crystallographic arrangement.

Figures 3.9(a-b) show TEM images of typical Pt NPs obtained under both (a) RT and (b) laser pulse heating conditions for the four-different electrodeposition driving forces. To ensure the TEM replication process was contamination free and successful, XEDS spectra were recorded for Pt NPs electrodeposited under both RT and laser heated conditions for all E_{dep}. Elemental analysis shows the presence of Pt and C only on the Cu-TEM grids.

The elemental composition was confirmed by XEDS as shown in Figure 3.10, suggesting only Pt, not PtOx, is present, and the particles are free from any potential contamination during transfer. Immediately apparent in Figure 3.9 is the difference in the structures formed under the two different temperature conditions. For both, the particles are clearly formed from much smaller nanoparticles, which themselves are composed of clusters of atoms, which aggregate together. Under RT conditions, the Pt NPs appear to aggregate much more tightly in a more spherical or quasi-spherical structures. In contrast, under laser pulse heating conditions the Pt particles are less well packed and more porous in nature. TEM shows they appear to be composed of aggregated Pt NPs, 2-5 nm in diameter, with the higher the E_{dep} the more loosely packed the structure. Similar morphologies have been obtained using solution-based synthesis approaches. Such structures are described in the literature as nanoporous or porous structures of high catalytic activity.[240, 421, 423]

Pt aggregates made by both procedures are polycrystalline, as shown by the Selected Area Electron Diffraction (SAED) patterns in Figure 3.11, which appear as concentric rings.[445] Also given are the crystal planes present in the NP. The colour of the SAED patterns was inverted using a script in accordance with reference 446. SAED shows that the Pt aggregates made by both procedures are polycrystalline; Figure 3.11.[445] Under RT conditions, it is possible to assign the visible (hkl) indices to; (111), (210), (310), (321), (200), (300), (320), (220), (311), and (331) of fcc Pt. Under elevated temperature conditions, the following (hkl) indices are observed; (111), (200), (220), (222), (422), (333), (511), (310), (330), (311), (322), (320), and (410).

Thus, the particles formed under higher temperature conditions have more of the higher index crystallites. These are thought to have a larger impact on increasing the catalytic activity, compared to lower index planes, due to the greater presence of dangling atomic bonds, steps, edges and kink sites.[447, 448]

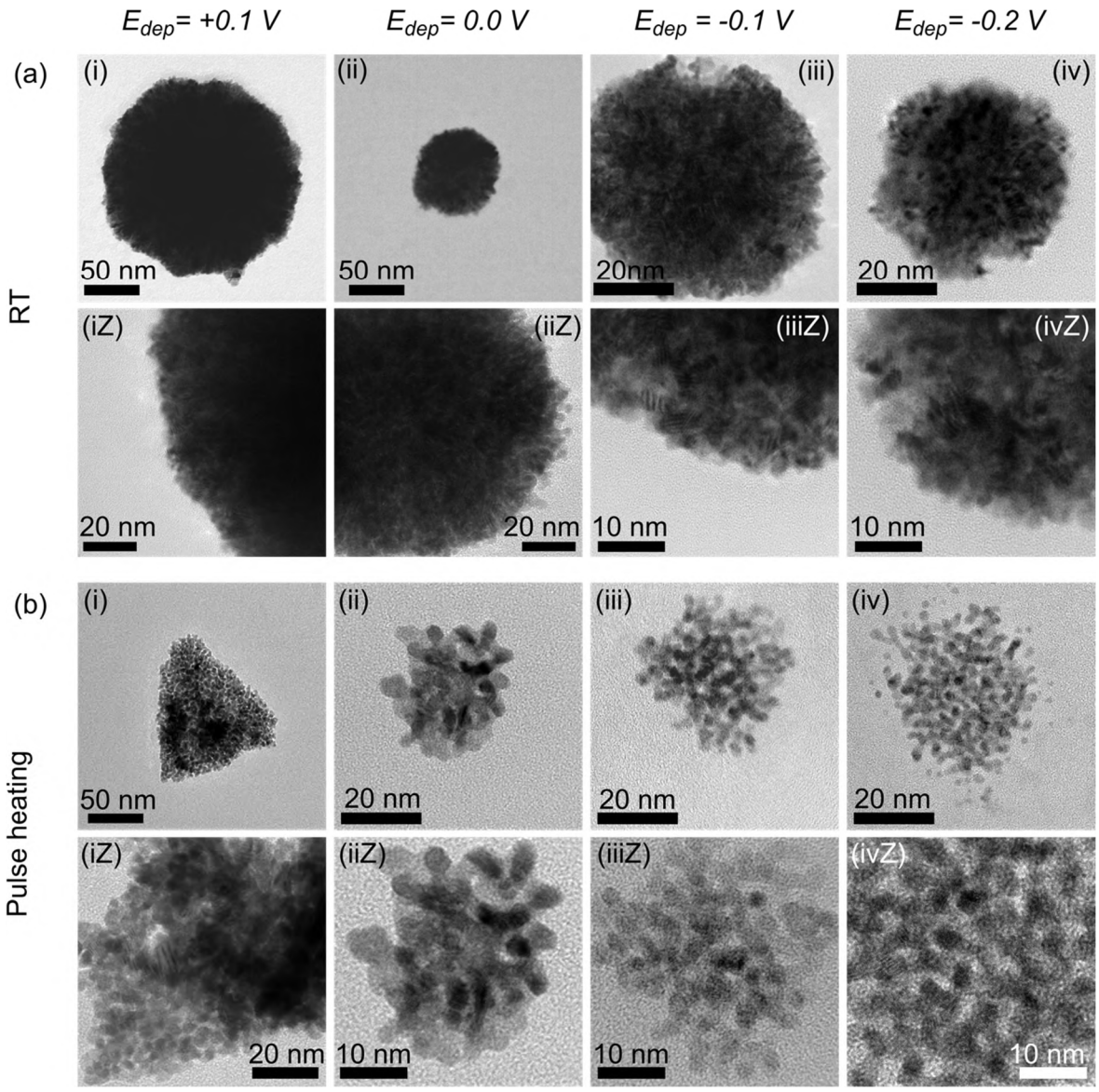

Figure 3.9: TEM images of Pt NPs obtained under (a) RT and (b) high temperature at E_{dep} of (i) +0.1 V, (ii) 0 V, (iii) -0.1 V and (iv) -0.2 V for t_{dep} = 5 s. (iZ - ivZ) present higher magnification TEM images of the Pt NPs.

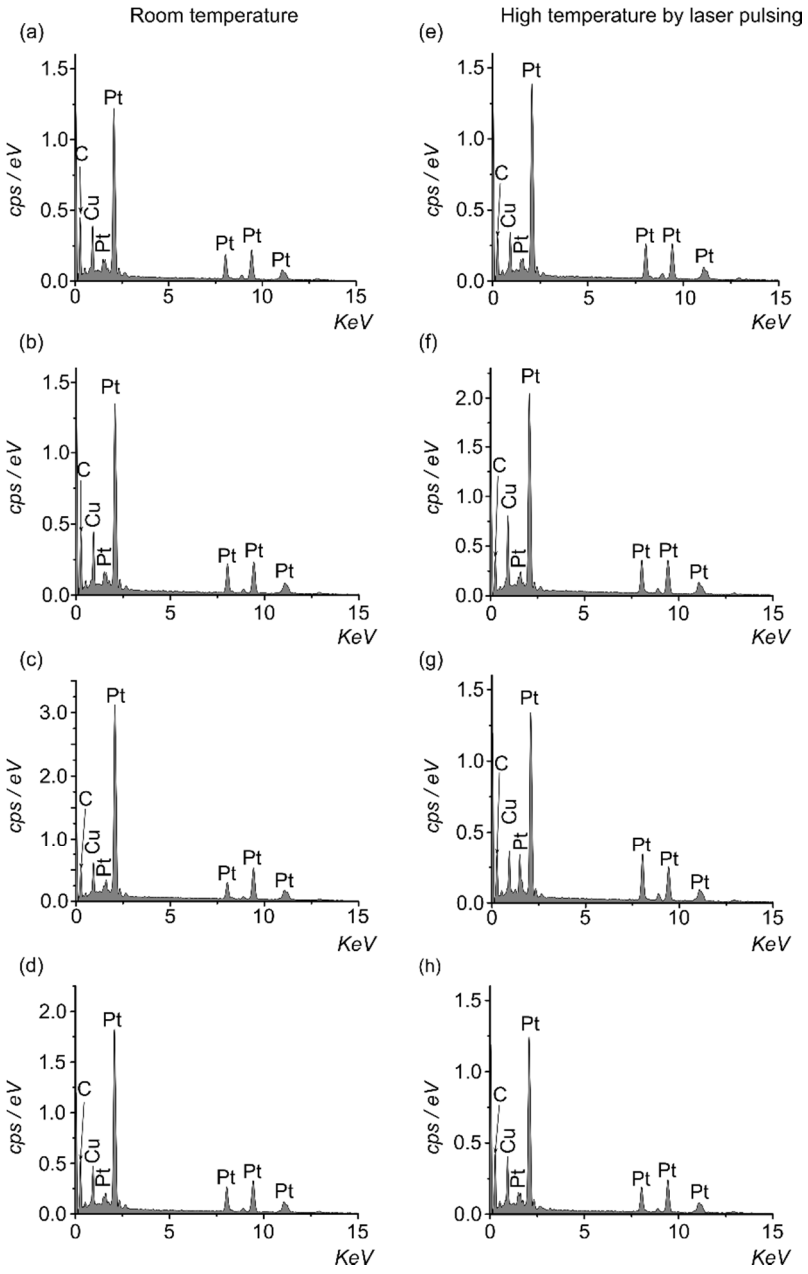

Figure 3.10: XEDS spectra taken of the Pt NPs electrodeposited under RT (a-d) and laser pulse heating conditions (e-h) at the different deposition potentials (a and e) +0.1 V, (b and f) 0 V, (c and g) -0.1 V and (d and h) -0.2 V for t_{dep} = 5 s.

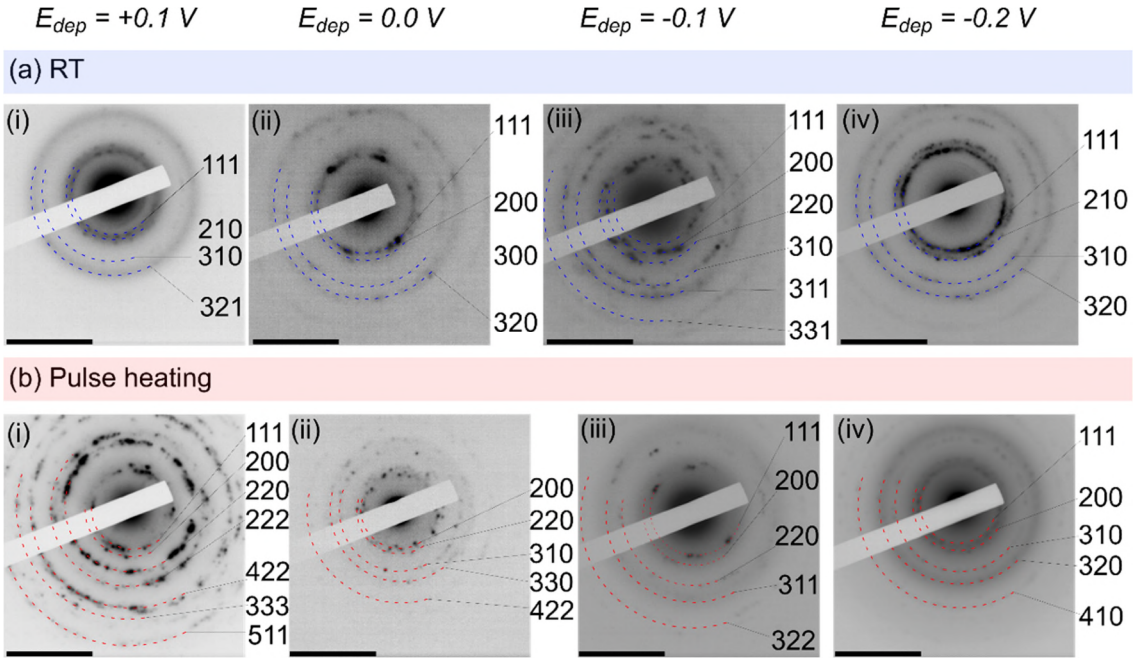

Figure 3.11: SAED patterns of Pt NPs synthesised under (a) RT conditions and (b) under laser pulse heating at an E_{dep} of (i) +0.1 V, (ii) 0.0 V, (iii) -0.1 V, and (iv) -0.2 V. Scale bars are 10 nm^{-1}.

From the AFM and FE-SEM data (Figures 3.6, 3.7, and 3.8), the main effect of pulsing the temperature, in combination with increasing E_{dep} was shown to be decreasing particle size and increasing mono-dispersity during electrodeposition. Crucially, TEM now reveals pulsing the temperature plays a key role in the creation of higher index facets during electrodeposition and increasing the porosity of the resulting structure. Interestingly the occurrence of the most, higher index facets occurs under laser pulsed conditions at the lowest E_{dep} (Figure 3.11) whilst qualitatively, the porosity appears greatest at the highest (most negative) E_{dep}. The latter could also have a contribution from depositing at a potential into the H_{ads} / H_2 evolution potential region. At these higher negative potentials and in the presence of the high temperature, a decrease of the solution viscosity and surface tension results,[449] allowing H_2 bubbles to break away from the surface with smaller diameters, potentially facilitating transport of these detached H_2 bubbles through the interior of the deposit.[450]

3.4.5 Electrocatalytic performance and methanol oxidation studies

The electrochemical response of the electrodes produced under both temperatures using all four electrodeposition driving forces was investigated in deaerated 0.5 M H_2SO_4, Figure 3.12. In electrocatalysis, size, structure and crystallographic orientation are

important.[451] Size influences the flux of reactant/product towards/away from the surface, whilst structure and crystallographic orientation can influence the binding ability of counter ions in solution and reactants/intermediates or products during inner sphere (electrocatalytic) electron transfer.[105, 452] For example for MeOH oxidation in acidic media the electroactivity of Pt, low index, single crystal planes was found to be (greatest) (100) > (110) > (111) (lowest).[453]

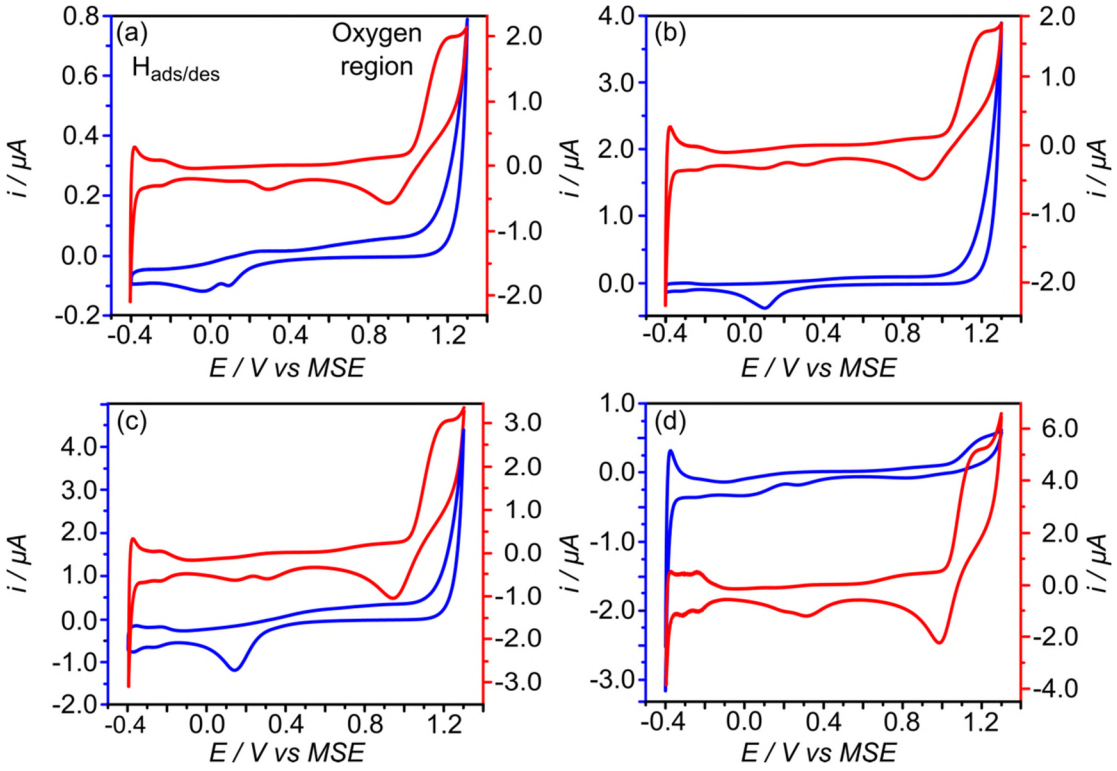

Figure 3.12: CVs of Pt NPs supported on BDD electrodes in deaerated 0.5 M H_2SO_4 solution at 0.05 V s^{-1} at RT. Electrodes were made by electrodeposition of Pt on BDD under (blue) RT and (red) laser pulse heating conditions using E_{dep} of (a) +0.1 V, (b) 0 V, (c) -0.1 V and (d) -0.2 V respectively at t_{dep} = 5 s. Note the y scales have been offset for clarity.

By recording CVs in acidic solutions, the H_{ads}/H_{des}, surface oxidation and $oxygen_{ads/des}$ ($O_{ads/des}$) features can also be used to highlight differences in the electroactivity of the electrodeposited aggregates. These responses are shown in Figure 3.12, where CVs were recorded by cycling the Pt NPs-BDD electrodes in 0.5 M H_2SO_4 at a scan rate of 0.05 V s^{-1} *vs.* MSE until a consistent response was obtained. The characteristic voltammetric features associated with Pt are visible in the acidic electrolyte, as discussed previously for Figure 3.4. The only difference being here (Figure 3.12) is that the Pt NPs are pre-formed on the electrode surface, removed from the electrodeposition

solution, and then cycled in acid. In general, the CVs confirm the polycrystalline nature of the electrodeposited Pt. Additionally, the shape and the charge passed due to $H_{ads/des}$ depend upon the size and structure of Pt NPs. Pt particles made by applying low driving forces (+0.1 V) at RT show one $H_{ads/des}$ peak. In contrast, at RT, Pt particles produced under high driving force conditions (0.0 V, -0.1 V and -0.2 V), show two peaks in the $H_{ads/des}$ regions. Under laser pulse heating electrodeposition different CV signatures are observed compared to RT. Two $H_{ads/des}$ peaks are observed for E_{dep} = +0.1 V, 0 V and -0.1 V whilst three peaks in the H_{des} region and two peaks in the H_{ads} regions are visible at E_{dep} = -0.2 V.

The $H_{ads/des}$ peaks are usually associated with different forms of adsorbed H and the contribution of different crystal facets;[421, 454] with the position on the voltage axis and number of peaks correlating with the dominant crystal planes present. Using single crystal electrodes, for the low index crystal planes, it has been found that the $H_{ads/des}$ peaks occur in the order (110) > (111) > (100),[454] with (110) being the most negative on the potential axis due to the weakly bonded state of H, whereas (100) promotes the strongest binding of H.[455] Labelling of the $H_{ads/des}$ features in Figure 3.12 to specific crystal planes is challenging especially given the SAED data in Figure 3.11, which illustrates the wide variety of different crystallographic orientations initially present prior to cycling in acid.

All Pt NPs electrodeposited under laser pulse heating, showed a greater ESA (from the H_{des} data) compared to RT electrodeposition conditions, as shown in Table 3.2. This could be due to a combination of factors, for example, aggregation into a more compact structure, as seen for RT electrodeposition, leads to a decrease in the ESA.

In the oxygen adsorption / desorption region, $O_{ads/des}$, (+0.7 V to +1.3 V) the currents passed are also very different. There are significant $O_{ads/des}$ currents associated with the laser pulsed deposited NPs, whereas there is little evidence of this process for NPs produced at RT. This suggests the presence of electrochemically accessible atomic arrangements, such as the higher index facets observed in SAED, on the laser heated Pt NPs which are more efficient at promoting oxygen adsorption in this potential region.[99, 447]

Table 3.2: Experimental values of the charge associated with H_{des} on Pt NPs and measurement of the corresponding ESA.

E_{dep} / V	Temperature / °C	QH_{des} / μC	ESA
+0.1	20.0	0.00183 ± 0.00005	8.69×10^{-6}
	66.4	0.02102 ± 0.00007	1.00×10^{-4}
0.0	20.0	0.00253 ± 0.00004	1.21×10^{-5}
	66.4	0.03658 ± 0.00005	1.74×10^{-4}
-0.1	20.0	0.06178 ± 0.00006	9.93×10^{-5}
	66.4	0.05636 ± 0.00005	2.68×10^{-4}
-0.2	20.0	0.02904 ± 0.00003	1.38×10^{-4}
	66.4	0.12170 ± 0.00007	5.80×10^{-4}

The electrochemical catalytic activity of the densely packed "compact" and "nanoporous" Pt particles for the oxidation of MeOH *i.e.* the methanol oxidation reaction (MOR) was also investigated using CV analysis. The ideal MOR catalyst is one which is able to efficiently oxidise MeOH, decompose water (to produce adsorbed OH which acts as a further oxidising agent) and weakly bind poisoning species, such as CO,[456] which inhibit further MeOH oxidation. CVs were measured in a deaerated aqueous solution of MeOH (CH_3OH, 1 M) and sulfuric acid (H_2SO_4, 0.5 M), between 0 and +1 V, as shown in Figure 3.13.

All MOR CVs show similar features where there is a peak current response due to MeOH oxidation on the forward scan (starting at 0 V *vs.* SCE and ending at +1.0 V *vs.* SCE)[457] and a prominent oxidative peak in the backward scan. The latter has been traditionally associated with residual (intermediate) carbon species poisoning the surface[458] (in particular CO_{ads}) rather than to the oxidation of freshly chemisorbed species.[459] As such the ratio of the forward peak current, $i_{p,f}$, to the back peak current, $i_{p,b}$ has been used extensively in the literature as a guide to the ability of the catalyst to tolerate CO poisoning. The more residual adsorbed species on the surface the more the catalyst is poisoned and the lower the ratio of $i_{p,f}/i_{p,b}$. Very recent preliminary research, however, has suggested that the back current does not reflect CO adsorption and poisoning,[460] but instead is indicative of Pt surface oxidation; the less free Pt the smaller the back current.[461]

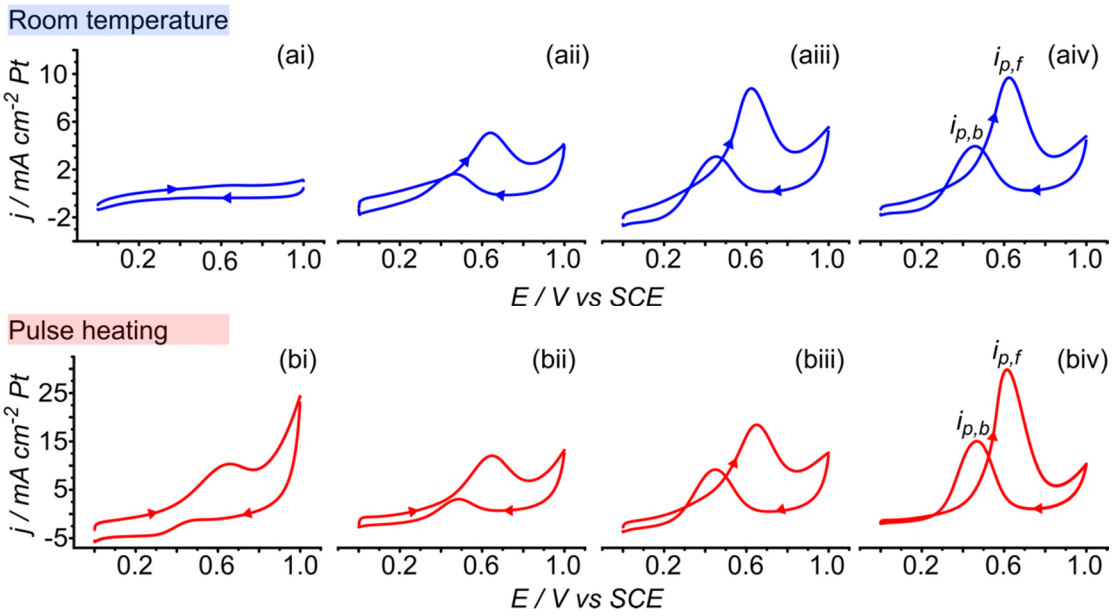

Figure 3.13: CVs recorded at 0.05 V s^{-1} for the oxidation of 1 M MeOH in a sulfuric acid (0.5 M H_2SO_4), catalysed by Pt NPs-BDD electrodeposited under (a) RT and (b) laser pulse heating conditions for E_{dep} of (i) +0.1 V; (ii) 0 V; (iii) -0.1 V; and (iv) -0.2 V and t_{dep} = 5 s.

In order to compare the difference in the electrocatalytic activity of the different Pt NPs towards MeOH oxidation the current passed is normalised with respect to the Pt NP surface area (ESA, calculated from H_{des}, displayed in Table 3.2) and then evaluated with respect to both $i_{p,f}$, and $i_{p,b}$ and the ratio of $i_{p,f}$ to $i_{p,b}$, Table 3.3.[462-464] Higher $i_{p,f}$

corresponds to a greater catalytic activity,[447] and if we take the traditional view, a higher ratio indicates a catalyst less subject to CO poisoning.[465]

Noticeably, both the forward ($i_{p,f}$) and the backward ($i_{p,b}$) peak current density for MOR increases with an increase in the electrodeposition driving force for Pt NPs-BDD electrodes prepared under both RT and laser pulse heating conditions. Previous reports have attributed enhancements in $i_{p,f}$ to the presence of specific crystallographic orientations, defects in the crystalline structure and the structure of the inter-grain boundaries.[432, 453, 466]

Table 3.3: Experimental measurement of the values of the current corresponding to MeOH oxidation and the tolerance of Pt NPs catalyst towards CO adsorption

E_{dep} / V	Temperature / °C	$i_{p,f}$ / mA cm^{-2}	$i_{p,b}$ / mA cm^{-2}	$i_{p,f}$ / $i_{p,b}$
+0.1	20.0	0.68 ± 0.01	0.36 ± 0.01	1.8 ± 0.01
	66.4	10.36 ± 0.02	1.18 ± 0.01	8.7 ± 0.02
0.0	20.0	5.08 ± 0.01	1.66 ± 0.02	3.1± 0.01
	66.4	12.02 ± 0.03	3.07 ± 0.01	3.9 ± 0.03
-0.1	20.0	8.79 ± 0.02	3.08 ± 0.03	2.8 ± 0.03
	66.4	17.61 ± 0.02	8.42 ± 0.02	2.1 ± 0.01
-0.2	20.0	9.68 ± 0.03	3.95 ± 0.03	2.4 ± 0.02
	66.4	29.84 ± 0.01	15.04 ± 0.01	1.9 ± 0.03

All of the more "porous" Pt particles, from pulse laser electrodeposition, show higher $i_{p,f}$ compared to those formed under RT, which we attribute to both a greater accessibility to, and increased number of, catalytically active sites,[467] as also evidenced by the TEM and SAED data (Figure 3.9 and Figure 3.11) and the CV data in Figure 3.12. The largest $i_{p,f}$ value is found for the nanoporous Pt particles electrodeposited under laser pulse heating conditions at the highest overpotential (-0.2 V).The highest $i_{p,f}/i_{p,b}$ value (Table 3.3) is found for Pt NPs synthesized at the lowest driving potential (+0.1 V) under laser pulse heating conditions ($i_{p,f}/i_{p,b}$ = 8.7). Although these particles show the most higher index planes (from SAED), they are less porous (from TEM) compared to those particles produced at more negative E_{dep} under laser pulsed conditions. Thus, whether all the identified crystal planes can be accessed is not known, due to the lower porosity. Note at this deposition potential the $i_{p,f}$ for MOR is still higher than for all values recorded on Pt particles deposited under RT conditions. Although catalytic, electrochemically accessible surfaces are preferred,[468] to produce the maximum $i_{p,f}$, such surfaces may also promote very efficient adsorption of residual MeOH oxidation intermediate products which can cause a poisoning effect. This may explain the data associated with the Pt NPs deposited under laser pulsed heating conditions at the largest overpotential. These particles show the highest ip,f data but also return the lowest $i_{p,f}/i_{p,b}$ ratio ($i_{p,f}/i_{p,b}$ =1.9), Table 3.3, (if the recognized view is upheld).

3.5 Conclusions

A new approach to producing nanoporous Pt NPs of high electrocatalytic activity has been introduced, namely electrodeposition in tandem with continuous heating and cooling of the electrode surface. The latter is achieved using a pulsed laser in conjunction with a high thermal conductivity electrode: boron doped diamond. Injecting bursts of heat via IR laser modulation into the interface and then rapidly cooling acts to both separate the nucleation and growth process, leading to NP size homogeneity and the production of "porous", electrochemically accessible, structures. TEM and SAED showed the particles to be composed of loosely packed Pt aggregates, 2-5 nm in size, containing high index crystal planes. In contrast, electrodeposition at RT resulted in much more densely packed "compact" structures.

Investigation of NP activity towards MeOH oxidation revealed a significantly higher catalytic activity for the nanoporous NPs prepared under laser heated conditions, compared to those electrodeposited at RT. The highest activity was found for the Pt NPs electrodeposited under laser heated conditions under the highest driving potential. Qualitatively, TEM also revealed these NPs to be the most porous. However, the ratio of $i_{p,f}$ to $i_{p,b}$ was highest for NPs deposited under laser heated conditions but with the smallest overpotential. If we assume the highest ratio indicates the NPs least susceptible to adsorbed CO poisoning, the data suggests that the most catalytically active NPs may also encourage binding of residual adsorbed CO and that a compromise must be reached.

Future work will look to further explore the role of temperature pulsing during electrodeposition on the resulting structure and catalytic activity of NPs, given that temperatures in excess of 100 °C in aqueous solutions are possible[340] using this approach.

Chapter 4

Tracking Metal Electrodeposition Dynamics from Nucleation and Growth of a Single Atom to a Crystalline Nanoparticle

4.1 Abstract

In electrodeposition, the key challenge is to obtain better control over nanostructure morphology. Currently, a lack of understanding exists concerning the initial stages of nucleation and growth, which ultimately impacts the physicochemical properties of the resulting entities. Using identical location scanning transmission electron microscopy (IL-STEM), with boron doped diamond (BDD) serving as both an electron transparent TEM substrate and electrode, we follow this process, from the formation of an individual atom through to a crystalline nanoparticle, under potential pulsed conditions. In doing so, we reveal the importance of electrochemically driven atom transport, atom cluster formation, cluster progression to a nanoparticle and the mechanism by which neighbouring particles interact during growth. Such information will help formulate electrochemical deposition procedures and promote wider uptake of electrodeposited structures in a wide range of societally important applications. This type of measurement is possible in the TEM because the BDD possesses inherent stability, has an extremely high thermal conductivity, is electron beam transparent, free from contamination and robust enough for multiple deposition and imaging cycles. Moreover, the platform can be operated under conditions such that we have confidence that the dynamic atom events we image are truly due to electrochemically driven deposition and no other factors, such as electron beam induced movement.

4.2 Introduction

Electrodeposition, the electrochemically driven formation of solid structures on an electrode surface, has the potential to be a key technology for advancing energy storage and conversion capabilities, aiding in the design of, for example, advanced electrode materials for water splitting, fuel cell technologies and carbon dioxide capture and turnover.[469-471] Many of these applications require precise control over the atomic-scale

architecture of the resulting metal structure.[472, 473] However, despite the huge technological possibilities, electrochemical deposition strategies have yet to realize their full potential. One decisive factor is related to the fact that surprisingly little is known about the mechanistic details of the initial stages of electrodeposition, at the atom level.[248, 279] Such information is crucial if the required control is to be obtained and implemented.

Electrochemically, growth is traditionally treated using either classical or atomistic theories, which describe the process as the formation of supercritical (stable) nuclei, which grow by direct addition of atoms, formed by electroreduction, on the nuclei surface, see *Chapter 1*, sections 1.4 and 1.5.[26, 232, 237] Experimentally, analysis is typically limited to current-time (*i*-*t*) measurements that give average, macroscopic information from which nanoscale behaviour is inferred, such as nucleation rate and number of growth nuclei.[26, 232, 237] However, studies making use of advancements in microscopic analysis often show that these models are inappropriate descriptors for the early stages of nucleation and growth.[272, 273, 278, 280, 332, 474] Such work has led to factors such as electrochemically driven surface diffusion and aggregation being postulated as important pathways,[273, 278] but to date such processes have yet to be dynamically visualized and thus confirmed. Furthermore, the resolution obtained using scanning probe techniques such as atomic force microscopy (AFM) and scanning electrochemical cell microscopy is typically limited to the nanoparticle (NP) level. Electrochemical scanning tunnelling microscopy measurements can resolve individual atoms, but studies typically focus on two-dimensional growth and dissolution.[475] Liquid cell transmission electron microscopy (TEM),[334] whilst making huge strides in monitoring dynamic electrochemical systems,[262] has limited resolution due to factors such as electron scattering in the liquid and electron-beam induced reactions. In contrast, ex-situ high resolution aberration corrected scanning TEM (STEM) techniques can not only resolve single atoms, but are able to quantify the number of atoms within a particle.[476]

Our aim is to dynamically visualize in detail the earliest stages of nucleation and growth, beginning with the smallest possible electrodeposited entity, a single atom,[14-16, 444, 477] with millisecond temporal resolution. We use identical location (IL)-STEM,[431, 478] with repeated electrodepositions and *ex-situ* STEM imaging of the same area, to follow and elucidate these initial stages, effectively taking "snapshots" of the

nucleation and growth process at defined time intervals. We also take care to minimize (and quantify) electron beam induced effects. We achieve our overall aim by employing IL-STEM in combination with a TEM substrate made of a conducting boron doped diamond (BDD),[122] that functions as both an electrode and inherently stable electron-transparent support. The BDD brings significant advantages to dual electrode-IL-TEM measurements such as its inherent robustness for repeat measurements, low atomic number, crystallinity, stability, extremely high thermal conductivity and very low Bremsstrahlung backgrounds.[479]

4.3 Experimental and methods

4.3.1 Solutions

Au electrochemical deposition solutions were prepared from potassium tetrachloroaurate ($KAuCl_4$, 99.99%, Sigma-Aldrich) with perchloric acid ($HClO_4$, 99.99%, Sigma Aldrich) as a supporting electrolyte in ultra-pure Milli-Q water (18.2 MΩ cm, Millipore Corp., U.S.) at 20 °C. All chemicals were used as received without further purification. Au^{3+} deposition solutions contained 1×10^{-3} M $[AuCl_4]^-$ in 0.1 M $HClO_4$ (pH = 1.09) which was deaerated with argon (Ar) for 20 minutes before electrodeposition to exclude oxygen. Ar flow was maintained over the solution during the experiment.

4.3.2 Materials and electrode fabrication

The experiments were performed using a freestanding microcrystalline BDD plate, suitably doped for electrochemical studies (boron dopant level of ~3×10^{20} B atoms cm^{-3})[122, 480] and grown using microwave chemical vapor deposition (ElementSix, Harwell, Oxford).[122] The plate was mechanically polished to ~50 μm thickness, with both sides showing a surface roughness of *ca.* 0.18 nm, measured using AFM on the surface of a grain (grain size *ca.* 2-8 μm). The plate was cut into disks of diameter 3 mm (suitable for insertion into the TEM holder) using laser micromachining and acid cleaned to remove machining debris. The plates were Ar^+ ion milled to electron transparency at an accelerating voltage of 6 kV and an angle of incidence of ~4°. The sample was mounted on a post support using glycol phthalate bonding wax (Agar Scientific) allowing continuous milling as the sample rotated. Each side was milled in

turn (*approx.* 2 hours each side) until a small hole (*ca.* 100-300 μm in diameter) was formed in the centre of the BDD disk. The disk was mounted into a clamp support for a final low energy ion mill of both sides of the disk at an accelerating voltage of 2 kV with a modulated ion beam, for 30 minutes, to provide a smooth surface finish. The BDD was acid cleaned after ion milling (0.1 M HNO_3 followed by 0.1 M H_2SO_4). To make an ohmic contact to the electrode the upper quarter of one of the edges was sputtered (Moorfield MiniLab 060 Platform) with Ti (20 nm)/Au (400 nm) and annealed in a tube furnace for 5 hours at 450 °C.[122, 375]

4.3.3 Electrochemical measurements

All electrochemical experiments were carried out using a three-electrode set-up controlled by a potentiostat (CHI730A, CH Instruments, Inc. Austin, TX). A commercial SCE was used as the reference electrode and a helical Pt wire served as the counter electrode. The BDD electrode was electrically connected using a fine metal clamp attached to the Au contact. The disk was dipped into the electrolyte solution using a manual *x,y,z* micropositioner (Newport, Oxford) such that the central hole was in the solution but the Au contact remained dry. The set-up is shown in Figure 4.1. Note that the counter covers the BDD WE from all direction, hence providing equal potential field for both sides of the deposition.

Immediately after Au deposition, the grid was rinsed with deoxygenated ultra-pure water and left to dry in a desiccator under an Ar atmosphere, and then stored under vacuum at 60 °C before transfer to the TEM. Electrodeposition snapshots were recorded for growth periods 0 to 5 ms (5 ms total nucleation and growth), 5 to 10 ms (10 ms total nucleation and growth) and 10 to 30 ms (30 ms total nucleation and growth).

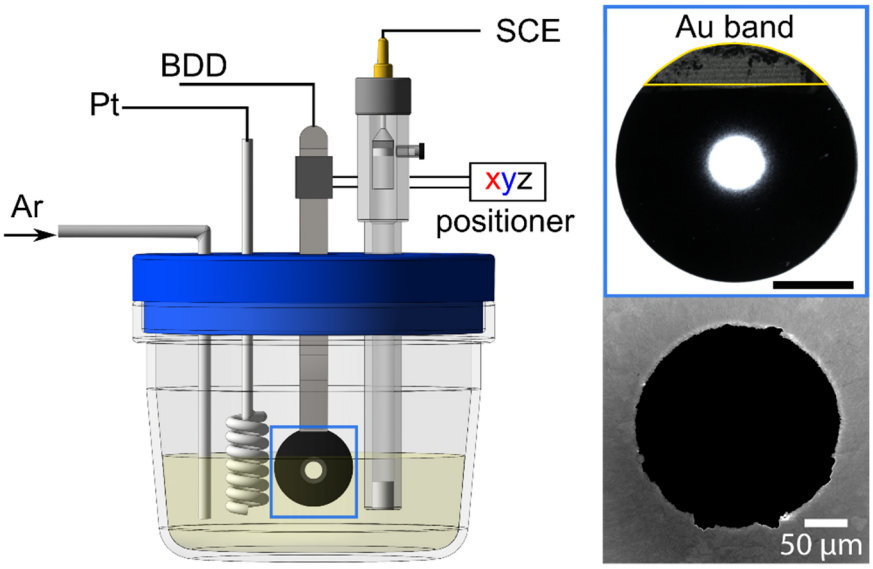

Figure 4.1: Schematic of the electrodeposition experimental set-up (left). The top right image shows an optical microscopy image of the BDD TEM platform, after ion milling to thin the BDD to electron transparency around the center of the hole (scale bar = 1 mm). A gold band is visible in the top quarter of the BDD disc that functions as an ohmic contact. The bottom right image shows an in-lens FE-SEM image of the BDD region around the hole after ion milling.

4.3.4 Surface characterization

FE-SEM: FE-SEM was used to image the BDD platform before and after ion milling and also to obtain low magnification images of the Au particles after electrochemical deposition. FE-SEM images were recorded using the In-lens and STEM detector on a Zeiss Gemini operating at 15 kV and 25 kV, respectively.

AFM: AFM was employed to measure the roughness of the surface before and after ion milling, AFM images were acquired at a low scan rate (0.25 Hz) in intermittent contact (tapping mode) using a Bruker Innova AFM.

TEM: For examining the suitability of BDD TEM supports for imaging and diffraction, TEM characterization was carried out on the BDD platform using a JEOL-JEM 2100 (LaB_6) microscope at 200 kV. The time dependent study of particle shape, structure, size, composition and evolution, during electrochemical nucleation and growth, were investigated by IL-ADF-STEM in a double aberration corrected JEOL JEM-ARM200F at 200 kV. Although deposition occurred on both sides of the platform, images were all

taken from the same face. ADF-STEM images were obtained using a JEOL annular field detector with a fine-imaging probe, and a current of 23 pA with a convergence semi-angle of ~25 mrad and an ADF detector inner angle of 50 mrad.

EELS: EELS was recorded on a JEOL JEM-ARM200F microscope operating at 200 kV with a Gatan GIF Quantum SE spectrometer. Measurements were performed at a total energy resolution of 3 eV, determined by measuring the full width at half-maximum (FWHM) of the zero-loss peak. The following conditions were chosen for the EELS spectra acquisition: convergence semi-angle 29 mrad, collection semi-angle 100 mrad, exposure time 0.05 s, dispersion 0.5 eV/ch and probe size < 0.1 nm.

4.3.5 DFT simulations

All DFT calculations were carried out with the all-electron, numerical atomic orbital code FHIaims[481] using tight integration settings and geometry optimizations down to a force threshold of 0.01 eV per Å. Dispersion corrected functional Perdew-Burke-Enzerhof (PBE) and long-range Van-der-Waals correction (derived by Tkatchenko and Scheffler)[482, 483] was employed. Barrier searches were performed using the Atomic Simulation Environment (ASE)[484] and the Climbing Image Nudged Elastic Band (NEB) procedure[485] with a threshold of 0.07 eV per Å. Global geometry optimizations were performed using ASE and the Minima Hopping method.[486, 487] The diamond (110) model surface was built using the optimized PBE lattice constant of 3.572 Å. The model is composed of 7 carbon layers and a vacuum orthogonal to the [110] direction of 32 Å. We model the experimental conditions by oxygen passivation of the surface at the top and bottom termination of the surface slab. Upon studying a variety of different possible oxygen functionalization using local and global optimization, we find the most stable surface to be represented by a reconstructed (2×1) surface unit cell of diamond (110) with 2 adsorbed oxygen atoms at the surface (see Figure 4.2 and Figure 4.11(c)). Both of them are adsorbed at the top carbon atoms, one as a double bonded ketone (C=O) group, the other one as an ether (O-C-O) group bridging across the (110) carbon ridges.

The two-dimensional energy landscape reported in Figure 4.11(c) was calculated using constrained local optimization, where a single gold atom was placed on the oxygen functionalized surface and only allowed to relax vertically. Based on this landscape,

climbing image NEB calculations were performed to calculate the two barriers of gold adatom diffusion along the C-C ridges [$1\bar{1}0$] and perpendicular to the ridges [001].

4.3.6 Atom counting procedure from STEM images

The signal from ADF STEM imaging is given as an arbitrary intensity and the objective is to calibrate this to give the number of atoms.[394] Due to the high density of distinct, individual gold atoms surrounding the larger nanoclusters, it is possible to obtain a measure of the intensity from one gold atom. Through comparison to simulations, this single atom intensity can be used to create a calibration curve from ADF intensity to the number of atoms in a vertical column, Figure 4.3. In measuring the intensity of the gold atoms, first the gold signal must be separated from the background BDD signal. On simple images, this can be sensibly approximated as a plane to be subtracted. However, for images with complicated background intensities, the background is calculated by masking the gold signal and infilling using interpolation (provided by MATLAB®'s region-fill). To remove the influence of noise when interpolating, a median and Gaussian filter is applied (with standard deviation of 0.017 nm and window size of 0.2 nm respectively). The intensity of a single atom is then obtained from averaging over a large number of single atoms (typically >100) and the uncertainty is measured as the standard error of the means.

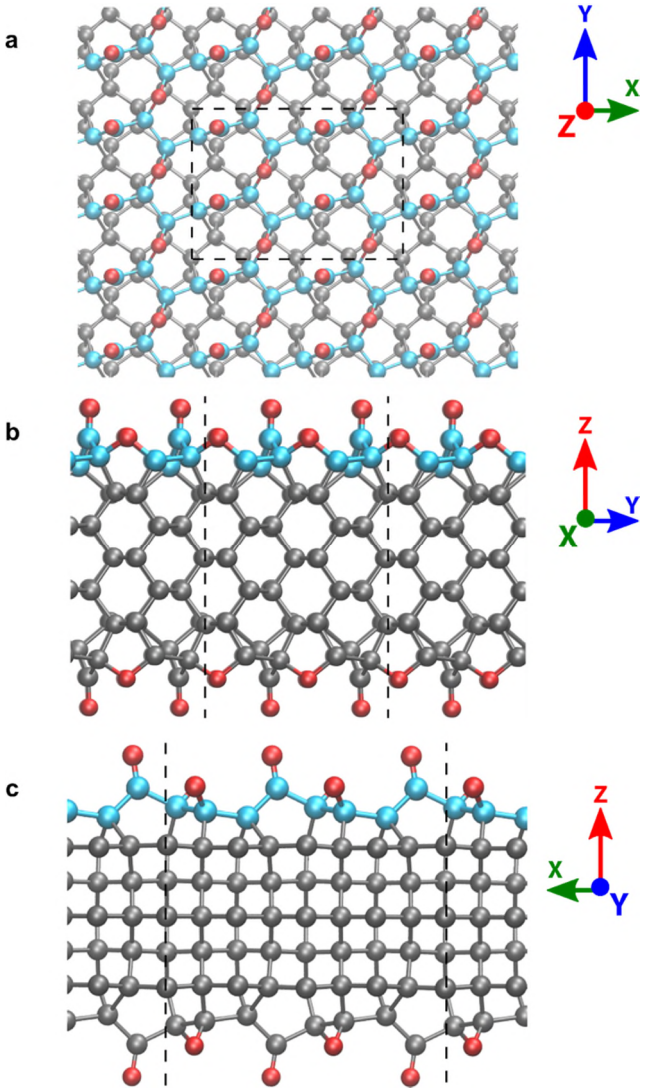

Figure 4.2: Ball-and-stick models of the global energy minimum of an oxidized diamond (110) surface slab as shown from the top (Z direction) (a), and from the side directions, X (b), and Y (c). The dashed lines correspond to the unit cell boundaries used in the simulations. The 1st layer carbon atoms are depicted in light blue, the remaining carbon atoms in grey, and the oxygen atoms in red.

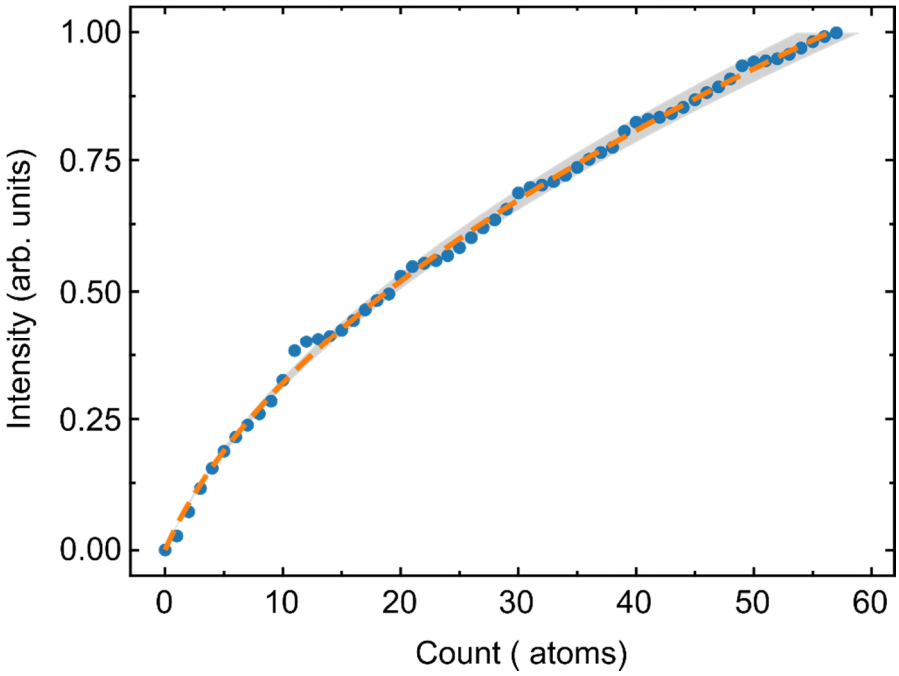

Figure 4.3: Simulation of Au intensity as a function of Au atom vertical (column) thickness, in either an AC or NP, on the surface of the BDD-TEM electrode.

Simulations were performed using QSTEM with 001 orientation gold with a column thickness ranging from 1-60 gold atoms. The microscope parameters used in the simulation were empirically determined from the microscope (200 kV accelerating voltage, detector radius 45-100 mrad, convergence angle of 25 mrad, spherical aberration 1 µm) and with 30 thermal diffuse scattering configurations. The total gold column intensity was then summed and fitted using a parabola. Note that the intensity has discontinuities due to channelling effects.

4.3.7 Statistical analysis of atom movement

Single atom tracking was performed using the MTrackJ plugin for ImageJ.[488] The measure of the deviation of the position of an atom with respect to its starting (*x,y*) position over time (here sequential acquirement/registration of ADF-STEM images referred to as sequence of frames) is presented as the mean squared displacement (MSD). MSD provides a measure of the spatial extent of atom motion over ten frames. The MSD is defined as Equation 4.1:[489]

$$MSD = \frac{\sum_{n=1}^{N}(x_n(t) - x_n(s))^2}{N} \qquad \text{Equation 4.1}$$

Where *N* is the number of frames to be averaged, $x_n(0) = x_s$ is the starting position of each atom, $x_n(t)$ is the position of each atom in determined time t (*i.e.* next frame).

4.4 Results and discussion

4.4.1 Operational Procedure for Monitoring Gold Nucleation and Growth

The BDD electrode-TEM platform was produced by ion milling a thin disc of chemical vapor deposited BDD to electron transparency (shown schematically in Figure 4.4(a)); the edge of the ion milled hole is typically less than 35 nm thick, as measured using electron energy loss spectroscopy (EELS). The EELS spectrum of the carbon (C) K ionisation edge in this area is shown in Figure 4.4(b). The C edge at 284 nm indicates sp^3 bonding (*i.e.* diamond). The thickness of the specimen is determined from the ratio of zero-loss electrons to the total transmitted intensity extracted from the low-loss part of the spectrum and the mean free electron path in diamond at an electron energy of 200 kV (97.6 nm).[490] A field emission scanning electron microscope (FE-SEM) image of the thinnest part of the BDD electrode surface after ion milling, is shown in Figure 4.4(c), whilst Figure 4.4(d) depict an ADF-STEM image of the BDD edge; where the differently doped grains are visible.

Figure 4.5 shows the corresponding cyclic voltammogram for Au^{3+} reduction. The response of the BDD TEM electrode towards Au deposition and stripping, in a solution containing 1 mM $[AuCl_4]^-$ in 0.1 M $HClO_4$ can be described as follow. The CV had a starting potential of +1.3 V, where no faradaic processes take place, and was scanned negatively to -0.5 V and then anodically to +1.5 V, at 0.1 V s^{-1}. The predominant species is Au^{3+} and the overall reduction process can be written as shown in Equation 4.2.[271]

$$[AuCl_4]^- + 3e^- \rightleftharpoons Au^0 + 4\,Cl^- \qquad \text{Equation 4.2}$$

The cathodic peak at +0.23 V is associated with Au^{3+} reduction. In the anodic direction, the oxidation peak at +1.29 V can be attributed to Au dissolution in this acidic media (most likely), or Au oxidation.[256, 491] A very similar response is seen for a 1 mm diameter BDD disk electrode.

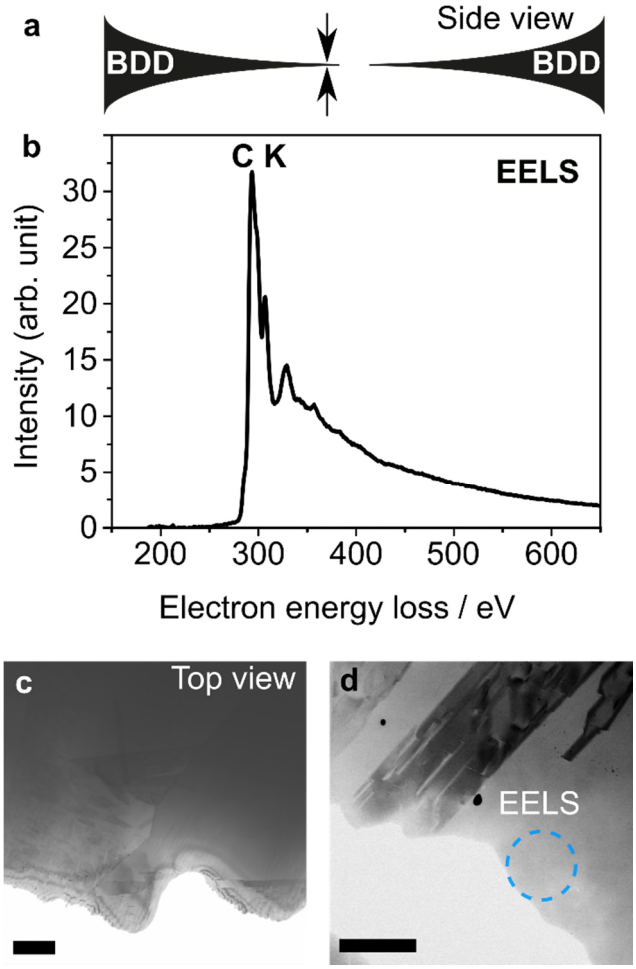

Figure 4.4: Experimental evidence of the suitability of the BDD electrode for TEM imaging and EELS analysis. (a) Cross-sectional schematic of the BDD-TEM plate after ion milling. (b) EELS of the BDD (on the BDD edge closest to the hole) showing the carbon K ionization edge. (c) FE-SEM image of the thinnest part of the BDD electrode surface after ion milling. (d) Annular dark field-STEM image of the BDD edge; the differently doped grains are visible. Scale bar in c and d, is 100 μm.

Total electrodeposition times of (a) 5 ms, (b) 10 ms and (c) 30 ms, in a solution containing deaerated 1×10^{-3} M $[AuCl_4]^-$ in 0.1 M $HClO_4$ (pH = 1.09), were employed to capture the initial stages of gold (Au) nucleation and growth on BDD. Specifically, each experimental cycle leading to a STEM snapshot of nucleation and growth involved: deposition for a defined time period; washing in deionized water; drying; holding at 60 °C for 8 hours under vacuum to eliminate any mobile hydrocarbons; STEM imaging.

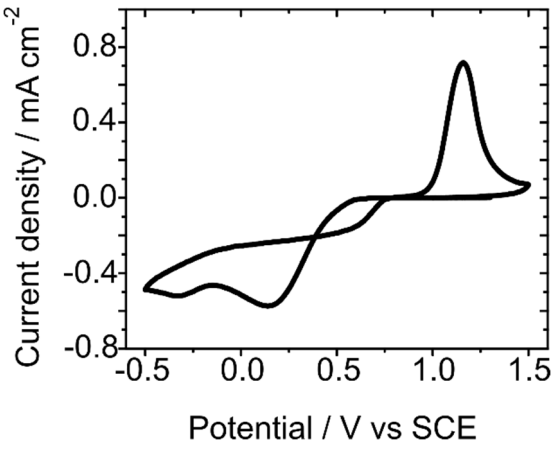

Figure 4.5: CV recorded at the BDD-TEM electrode for Au electrodeposition, in a solution containing 1×10^{-3} mol dm^{-3} $[AuCl_4]^-$ in 0.1 M $HClO_4$ at 0.1 V s^{-1}.

The first deposition constituted 5 ms, the second a further 5 ms and the third, an additional 20 ms. Note, for the electrode area employed (~0.04 cm^2), as the capacitive current contribution decays in ~ 0.1 ms, 98%, 98% and 99.5% of the currents observed, in the corresponding *i-t* profiles recorded over 0-5 ms, 5-10 ms and 10-30 ms respectively, are due to faradaic processes. The distinctive shape of the edge of the BDD support was used as a reference point to allow imaging of the same area in each cycle. All IL imaging was carried out in annular dark field (ADF)-STEM mode using a fine probe (current 23 pA, convergence semiangle ~25 mrad, 8 μs per pixel), with each area imaged only once per electrodeposition time, unless otherwise stated. A typical sequence of IL-ADF-STEM images from the same area are shown in Figure 4.6. Similar electrodeposition dynamics where observed close to, and up to a radial distance of ~500 nm (the limit of the electron beam transparency of the substrate), from the edge of the hole.

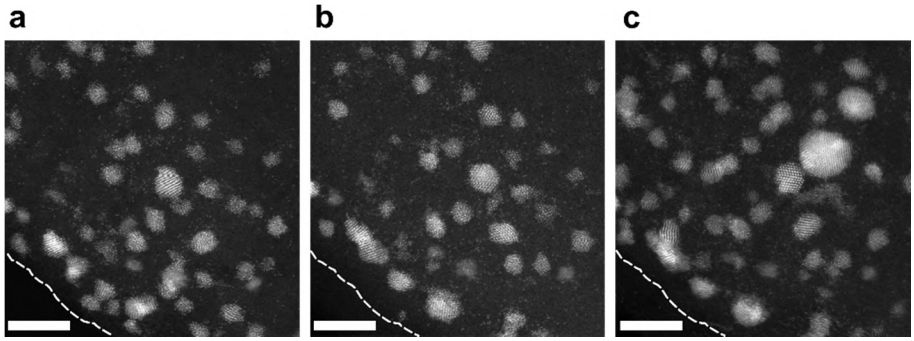

Figure 4.6: IL-ADF-STEM images of the BDD-TEM platform after Au electrodeposition recorded in a solution containing 1×10^{-3} M $[AuCl_4]^-$ in 0.1 M $HClO_4$ for total growth times of (a) 5 ms (b) 10 ms and (c) 30 ms for η of -1.2 V. Scale bar is 20 nm.

Further data analysis was carried out by examining selected regions of these and other images. Electrodeposition of Au was driven at a potential of -0.5 V *vs.* a saturated calomel reference electrode (SCE), which equates to an overpotential, η, of -1.2 V. At this potential, a faradaic current contribution for the evolution of hydrogen, on the deposited Au nanostructures, is not expected, based on the data shown in Figure 4.5. Under these conditions, the size of the critical nucleus, N_c, is calculated to be smaller than a single atom, using the atomistic theory of nucleation.[15, 16, 237] Here the number of atoms in the critical nuclei, N_c, can be determined by examining the dependence of the nucleation rate, J (nuclei cm^{-2} s^{-1}), on η in accordance with Equation 4.3:[16, 237]

$$\frac{\partial \ln J}{\partial |\eta|} = \frac{-N_c z F}{R T} \qquad \text{Equation 4.3}$$

where z is the number of electrons involved in the reduction process = 3, F is the Faraday constant (F = 96485 C mol^{-1}), R is the gas constant = 8.314 J K^{-1}mol^{-1}, and T is the temperature (T = 293 K). J was determined from analysis of IL-ADF-STEM images for the same deposition area over three growth periods, 0 to 5 ms, 5 to 10 ms and 10 to 30 ms, (*i.e.* three images in total). This analysis was then performed in two other growth areas, also over the three different time periods, leading to nine images in total analysed. Three such IL-ADF-STEM images recorded in the same area, are shown in Figure 4.6, which were used to extract the number of Au nuclei on the surface. From the nine analysed images, J and N_c were determined as 1.33×10^{19} cm^{-2} s^{-1} ($\pm 3.6 \times 10^{17}$ cm^{-2} s^{-1}) and 0.14 ± 0.004 atoms (Figure 4.7), respectively; the latter indicating that single electrodeposited atoms should be stable on the surface. Note, the experimentally

measured nucleation densities and *J* values are orders of magnitude greater than those predicted by analysis of the recorded *i-t* curves using classical growth theories.[278, 280]

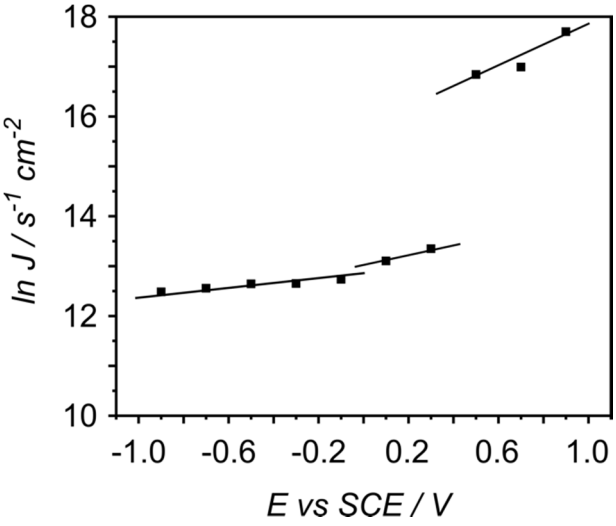

Figure 4.7: Potential dependence of the nucleation rate on the η. The slope over a range of η can be used to determine the size of the critical nucleus, where Nc = slope = 0.14 ± 0.004 atoms $0 \leq \eta \leq 1$.

4.4.2 Electrochemically Driven Single Atom Motion

After 5 ms (Figure 4.6(a) and Figures 4.7(a) to (d)), the surface contains three distinct electrodeposited structures: isolated, single atoms on the electrode surface (Figures 4.7(a) and 4.7(b)); clusters (or aggregates) of Au atoms lacking any form of crystallinity that vary in size and number of atoms, which we term atom clusters (ACs, Figure 4.7(c)); and particles with crystallinity, typically 1-3 nm in diameter, which we call NPs (Figure 4.7(d)). If the BDD support crystal is aligned to the electron beam, its crystal structure also becomes evident, as shown in Figure 4.7(a), although such conditions were generally avoided to give a clearer view of the deposited Au. This, and other measurements (Figure 4.8) showed that the BDD surface orientation was (110), as expected for CVD polycrystalline BDD growth.[492] Figure 4.8 shows a bright field TEM image of boron doped diamond. The [110] plane is evident from the inset electron diffraction pattern.

Although our primary interest is in capturing the dynamics and mechanism of early stage electrodeposition it is first necessary to ascertain whether momentum transfer from the highly energetic (200 kV) electron beam to the particles themselves, induces surface diffusion. Since the largest effect is expected on the least massive particles our

focus was on isolated atoms. To separate the effects of electrochemically induced motion from that of the electron beam, we quantified electron-beam induced atom movements for a series of ADF-STEM images recorded at different time intervals in the same area. A representative series of ten ADF-STEM images containing 41 tracked atoms (coloured for clarity) as well as a NP that does not change position, is shown in Figure 4.9. Note each frame receives an electron dose equivalent to that for each time-stamped IL-STEM image, thus the tenth image has received an electron dose ten times the electron dose used per IL-STEM image.

The atom movements observed from Frames 1 to 2 and Frames 1 to 10 are also shown in Figures 4.9(a), 4.9(b) and 4.11(a and b), respectively. After two electron doses, there is negligible movement of any of the atoms (Figure 4.9(a)). Even after an excessive ten doses (Figure 4.9(b)), 66% of the atoms have moved a mean square displacement of less than 0.1 $Å^2$ (Figure 4.10), whilst the NP changed its orientation. This demonstrates that the effect of the electron beam on isolated atom movement is negligible under the conditions we employ for IL-STEM imaging.

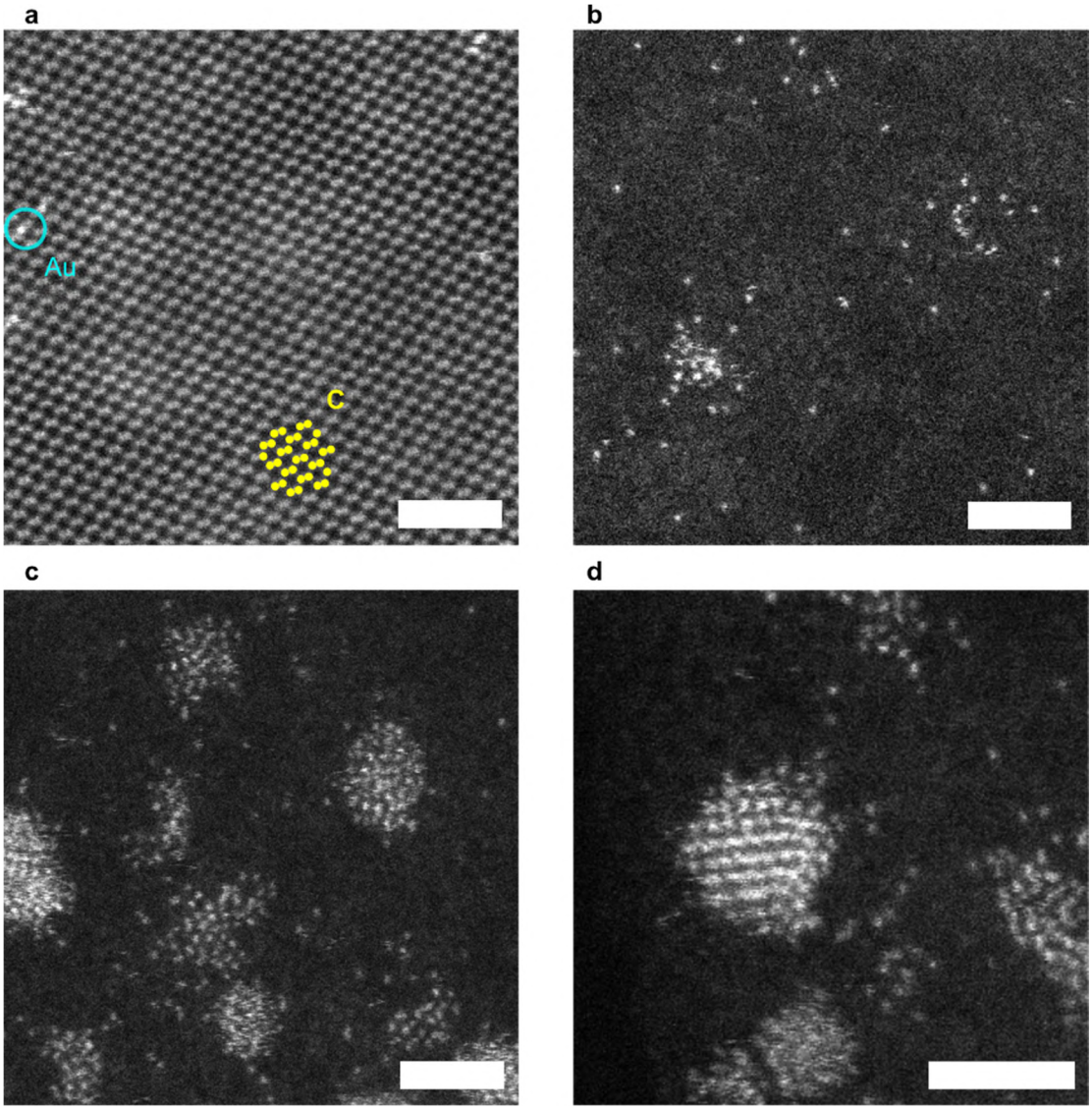

Figure 4.8: ADF-STEM images of (a) isolated Au atoms (blue circles), and the underlying (110) plane of carbon (C) atoms (pattern structure highlighted in yellow in left hand image) in the BDD TEM platform; (b) isolated Au atoms (c) Au atom clusters and (d) Crystalline Au NPs, electrodeposited on BDD. Scale bar is 2 nm. Electrodeposition was carried out at η = -1.2 V for 5 ms.

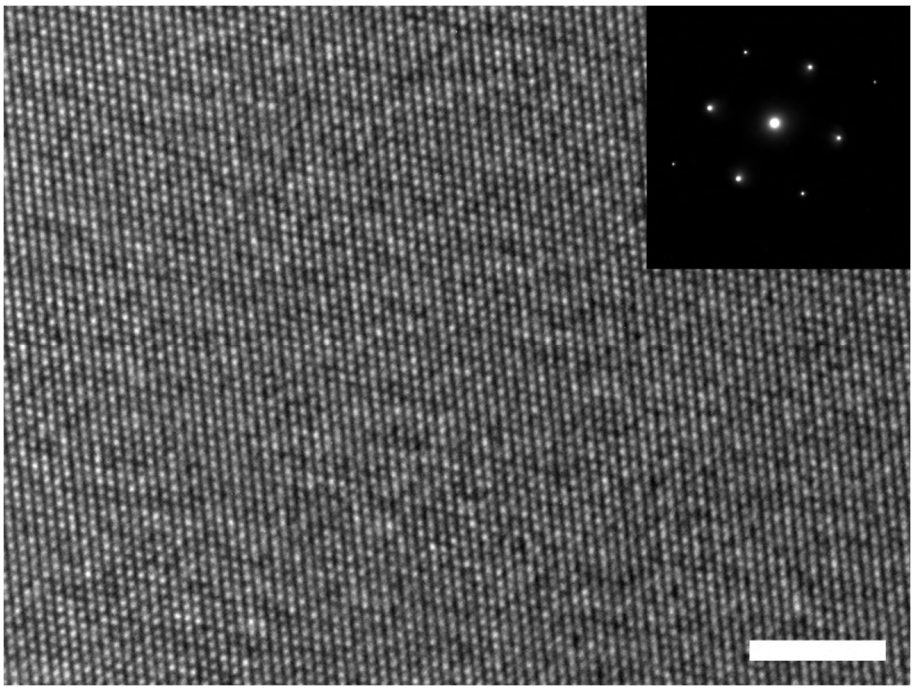

Figure 4.9: TEM image of the BDD-TEM platform. Inset: electron diffraction pattern showing the [110] crystallography of the surface. Scale bar is 3 nm.

Dispersion-corrected density functional theory (DFT) calculations[481] were also employed to determine the energy required to move isolated Au atoms over the (110) surface of BDD. A fully oxidized (110) surface was modelled. A mixture of ether (C-O-C) and ketone (C=O) groups on the surface were found to be the most energetically favourable configuration, Figure 4.2.

Figure 4.11(c) depicts the energetic landscape for Au atom motion across the (110) surface; two preferred directions of travel, $[1\bar{1}0]$ and [001], were elucidated, with thermal barriers to atom diffusion of 0.16 eV and 0.25 eV respectively. Since a temperature of 60 °C (thermal baking temperature) corresponds to 0.029 eV of thermal energy per atom, movement of atoms on the BDD platform during thermal baking is thus also of minor concern.

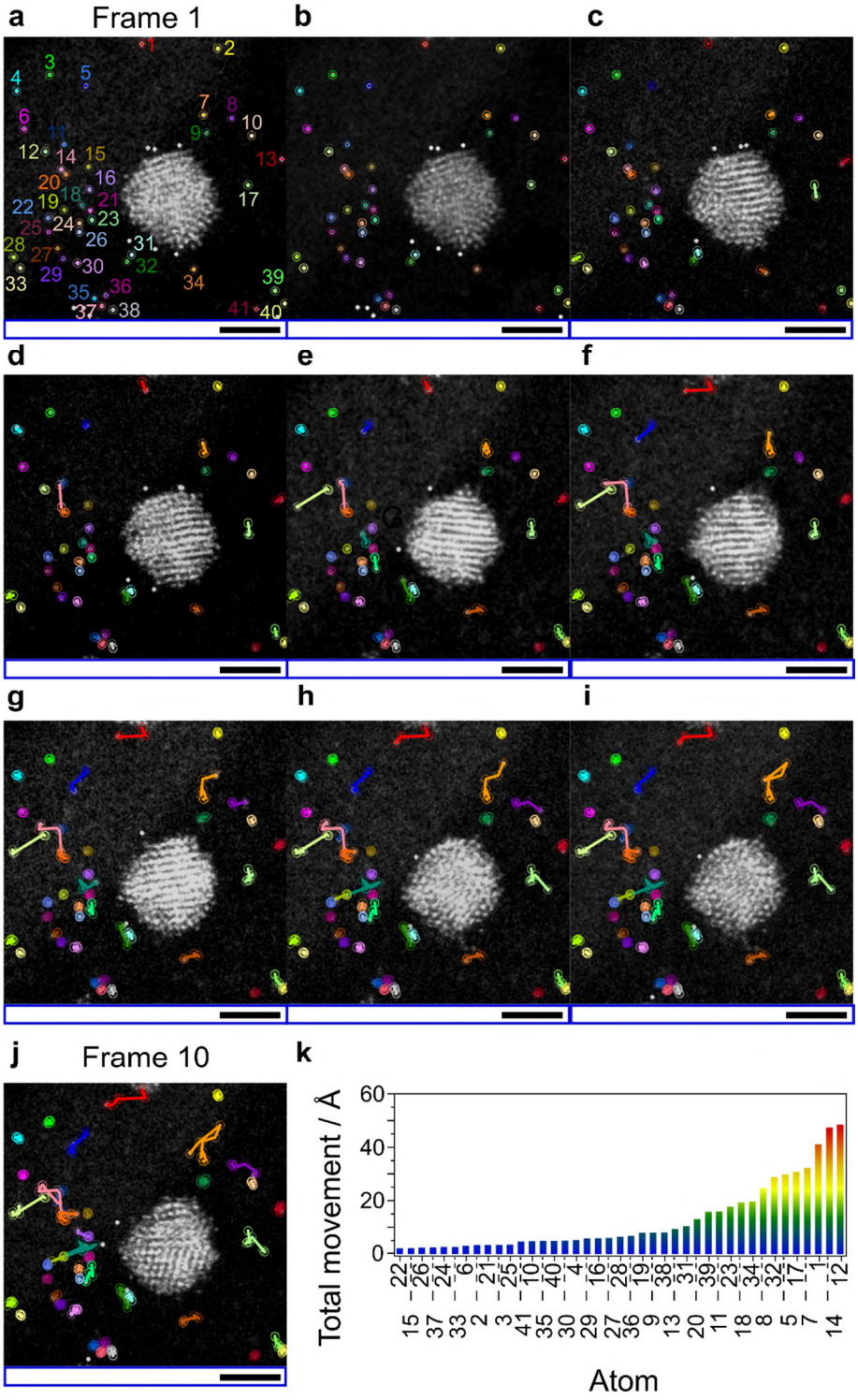

Figure 4.10: Atom tracking over ten frames using MTrackJ/ImageJ[488] to examine the effect of multiple irradiations of an area. (a-j) Atom movement, over a period of ten consecutive frames, is shown as coloured trajectories. Scale bar is 2 nm. (k) Total movement of each atom relative to starting position, after ten frames.

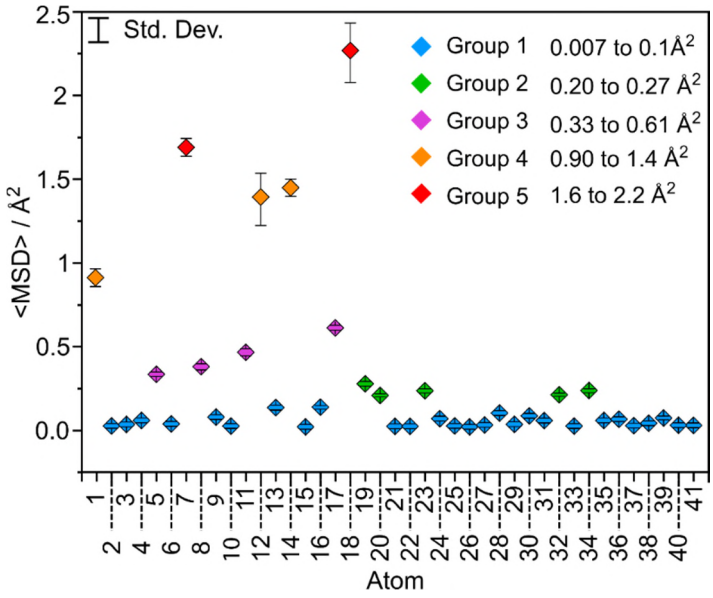

Figure 4.11: MSD of 41 atoms over ten frames. Atom MSD can be classified into five groups, as displayed in the Figure.

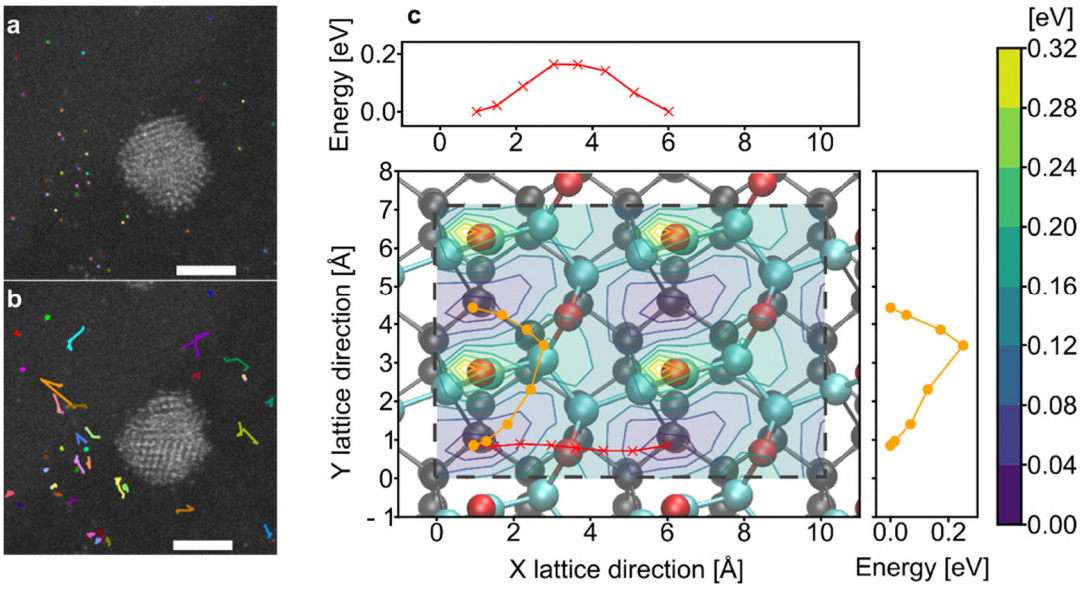

Figure 4.12: (a and b) Effect of the electron beam on atom mobility. In one location, containing a single NP and 41 atoms (identified by the coloured spots), ten consecutive images were recorded. Atom movement from (a) frames 1 to 2 and from (b) frames 1 to 10 is displayed. Scale bar is 2 nm. (c) Energy landscape for adsorption of a single Au atom on an oxidized diamond (110) surface. Shown is a contour plot with contour energies in eV according to the colour bar on the right. The background shows a ball-and-stick model of the surface with carbon atoms in grey, oxygen atoms in red and 1st layer carbon atoms in light blue. Minimum energy barriers along the $[1\bar{1}0]$ (in red) and the [001] (in orange) directions are also depicted.

Importantly, we also find that the Au-BDD-TEM platform is stable over long time periods. Figure 4.12 shows two images of the same area, the first recorded immediately after the final electrodeposition and the second, 73 days later (stored at room temperature under vacuum). Differences are negligible, even to the extent that individual atoms remain in identical locations.

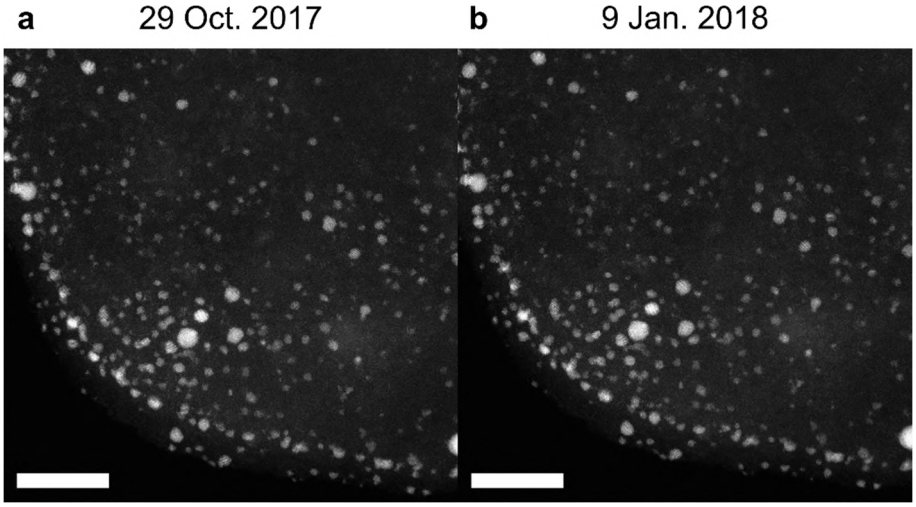

Figure 4.13: IL-ADF-STEM images showing the Au-BDD platform (30 ms Au deposition) recorded on (a) the 29th October 2017 and (b) on the 9th January 2018, after being stored under vacuum, in between imaging. Scale bar is 20 nm.

4.4.3 Early Stage Au Nucleation and Growth from Single Atom to Nanoparticle

Having established the validity of our experiment, we now demonstrate quantitative analysis of early stage Au nucleation and growth using the IL approach in combination with STEM. Quantified analysis of electron scattering is well-established;[394] here we use the contrast of individual Au atoms, together with multi-slice image simulations to calibrate and convert ADF-STEM intensity to a count of Au atoms[394] (see Figure 4.3). We first track the effect of an electrochemical deposition potential on the behaviour of isolated atoms and ACs. Figure 4.13 shows representative IL-ADF-STEM images after total deposition times of (a) 5 ms and (b) 10 ms. Six areas of interest are highlighted; squares 1-5 each contain a single AC, whilst square 6 contains isolated atoms. These squares have the same area and sit in the same position in Figures 4.13(a) and 4.13(b). The total number of atoms have been counted in each (Table 4.1).

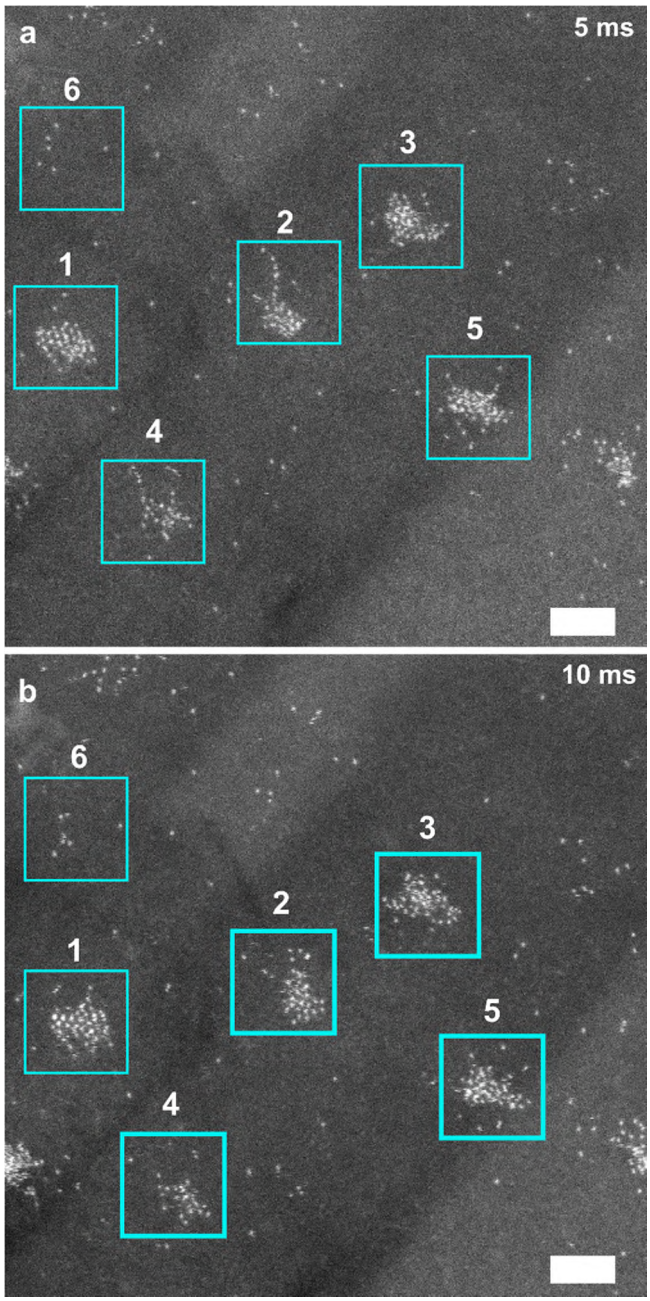

Figure 4.14: IL-ADF-STEM "snapshot" images of early stage electro-nucleation and growth focusing on isolated atoms and ACs. (a and b) Show the rearrangement process atoms undergo in response to an applied potential, over 10 ms. Scale bar is 2 nm. Electrodeposition was carried out at η = -1.2 for (a) 5 ms and (b) 10 ms.

Somewhat surprisingly in the 5 ms of electrodeposition between Figures 4.13(a) and 4.13(b) there does not appear to be any significant change in the atom count of the ACs, in the numbered squares, within experimental error. Although note the total atom count for the whole image does increase from 316 ± 4 atoms (Figure 4.13(a)) to 345 ± 3 atoms (Figure 4.13(b)).

Table 4.1: Number of atoms in each atom cluster and associated error as function of electrodeposition time for the images presented in Figure 4.13(a) (5 ms) and 4.13(b) (10 ms).

AC	5 ms (atoms)	10 ms (atoms)
1	57 ± 5	64 ± 4
2	29 ± 4	24 ± 3
3	46 ± 6	50 ± 4
4	65 ±6	57 ± 4
5	57 ± 6	59 ± 3
6	7	7

However, what is different is the atoms have changed position, reorganizing themselves, in response to the applied electrode potential. This rearrangement is especially evident in squares 2, 3 and 4 where for the former, square 2, the "line" of six atoms connected to the cluster has now become incorporated into the AC. Since we are confident that our STEM measurement methods do not affect the atom locations significantly, we can also assign the rearrangement of individual atoms towards each other in square 6, as a result of the applied potential.

A second example of electrochemically driven atomic rearrangement is shown in Figures 4.14(a) to 4.14(c) (and at lower magnification in Figure 4.15). The NP (identified with a blue circle) acts as a reference point. The highlighted AC (blue square) does not change its total number of atoms in Figures 4.14(a) and 4.14(b) (160 ± 10 *vs.* 160 ± 20 atoms) however, the position of the atoms has clearly changed as the system moves to adopt a lower energy configuration (perimeter of AC also decreased from 3.37 nm to 3.01 nm). After a further 20 ms of applied potential, Figure 4.14(c), the AC transforms into a smaller and more ordered NP (see inset) comprised of only 82 ± 7 atoms (perimeter 1.39 nm). The AC upon converting to a more stable NP has actually lost atoms (although their final location is unclear from these images). Such phenomena have not been considered in the electrodeposition literature and is certainly not currently predicted by any electrodeposition theory. Figure 4.14 thus not only

demonstrates the level of detail IL-ADF-STEM can reveal on early stage growth using the BDD-TEM platforms but enables the elucidation of mechanisms and growth pathways previously not described at the atomic level.

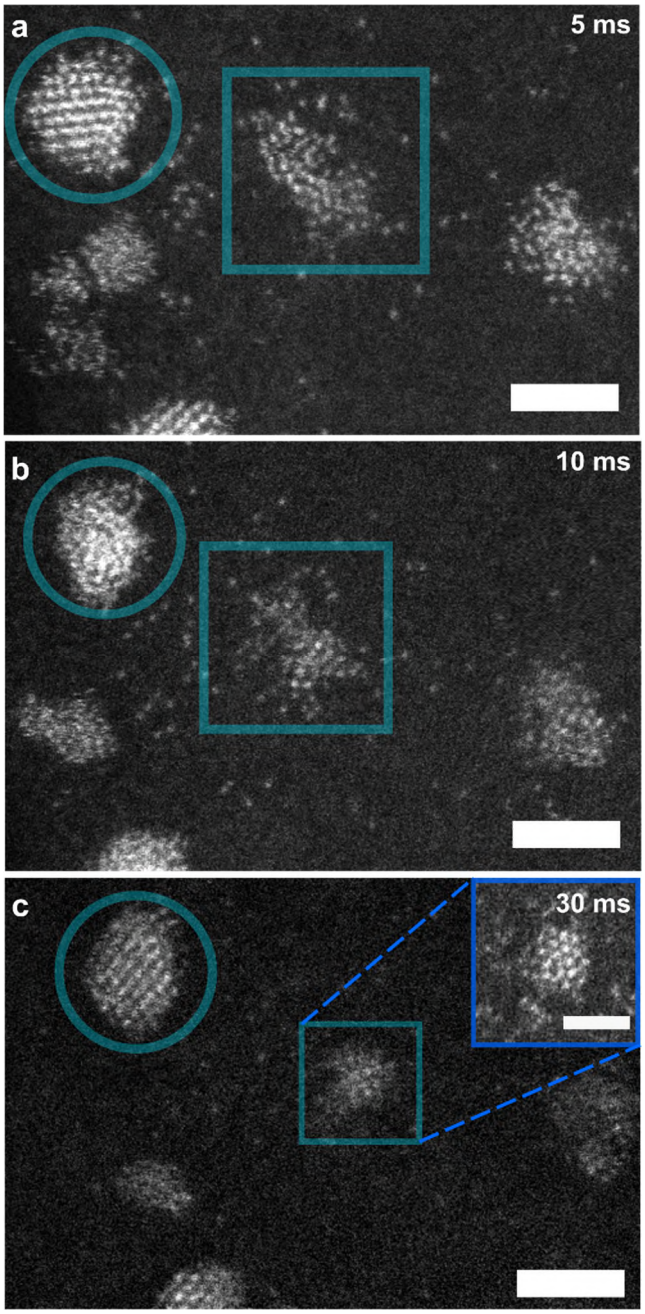

Figure 4.15: IL-ADF-STEM "snapshot" images of early stage electro-nucleation and growth focusing on isolated atoms, AC and NP. (a to c) One example of how a NP forms from an AC over a 30 ms electrodeposition time period. Scale bar is 2 nm. Electrodeposition was carried out at η = -1.2 for (a) 5 ms (b) 10 ms and (c) 30 ms.

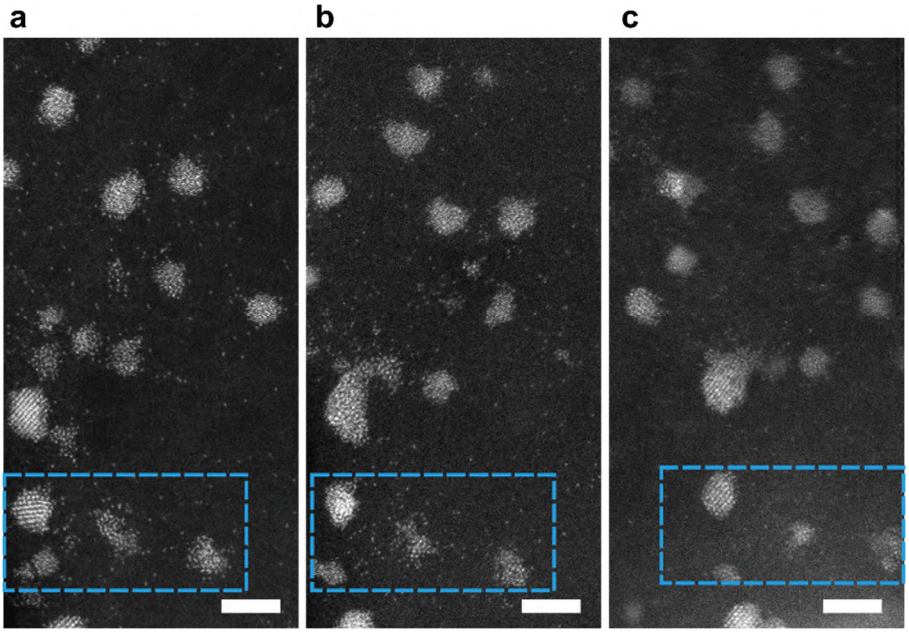

Figure 4.16: Lower magnification IL-ADF-STEM image of tracked nucleation and growth of Au entities shown in Figures 5(a) to 5(c) (highlighted with the square). Scale bar is 3 nm.

4.4.4 Growth Interactions Between Neighbouring ACs and NPs

Also, of considerable interest is how neighbouring entities (ACs and NPs) interact. We have shown single atoms aggregating into ACs and ACs converting to NPs but have yet to discuss possible interactions between ACs and NPs. The images as shown in Figure 4.6 provide a wealth of "snapshot" data from which such information can be obtained, as illustrated by Figures 4.16(a) to 4.16(c), which show a series of electrodeposition dynamics from three different locations. In Figure 4.16(a) at 5 ms, two dominant features are present, a crystalline NP (269 ± 9 atoms) and a disordered AC (153 ± 5 atoms). After a further 5 ms of growth the almost complete disassembly of the AC has occurred via streams of atoms into the NP, which move across both the surface and each other. In response, the NP has become disordered, with clearly not enough time for recrystallization. After a further 20 ms, atom movement is complete resulting in the formation of one single crystalline NP (730 ± 30 atoms), with the surrounding area now devoid of isolated atoms. The size of the NP indicates that during growth not only did the NP incorporate all atoms from the neighbouring AC but also incorporated atoms from other sources, most likely due to direct attachment *i.e.* by direct reduction of Au ions to Au atoms at the NP surface. Figure 4.16(b) features a monocrystalline Au NP (labelled 1, 222 ± 7 atoms at 5 ms), surrounded by five ACs,

(2, 3, 4, 5, 6) with atom sizes of (34 ± 1; 40 ± 1; 35 ± 1; 48 ± 2 and 59 ± 2) respectively. After a further 5 ms, the nearest AC (AC 2) has already been incorporated into NP 1, while ACs 3, 4 and 5 undergo movement and disassembly to provide streams of atoms which also feed into NP 1. This process causes NP 1 to lose crystallinity and become disordered (atom count = 710 ± 30 atoms). This size cannot be accounted for by only considering AC incorporation and again indicates direct atom attachment (from solution). AC 6 does not take part in the disassembly process but instead grows in size to 127 ± 5 atoms, itself becoming a crystalline NP.

This is an example of an AC progressing to a crystalline NP structure by increasing in atom number, in contrast to the data in Figures 4.14(a) to 4.14(c). One difference is the fact that AC 6 in Figure 4.16(b) is clearly more spherical in nature than the AC captured in the Figure 4.14 "snapshot". Our data thus indicates that ACs, dependent on their stage of morphological evolution, will either gain or lose atoms during a rearrangement process in their progression to become crystalline. After 30 ms, integration of AC's 3, 4 and 5 into NP 1 is almost complete, with NP 1 reordering into a crystalline structure of size 650 ± 30 atoms. The NP which was AC 6, after a further 20 ms electrodeposition has an atom count of 115 ± 5 atoms, suggesting it has not grown in size during this period.

Figures 4.16(a) and 4.16(b) clearly show that on this timescale, ACs and NPs cannot be considered non-interacting, contrary to classical theories.[26] They also demonstrate that a traditional definition of aggregation where two particles or clusters move across the surface to come together is not strictly true here. Rather, if there is a suitable distance between NP and AC, it is the disordered AC which loses atoms to the more stable crystalline NP. Whilst this process happens, the NP becomes liquid-like (disordered) and only recrystallizes once the process has (almost) fully completed.

Integration of many ACs into one dominant structure will have implications on the final structure of the NP *e.g.* by creating faults, twin boundaries, defects or leading to irregular structures; all features which can greatly impact the electrocatalytic activity of Au NPs.[493] It is also interesting to consider whether what we observe falls under the definition of electrochemical Ostwald ripening, where less stable particles dissolve to provide atoms for growth of the larger, more stable particle.[494]

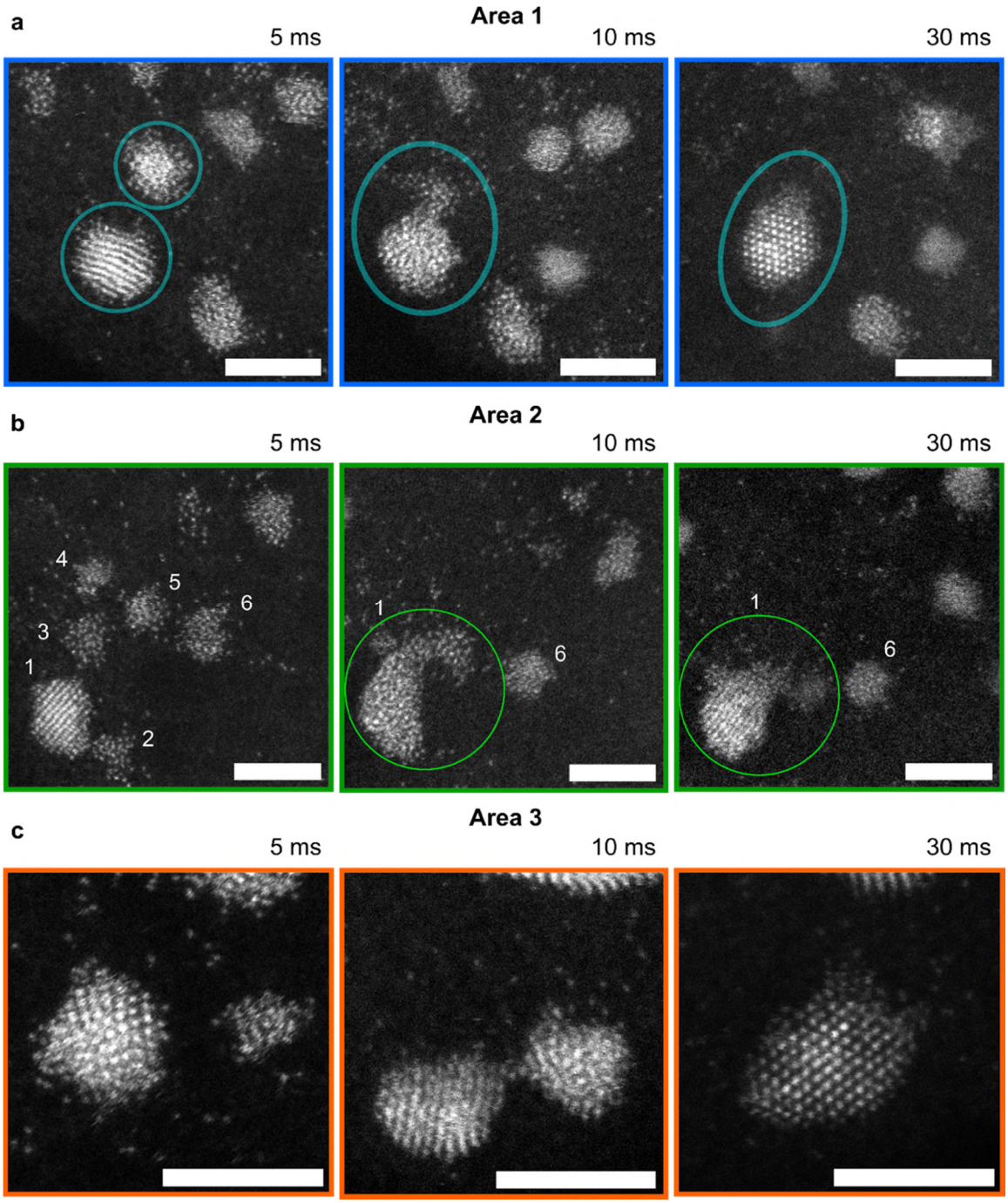

Figure 4.17: IL-ADF-STEM images of atomic cluster – NP dynamic interactions during electrodeposition. (a to c) AC and NP interactions during Au electrodeposition in three different areas for "snapshot" growth times of 5 ms, 10 ms and 30 ms at an electrodeposition η = -1.2. ACs dissemble to provide atoms to a neighbouring crystalline NP, which becomes disordered as a result, followed by recrystallization. Scale bar is 3 nm.

Here, we observe the more stable NP grow at the expense of the less stable AC, however it is not a dissolution event, whereby atoms from the AC dissolve and directly redeposit into the crystalline NP. Thus, we speculate we are witnessing either, what we term "surface mediated" Ostwald ripening, where the supercritical atoms do not dissolve but simply translate from one site to another,[495] or coalescence followed by recrystallization. Figure 4.16(c) presents further information on this process, again showing the interaction between a NP and an AC. After 5 ms electrodeposition, Figure 4.16(c) (5 ms), the NP (290 ± 20 atoms) and AC (50 ± 3 atoms) are located within ~ 1.62 nm of each other (face to face). After a further 5 ms electrodeposition, Figure 4.16(c) (10 ms), it is only the AC that has significantly taken on atoms (from neighbouring sources or via direct attachment), growing in size to 220 ± 10 atoms; in doing so the face to face separation has reduced to ~0.77 nm and an atom bridge linking the two structures is now evident. The NP has remained fairly consistent in size, 260 ± 10 atoms. After a further 20 ms of growth, one crystalline NP remains (450 ± 20 atoms), Figure 4.16(c) (30 ms). Given the atom count, this NP is unlikely to have gained atoms through direct attachment, but as a consequence of atom transfer from AC to NP.

4.5 Conclusions

Our results, using IL-STEM in conjunction with BDD TEM electrodes, provide a tantalizing atom-level insight into the mechanistic dynamics of early stage metal nucleation and growth, the results of which are not described by classical electrodeposition theories. Such knowledge can lead to better control of electrodeposition morphology and the creation of electrochemical deposition methods. We show direct evidence for potential-induced atom movement, atom clustering and cluster transformation, into crystalline NPs, possible via both gain or loss of atoms. Discrete entities are also shown to be interactive with a clear tendency for disordered clusters to be consumed within a closely spaced NP, via a cluster disintegration process which sees the NP transition through a disordered state first. More wide ranging, the electrochemical production of stable isolated metal atoms on the BDD platform holds considerable promise for single atoms studies in *e.g.* electrocatalysis[496] and magnetism.[497] Finally, the universality of the approach means this technology can reveal the atomic-scale intricacies of a myriad of technologically important

electrochemical processes[498] which undergo a morphological change with applied potential.

Chapter 5

Feasibility of Electrochemical deposition of palladium from acetonitrile-water mixed solvent and recovery from organic synthesis solution

5.1 Abstract

Electrodeposition for metal recovery is only achieved via electron transfer when metal ions of transition metal compounds such as Pd-acetate are completely dissociated and solvated by the solvent molecules. If the metal centre is strongly coordinated to ligands, then this situation rarely happens without harsh digestion/decomposition using environmentally unfriendly strong acids or bases. The status of the occupied/unoccupied molecular orbitals governs the possibility for phase transition from soluble ions to a solid crystalline phase. Most transition metals (*e.g.* Pd) have unoccupied d-orbitals, which make the process of electron tunnelling and deposition feasible. However, if they are coordinated to ligands that contain electron donor atoms such as oxygen or nitrogen, Pd and its ligands form hybridised orbitals. Then, Pd is not in the ionic form, and there are no free orbitals to accept electrons during the reduction process. Additionally, the coordination bond can be classified as a covalent bond, consequently the whole molecule is solvated by the solvent molecules. This represents the case of most organometallic compounds in non-aqueous solvents in this study; Pd-acetate in acetonitrile, a well-known catalyst system, which is used heavily in pharmaceutical and chemical industries. Moreover, Pd recovery in a metallic form is economically extremely important. Here, we demonstrate that it is possible to alter the strong coordination bond between palladium and the acetate groups in the trimeric cyclic palladium acetate complex, to overcome the solvation barrier and make Pd ions free of any association to ligands in liquid and can then be electrodeposited. This effect is achieved by controlled water addition. In solutions that contain low mole fraction of water (< χwater = 0.553), Pd is solvated by the acetonitrile molecules only, however, competition from water molecules cannot be ignored. Conversely, water replaces acetonitrile molecules from the Pd inner shell, when water content exceeds χwater = 0.871 due to the strong water-acetonitrile interaction that overcomes Pd-acetonitrile interaction. This mechanism might allow for the exploitation of mixed solvent systems

to design solution mixtures by addition of a second green solvent, which ultimately facilitates ion-solvent and solvent-solvent interaction for a wider application of metal recovery from spent nuclear waste, batteries, and electronics.

5.2 Introduction

Regulator's ever-increasing demand for metal free medicine and the development of environmentally friendly industries, or what is now known as green chemistry, has attracted great attention during the past decade at both the research and the industry level.[499] This addresses the elimination or reduction of toxic and heavy metals as well as hazardous substances; described as a challenging issue.[500-503] The importance of green chemistry and the aim to design safe manufacturing processes, has driven international, as well as governmental entities, such as the World Health Organization (WHO), the European Medicines Agency, the British Pharmacopeia and the United States Food and Drug Administration, to set stringent rules for the levels of metal residues in drug products.[369, 504]

The pharmaceutical industry has advanced over the last two decades to provide a range of effective drugs, typically constituting the excipient(s) and the active pharmaceutical ingredient(s) (APIs).[505] According to WHO, APIs are defined as "a substance used in a finished pharmaceutical product, intended to furnish pharmacological activity or to otherwise have direct effect in the diagnosis, cure, mitigation, treatment or prevention of disease, or to have direct effect in restoring, correcting or modifying physiological functions in human beings".[502] APIs can be produced through catalytic organic synthesis (*i.e.* one of many synthesis routes but results in a good product yield),[506] which is often described as a clean process.[505] However, transition metal catalysts are used as part of the synthesis process.[505] These catalysts contain at least one metal which belongs to the platinum group of metals (PGMs),[507, 508]

PGMs include platinum (Pt), palladium (Pd), ruthenium (Ru), rhodium (Rh), osmium (Os) and iridium (Ir). They are well known to catalyse the reactions of carbon-carbon bonds and carbon-heteroatom bonds. For example, the Suzuki and Heck reactions employ Pd based catalysts,[509] such as the ones shown in Figure 5.1.[369, 510]

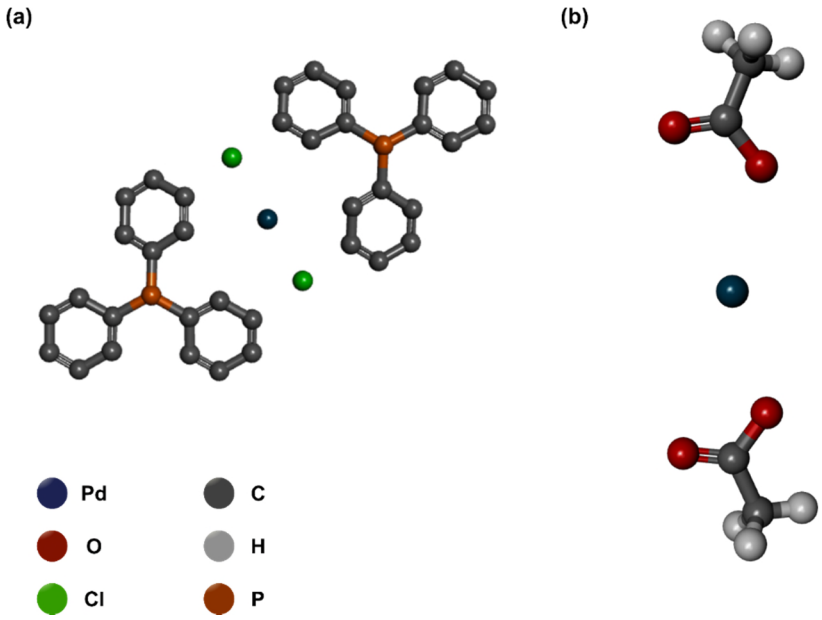

Figure 5.1: Example of Pd catalysts commonly used in pharmaceutical synthesis. (a) bis(triphenylphosphine)palladium(II) dichloride, and (b) palladium diacetate.

PGMs are chemically reactive, catalyse oxidation-reduction reactions and are considered toxic, as highlighted in many reports, for example see reference **511**. PGMs, unless removed, will contaminate the pharmaceutical product, as outlined in the guideline on the specification limits for residues of metal catalysts or metal reagent by the European Medicines Agency.[369, 504] For instance the maximum UK dietary intake is 0.2 µg/day of Pt for adults.[504] More information about the maximum limit of trace metals residue in medicine products is outlined in Table 5.1.

Table 5.1: Maximum level of metal residue in APIs.[512-515]

	Concentration (PPM)	
Metal	Oral	Parenteral
Pt, Pd, Ir, Rh, Ru, Os	5 ± 0.1	0.5 ± 0.3
Mo, V, Ni, Cr	10 ± 0.2	1 ± 0.5
Cu, Mn	15 ± 0.1	1.5 ± 0.2
Zn, Fe	20 ± 0.3	2 ± 0.4

5.2.1 Current approach for metal removal and why electrodeposition should be considered

Based on the above, the process of metal elimination is considered a critical part of the synthetic process, to meet the specification of regulation. Consequently, there are different methodologies available to remove or minimize the catalytic metals present in drug substances and efforts are undergoing to effectively remove metal catalyst.

Several methods have been developed to remove residual metal catalysts from the reaction mixture[516] based on removal during the purification process.[369] Purification typically includes distillation, crystallization, extraction and adsorption.[504] These methods are currently the most widely used in manufacturing facilities.[506] Distillation is based on the fact that PGMs are heavy metals and non-volatile, therefore APIs can be collected and the catalyst can precipitate and be removed.[504] Crystallization can be utilized when the product solubility is substantially different from the metal catalyst in the solvent, hence metal contaminant can be reduced and eliminated.[517] Extraction is a form of metal isolation technique using tailored extraction reagents such as phenyloximes.[517] The metal to be removed should have an oxidation state greater than zero and have a high affinity for the extraction reagent. However, a few disadvantages stem from the extraction process, first it can involve extraction of other substances. For example, excipients that contain metal like magnesium stearate that exist in the same medium. Second the extraction agent should be non-toxic and selective, and finally extraction reagents should be easily removable at the end of the process.

Many methods of metal removals are classified as absorption. The process can be implemented either by adsorption of the metal catalyst on supported chelating agents or by complexation of the metal catalyst and solubilisation in a non-drug phase, followed by extraction. Examples of materials that are used in adsorptive metal recovery include, activated carbon,[518] ion exchange resin,[519] solid trimercaptotriazine,[520] glass bead sponges,[521] Smopex™ fibers,[522] and silica bound scavengers. When the above methods fail, specialty scavengers are used, where a scavenger is defined as a selective adsorbent that is made of a macro-porous polymer resin or silica functionalized with end groups containing S or N.[369, 523]

Beside their expensive price, pharmaceutical industries have reported that scavengers do not help completely in the removal of metal contaminant.[369] This is due to the nature

of the solvent (*i.e.* polar protic, polar aprotic and non-polar) used in the synthetic process such as the ones mentioned in Table 5.2, which may bind preferentially to the scavenger site preventing metal adsorption on the surface.

Table 5.2: List of solvents used in the pharmaceutical industries.

Solvent	**bp/°c**	**density/ g cm^3**	**viscosity/ep**	**conductivity/ S cm^{-1}**	**relative permittivity**
Polar protic					
Methanol	64.5	0.7864	0.551	1.5 X 10^{-9}	32.7
Polar aprotic					
Acetonitrile	81.6	0.8887	0.7765	6 X 10^{-10}	35.9
THF	66.0	0.889	0.455	-	7.58

Efforts have been made to advance scavenger technology, as there are product losses during treatment due to the use of a solid adsorbent scaffold, and the introduction of impurities. In recent research by Wang et al.,[369] two steps were suggested to recover the metal catalyst. A binary system (*i.e.* a system that contains two adsorption sites; chelating agent and activated carbon) which contains a chelating agent was used to bind to the metal catalyst, followed by the use of activated carbon or silica gel to adsorb the metal catalyst and chelating agent.[369] However, the development of metal chelating agents covalently bound to inorganic or polymer supports that behave as an adsorbent have become more common due to their ability to offer better effectiveness, broad applicability and, ease of use. Such scavengers are still expensive and in some cases it can be problematic to remove the scavengers themselves, which limit their use for metal recovery from the larger scale synthesis.[369]

5.2.2 Electrodeposition as an alternative route

Whilst the theory of electrodeposition and metal particles and metal layer formation is still very much under debate (see *Chapter 4*),[242, 278] electrodeposition remains one of the oldest techniques that has proven useful for metal recovery due to the ease of set up and effectiveness of recovery from low concentrations, which can be in the range of 50-250 ppm.[524, 525] In addition, electrodeposition is simpler and can be operated at very

low cost compared to other techniques that can include different treatment stages and sophisticated materials. It is also able to meet low limit detection, comparable to sophisticated techniques such as inductively coupled plasma-mass spectrometry (ICP-MS).[526, 527] Although, electrodeposition (and removal) of toxic metals from water and industrial waste has gained great attention,[500, 528] electrodeposition has not been explored in detail for metal recovery from industrial solutions mainly comprising organic solvents containing metal catalyst such as the Pd based ones.[529] Such metals are ligand stabilized *e.g.* with acetate ions as shown in Figure 5.1.[530]

Electrodeposition, as described in detail in *Chapter 1*, can be achieved galvanostatically or potentiostatically using electrodes immersed in a solution that contains the metal precursor of interest.[531] In brief, electrodeposition features two main stages for metal formation on the surface, nucleation and growth.[10, 532] Prior to nucleation, metal ions in the double layer region are solvated with the solvent molecules (see *Chapter 1*, Section 1.3.4), for example water molecules in aqueous media and organic molecules (*e.g.* MeCN) in a non-aqueous solvent.[25, 31, 32, 533, 534] In the nucleation stage, atoms of metal ions from the solution regroup themselves to form nuclei (*i.e.* a stable structure and indication of phase formation), and in the growth stage, atoms from the solution combine with the nuclei centers, which has been addressed and investigated in *Chapters 1, 3* and *4*.[10, 24] The electrode material, chemical nature of the solvent and the chemical identity of the metal salt are key parameters governing the electrochemical deposition process.

Metals in the periodic table are classified based on their electronic structure configuration, chemical, thermodynamic and physical properties.[535, 536] This influences the electrochemical series, which is built up by arranging various redox equilibria in order of their standard electrode potentials (E^0). Hence, some metals such as Cu, Pd, and Pt can be deposited from both aqueous and non-aqueous media,[95, 537] Metals such as Al or Li, can only be deposited from organic or ionic liquid media owing to their high overpotential of reduction, beyond water electrolysis and hydrogen evolution.[538-540] Nonetheless, Pd or Cu or Pt may not deposit if the d-orbital is full or they are strongly bound to electron donor ligands, hence the deposition is structure dependant,[78] as we shall discuss and elaborate more further in the results section. For example, Co electrodeposition from solutions containing thiocyante and Cl ions as ligands shows that by increasing the concentration of ligands, electrodeposition is hindered.[541] In other

reports, ligands can slow down electrodeposition or inhibit it completely by adsorption of the ligands on the surface.[542] It is also important to note that for effective recovery of metals from aqueous solutions, acidic or basic media have been heavily used for sample digestion and electrochemical recovery enhancement.[543, 544] For example, Pd-acetate or $PdCl_2$ will dissolve in organic solvents but to dissolve in water, acid such as HCl should be added. For the industrial case, where electrodeposition has to be carried out from a solution containing diverse organic and inorganic molecules, addition of acids or bases may impact the structure of the APIs as an example. Hence, addition of acids or bases is not recommended. For our studies, we focus on Pd recovery, from Pd-acetate in MeCN, due the prevalence of this PGM, especially in the pharmaceutical industry.[368] Pd is described as a 4d-block transition metal, for more detailed properties data see Table 5.3,[535] which can form strong bonds because of its susceptibility to form hybridized orbitals along the direction of the d-orbitals by using ligand electrons.[545, 546]

Because Pd is attached to oxygen containing ligands (in this case Pd is coordinated to the acetate groups), they form a strong coordination bond that can be described as a covalent bond because both Pd and O atoms are sharing their electrons. Pd phase transformation from the positively charged ion to Pd metal on the surface is then not possible. This is because it is difficult to extract electrons from the hybridised orbitals in this Pd-acetate structure and Pd is not solvated by the solvent molecules (*i.e.* we can think of it as the Pd ions being caged by their ligands and not free in the solution).[530] In contrast, if we were studying alkali and alkaline earth metals, then these metals have a tendency to lose electrons from the outermost shell (*e.g.* S orbital) and form ionic bonds and thus they are less susceptible to the ligand effects, which in many cases hinder metal deposition.[78]

To the best of our knowledge there is no literature discussing either Pd electrodeposition from its Pd-acetate salt in MeCN or the effect of adding water in controlled amounts. Only a few reports have investigated different Pd catalysts systems including Pd-acetate to drive possible mechanisms pathways during organic or inorganic synthesis.[83-85, 367, 510, 530, 547-553] Using mixed solvent media for electrodeposition studies is not common either (*e.g.* MeCN-water), possibly as the presence of one solvent in the other may be considered a contamination problem.[29] However, the MeCN-water solution system has been used to study electrodeposition of Ag from its nitrate and cyanide solution.[21]

Table 5.3: Physical properties and electronic configuration of Pd.

Electronic configuration	$1s^2$ $2s^2 2p^6$ $3s^2 3p^6 3d^{10}$ $4s^2 4p^6 5s^0 4d^{10}$	**Metallic radius**	1.37 Å	**First ionisation potential**	8.337 eV	**Van der Waals radius**	1.63 Å
Electron affinity	0.562 eV	**Density**	12.02 g/cm^3	**Pauling electronegativity**	2.20 Å	**Covalent radius**	1.31 Å
Ionic radius	0.78 Å	Pd^{2+} coordination number is 4	1.00 Å	Pd^{2+} coordination number is 6	0.90 Å	Pd^{2+} coordination number is 6	

5.3 Experimental, methodology and materials

5.3.1 Chemicals and solution preparation

For the first part of the study, experiments were carried out using a solution of (i) 1×10^{-3} M Pd-acetate + 0.1 M tetrabutyl ammonium tetrafluoroborate ($TBABF_4$) as a supporting electrolyte in MeCN (organic solutions); (ii) 1×10^{-3} M Pd-acetate + 0.1 M HCl + 0.05 M KCl in water (aqueous solutions) previously de-aerated by Ar and (iii) mixed-solvent systems, prepared using variable ratios of MeCN, water, $TBABF_4$, HCl, and KCl, but keeping the concentration of Pd-acetate fixed at 1×10^{-3} M, detailed in Table 5.4. The solutions were prepared with trace element grade chemicals, described in detail in *Chapter 2* and all chemicals were used as received without further purification. 99.99% HPLC far UV-Vis grade MeCN and deionised water from a Purite Select HP system were used for solution preparation. Prior to each preparation, MeCN was dried over molecular sieves (3 Å, Merck chemicals) to ensure the absence of water. Pure 99.999% Ar and N_2 (BOC industries, UK) were used to de-aerate the solutions. For NMR studies, deuterated MeCN (MeCN-d3) (99.999%, superseal, flushed and stored under Ar) and deuterium oxide (D_2O) were purchased from Acros organics.

Table 5.4: Composition of the solutions used in Pd solvation and electrodeposition study.

#	MeCN	H_2O	D_2O^*	Pd-acetate	$TBABF_4$	HCl	KCl	Mole fraction (χwater)
1	100%	0%	0%	1×10^{-3} M	0.1 M			**0**
2	95%	4%	1%	1×10^{-3} M	0.1 M			**0.132**
3	90%	8%	2%	1×10^{-3} M	0.1 M			**0.243**
4	80%	16%	4%	1×10^{-3} M	0.1 M			**0.419**
5	70%	24%	6%	1×10^{-3} M	0.1 M			**0.553**
6	60%	32%	8%	1×10^{-3} M	0.1 M			**0.658**
7	50%	40%	10%	1×10^{-3} M	0.1 M			**0.743**
8	40%	48%	12%	1×10^{-3} M	0.05M		0.05M	**0.812**
9	30%	56%	14%	1×10^{-3} M	0.04		0.06	**0.871**
10	20%	64%	16%	1×10^{-3} M	0.03		0.07	**0.920**
11	10%	72%	18%	1×10^{-3} M	0.02		0.08	**0.963**
12	5%	76%	19%	1×10^{-3} M	0.01		0.09	**0.982**
13	1%	79.2%	19.8%	1×10^{-3} M			0.1 M	**0.997**
14	0%	80%	20%	1 mM		0.1 M	0.05 M	**1.000**

*D_2O was only used for IR and NMR studies

5.3.2 Chemical synthesis of 4-Acetylbiphenyl (Suzuki reaction)

To investigate Pd electrochemical recovery from industrially-relevant solutions, chemical synthesis of 4-acetylbiphenyl was carried out under a N_2 atmosphere, using the Suzuki reaction, and Pd was then electrochemically recovered at the end of the synthesis process. A two-necked flask, 100 mL, fitted with a reflux condenser was used for the synthesis. The inert atmosphere was maintained by attaching a N_2 line to the synthesis set-up. At room temperature, phenylboronic acid (0.0012 mol, 1.2 eq,

0.73 g mass), 4-bromoacetophenone (0.001 mol, 1.0 eq, 1.0 g mass) and potassium carbonate (0.003 mol, 3.0 eq, 2.1 g mass) were dissolved in 50 mL MeCN. The order of addition was as follow; first solid reagents were added to the dry empty flask after removing the condenser, then MeCN was added. Following addition of the solvent, the subaseal was placed. The mixture was then sparged with N_2 (deoxygenated by bubbling N_2 through the mixture) for 10 minutes using a PTFE needle and a gas outlet. The palladium acetate catalyst (Pd-acetate, 0.0001 mol, 0.01 eq, 0.0112 g mass) was added and the mixture sparged for a further 5 minutes. The reflux condenser (attached to a N_2 inlet) was reattached to the flask and flushed for 2 minutes with N_2. The stirred mixture was then heated at 60 ºC for three hours. At the end of this time the reaction was allowed to cool for 15 minutes and a sample was taken for thin layer chromatography (TLC) analysis in a solvent system made up by mixing petroleum ether and ethyl acetate (4:1) against the 4-bromoacetophenone (the starting material). The reaction was completed after three and half hours, and the resulting mixture was further tested using ^{1}H NMR and IR (step 1). The resultant crystalline solid *i.e.* crude coupling product was purified by a simple recrystallization process (step 2). This involved addition of 10% water (H_2O) and 15% dichloromethane (CH_2Cl_2) to the reaction, the product and the reaction mixture were then transferred to a separating funnel to separate the lower layer, dichloromethane, which contains the product (4-acetylbiphenyl). The remaining aqueous layer was extracted further twice with a similar volume of dichloromethane. The three different dichloromethane extracts were combined and together washed with water (twice, about 10 ml each time) using a separating funnel. The dichloromethane solution was dried using magnesium sulfate ($MgSO_4$) and then, after filtration, the solvent was removed by rotary evaporator (30 ºC and low speed rotation) to yield the crude product and the mass was recorded. The last stage includes a purification of the product using column chromatography on SiO_2 using petroleum ether and ethyl acetate (4:1 mixture). Finally, ^{1}H NMR and MS-TOF spectra were collected of the final product.

5.3.3 Electrochemical studies

Electrochemical measurements were performed using a CHI potentiostat (750C) and IVIUM Compactstat potentiostat in a three-electrode configuration with a $Ag|Ag^+$ double junction reference electrode. The reference electrode was constructed from a

Ag wire immersed in a MeCN solution containing 0.1 M $TBABF_4$ and separated from a compartment containing the same solution by a porous Vycor tip (BASI). The latter compartment was in turn separated from the main solution by a second Vycor tip and a Pt or carbon felt (very high surface area) were used as counter electrodes. The working electrode was BDD (see *Chapter 2*, Section 2.1.2). Prior to each experiment, the BDD electrode was polished with alumina slurry (0.05 μm sized particle, micro polish, Buehler) on a DI water saturated polishing pad (Micro cloth, Nuehler, Germany) to obtain a mirror surface. This was followed by a polish on DI water saturated pad only to remove debris. The electrode was thoroughly rinsed with Milli-Q ultrapure water and dried under Ar and kept in a desiccator under vacuum.

The electrochemical setup is shown in Figure 5.2 and was used for electrochemical and bulk electrolysis and recovery. All voltammetry experiments were completed using organic media thoroughly degassed with Ar, under anaerobic conditions in a glovebox (Plas Labs, Mich, US) filled with nitrogen (O_2 < 7 ppm, H_2O < 2 ppm) and at an ambient temperature of 22 ± 2 ºC. CV and chronoamperometry (CA) using rotating disk electrode (RDE) were carried out to determine the dynamics of the reduction-oxidation of Pd species. For Pd recovery, a 25 mm diameter BDD RDE was used and was compared to recovery using a high surface to area BDD (1 cm wide ×10 cm long).

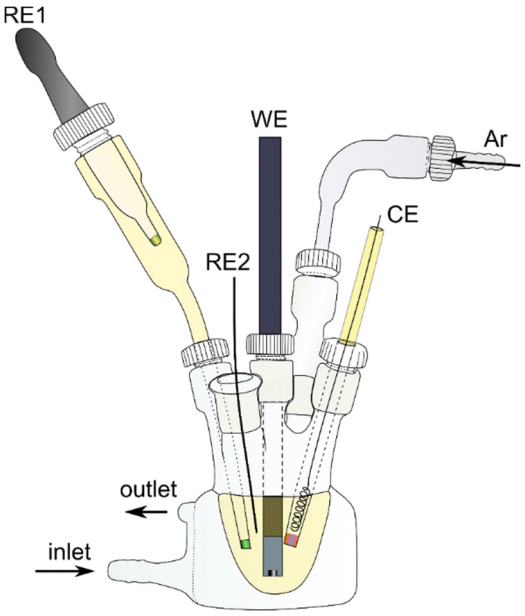

Figure 5.2: Experimental set-up for the electrochemical studies of Pd systems.

To calculate the free energy of transfer, cyclic voltammetry experiments were carried out in a four-electrode system using a conventional glass cell (biphasic system). Two platinum wires were used as counter-electrodes (C1 and C2), and the reference electrodes (R1 and R2) were Ag/Ag^{+}.

5.3.4 Microscopy Characterisation

Microscopic studies were carried out *ex-situ* after electrodeposition. After electrodeposition, the electrode was rinsed with de-oxygenated water, dried in the glove box and kept in a desiccator to avoid any contamination during transfer and prior imaging. The morphology of the deposited Pd material was characterised by *ex-situ* techniques using scanning electron microscopy (FE-SEM) for low magnification and transmission electron microscopy (TEM) or scanning ((S)TEM) for higher resolution. FE-SEM images were recorded using the In-lens, ESB, SE2 and STEM detectors on a Zeiss Gemini or Zeiss Supra 55-VP operating at 5 kV, 15 kV and 25 kV, respectively.

For each deposition, at least three images were recorded in different areas of the surface for both FE-SEM and TEM/(S)TEM measurements. X-ray energy dispersive spectrometry (XEDS) spectra were recorded using the XEDS unit equipped (OXFORD instruments) with the FE-SEM instrument, at a working distance of 10 mm and accelerating voltage of 15 kV. For high resolution TEM/(S)TEM imaging, deposition was carried on using the BDD TEM plate surface (*Chapters 2* and *4*). TEM/(S)TEM was conducted using a JEOL-JEM 2100 TEM microscope operated at 200 kV (LaB_6 filament) equipped with Selected Area Electron Diffraction (SAED) and a double aberration corrected JEOL JEM-ARM200F performed at 200 kV. The later was used to collect ADF-STEM images using a JEOL annular field detector with a fine-imaging probe, and probe current of 23 pA cm^{-2} with a convergence semi-angle of ~25 mrad and an inner angle of 50 mrad, and camera length of 8 cm.

5.3.5 Fourier-transform infra-red (FT-IR), ultraviolet-visible (UV-Vis), X-ray powder diffraction and inductively coupled plasma mass spectrometry (ICP-MS)

The pure and mixed solvent systems were analysed using a Bruker FTIR ATR spectrometer from 4000 to 500 cm^{-1}. MeCN-water mixtures were prepared by mixing MeCN with water containing 20% D_2O. The O-D and C≡N stretching bands for HDO

and MeCN in the mixtures at various water mole fractions or percentage (χH_2O) were measured at room temperature (25 °C) from 2000 to 3000 cm^{-1}. UV-Vis absorbance spectra were collected using an Agilent Cary 60 UV-Vis from 200 nm to 800 nm. A Panalytical X-Pert Pro MPD diffractometer equipped with a curved Johansson monochromator giving pure focussed Cu $K_{\alpha 1}$ radiation and a solid-state PiXcel detector was used to examine the structure of commercial Pd-acetate before dissolving in MeCN, water and mixed liquid of both.

For ICP-MS experiments, an Agilent 7900 ICP-MS Instrument was used. The set up follows (1) plasma gas 15 L/min, auxiliary gas 0.8 L/min, make-up gas 0.15 L/min, (2) RF power 1550W, RF matching 1.8 V, analog HV 1700 V, Pulse HV 1100V, (3) spray chamber temperature 10°C, nebuliser pump 0.1 rps, collision gas (He) 3.6 ml/min. The Internal standard (50 ppb, Er solution), was introduced into the sample flow through a T-pieces. Before acquisition the uptake speed was 0.3 rps, uptake time was 30 seconds and stabilisation time was 30 seconds. After acquisition, the probe was rinsed on rinse port with water for 10 seconds, then 30 seconds with 3% nitric acid at 0.2 rps, followed by water for 80 seconds at 0.15 rps. All reading was done in triplicates.

5.3.6 Nuclear magnetic resonance and mass spectrometry

^{1}H NMR, ^{13}C NMR and ^{19}F NMR analysis was performed using Bruker Avance III HD 500 MHz and Bruker Avance III 400 MHz spectrometers. Chemical shifts were quoted in parts per million (ppm) and coupling constant in Hz. For these experiments, the MeCN-water mixtures were prepared using D_2O and MeCN-d_3. A Bruker MaXis Plus Q-TOF mass spectrometer (ESI-HR-MS/MS) was used for characterisation of the product of 5.5.2.

5.4 Results and discussion

The structure of Pd-acetate has been described previously as a non-trivial one either in its solid form or when dissolved in solvents.[554, 555] Most commercially available Pd-acetate salts contain other Pd by-products or adducts such as $Pd_3(OAc)_5(NO_2)$ or polymeric Pd structures (*e.g.* $[Pd(OAc)_2]_n$), which are less soluble than Pd-acetate).[556] Powder XRD was used for phase identification and to determine the solid structure of the powdered form of Pd-acetate. The resulting XRD spectrum of the solid powder, in

Figure 5.3(a), along with the corresponding Table 5.5, shows that Pd forms a triangular cluster, with two of the three acetate groups in bridging positions on each side of the triangle.[557] Pd-acetate then in the powder form is known as trimeric Pd-acetate or simply $Pd_3(OAc)_6$, depicted in the inset of Figure 5.3(a).[557-559]

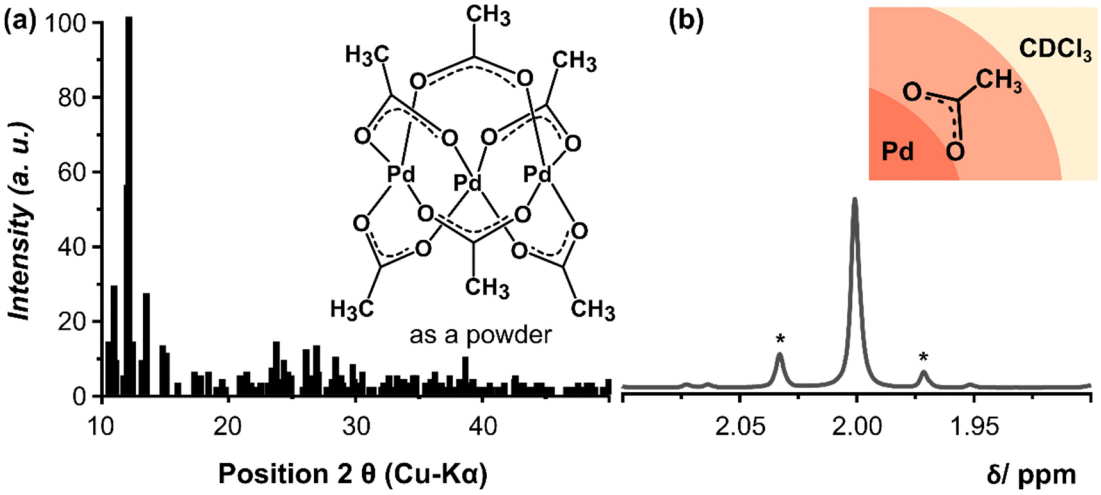

Figure 5.3: (a) XRD pattern recorded for trimeric Pd-acetate ($Pd_3(OAc)_6$). (b) ^1H NMR spectrum taken at 500 MHz in solution of $CDCl_3$ containing Pd-acetate.

By dissolving Pd-acetate in $CDCl_3$, the corresponding ^1H NMR spectrum shown in Figure 5.3(b), exhibits a single peak at 2.001 ppm, which corresponds to H in the acetate group (acetate = $OCOCH_3$ = Ac). The presence of the additional small peaks of different intensities indicate hydrolysis of the Pd-acetate compound in $CDCl_3$ due to trace water impurities, and can be assigned to $Pd_3(\mu\text{-}OH)(OAC)_5$.[554] A similar ^1H NMR spectrum of Pd-acetate has been observed when dissolved in MeCN, Figure 5.4. A single ^1H NMR peak of the acetate group was observed, shifted downfield to a higher ppm value (2.169 ppm) due to the strong solvation properties of MeCN in comparison to $CDCl_3$ and the presence of a more electronegative element (N). Both NMR spectra in Figures 5.3 and 5.4 suggest that Pd-acetate retains its cyclic trinuclear structure in solution, with the possibility of the existence of linear trimer or dimer Pd-acetate.[560]

Table 5.5: List of angles, and the corresponding intensity and lattice planes of trimeric Pd-acetate ($Pd_3(OAc)_6$).

2θ [°]	**i [%]**	**h**	**k**	**l**
10.555	13	0	0	2
10.97	28	0	1	2
12.002	55	0	4	0
12.143	100	0	2	2
12.46	13	1	1	-2
13.508	26	1	2	-2
14.802	12	1	3	0
15.079	10	1	3	-2
23.747	13	2	3	-1
23.747	13	1	6	-3
26.096	11	0	5	4
26.933	12	1	8	0
27.066	5	1	4	-5
28.417	9	1	7	2

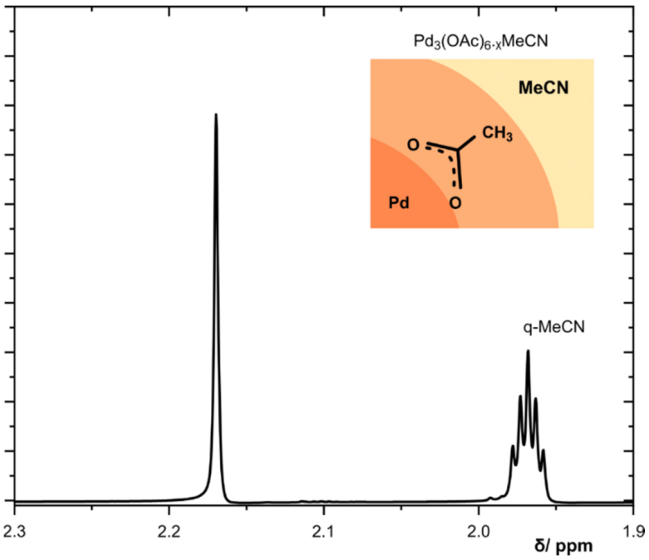

Figure 5.4: ^{1}H NMR spectrum taken at 500 MHz in MeCN solution containing Pd-acetate.

5.4.1 Understanding the solvation structure of Pd-acetate, Pd^{2+} and the acetate group using IR and UV-Vis spectroscopy

To further understand the behaviour of Pd-acetate in solution, analysis of the solution structure was further investigated using FT-IR, UV-Vis spectroscopy and electrochemical methods. These spectroscopic techniques will provide information about the environment directly surrounding the metal cation, whilst the electrochemical method informs on the ion interaction with the solution outside the primary solvation shell.[561]

IR spectroscopy is a diagnostic tool used to probe solvent-solvent interaction and ion-solvent interactions.[562, 563] Coordination of MeCN and anions (either the acetate or the background electrolyte, in this study tetrafluoroborate BF_4^-) to the Pd centres and/or the acetate group can cause measurable shifts in the IR modes associated with these interactions. The IR spectra of MeCN only and MeCN-Pd-acetate are shown in Figure 5.5. Figure 5.6(a) highlights the IR C≡N stretching region, whilst Figure 5.6(b) displays the UV-Vis spectrum of Pd-acetate in MeCN.

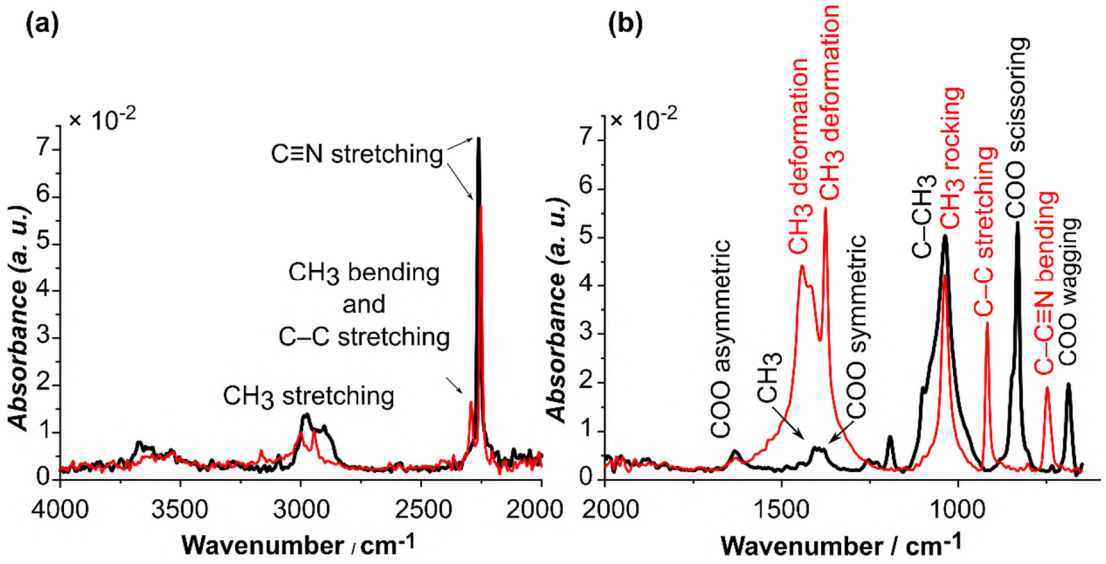

Figure 5.5: IR absorption spectra of MeCN (red line) and 1×10^{-3} M Pd-acetate in MeCN (black line) in the regions (a) from 4000 cm^{-1} to 2000 cm^{-1} and (b) from 2000 cm^{-1} to 700 cm^{-1}.

Figure 5.5 shows the IR regions that are most sensitive to Pd^{2+} and the acetate group. In the IR region from 2550 cm^{-1} to 2000 cm^{-1} (Figure 5.5(a)), the CH_3 bending, C–C stretching and C≡N stretching modes are indicators of free MeCN molecules and/or coordinated MeCN. In the low wavenumber region information about the chelated and bridged acetate can be derived (Figure 5.5(b)). The strength of the MeCN interaction with Pd^{2+}, can be interrogated by evaluating the C≡N stretching mode at 2252 cm^{-1}. The MeCN solvent coordinates to Pd^{2+} through partial donation of the lone pair on the nitrogen (N) atom, resulting in a shift of the C≡N stretch to the higher wavenumber 2260 cm^{-1} (peak P1 in Figure 5.5(a) and Figure 5.6(a)). Perturbation of the number of C–H stretch modes can be due to the effect of Pd^{2+} coordination to MeCN; however, the C–H stretch mode is less diagnostic of Pd^{2+} coordination.

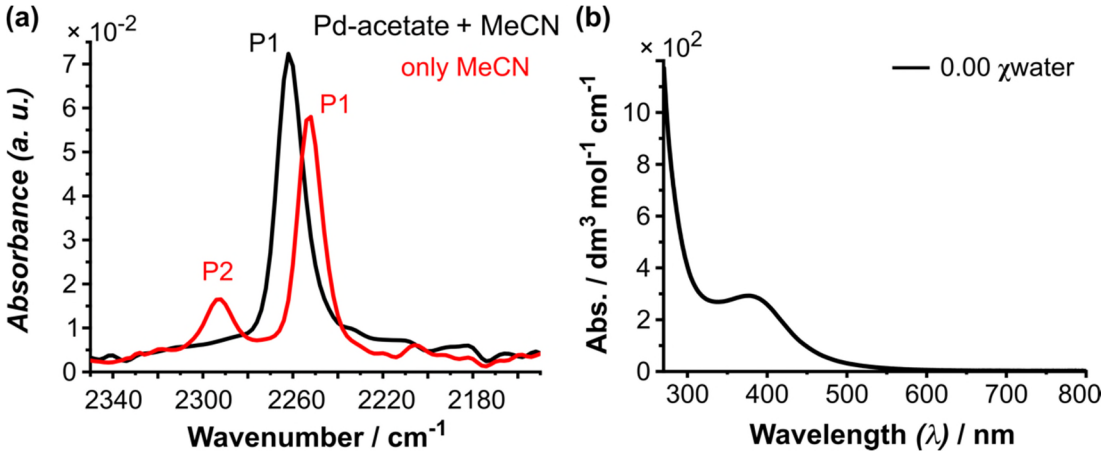

Figure 5.6: (a) IR absorption spectra of MeCN (red line) and 1×10^{-3} M Pd-acetate (trimeric) in MeCN (black line) in the region from 2345 cm^{-1} to 2160 cm^{-1}. (b) UV-Vis absorbance spectrum of 1×10^{-3} M Pd-acetate in MeCN.

The IR spectra in the region from 2000 cm^{-1} to 700 cm^{-1}, contain the absorption bands ν_{as}(COO) and ν_{s}(COO) at 1634 cm^{-1} and 1380 cm^{-1} indicating a cyclic structure or linear trimeric structure of the Pd-acetate compound in MeCN.[564] The broad ν_{as}(COO) and ν_{s}(COO) bands suggest that the bridging COO groups of the trimeric Pd-acetate are not equivalent. Hence, the structure is likely to be asymmetric due to interaction with the solvent molecules. The UV-Vis spectrum of 1×10^{-3} M Pd-acetate in MeCN exhibited only one absorption band around 400 nm assigned to the trimeric Pd-acetate due to d-d absorption, indicating strong coordination of the acetate groups to the Pd^{2+} centres in solution and further confirms the structure as trimeric, Figure 5.6(b).[554, 565, 566] The role of the acetate group is to bridge the Pd centres, hence keeping the triangular Pd_3 elements together in a cyclic form.[564] Consequently, the distance between Pd···Pd···Pd in such trinuclear cyclic structure is large enough and thus there is no bonding interaction in the ground state.[566] Also, the trimeric Pd-acetate ($Pd_3(OAc)_6$) is square planar, though the Pd centres are slightly displaced out of the plane and the overall symmetry is approximately D_{3h}.[566] As a result, an absorption band due to metal-metal interaction is not expected.

5.4.2 Electrochemical behaviour of Pd-acetate in aqueous (water) only and non-aqueous (MeCN) only solvents

IR, NMR, and UV-Vis experiments did not provide enough information about the oxidation state of Pd, but the inner shell of Pd ions in solution is occupied by the acetate groups, while the whole Pd-acetate structure is associated with MeCN molecules. To understand the electrochemical behaviour of Pd-acetate and extract information about oxidation state, possible phase formation via electrodeposition, CV, chronoamperometry, NMR and surface imaging studies were carried out for Pd-acetate dissolved either in water or MeCN. The potential at the BDD electrode was swept at 0.1 V s^{-1} in the cathodic direction, and the voltammetric behaviour of Pd acetate in aqueous and MeCN solutions are shown in Figures 5.7 and 5.8, respectively.

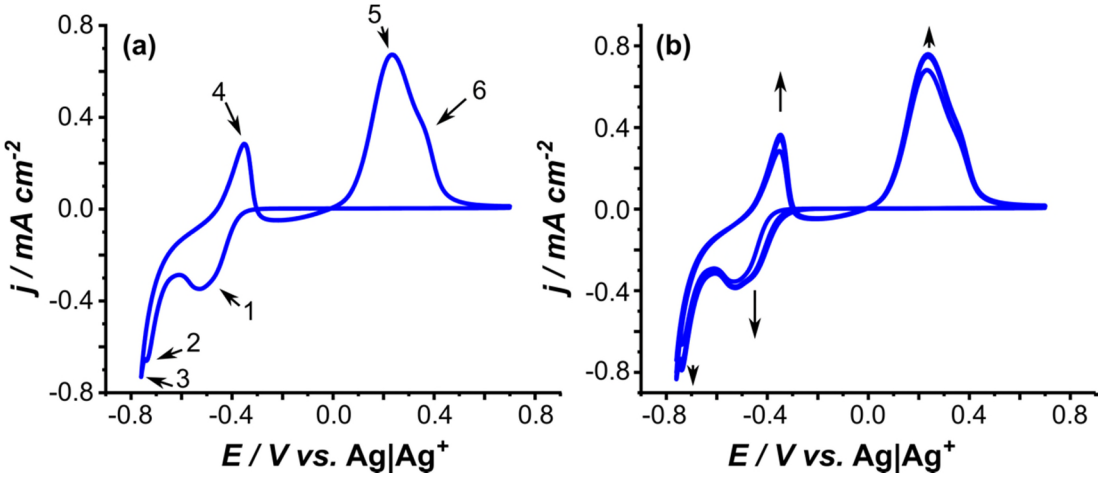

Figure 5.7: CV for studying Pd electrochemical behaviour from solutions containing 1×10^{-3} M Pd-acetate + 0.1 M HCl + 0.05 M KCl (pH = 1.8) at $\nu = 0.1$ V s^{-1}, (a) first cycle and (b) four subsequent cycles following the first cycle of Pd-acetate electrochemistry.

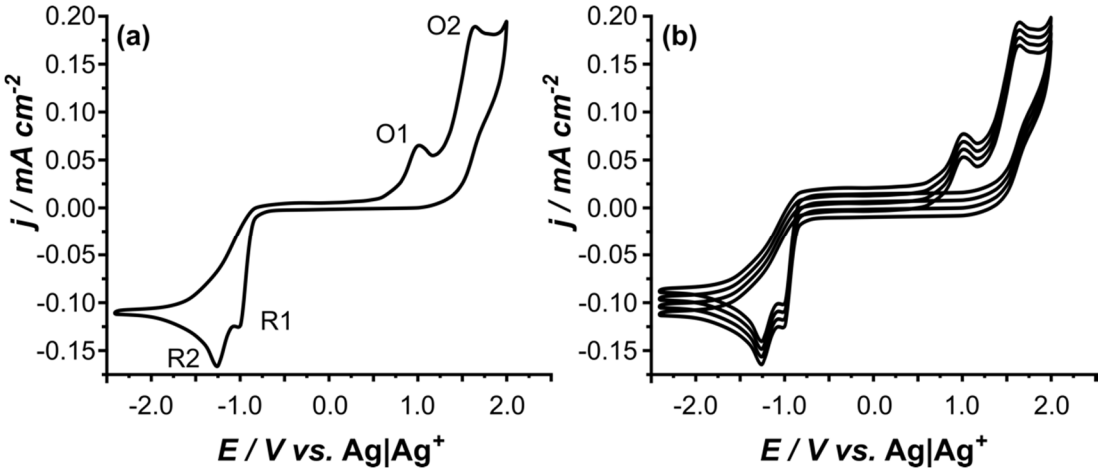

Figure 5.8: CV for studying Pd-acetate electrochemical behaviour from solutions containing 1×10^{-3} M Pd-acetate + 0.1 M $TBABF_4$ in MeCN only at $\nu = 0.1$ V s^{-1} (in absence of oxygen), (a) first cycle and (b) four subsequent cycles following the first cycle of Pd-acetate electrochemistry. The four cycles in (b) are offset for clarity.

From the CV obtained in aqueous pH = 1.8 solution, Figure 5.7(a) and (b), there is a distinctive peak (peak number 1) on the forward sweep at -0.51 V (half wave potential, $E_{1/2}$, of -0.43 V and charge, Q = 0.49 C) that can be assigned to the reduction of Pd^{2+} to Pd^0, followed by H_2 absorption at -0.73 V (peak number 2, Q = 0.48 C) on the newly formed Pd phase, then hydrogen evolution started at -0.76 V (peak number 3) ($2H^+ + 2e^- \rightarrow H_2$). By reversing the scan direction, the H desorption comes first at -0.36 V (peak number 4, Q = 0.2 C) followed by Pd dissolution then Pd stripping (peaks 5 and 6, Q = 1.2 C) in the range from +0.2 V to +0.6 V (Equations 5.1 and 5.2).[567]

$$Pd + H_2O \rightarrow PdO + 2H^+ + 2e^- \quad Equation\ 5.1$$

$$PdO + 2H^+ \rightarrow Pd^{2+} + H_2O \quad Equation\ 5.2$$

In the region of Pd stripping, the Pd stripping peak is not distinctive from the peak due to surface oxide formation (PdO) and appears as a hump in a broad peak. The crossovers of the anodic and the cathodic part of the cycle are noticed at -0.3 V and -0.01 V, which denote nucleation of solid metal on the electrode surface and/or the newly formed phase of Pd.[568] Further cycling, Figure 5.7 (b), show similar features to the first cycle, with the appearance of a small reduction wave at -0.4 V indicative of reduction of Pd^{2+} species on previously electrodeposited Pd. Also, both the current and the charge increase indicating an increase in the surface area as a function of each successive cycle.

In contrast in MeCN solutions, the "aqueous" behaviour of Pd electro-reduction and subsequent oxidation/dissolution is not observed (Figure 5.8), (note the solution was de-oxygenated for 30 minutes), even when scanning out to a wider negative potential window. In the cathodic scan, two consecutive reduction peaks (R1 and R2) were registered at -1.01 V (Q = 0.15 μC) and -1.25 V (Q = 0.49 μC), respectively and two oxidation peaks were observed at +1.01 V (Q = 0.17 μC) and +1.57 V (Q = 0.53 μC), respectively in the anodic direction. In previous reports by Asselt et al. and Amatore et al.,[530, 550] palladium complexes containing rigid bidentate ligands systems in non-aqueous media were suggested to undergo reduction reactions that involve multiple electron transfer stages to form radical or Pd^{1+} and Pd^{0} complexes in solution, with the Pd being described to be strongly ligated to its ligand. The two peaks may then be indicative of the two processes occurring as proposed in Scheme 5.1 (Equations 5.3 and 5.4).

$$Pd_3^{2+}(OAc)_6 + 1e^- \rightarrow [Pd_3^{1+}(OAc)_6]^{-1} \quad Equation\ 5.3$$

$$\left[Pd_3^{1+}(OAc)_6\right]^{-1} + 1e^- \rightarrow \left[Pd_3^{0}(OAc)_6\right]^{-2} \quad Equation\ 5.4$$

Scheme 5.1: Proposed electro-reduction steps of Pd-acetate in MeCN medium only.

Further electrolysis experiments were conducted, employing a highly negative overpotential (η = -1 V for t_{dep} = 1 hour) to the electrode (theoretically sufficient to reduce Pd^{2+} to Pd^{0}) in both aqueous and non-aqueous solvents. Note hydrogen evolution will contribute to the process of electrodeposition from the aqueous solutuion,[569] but high η is required to drive reduction of metal ions in non-aqueous medium. The surface of the electrode was examined post electrolysis, using FE-SEM and XEDS to image any formation of a deposit and confirm the elemental composition as shown in Figures 5.9 and 5.10. The impact of continuous electro-reduction on the chemistry of the solution was further studied using NMR to assess changes associated with the chemical environment around the metal centre (Pd), as shown in Figure 5.11. Though NMR is not known as a technique for oxidation state determination, metal reduction or oxidation leads to a change in the electronegative properties of the metal, hence H within the vicinity of the metal centres will shift upfield or downfield based on the electronegativity. Thus, we can assess whether stable Pd^{0}-acetate molecules

have been formed in solution rather than the deposition of metallic Pd materials on the electrode surface as well.

The resulting chronoamperometric *i-t* curve during electrodeposition in water is shown in Figure 5.9(a). Initially, the current decays due to the charging of the solid-liquid interface, then a sharp increase was observed due to a combined high nucleation and growth rate, owing to the formation of metallic Pd and the evolution of hydrogen. After this sharp increase, the current started increasing slightly with time, with the dominant process being hydrogen evolution, indicated by the large value of the charge passed over the course of the electrodeposition. Elemental analysis and FE-SEM microscopy revealed, upon deposition from aqueous solution, a silvery metallic deposit of Pd on the surface of the electrode. This lustre deposit was easily detached from the BDD electrode upon removal from the solution. The elemental analysis using XEDS along with FE-SEM imaging showed that Pd was deposited in the metallic form, appearing as a broken film as shown in Figure 5.9(b and c).

Unlike electrodeposition from aqueous solution, the *i-t* curve for Pd-acetate in MeCN under the same conditions for electrolysis in aqueous, showed first a sharp decrease in current due to charging of the surface interface followed by a constant slightly decreasing current (Figure 5.10(a)). Also, the charge passed was smaller in comparison to the charge passed during electrodeposition of Pd from its aqueous solution. Both elemental analysis (XEDS) and FE-SEM, Figure 5.10(b and c), show no evidence for Pd electrodeposition. NMR spectra of Pd-acetate in MeCN only shown in Figure 5.11 (before electrolysis) demonstrates a shift of the ^{1}H NMR peak associated with Pd^{2+}-acetate from 2.17 ppm up-field to a lower chemical shift value at 2.16 ppm (after electrolysis). This is indicative of the formation of Pd^{0}-acetate in solution rather than phase formation of the metallic Pd. The emergence of low intensity peaks may also indicate ligand attachment and structural change.

The data suggests that Pd electrodeposition from MeCN is not possible, in contrast, Pd electrodeposition occurs easily in aqueous solution. In acidified solution, the complex Pd-acetate structure is decomposed completely into labile Pd ions surrounded by water (*i.e.* Pd ions are not bonded to the acetate groups).[570] This facilitates the reduction of Pd^{2+} to Pd^{0} on the electrode surface. In MeCN only, CV, NMR, chronoamperometry, XEDS and SEM data agree with the data suggested in section

5.4.1 *i.e.* Pd^{2+} ions are bound to the acetate ligands, even after reduction to the Pd^{0}; thus, electrodeposition is not feasible from MeCN only.

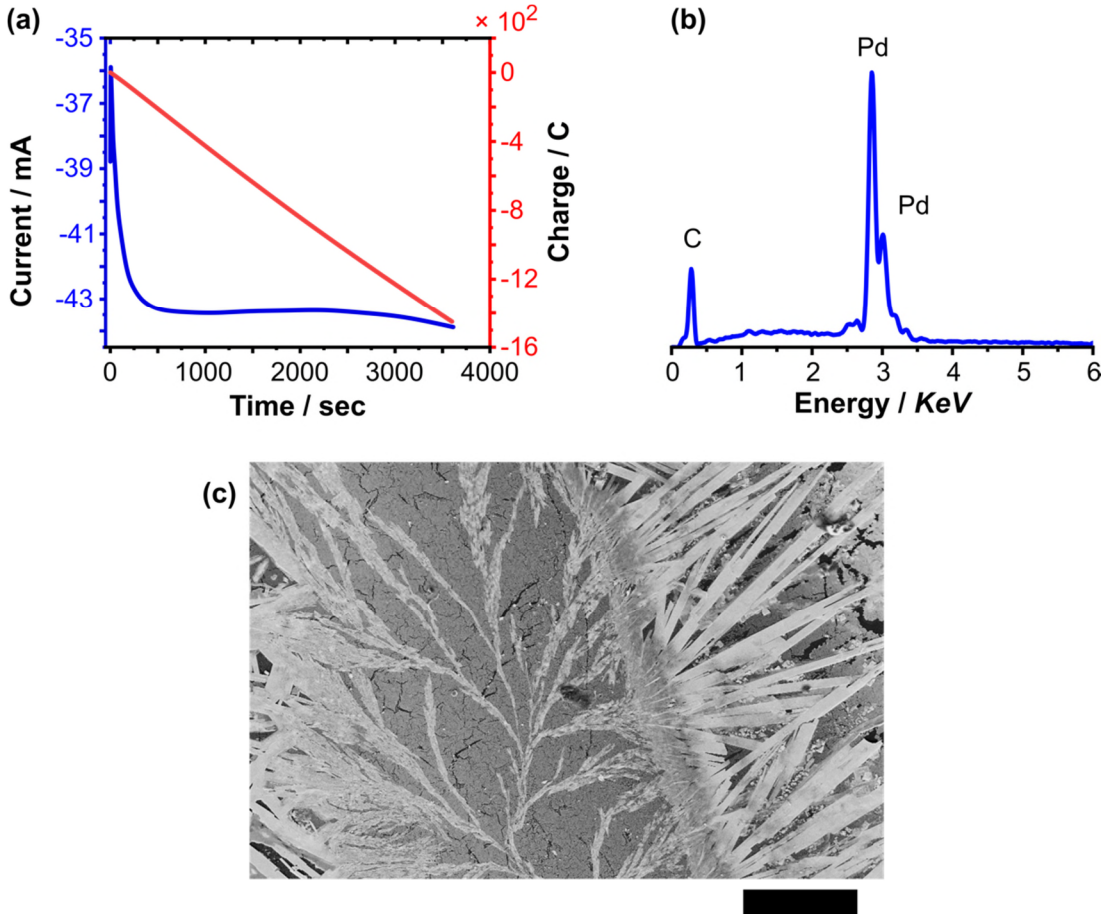

Figure 5.9: Chronoamperometric plot, XEDS-spectrum and FE-SEM image of Pd electrodeposition from aqueous solution. (a) *i-t* transient for Pd electrodeposition from solution containing 1×10^{-3} M Pd-acetate + 0.1 M HCl + 0.05 M KCl obtained at η = -1 V for t_{dep} = 3600 s. (b) XEDS fingerprint and (c) FE-SEM image of the Pd deposit. Scale bar = 100 µm.

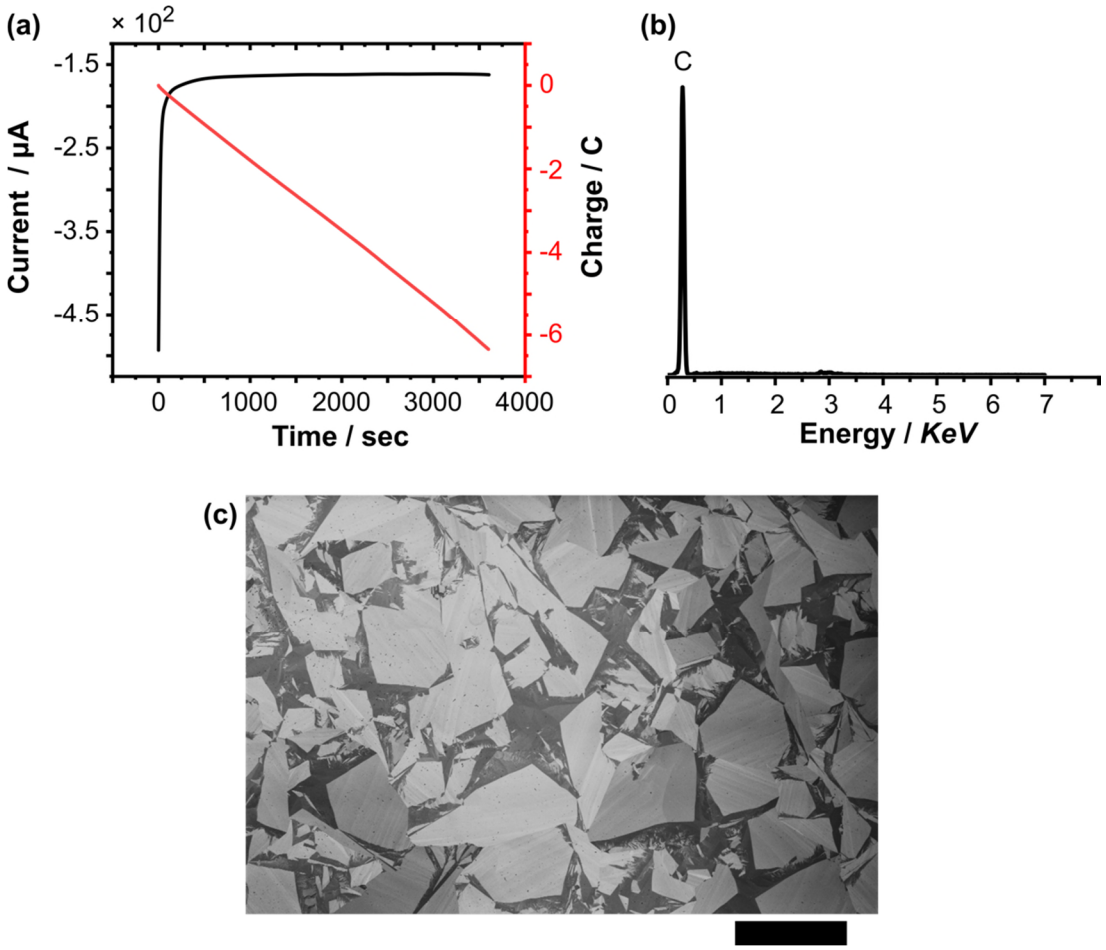

Figure 5.10: Chronoamperometric plot, XEDS-spectrum and FE-SEM image of Pd electrodeposition from non-aqueous. (a) *i-t* transient for Pd electrodeposition from solution containing 1×10^{-3} M Pd-acetate + 0.1 M $TBABF_4$ in MeCN only obtained at η = -1 V for t_{dep} =1 hour. (b) XEDS fingerprint and (c) FE-SEM micrograph of the surface. Scale bar = 100 µm.

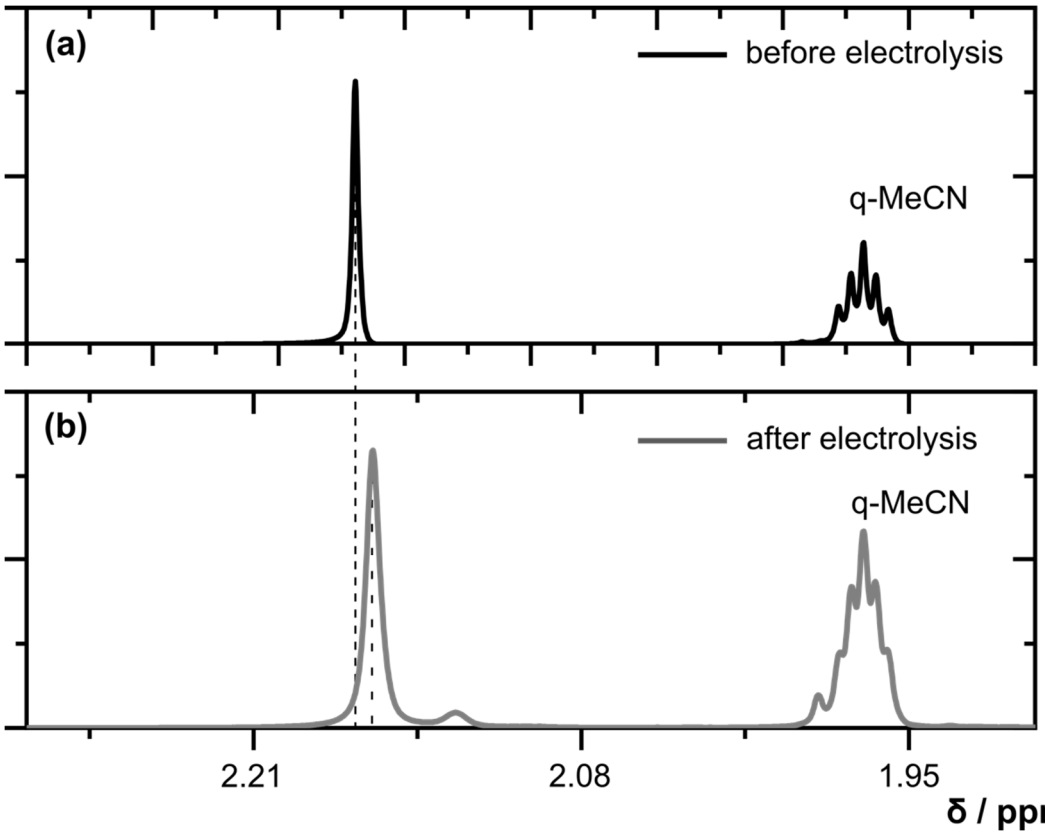

Figure 5.11: ^{1}H NMR spectrum taken at 500 MHz of 1×10^{-3} M Pd-acetate in MeCN solution only (a) before (black) and (b) after (grey) electrodeposition.

5.6.3 Understanding Pd acetate complex structure in biphasic (water:MeCN) systems

Obviously, the spectroscopic and the electrochemical data show that the acetate groups are strongly attached to the Pd centres. However, hydration of the acetate groups is possible in the presence of water, as it coordinates to the carboxylic group of the acetate ions.[571] This is linked to the hydrophobic interaction of water with the methyl (CH_3) group and the strong tendency of small O-containing anions, with a localised charge such as the acetate group, forming hydrogen bonds.[363, 572] Also, water is classified as a hard acid and a hard base, hence water molecules solvate strongly to anions with a negative charge localised on the oxygen atom (*e.g.* CH_3COO^-, CH_3O^-, etc.) and hard base anions such as F^-.

Thus, water addition may help perturbing the Pd-acetate association. To study this hypothesis, mixed solvent systems was considered. An immiscible biphasic MeCN - water system was established by dissolving potassium chloride (1 M) in the aqueous

phase before adding to it an equal volume of MeCN, which contains 0.1 M $TBABF_4$, as shown in Figure 5.12(a-c). The system was first mixed carefully then Pd-acetate was added to the mixed biphasic system, so it distributed between both phases by vigorous stirring. After leaving the solution to sit a stable biphasic system results with the less dense MeCN-rich phase on top and the denser aqueous water-rich phase at the bottom, Figures 5.12(d-h) and 5.13(a).

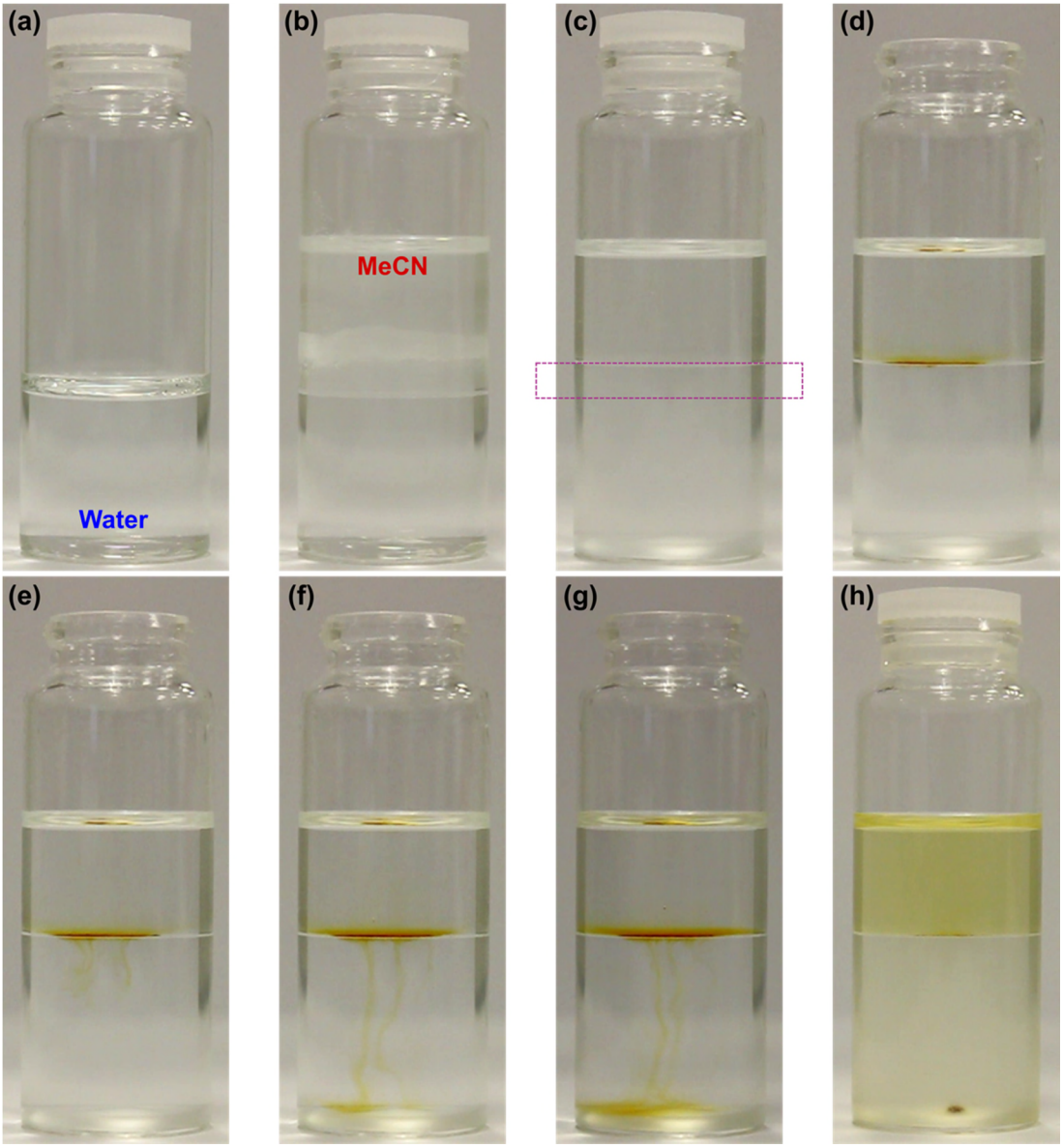

Figure 5.12: Image sequence of steps involved in the formation of an immiscible biphasic MeCN-water system. (a) Only water + 1 M KCl. (b) addition of MeCN + 0.1 M $TABAF_4$. (c) Part of MeCN dissolved in water. (d-g) Addition of Pd-acetate to the biphasic system and (h) dissolving Pd-acetate via vigorous stirring and mixing.

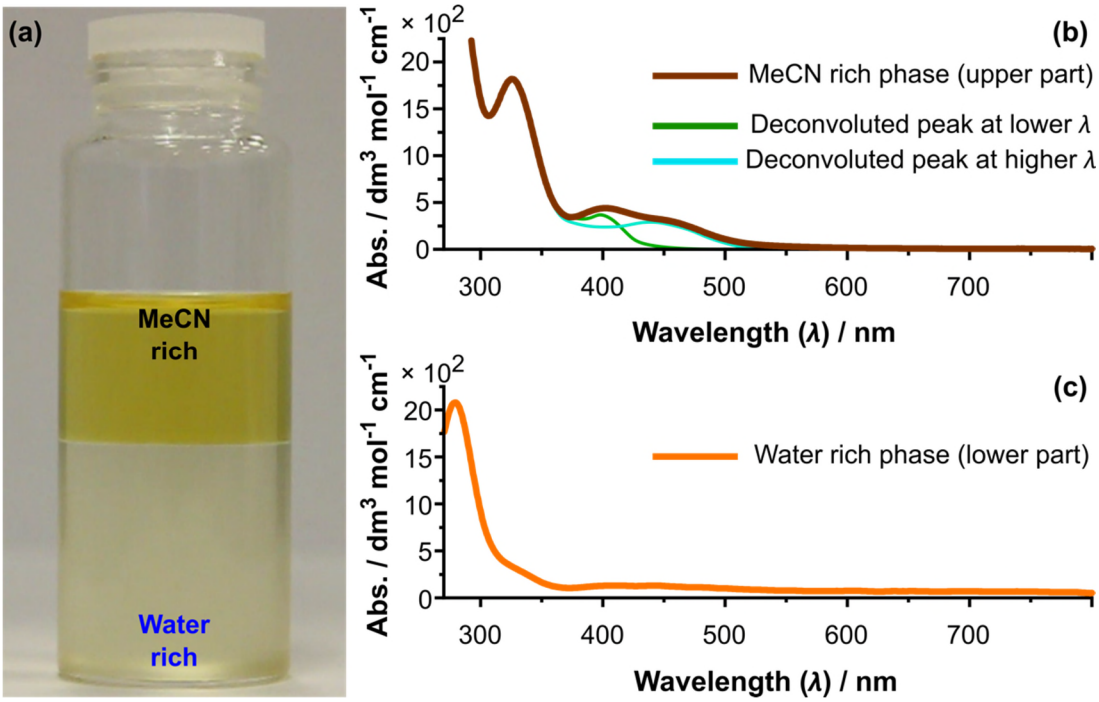

Figure 5.13: (a) Image of the biphasic system after complete Pd-acetate mixing and dissolution. UV-Vis absorbance spectra of 1×10^{-3} M Pd-acetate in a biphasic system composed of (b) MeCN-rich phase (yellowish orange) and (c) water-rich phase (light yellow).

The biphasic systems will allow the examination of the influence of water addition on facilitating Pd electrodeposition from MeCN. We first examined Pd coordination in both phases by collecting the UV-Vis absorption spectra from the MeCN-rich and water-rich phases, respectively, in the absence of air as shown in Figure 5.13(b). Note MeCN-rich or water-rich refers to sample collection from the upper or lower phase, respectively, of the biphasic solution, as shown by the labels in Figure 5.13.

The colour of the solution is generally associated with d-d transitions. For Pd-acetate a change in the electron distribution between the metal and the ligands will give rise to LMCT and/or splitting of the d-orbital energies results, thus bands associated with these transitions can be registered when performing UV-Vis. The UV-Vis spectra can thus be utilised to study transitions involved in the rearrangements of valence electrons associated with the nature of the ligands surrounding the Pd centres. The UV-Vis spectrum of Pd-acetate in the MeCN-rich phase (yellowish orange) exhibits an intense UV absorbance at 325 nm and a broad band, which can be deconvoluted into two peaks with maximum of 402 nm and 456 nm, Figure 5.13(b). On the other hand, the

UV-Vis spectrum in the water-rich phase (light yellow) shows one absorption peak only at 279.5 nm, Figure 5.13(c).

The colour of the MeCN rich part is strong yellowish orange, indicative of electronic transitions among the various energy levels of the d-orbitals of Pd. This give rise to the absorption peak at 402 nm in the UV-Vis spectrum, shown in Figure 5.13(b) in agreement with the UV-Vis spectrum of Pd-acetate in MeCN only. Although the system shows two "immiscible" layers of MeCN and water, dissolution of MeCN in water and vice versa can't be neglected, in fact this is clear in Figure 5.12(b-d), where the volume of water has increased due to the high tendency of MeCN to dissolve in water.[573] Prior to assigning all UV-Vis peaks, we first look at how water addition to the MeCN phase can lead to hydrolysis of Pd-acetate as shown schematically in Figure 5.14.[555, 574]

Incorporation of water into the trimeric Pd-acetate leads to the opening of the acetate ring via transfer of water and formation of a linear open chain (step 1 and step 2, Figure 5.15). Furthermore, the Pd···Pd distances decrease, the planes of the coordination spheres turn toward each other, and Pd atoms are arranged along a straight line. Dimer Pd-acetate or singular Pd-acetate (step 3, Figure 5.15) can also form. Consequently, the UV-Vis absorption peak at 456 nm can be assigned to $d\sigma^* \rightarrow p\sigma$ excited state transitions which involve the Pd-Pd interaction in Pd-acetate (Figure 5.14 (b)). This shows that the presence of water domains, which leads to structure transformation from cyclic trimeric to linear trimeric or palladium diacetate, respectively, where the former presumably provide a more stable structure in the MeCN-rich phase.

Since Pd-acetate dissociation due to water addition is feasible, then Pd will seek to associate with electron donor species. In fact, both MeCN and tetrafluoroborate (BF_4^-) can function as ligands to Pd^{2+} as both have high energy lone pairs. Thus, association to the Pd centre, which contains low lying empty orbitals, can occur when the acetate groups start dissociating from the trimer cycle. Consequently, the intense absorption peak at 325 nm can stem from LMCT but in this case MeCN molecules are the ligands (MeCN)$\rightarrow$Pd.

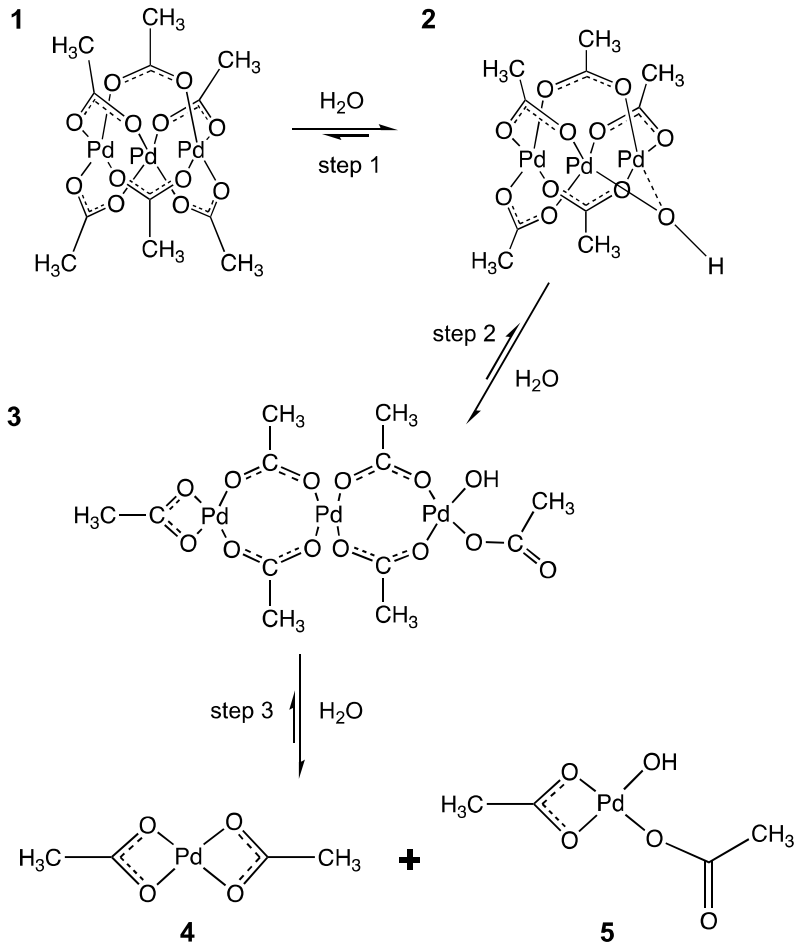

Figure 5.14: Hydrolysis of trimeric Pd-acetate assisted by water.

It is worth noting that the Gibbs free energy of hydration of the acetate group is much lower than hydration of Pd^{2+} ions, Table 5.6, which suggests preferential hydration of the acetate groups in water by forming H-bonds or association to labile H^+. Thus, when Pd-acetate transfers to the water-rich phase, it is expected to dissociate into its constituent, Pd cations and acetate anions according to the mechanism shown in Figure 5.15 (step 4). If this scenario occurs, then an absorption peak will appear in the UV region associated with the Pd species in water-rich phase. Hence, the intense UV-Vis absorption peak at 279.4 nm (low wavelength value, Figure 5.13(c)), can be assigned to LMCT arising from coordination of water molecules that have replaced MeCN molecules in the inner sphere, $(H_2O)\rightarrow Pd$. It can also be assigned to $n\rightarrow\pi^*$ transition in the carbonyl group (C=O). Note, competition from the MeCN molecules to associate with the Pd cations is still possible.

Table 5.6: Standard molar Gibbs energies of ion transfer from a source solvent (water) to neat target.

Ion	**$-\Delta_h H_I^\infty$ / kJ mol^{-1}**	**$-\Delta_h S_I^\infty$ / J K^{-1} mol^{-1}**	**$-\Delta_h G_I^\infty$ / kJ mol^{-1}**
Pd^{2+}	2054	324	1957
CH_3COO^-	425	169.4	374

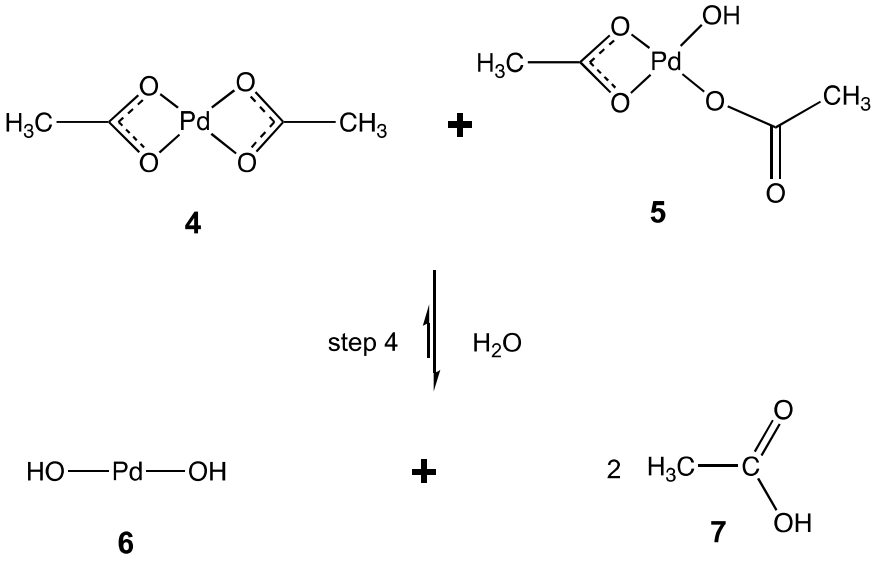

Figure 5.15: Dissociation of Pd-acetate in water-rich phase.

Since more information is required to assess the chemical structure, bonding and link changes during hydrolysis to the physical and chemical properties of the solution, both IR and NMR spectroscopic data were collected from the MeCN-rich and water-rich layers, Figures 5.16 and 5.17. The IR spectra, Figure 5.16(a-b), can be interpreted as follow. In the region from 4000 cm^{-1} to 2500 cm^{-1}, Figure 5.16(b), a band associated with the O–H stretching vibration near 3490 cm^{-1} is noticed in both phases, MeCN-rich and water-rich. In the former, the O–H band appears at a slightly higher wavenumber, and two sharp peaks are distinctive just below 3000 cm^{-1}. These observations can be associated with O–H·····N≡C in the MeCN-rich phase, while in water the O–H stretching is shifted to a lower wavenumber indicative of free water and hydrogen bonded water. The observation of the O–H band in the MeCN-rich phase is surprising, as MeCN is well known to dissolve faster in water, but the water has less tendency to dissolve in MeCN.[61]

The region between 2550 cm^{-1} and 1600 cm^{-1}, Figure 5.16(c), is more representative for the IR modes in MeCN. First there is a peak at 2350 cm^{-1} recorded in the MeCN-rich phase which does not exist in the water-rich phase. This peak is due to H-bonded acetate. In both phases, two peaks emerge around 2260 cm^{-1} and 2252 cm^{-1}, which can be assigned to a combination of CH_3 bending and C–C stretching in free MeCN. This peak shifts slightly to a higher wavenumber in the water-rich phase, but it indicates the presence of free MeCN. The later vibration peak is thought to be due to a C≡N stretching band, which shifts to a higher wavenumber in the water-rich phase. This behaviour represents MeCN-water interaction, though the shift is not prominent.

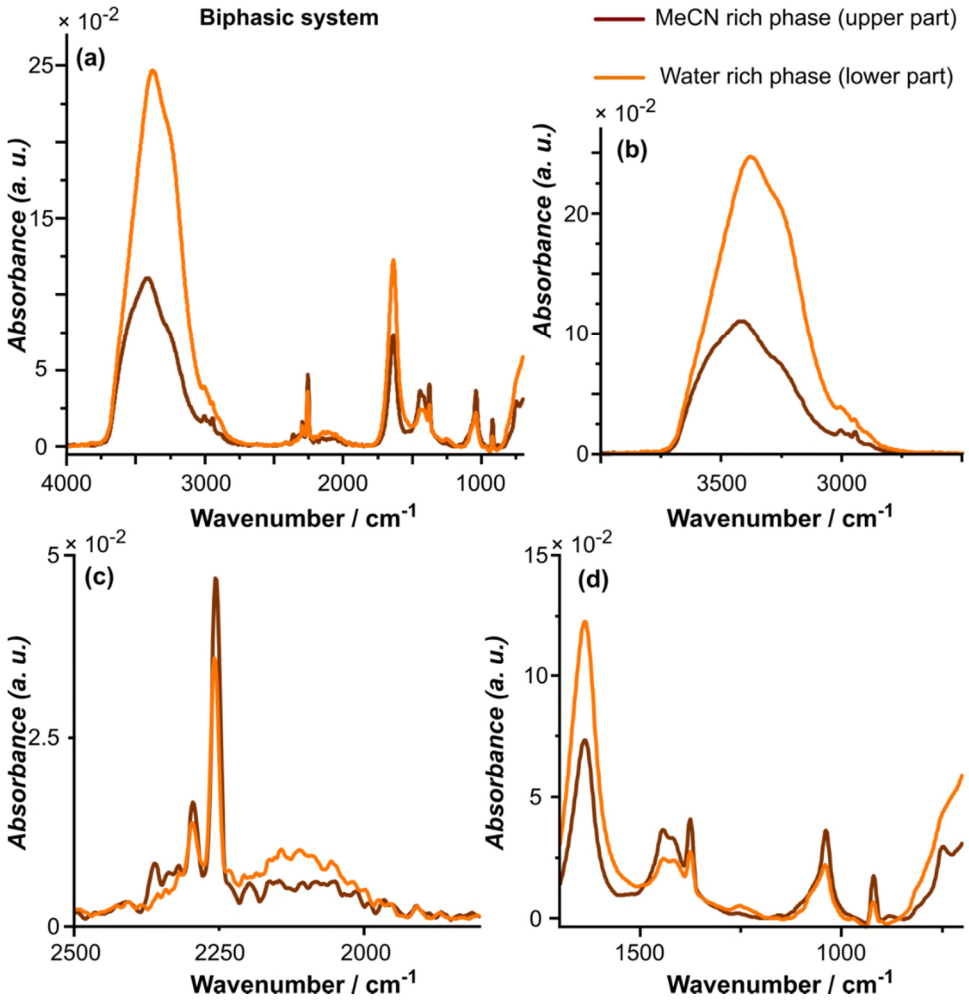

Figure 5.16: Infra-red (IR) absorption spectra of MeCN-water biphasic system. MeCN-rich phase is presented by the brown line and water-rich phase is presented by the orange line. (a) The full spectra scan from 4000 cm^{-1} to 700 cm^{-1}. (b) The OH stretching region. (c) C≡N stretching and combination of CH_3 bending and C-C stretching regions. (d) H-O-H, C-CH_3, C-C≡N and COO symmetric and asymmetric regions.

The third region, Figure 5.16(d), represents IR modes of the acetate groups and MeCN. Both MeCN-rich and water-rich phases have almost similar IR modes, with minor changes related to the shape (intensity) or the presence of peaks associated with MeCN but their intensity are weak such as C–C≡N bending around 750 cm^{-1} in the MeCN-rich phase. Around 1600 cm^{-1}, a strong COO asymmetric band was observed, followed by CH_3 deformation, COO symmetric, and a broad band of C–CH_3 and CH_3 rocking at 1490 cm^{-1}, 1480 cm^{-1} and 120 cm^{-1}, respectively. These IR bands demonstrate that water molecules exist in the MeCN-rich phase and MeCN molecules exist in the water-rich phase.

The previous techniques were complemented with ^1H NMR analysis as shown in Figure 5.17. This way the environment around the Pd^{2+} cations and the status of the hydrolysis of the acetate groups can be examined, *i.e.* if water may induce any effect for example ligand exchange. To test this hypothesis, ^1H NMR spectrum was recorded for (a) $Pd(CH_3CN)_4(BF_4)_2$ in the presence of ammonium acetate in MeCN only first, (b) commercial Pd-acetate in MeCN only (c) Pd-acetate in MeCN-rich phase and (d) Pd-acetate in water-rich phase. In solution (a) the ^1H NMR spectrum shows two singlet peaks, peak 1 at 1.99 ppm and peak 2 at 2.16 ppm. Solution (b) exhibits only a prominent peak (peak 2) at 2.15 ppm. Consequently, peak 1 can be assigned to H atoms of the CH_3CN ligated to the Pd centre, and peak 2 represents the H atoms in the acetate groups of trimeric Pd-acetate.

The ^1H NMR spectra of the Pd-acetate in the biphasic system, Figure 5.17(c and d) show two singlet peaks in MeCN-rich phase and three singlet peaks in the water-rich phase. In the MeCN-rich phase, a singlet peak 1U exhibits a similar chemical shift to peak 1 in Figure 5.17(a), 1.99 ppm, hence it can be assigned to H atoms of the CH_3CN ligated to the Pd ions. Peak 2U is a singlet, and exhibits a higher chemical shift at 3.29 ppm, indicating solvation of the acetate groups by both MeCN and water, which shifts the peak downfield.

In the water-rich phase, the spectrum can be explained as follow. If we assume complete hydrolysis of Pd-acetate in water, then the singlet peak of 2.15 ppm chemical shift is associated with free acetate groups in water. Given the high tendency of MeCN to dissolve in water, then MeCN molecules that have replaced the acetate group will coordinate to water, thus peak 2L was shifted downfield to 2.35 ppm. Finally, the singlet peak (3L) at 4.7 ppm indicates ligation of Pd with water (HO·····Pd·····OH).

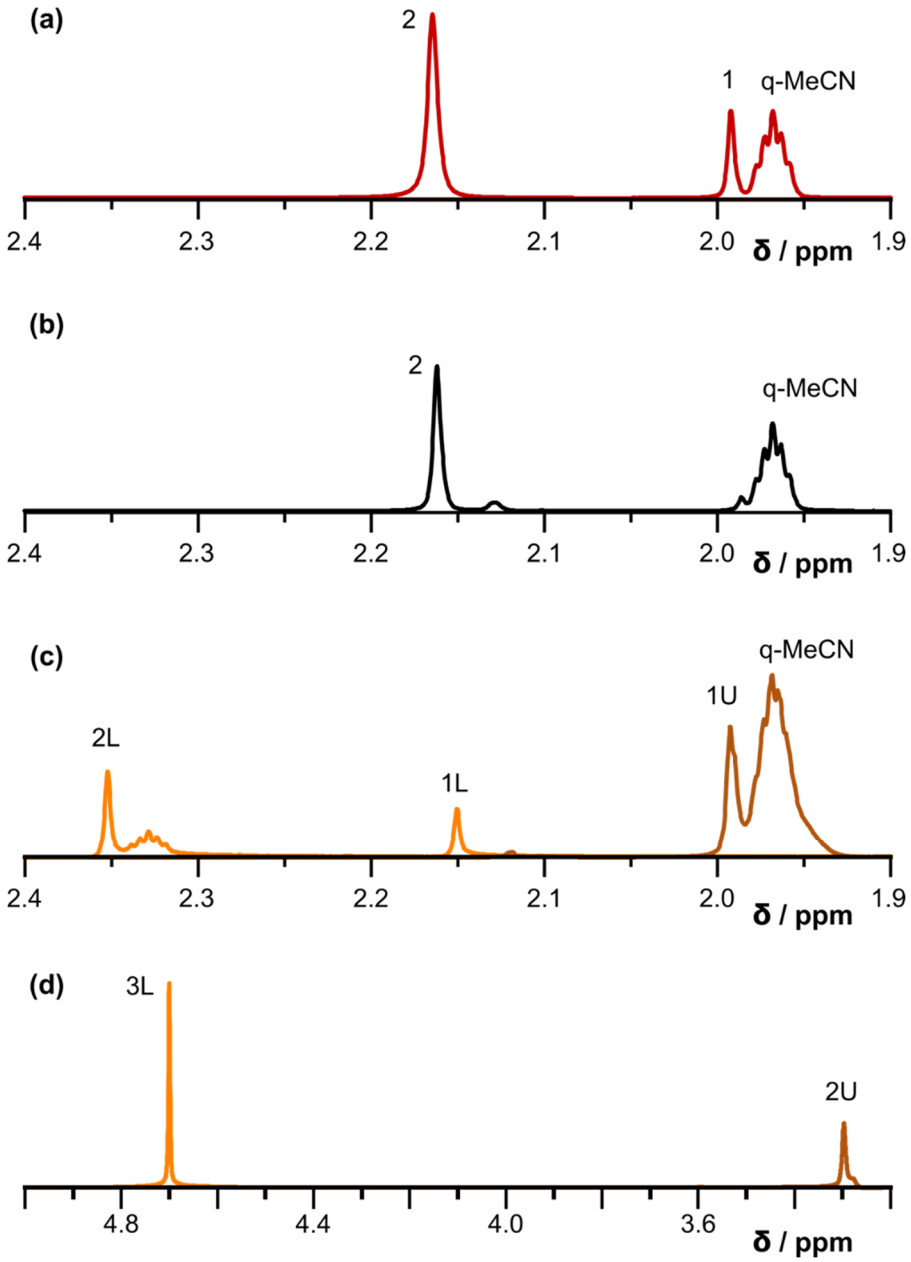

Figure 5.17: ^{1}H NMR spectrum of (a) 1×10^{-3} M $Pd(CH_3CN)_4(BF_4)_2$, (b) 1×10^{-3} M Pd-acetate in MeCN solution only, (c and d) 1×10^{-3} M Pd-acetate in MeCN-rich phase (brown) and water-rich phase (orange), respectively.

5.4.3 Electrodeposition from the biphasic system

UV-Vis, NMR, and IR data of the biphasic system demonstrate that in the presence of water, Pd-acetate hydrolysis will occur, which leads to free Pd ions. When water domains exist in MeCN-rich solution, Pd will be solvated by MeCN molecules but we cannot expect complete hydrolysis of the Pd-acetate molecules. When Pd ions transfer to water, they are almost associated with water molecules only. To explore

electrodeposition in this biphasic system, a BDD plate electrode (dimensions 1 cm × 10 cm) was inserted through both phases, as shown in Figure 5.18. Note that the RE was placed in the MeCN-rich phase. Electrodeposition was carried out at room temperature by applying a driving potential, η = -1 V for t_{dep} = 600 s to explore the Pd solid metal phase formation from both phases. Representative FE-SEM images and an XEDS map recorded for the interface between the MeCN-rich and water-rich phases in the biphasic system post electrodeposition are shown in Figure 5.18.

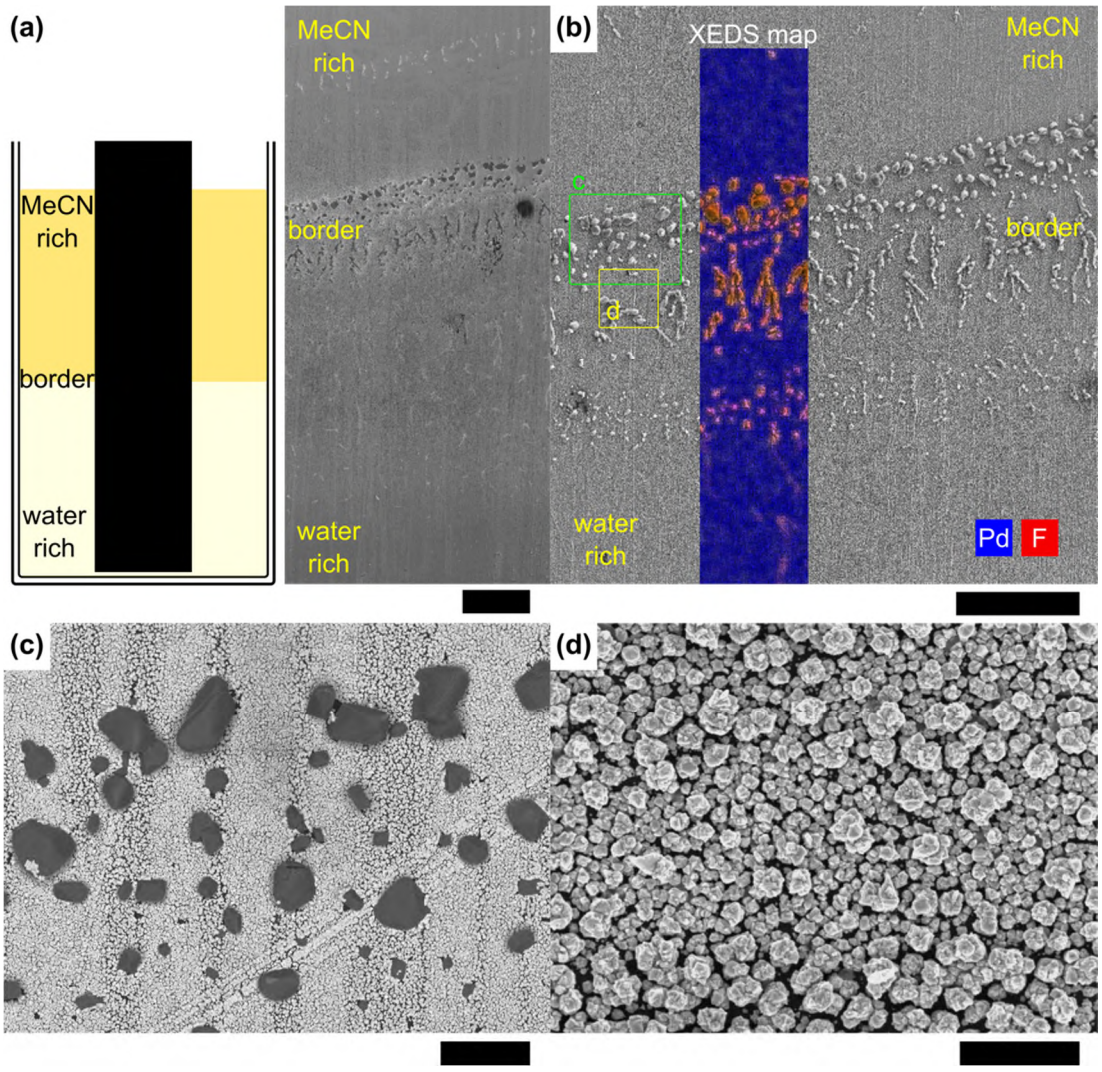

Figure 5.18: FE-SEM images of a BDD electrode immersed in the biphasic system, showing the electrodeposition of Pd at the interface between the MeCN-rich and water-rich phases at different magnifications (a), scale bar = 100 µm, (b), scale bar = 50 µm, (c) scale bar = 3 µm, and (d) scale bar = 600 nm.

Pd has been deposited from both sides of the biphasic system interface, Figure 5.18(a and b). The XEDS map shows the presence of Pd. At the interface between the two

solvents a signal from fluoride emerges. Higher magnification images of the interface, Figure 5.18(c), shows the presence of large polyhedral crystals on top of a layer of more homogenous smaller crystals.

To explore the deposition morphology away from the MeCN-water interface, FE-SEM images depicted in Figure 5.19(a and b) were collected for the top part of the electrode immersed in the MeCN-rich phase, and the bottom part immersed in the water-rich phase. The top and the bottom regions of the electrode appear free of the large polyhedral crystals, found in the interfacial region. These imaged at a higher magnification (Figure 5.19(d)) are similar to the crystals that were observed in this interfacial region. The high magnification FE-SEM images and the XEDS signal (Figure 5.19(d and e), blue line) measured from the large crystals and homogeneous deposition layer show that the large crystals are made of $Pd(BF_4)_2$ whereas the layer is Pd. A possible explanation for the formation of $Pd(BF_4)_2$ can be related to the high probability of supporting electrolyte salt hydrolysis.[575] It is known that $TBABF_4$ is a very sensitive salt towards ligand exchange via hydrolysis in the presence of water traces, with a susceptibility to form HF.[55, 575] Both the acetate and F^- anions are competing to coordinate to Pd^{2+} cations as Lewis bases. As well, Pd^{2+} and Bu_4N^+ are competing to interact with the ligands. Also, the concentration of the background electrolyte ($TBABF_4$) is 100 times higher than Pd-acetate, so ligand relaxation and anion exchange are possible when hydrolysis is occurring.

The morphology of the electrodeposit is also very different, in both cases, Figure 5.20(a and b). Further high magnification FE-SEM images of Pd electrodeposition from the MeCN-rich phase and water-rich phase are shown in Figures 5.21 and 5.22, respectively. The electrodeposited Pd from the MeCN-rich phase appears as a dense packing of Pd defined nanostructures, building up on top of each other, Figure 5.21(a-e). In contrast, Pd electrodeposited from the water-rich phase appears more much fractal like or dendritic, Figures 5.22(a-e). Additionally, in some parts of the electrode only partial deposition of the dendritic nanostructures was observed, Figure 5.22 (f).

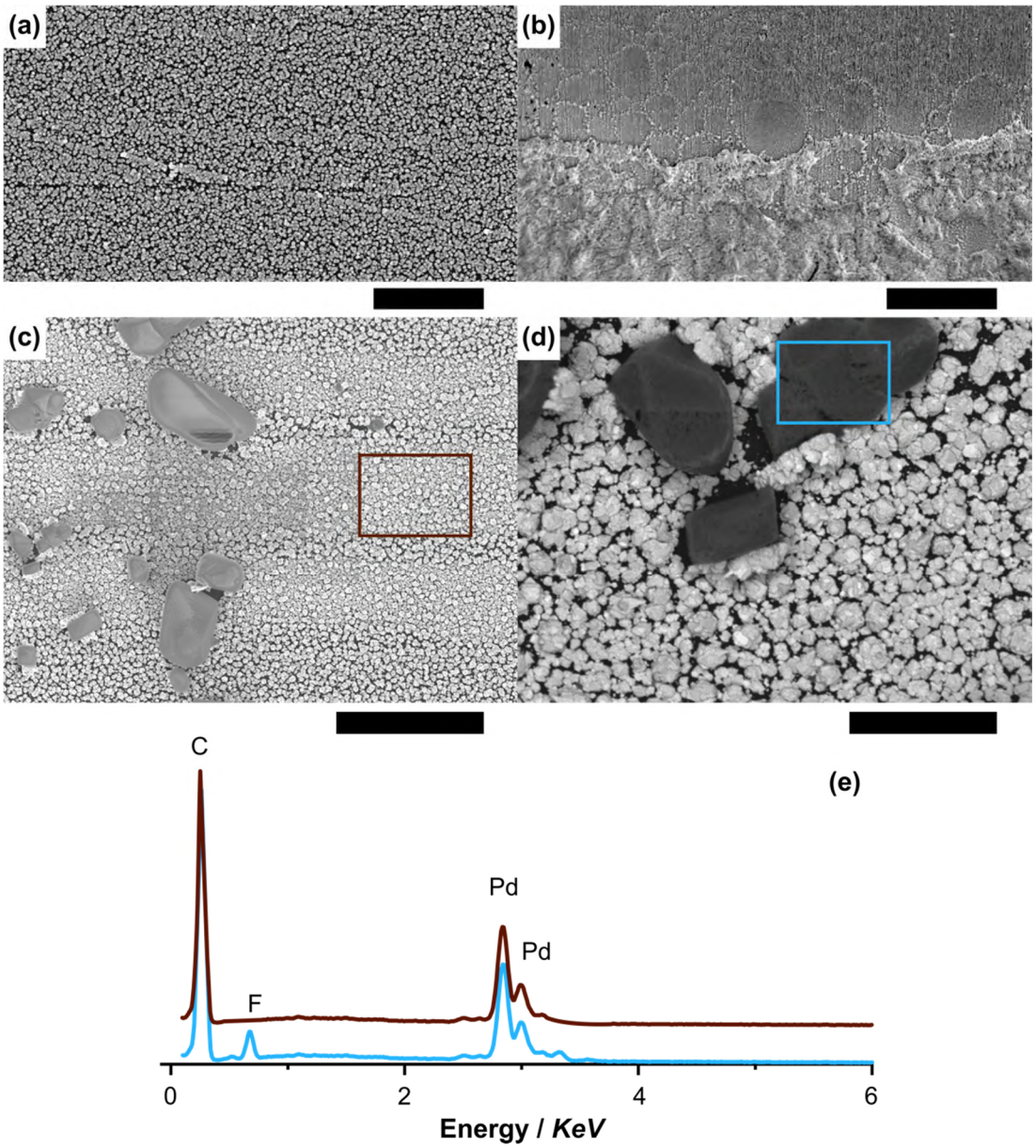

Figure 5.19: FE-SEM images of a BDD electrode after electrodeposition of Pd (a) from a MeCN-rich phase, scale bar = 2 µm. (b) from water-rich phase, scale bar = 100 µm. (c and d) A high magnification of the Pd structure deposited exactly at the MeCN-water interface, scale bars = 4 µm and 400 nm, respectively, and (e) the corresponding XEDS spectra of the Pd and $Pd(BF_4)_2$ structure.

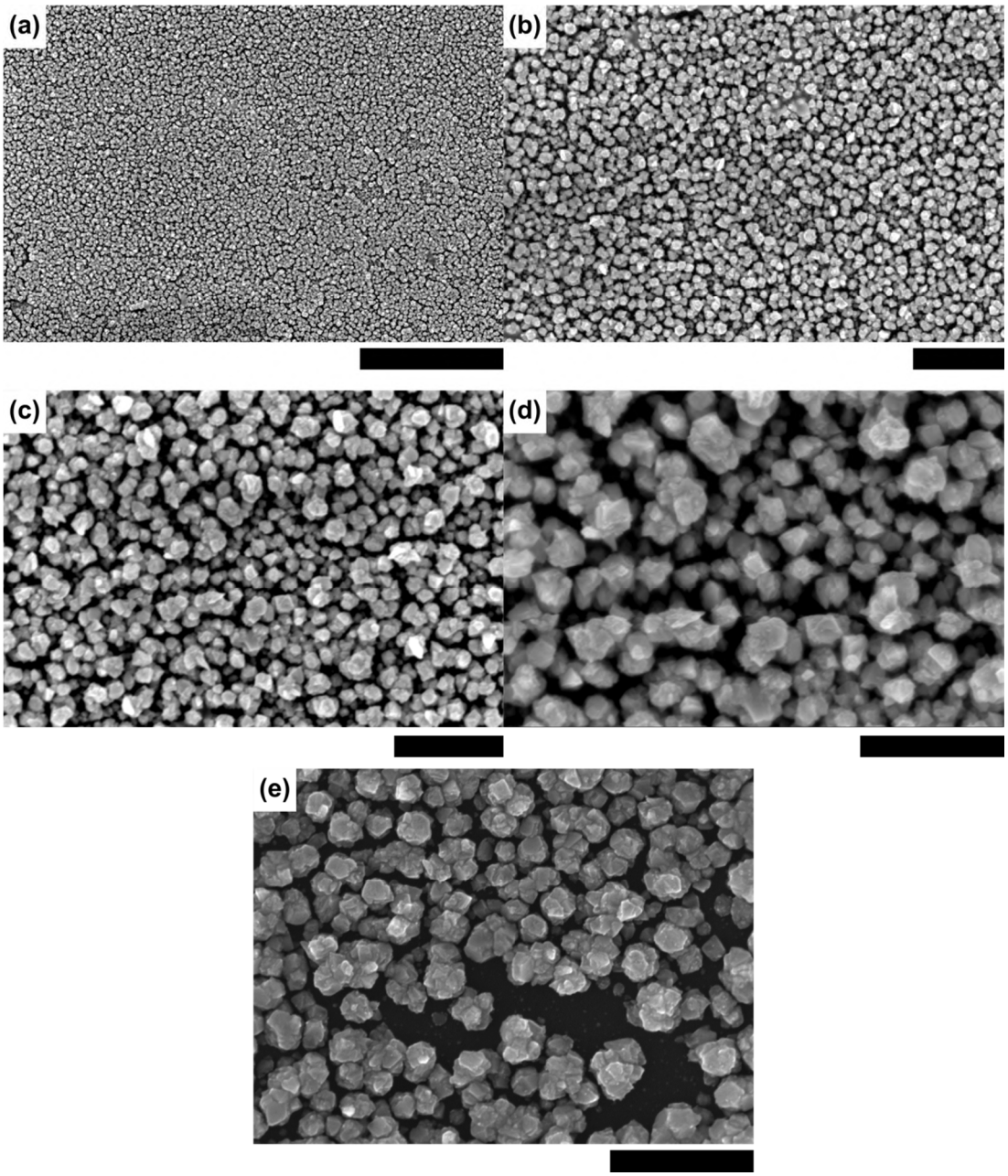

Figure 5.20: FE-SEM images representing the morphology of the electrodeposited Pd from its MeCN-rich phase. (a) scale bar = 4 μm, (b) scale bar = 1 μm (c) scale bar = 600 nm (d) scale bar = 400 nm, (e) scale bar = 400 nm.

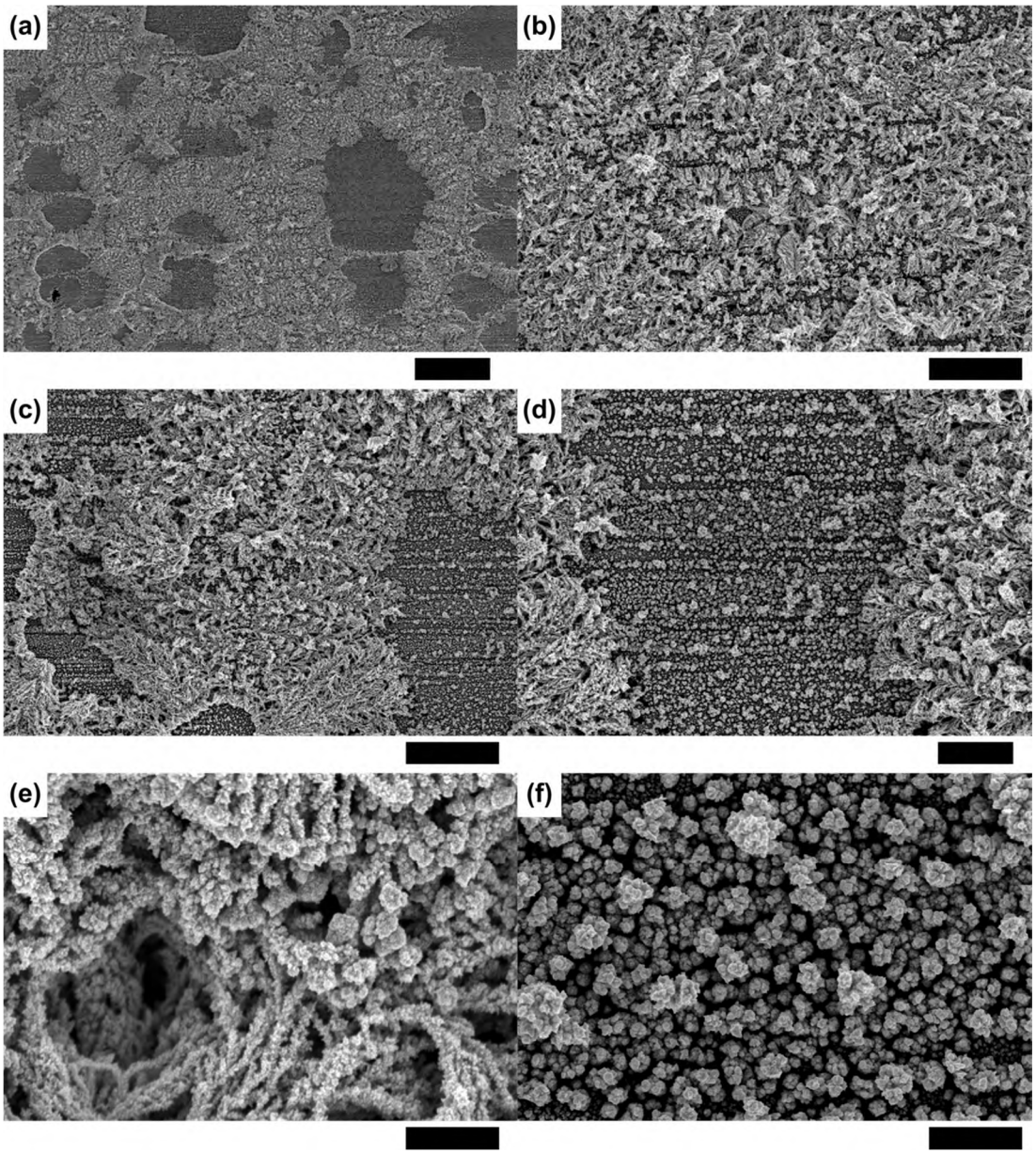

Figure 5.21: FE-SEM images representing the morphology of the electrodeposited Pd from its water-rich phase. (a) 40 µm, (b) 10 µm, (c) 10 µm, (d) 4 µm, (e) 500 nm(f) 500 nm.

5.4.4 Spectroscopic behaviour of Pd-acetate in different composition mixed MeCN-water solvents

Mixtures of Pd^{2+} ions and acetate groups (CH_3COO^-) exhibit heteroselective solvation in MeCN-water system (*i.e.* Pd ions prefer to dissolve in MeCN, while the acetate groups will dissolve easily in water). This is because MeCN molecules are known as weak acid, hence MeCN molecules are weak H-bond donors and solvate only very weakly to small anions (CH_3COO^-, F^-, etc), thus small anions are very reactive in such

solvents. In contrast, a solvent with strong acidity (water) easily solvates to small anions by H-bond formation and weakens their reactivity. Thus, the transition from a cyclic trimer to open linear or dimer or singular Pd-acetate can be promoted by the addition of water as shown in Figures 5.14 and 5.15.

The FE-SEM data and elemental analysis show the feasibility to electrodeposit Pd from its acetate salt in MeCN, but **only** in the presence of water. However, the observations of structural changes elucidated from UV-Vis, IR and NMR, and specifically Pd coordination to H_2O or OH in water requires further investigation. To this end, the electrochemical and spectroscopic behaviour of Pd-acetate from MeCN solutions, which contain different mole fractions of water (χwater), by varying MeCN:water v/v ratio, over the range χwater = 0 – 1, are further explored.

The UV-Vis spectra of Pd-acetate in various MeCN:water mixtures are shown in Figure 5.22. In MeCN only, and in low content water, χwater = 0.132 (95%:5%, v/v), one absorption peak appears around 400 nm, Figure 5.22(a). Increasing water mole fraction, χwater ≥ 0.243, shows the emergence of a second band at 320 nm, Figure 5.22(a-d), which is present at all higher χwater values. Note that Pd-acetate partially dissolves in water, χwater ≥ 0.997, due to its high stability constant $log\beta$ = 9.30 ± 0.3.[576]

The λ_{max} ~ 400 nm band is present in all spectra regardless of water content and results from d-d transitions on the metal centre. When χwater equals and exceeds 0.243, a new absorption band emerges ~ 320 nm, which is likely due to LMCT that represent ligand exchange has occurred, Equation 5.5

$$Pd_3^{2+}(OAc)_6 + H_2O \rightarrow Pd_3^{2+}(OAc)_5(H_2O) \quad \text{Equation 5.5}$$

Interaction of ligands with Pd (d-orbitals) creates a splitting due to the electrostatic environment. Both the nature of the ligand and the oxidation state determine the splitting value. The spectrochemical series shows that water molecules will induce larger splitting and hence association of Pd to water will lead to a shift of the UV-Vis absorption band to a lower wavelength (higher energy), as shown in Figure 5.22. Additionally, by adding water, linear trimeric and dimers start to form as shown from the biphasic system studies described in section 5.6.3, in addition to ligand exchange where acetate groups in the inner shell of Pd ions are replaced with either MeCN or

water. Square planar Pd complexes result, which induce greater crystal field splitting and consequently a shift of the absorption band to a lower λ.

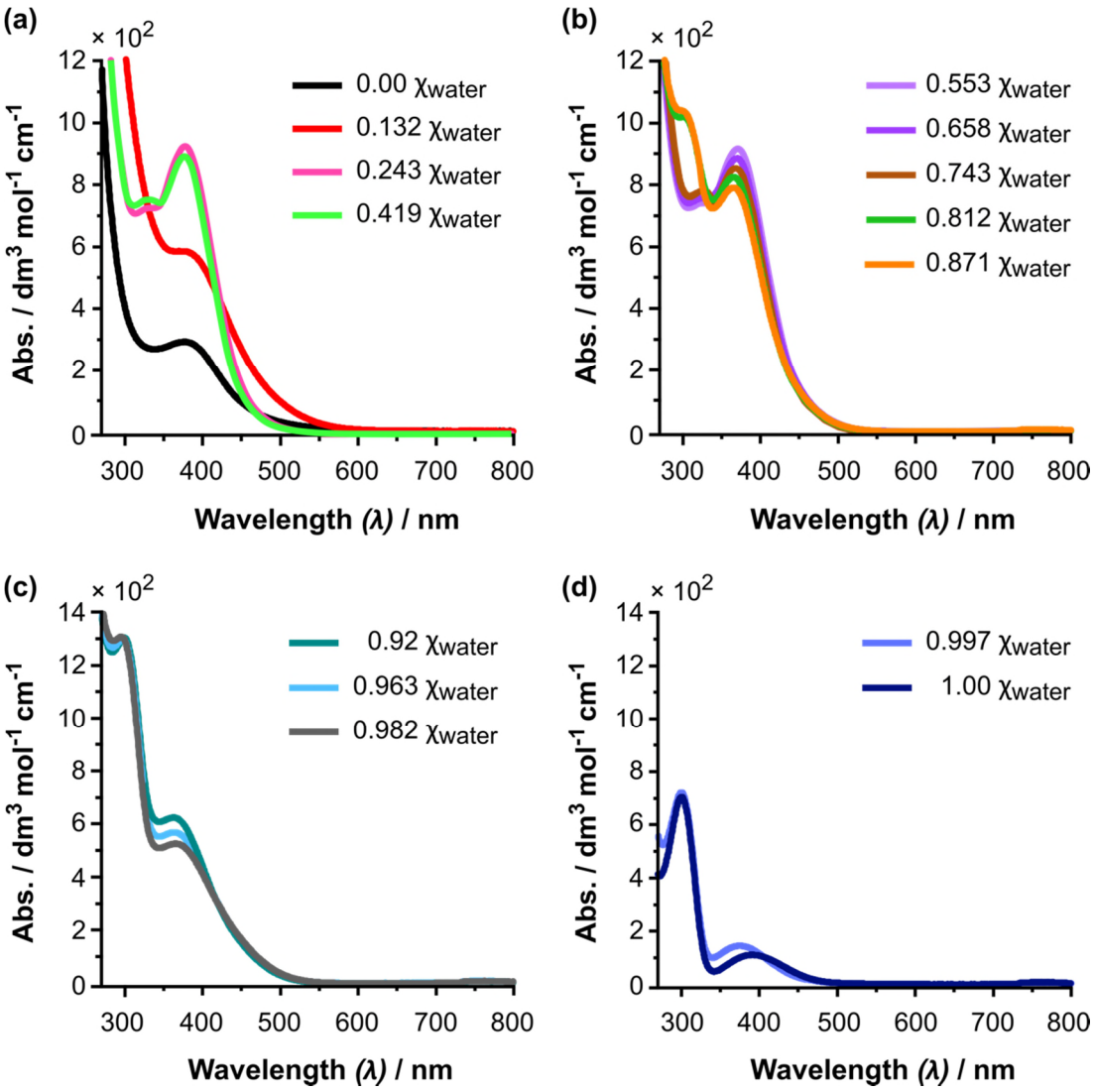

Figure 5.22: UV-Vis absorbance spectrum of 1×10^{-3} M Pd-acetate in different solution composition, MeCN only, water only and MeCN: water mixed solvent taken in absence of air. (a) Low mole fraction of water. (b) medium mole fraction of water. (c and d) High mole fraction of water.

Changes of the absorbance may indicate the degree of the charge transfer between the ligands and the metal centre, with changing water moles fraction, where d-d transitions as well are known to have less absorbance values.[380] These effects are shown for λ_{max} ~ 400 nm and λ_{max} ~ 320 nm in Figure 5.23.

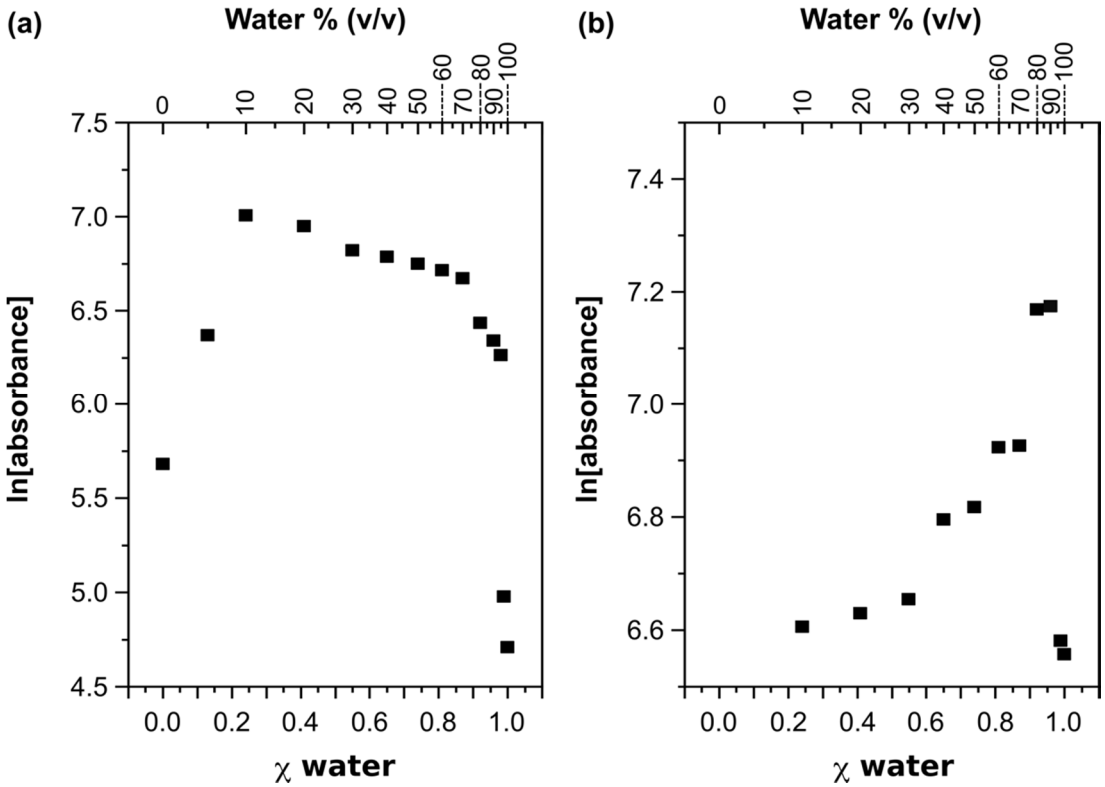

Figure 5.23: The influence of water addition on Pd-acetate structural changes in MeCN:water mixed solvent systems. (a) ln[absorbance] *vs.* χwater for absorbance peak at λ_{max} ~ 400 nm and (b) ln[absorbance] *vs.* χwater for absorbance peak at λ_{max} ~ 320 nm.

Absorbance due to d-d transition decreases with increasing χwater, while the absorbance of the low λ UV absorption peak increases except when χwater > 0.997. These observations indicate that the Pd-acetate undergoes ligand exchange by replacing the acetate group with water or MeCN molecules. Certainly, the absorbance will drop in high mole fraction water, because of the low solubility of Pd-acetate.[570]

Though Pd-acetate hydrolysis is facile, an equilibrium still exists. To examine ligand exchange and replacement of the acetate groups with anions such as BF_4^- or MeCN and water molecules, the change of ^1H NMR spectra of Pd-acetate as function of χwater are shown in Figures 5.24, 5.25 and 5.26 for solutions containing χwater = 0.243 (Figure 5.24(a)), 0.553 (Figure 5.24(b)), 0.743 (Figure 5.25), 0.871 (Figure 5.26(a)), 0.963 (Figure 5.26(b)).

Figure 5.24(a) shows two singlet peaks at 1.991 ppm and 2.256 ppm, which matches the peaks observed for $Pd(CH_3CN)_4(BF_4)_2$ in MeCN only, in Figure 5.17(a). Thus, adding water induces ligand relaxation and exchange and Pd ions start to coordinate

with MeCN molecules and BF_4^- anions. Note, not all the Pd-acetate molecules undergo complete dissociation due to the presence of a peak at 2.256 ppm, which corresponds to the acetate group attached to Pd.

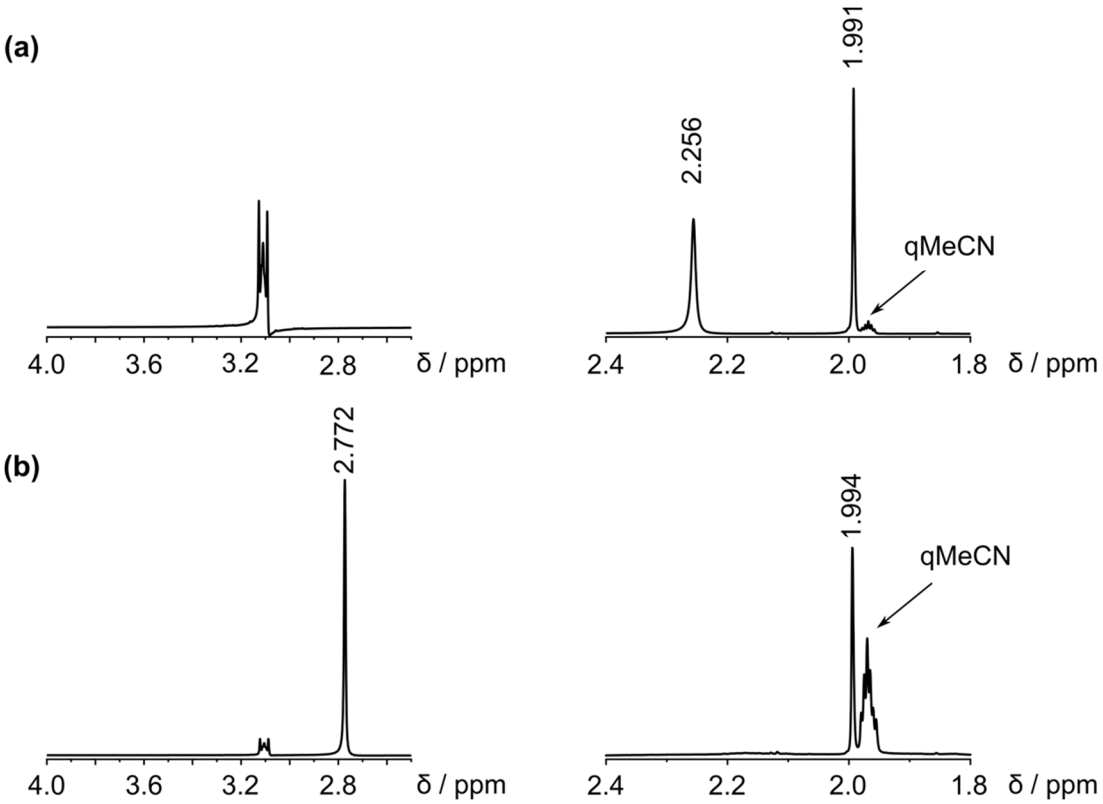

Figure 5.24: ^{1}H NMR of 1×10^{-3} M Pd-acetate after dissolving in solution made of (a) χMeCN = 0.757 and χwater = 0.243 (90%: 10% MeCN: water, v/v) (b) χMeCN = 0.447 and χwater = 0.553 (70%: 30% MeCN: water, v/v).

By increasing χwater = 0.553 (MeCN:water 70%:30%, v/v), the ^{1}H NMR peak assigned to the acetate groups coordinated to Pd (at 2.256 ppm in presence of χwater = 0.243) starts to shift downfield to 2.772 ppm, as water competes with MeCN to occupy the outer shell of Pd ions. When χwater reaches = 0.743 (MeCN:water 50%:50%, v/v), more water molecules replace MeCN in the outer sphere of the Pd ions. Therefore, the ^{1}H NMR peak associated with the acetate group shifts downfield to 3.138 ppm. Hydrolysis of BF_4^- occurs leading to Pd ions being coordinated to MeCN shifting its ^{1}H NMR peak upfield to 1.907 ppm.

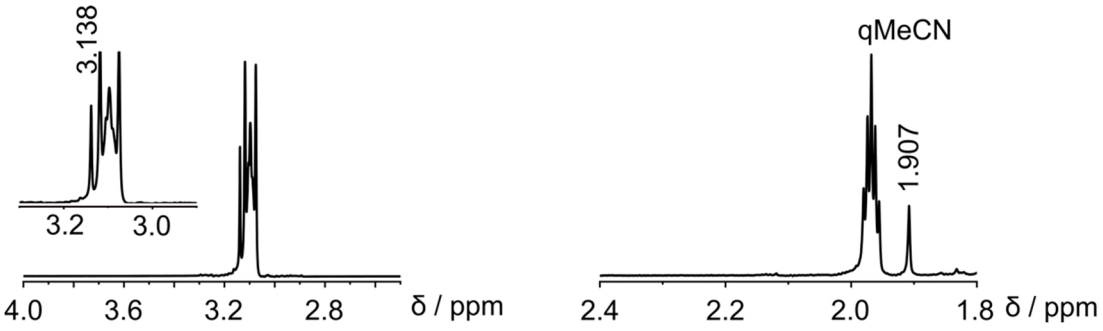

Figure 5.25: ^{1}H NMR of 1×10^{-3} M Pd-acetate after dissolving in solution made of χMeCN = 0.257 and χwater = 0.743 (50%:50% MeCN: water, v/v).

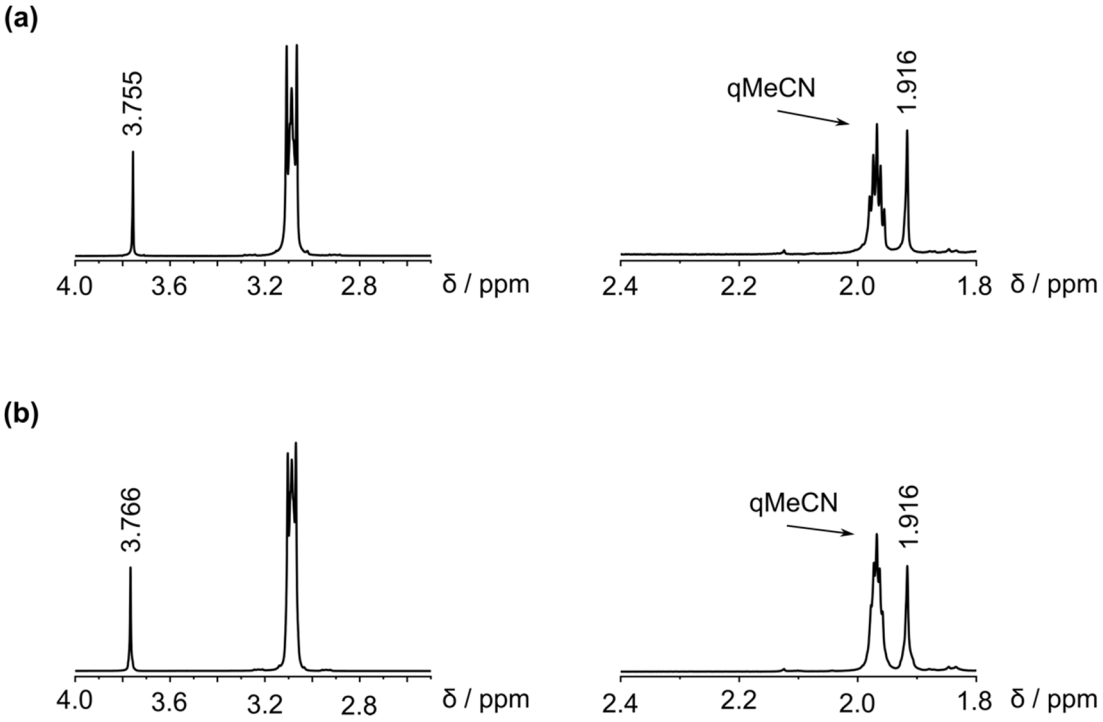

Figure 5.26: ^{1}H NMR of 1×10^{-3} M Pd-acetate after dissolving in solution made of (a) χMeCN = 0.132 and χwater = 0.868 (30%: 70% MeCN: water, v/v) (b) χMeCN = 0.037 and χwater = 0.963 (10% : 90% MeCN:water, v/v).

Similar ^{1}H NMR spectra were observed for solutions containing χwater = 0.871 and 0.963, respectively. Only ^{1}H NMR peak resulting from the protons in the acetate group shifts downfield to 3.755 ppm (χwater = 0.871) and 3.766 ppm (χwater = 0.963), respectively. ^{1}H NMR assigned to protons of MeCN molecules coordinated to Pd give rise to a chemical shift at 1.916 ppm for both solutions containing χwater = 0.871 and 0.963. Many studies have used IR spectroscopy to investigate MeCN-water interactions as function of increasing the mole fraction of water and vice versa.[365, 577-

[579] The premise of the study herein is to repeat such experiments to monitor IR wavenumber shifts as function of χwater in MeCN-water mixed solvent, which contains 20% D_2O and in presence of Pd-acetate and $TBABF_4$.[365] In Figure 5.27, over the wavenumber range 2320 cm^{-1} to 2220 cm^{-1}, the wavenumber shift of the C≡N stretching mode (at 2251.9 cm^{-1}) is monitored as a function of increasing χwater from 0.00 to 1.00 (this reflects the extent of H-bond formation between MeCN and water molecules). Similarly, we monitor the IR band of CH_3 bending and C-C stretching at 2292.7 cm^{-1}, as a function of χwater which represents the presence/absence of free MeCN molecules.

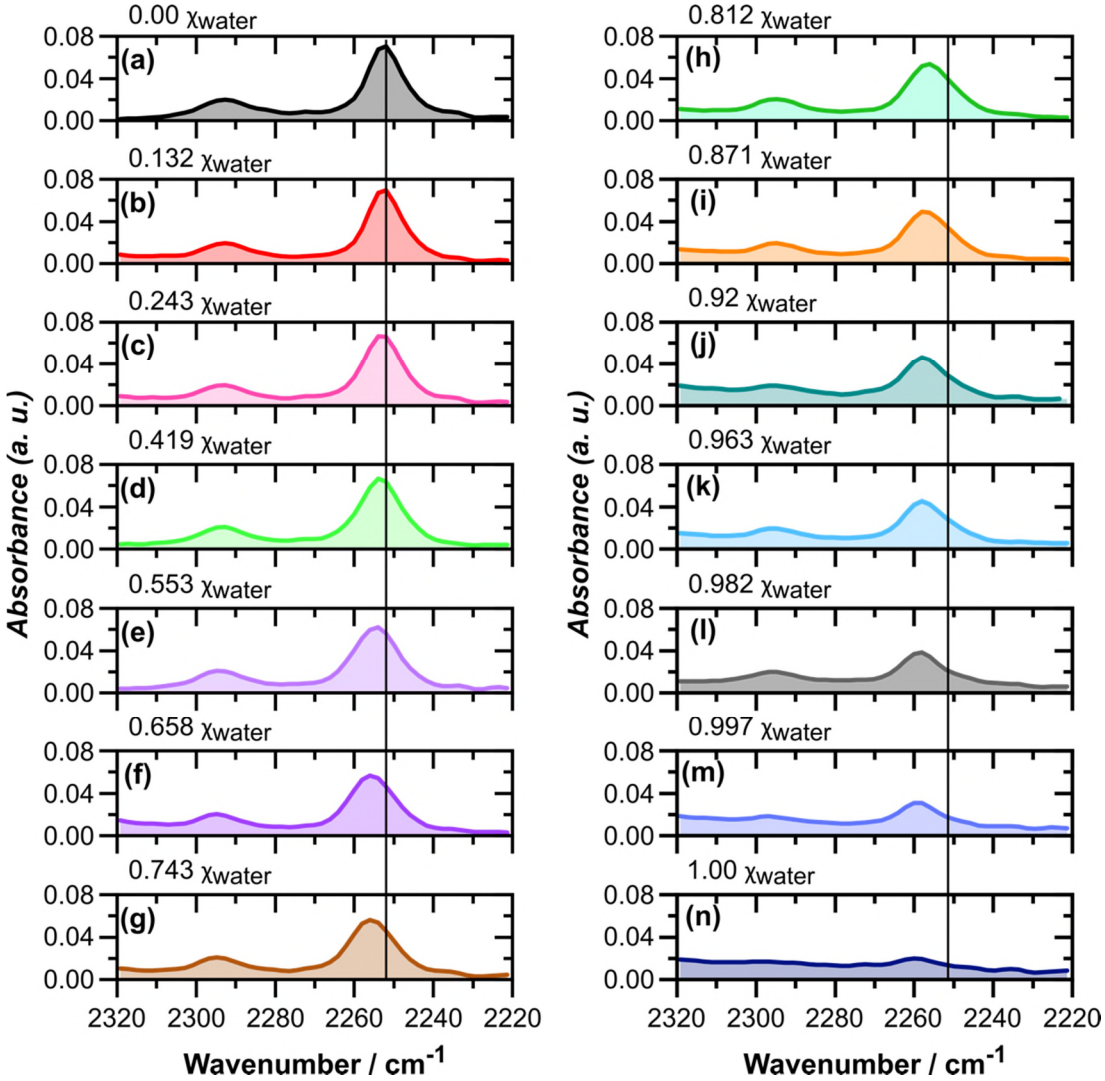

Figure 5.27: Infra-red (IR) absorption spectra from 2320 cm^{-1} to 2220 cm^{-1} of MeCN:water mixtures containing 1×10^{-3} M Pd-acetate + 0.1 M $TBABF_4$ as a function of increasing water mole fraction (χH_2O) from χH_2O = 0.00 to 1.00. The water contains 20 % D_2O.

In Figure 5.28, over the range from 2800 cm^{-1} to 2300 cm^{-1}, the wavenumber shift of the O-D stretching mode of HDO (at 2495 cm^{-1}) as a function of increasing χwater from 0.00 to 1.00, is monitored. This reflects the extent of the formation of H-bonds between water molecules (*i.e.* hydrogen bonded network).

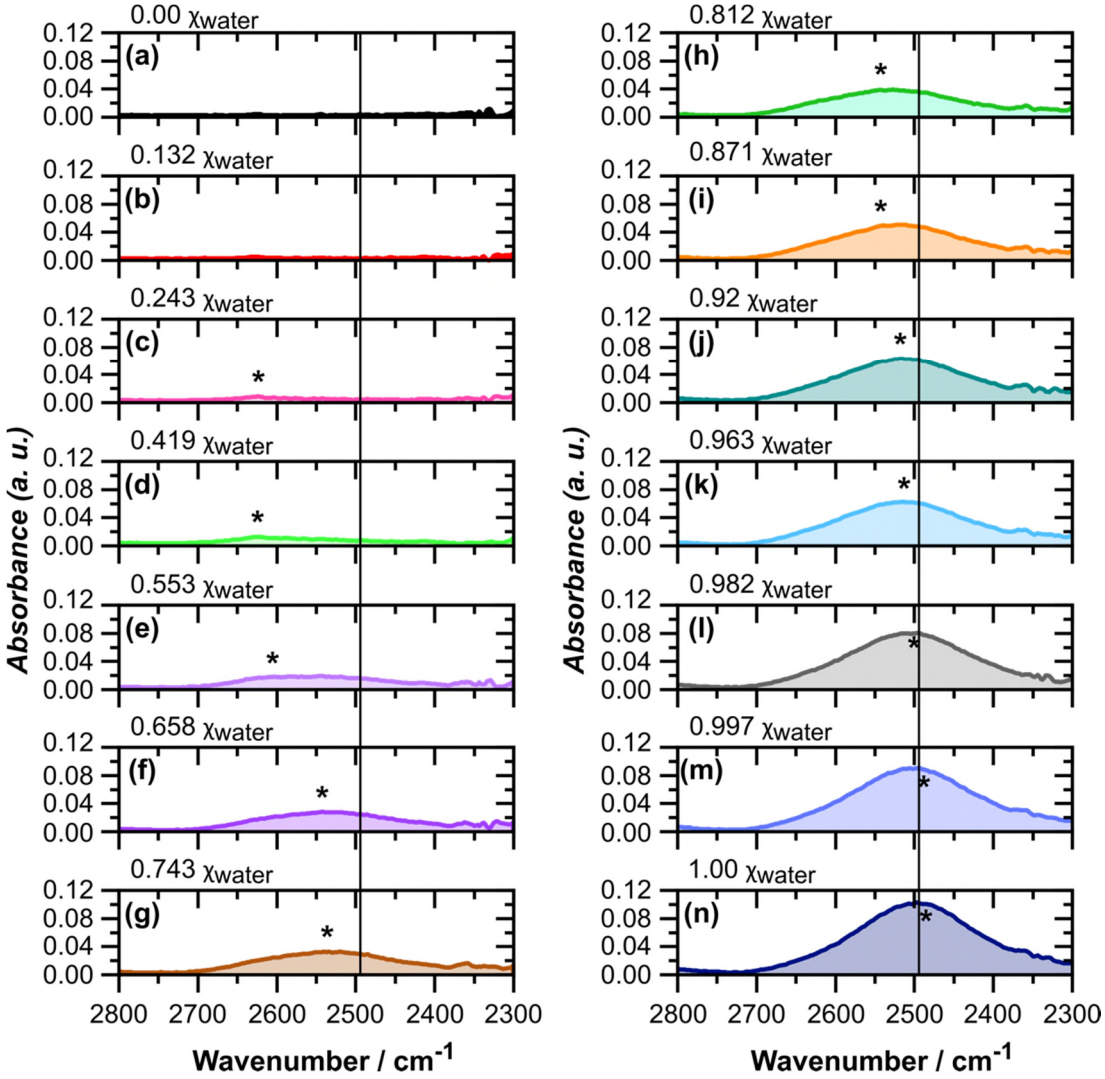

Figure 5.28: Infra-red (IR) absorption spectra from 2800 cm^{-1} to 2300 cm^{-1} of MeCN:water mixtures containing 1×10^{-3} M Pd-acetate + 0.1 M $TBABF_4$ as a function of increasing water mole fraction (H_2O) from $\chi H_2O = 0.00$ to 1.00. The water contains 20 % D_2O.

The wavenumbers of the C≡N and the O-D stretching modes were plotted as a function of χwater in Figures 5.29(a) and (b). By increasing χwater, Figures 5.27 and 5.29(a), the IR band of the C≡N stretching mode starts to shift to a higher wavenumber, which can be attributed to the formation of hydrogen-bonded MeCN molecules. Also, the IR

band associated with free MeCN at 2292.7 cm^{-1} starts to diminish, hence only free MeCN will exist for χwater <0.812.

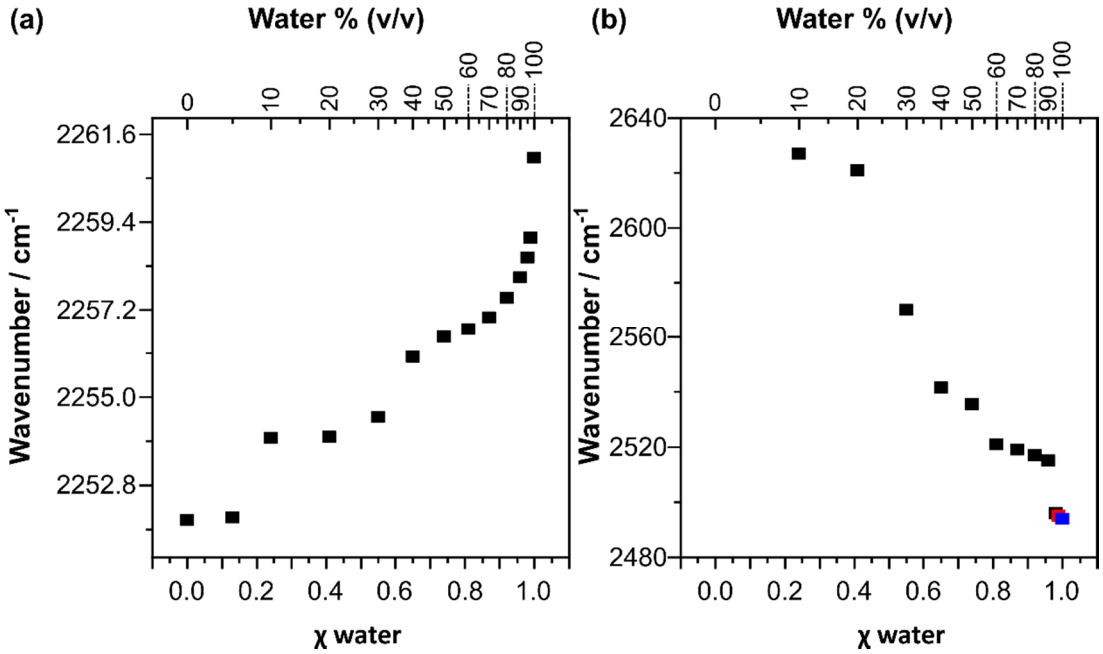

Figure 5.29: Infra-red (IR) wavenumbers for (a) the C≡N stretching mode and (b) the O-D stretching mode as a function of increasing water mole fraction (χH_2O) from χH_2O = 0.00 to 1.0. The water contains 20 % D_2O and the MeCN:water mixtures contain 1 × 10^{-3} M Pd-acetate + 0.1 M $TBABF_4$.

Akin to previous studies,[61, 365, 577] the wavenumber of the O-D stretching mode did not exist for MeCN-water mixtures containing χwater <0.419. With increasing χwater > 0.553, the IR band associated with the O-D stretching mode started to appear, which shifts to a lower value with increasing χwater. This behaviour can be described as follows, first below χwater < 0.658, water molecules do not form a H-bond network. Second, as χwater increases, progressive weakening of the O-D bond occurs due to the formation of a H-bond network, where the strength of the H-bond network increase with increasing χwater.[365] IR spectroscopic data was also obtained over the wavenumber range 3790 cm^{-1} to 2775 cm^{-1} (Figure 5.30), 1800 cm^{-1} to 1300 cm^{-1} (Figure 5.31), 1300 cm^{-1} to 700 cm^{-1} (Figure 5.32).

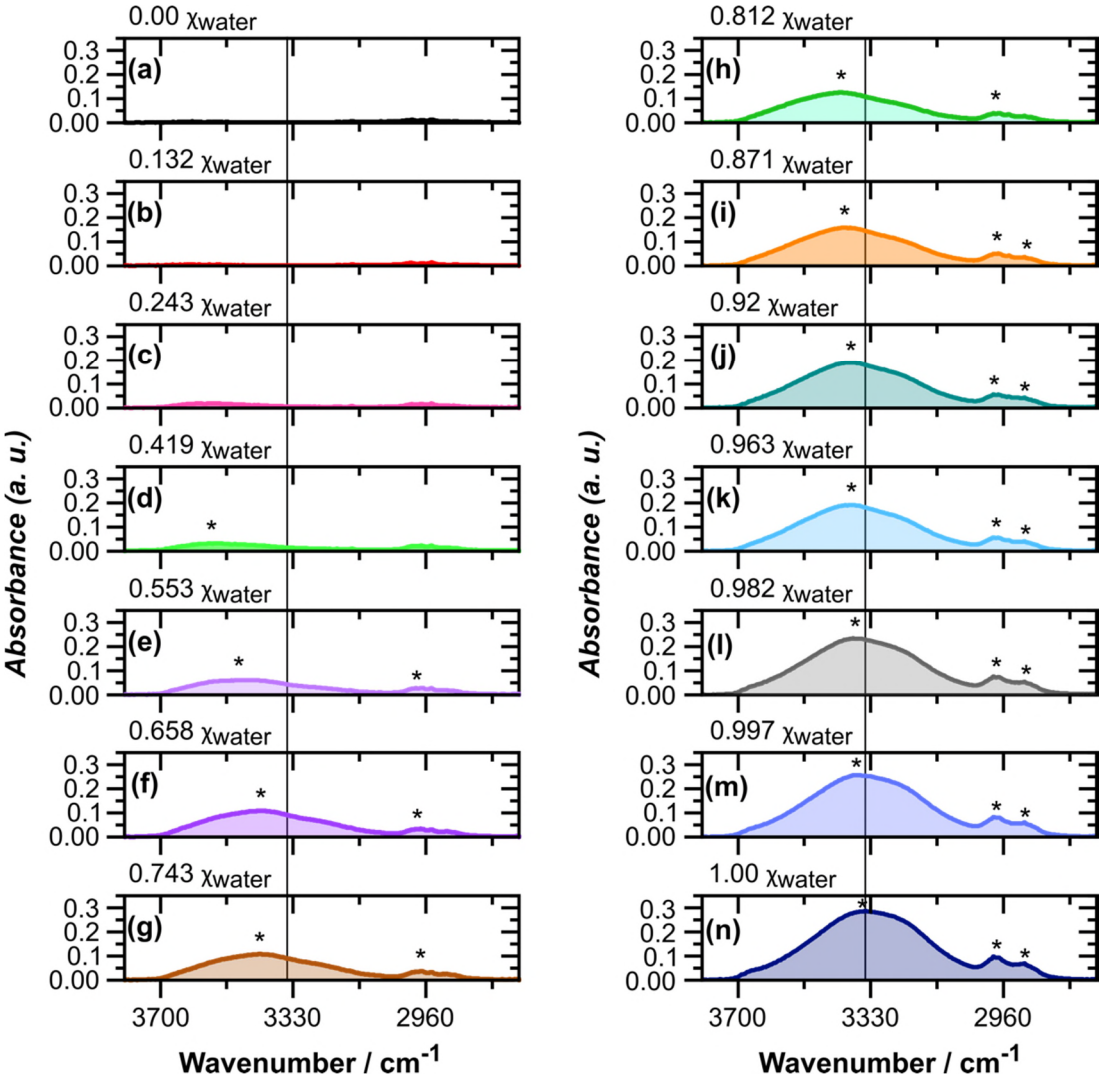

Figure 5.30: Infra-red (IR) absorption spectra from 3790 cm^{-1} to 2775 cm^{-1} of MeCN:water mixtures containing 1×10^{-3} M Pd-acetate + 0.1 M $TBABF_4$ as a function of increasing water mole fraction (χH_2O) from χH_2O = 0.00 to 1.00. The water contains 20 % D_2O.

In Figure 5.30, the emergence of an IR band between 3700 cm^{-1} and 3000 cm^{-1}, when χwater exceeds 0.553, is attributed to the O-H stretching band in water. The weak intensity peaks arise from C-H asymmetric and C-H symmetric mode at 2986 cm^{-1} and 2900 cm^{-1}, respectively, indicating the presence of the acetate group in water.

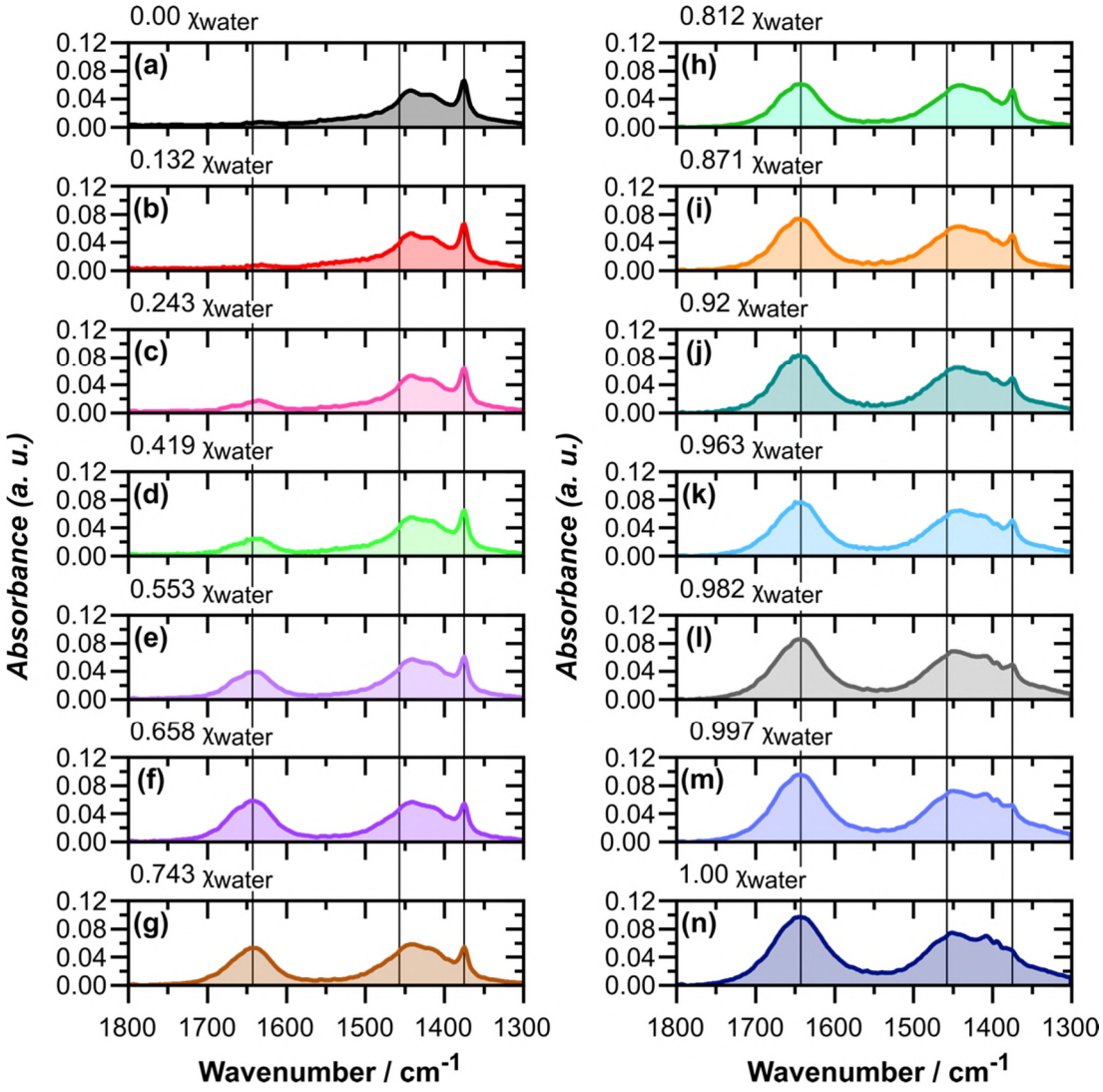

Figure 5.31: Infra-red (IR) absorption spectra from 1800 cm^{-1} to 1300 cm^{-1} of MeCN:water mixtures containing 1×10^{-3} M Pd-acetate + 0.1 M $TBABF_4$ as a function of increasing water mole fraction (χH_2O) from χH_2O = 0.00 to 1.00. The water contains 20 % D_2O.

In Figure 5.31, IR bands associated with different vibrational modes in the acetate group become more dominant. For example, IR band starts to appear around 1650 cm^{-1} attributed to the COO asymmetric mode, which reflects breaking of the Pd-acetate structure and making of H-bonded acetate molecules.

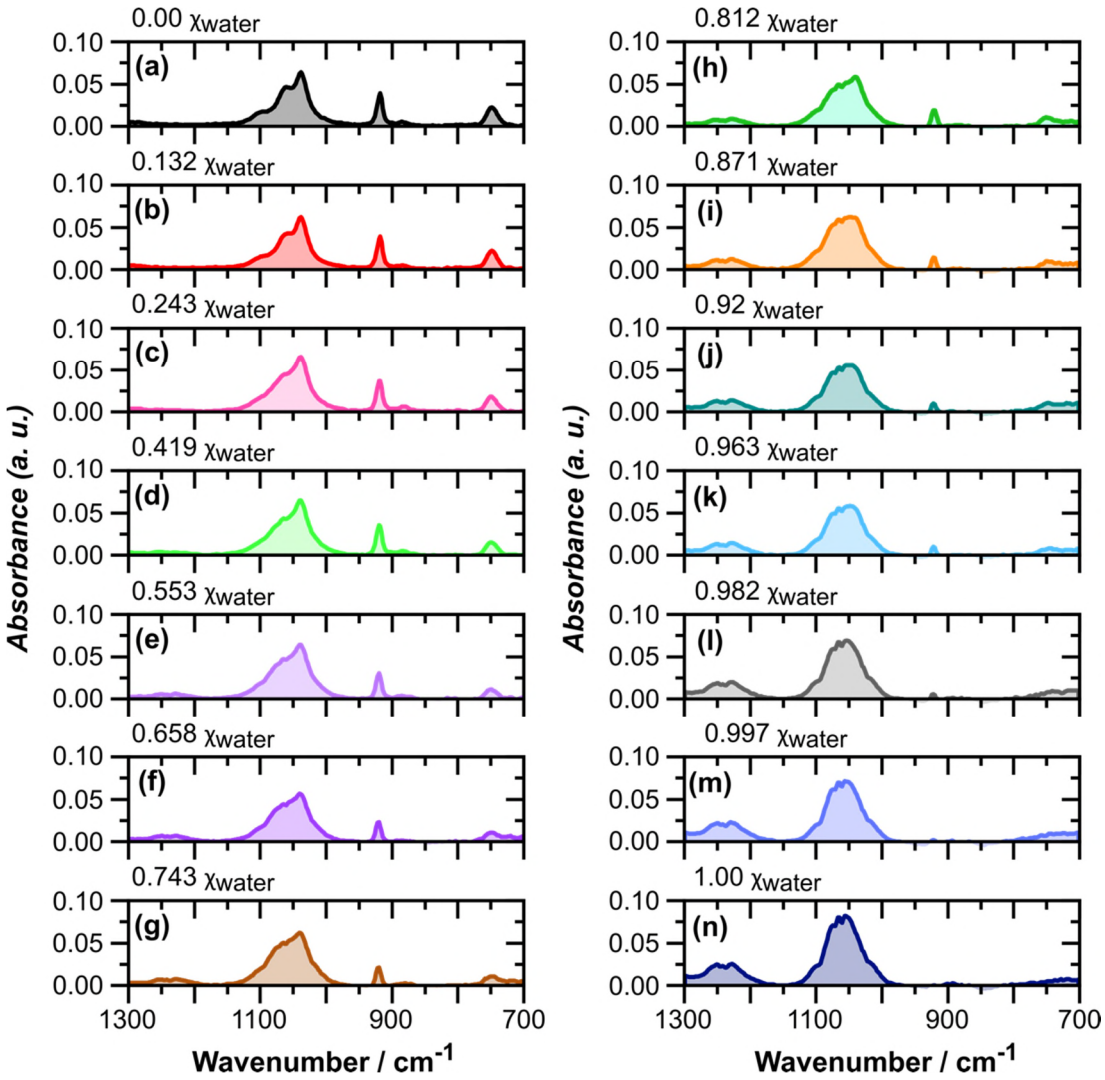

Figure 5.32: Infra-red (IR) absorption spectra from 1300 cm^{-1} to 700 cm^{-1} of MeCN:water mixtures containing 1×10^{-3} M Pd-acetate + 0.1 M $TBABF_4$ as a function of increasing water mole fraction (χH_2O) from χH_2O = 0.00 to 1.00. The water contains 20 % D_2O.

Figure 5.32 exhibits sharp IR bands between 1150 cm^{-1} and 1000 cm^{-1} in MeCN only, attributed to the C-CH_3 bond in Pd-acetate. These sharp peaks start to broaden and coalesce as a function of increasing χwater due to ligand exchange and breaking of the Pd-acetate structure by hydrolysis of the acetate group.

5.4.5 Electrochemical behaviour of Pd-acetate in different composition MeCN-water solvents

IR, NMR, and UV-Vis data demonstrate the following; (i) in MeCN only, Pd-acetate is a complex compound, where the acetate group occupy the inner shell of Pd. Thus, its CV and CA behaviour show no evidence of electrodeposition. (ii) By adding water, the structure of the Pd-acetate changes, where the acetate groups prefer to coordinate to water. Consequently, ligand exchange commences *i.e.* Pd starts to coordinate with either MeCN or water. (iii) When χwater exceeds 0.658, Pd centres are almost solvated by either MeCN or water, and mostly the acetate groups are hydrated. Finally, (iv) for solutions containing χwater below 0.553, MeCN molecules occupy the inner shell of Pd, whereas water molecules replace MeCN ones, above this value.

Since water addition then causes the aforementioned structural changes; various MeCN:water mixtures were examined for electrodeposition. Figure 5.33 shows the first cycle of CVs of Pd-acetate in various solution mixtures made of (a) 95% MeCN and 5% water (v/v, χMeCN = 0.868 and χwater = 0.132), (b) 90% MeCN and 10% water (v/v, χMeCN = 0.757 and χwater = 0.243), (c) 70% MeCN and 30% water (v/v, χMeCN = 0.447 and χwater = 0.553), (d) 50% MeCN and 50% water (v/v, χMeCN = 0.257 and χwater = 0.743), (e) 30% MeCN and 70% water (v/v, χMeCN = 0.129 and χwater = 0.871), and (f) 10% MeCN and 90% water (v/v, χMeCN = 0.037 and χwater = 0.963) at a scan rate 0.1 V/s cycled from +1.5 V to -1.5 V (note that the first cycle only started from +1.0 V, and the dotted line represents the start of the second cycle).

In the cathodic scan, the first cycle of the solution that contains 5% water (Figure 5.33(a)) shows one reduction peak (R1) assigned to Pd^{2+}-acetate reduction (Equation 5.6) and by reversing the scan (anodically) two oxidation peaks (O1 and O2) appear.

$$Pd_3^{2+}(\mu OH)(OAc)_5 + 2e^- \rightleftharpoons Pd_3^0(\mu OH)(OAc)_5 \quad Equation\ 5.6$$

We suggest that O1 corresponds to oxidation of any Pd deposit, as indicated by the presence of the nucleation loop, which refers to the possibility of electrodeposition. O1 is followed by O2, which could be due to the oxidation of the Pd^0-acetate species, where the majority of Pd centres are still associated with acetate groups (see Figures 27-32 and the discussion in section 5.4.4).

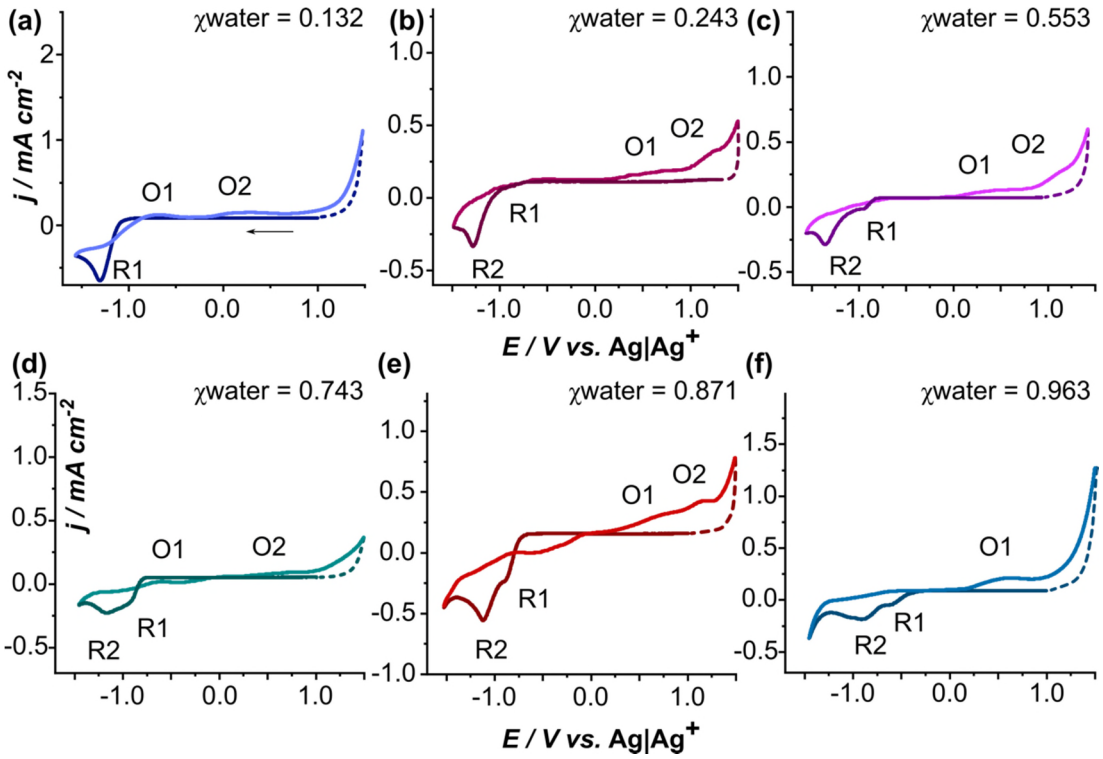

Figure 5.33: First cycle CVs for studying Pd-acetate electrochemical behaviour at ν = 0.1 mV s^{-1}, from solutions containing 1 × 10^{-3} M Pd-acetate in solution made of (a) χMeCN = 0.868 and χwater = 0.132 (95%: 5% MeCN: water, v/v), (b) χMeCN = 0.757 and χwater = 0.243 (90%:10% MeCN: water, v/v), (c) χMeCN = 0.447 and χwater = 0.553 (70%:30% MeCN: water, v/v), (d) χMeCN = 0.257 and χwater = 0.743 (50%:50% MeCN: water, v/v), (e) χMeCN = 0.129 and χwater = 0.871 (30%:70% MeCN: water, v/v), and (f) χMeCN = 0.037 and χwater = 0.963 (10%:90% MeCN: water, v/v).

Further addition of water (Figure 5.33(b to f)) results in the appearance of two reduction peaks (R1 and R2), which are assigned to Pd^{2+} reduction from its species that are solvated by MeCN and water, Equation 5.7 (see the ^{1}H NMR spectra in Figures 5.24, 5.25 and 5.26 and note that solution made of χwater = 0.132 exhibits similar ^{1}H NMR spectrum to χwater = 0.243 but it is not presented here) and Pd^{2+}-acetate reduction, respectively (Equation 5.6). As water mole fraction increases both R1 and R2 shift to more positive potential values and this shift is more significant when χwater = 0.963.

$$Pd_3^{2+}(MeCN)_x(H_2O)_y + 2e^- \rightarrow Pd^0 \quad Equation\ 5.7$$

Reversing the scan anodically, Figures 5.33(b to f), results in the appearance of two oxidation peaks (O1 and O2), which may correspond to the oxidation of the Pd deposit layer and the oxidation of the Pd^0-acetate species. The three consecutive cycles, after those shown in Figure 5.33, are given in Figures 5.34 and 5.35, where further cycling exhibits slight changes in the cathodic and anodic scans. For all solutions containing different χwater values, two reduction peaks exist starting from the second cycle. For the anodic scan, three oxidation peaks were observed for the solution made of χwater = 0.132, while all oxidation peaks of solutions containing χwater = 0.243, 0.553, 0.743, and 0.871 observed in the first cycle (Figure 5.33) merged into one broad oxidation peak (O3), which may indicate complicated processes of surface oxidation of the Pd deposit accompanied with Pd^0-acetate species oxidation. On the other hand, the solution, which contains χwater = 0.963 showed only one oxidation peak for the three consecutive cycles.

In the second cycle (χwater = 0.132) a new reduction peak (R2), Figure 5.34(ai), resulting from the reduction of Pd^{2+} ions on the recently formed Pd^0 phase is seen (Pd-acetate species have been hydrolysed to yield Pd^{2+} cations, which are solvated by the solvent molecules), followed by Pd^{2+} reduction on the BDD surface (R1), Equation 5.7. Anodically, three oxidation peaks arise, which can be attributed to first oxidation of the newly formed metallic Pd (O1) (Equations 5.1 and 5.2), then the oxidation of the Pd^0-acetate species (O2), followed by Pd stripping (O3), Equation 5.8. The third and fourth cycles (Figure 5.34(aii and aiii)) exhibit similar peaks to the second cycle, with the emergence of $H_{ads/des}$ peaks between -1.1 V and -1.3 V.

$$Pd^0 \rightarrow Pd_3^{2+}(MeCN)_x(H_2O)_y + 2e^- \quad Equation\ 5.8$$

For solutions that contain χwater = 0.243, 0.553, 0.743, 0.871 and 0.963, Figures 5.34, and 5.35(bi, ci, di, ei and fi), in the cathodic scan of the second cycle both R1 and R2 shift to a more positive potential, indicative of possible change of BDD surface as Pd^0 has started to form on the substrate, which influence the reduction process. Interestingly, $H_{ads/des}$ peaks were observed in the second cycle of the Pd-acetate CV in solutions containing χwater = 0.871 and 0.963, which may indicate either active Pd surface or dependence on the concentration of water. In the third cycle, both R1 and R2 have now merged into one broad peak (R1/R2), for solutions that contain χwater = 0.243, 0.553, and 0.743 as shown in Figures 5.34 and 5.35(bii, cii and dii). No changes

were observed in the anodic scan. Note that R1/R2 peak shown in Figure 5.34(bii) is present in the fourth cycle as displayed in Figure 5.34(biii) for χwater = 0.243 solution. On contrary, R1/R2 peak shown in Figure 5.34 and 5.35(cii and dii) is resolved into R1 and R2 peaks in Figures 5.34 and 5.35(ciii and diii) for χwater = 0.553, and 0.743 solutions. Also, starting from the third cycle, we notice the emergence of the $H_{ads/des}$ peaks between -1.1 V and -1.3 V, which influence the process of the electrodeposition. This is evident as the nucleation loop starts to disappear from the third cycle.

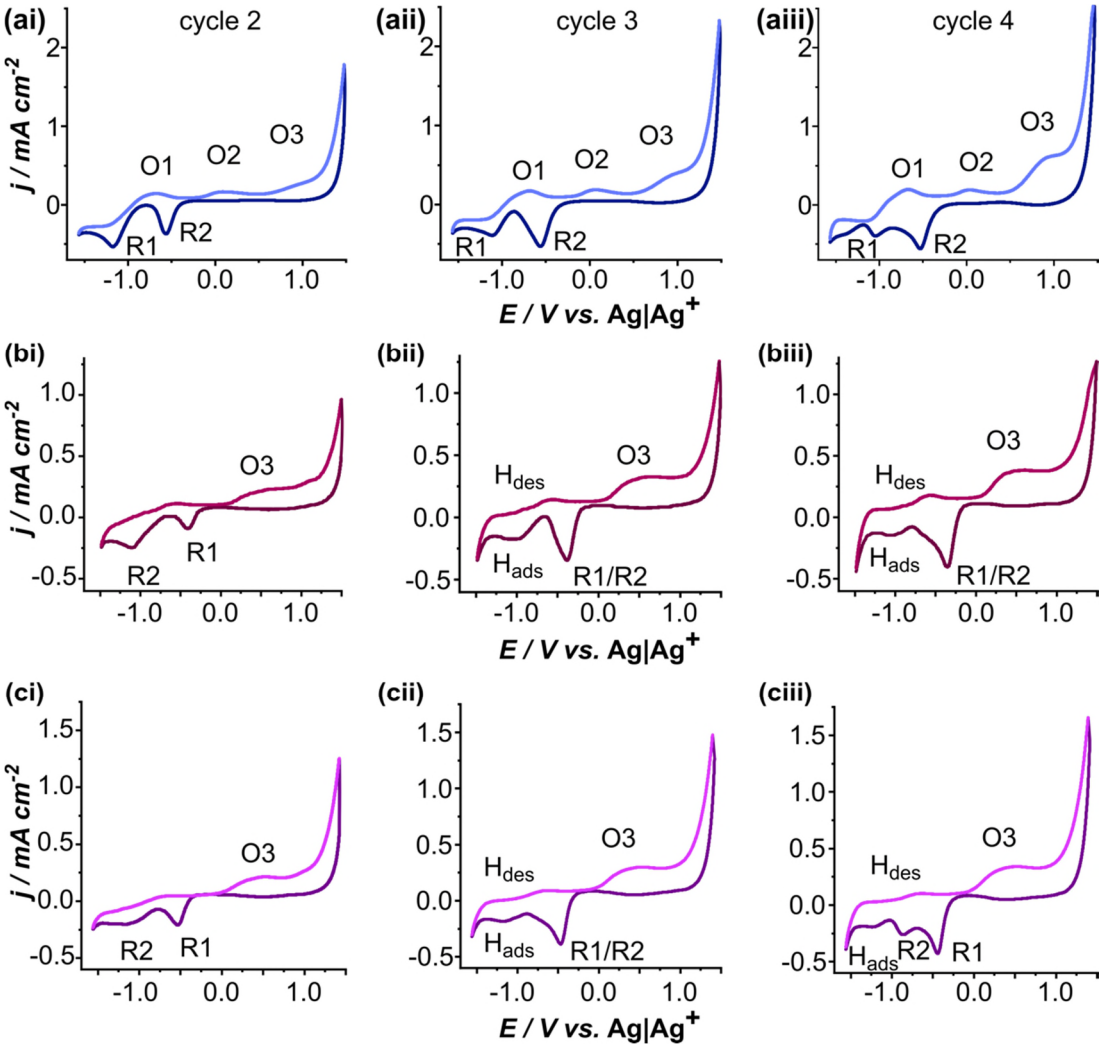

Figure 5.34: CVs for studying Pd-acetate electrochemical behaviour at ν = 0.1 mV s^{-1}, from solutions containing 1 × 10^{-3} M Pd-acetate in solution made of (a) χMeCN = 0.868 and χwater = 0.132 (95%: 5% MeCN: water, v/v), (b) χMeCN = 0.757 and χwater = 0.243 (90%: 10% MeCN: water, v/v), (c) χMeCN = 0.447 and χwater = 0.553 (70%: 30% MeCN: water, v/v), (i) second cycles, (ii) third cycle and (iii) fourth cycle.

Unlike the previous situation, when χwater exceeds 0.871 both R1and R2 exist in the second, the third and fourth cycles as shown in Figure 5.35(ei – fiii), moreover $H_{ads/des}$ peaks are apparent. From the IR knowledge (see Figures 5.27 to 5.32), Pd^{2+} ions is surrounded by water in the inner shell when χwater exceeds 0.871 (*Chapter 1*, Section 1.3.2 and Figure 1.7). Consequently, Pd^{2+} ions reduction can be more facile than the case for χwater < 0.743 where a strong competition with strong ligands such as the acetate groups, BF_4^- and MeCN may influence the stability of the Pd complexes and hence further η is required to force the reduction and the deposition. Also, IR data (Figure 5.30) shows the existence of free water molecules, and hence more labile H, which can catalyse $H_{ads/des}$ at earlier stages.

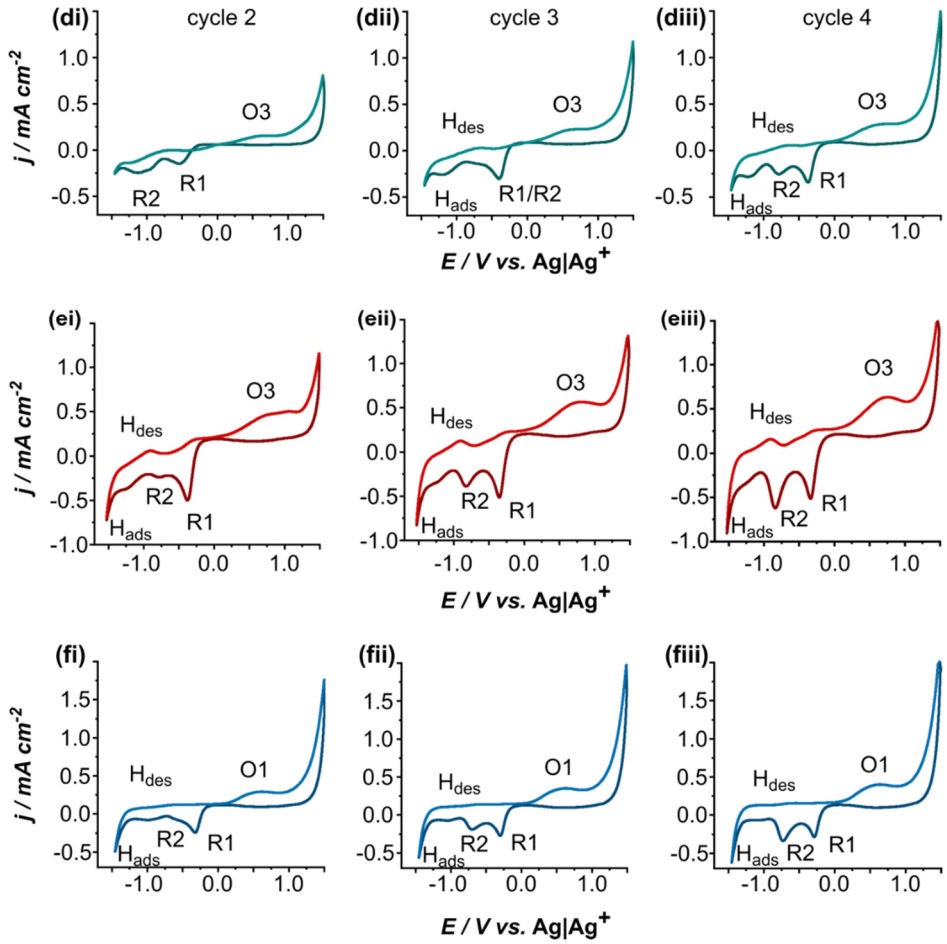

Figure 5.35: CVs for studying Pd-acetate electrochemical behaviour at ν = 0.1 mV s^{-1}, from solutions containing 1 × 10^{-3} M Pd-acetate in solution made of (d) χMeCN = 0.257 and χwater = 0.743 (50%: 50% MeCN: water, v/v), (e) χMeCN = 0.129 and χwater = 0.871 (30%: 70% MeCN: water, v/v), and (f) χMeCN = 0.037 and χwater = 0.963 (10%:90% MeCN: water, v/v), (i) second cycles, (ii) third cycle and (iii) fourth cycle.

5.4.6 Ion-solvent and solvent-solvent interaction discussion

The aforementioned discussion shows that the behaviour of the electrolyte as seen from the electrochemical and spectroscopic data rely very much on ion-ion and ion-solvent interactions. There is a competition between the solvent molecules either water or MeCN and BF_4^- ions to bind to Pd^{2+} ions. Additionally, there is a competition between water and MeCN molecules themselves either to coordinate with each other or with the Pd centres.[578, 579] Since MeCN and water possess different properties, for example water is protic *vs.* MeCN, which is aprotic and each has a different donor number (DN). Consequently, it is possible to study the interaction of ions with the component of a mixed solvent system and infer contribution to cations and anions solvation from the free energy of transfer between the two dissimilar solvents.[561]

In general, the free energy of transfer *i.e.* the difference between the free energies of solvation of an ion in two different solvents or solvent mixtures, and the solvation numbers of ions, are used to describe ion-solvent interactions. Their interactions can be studied using electrochemical techniques such as CV and chronoamperometry.[580] The free energy of transfer of Pd ions ($\Delta G_t(Pd^{2+})$) in binary solvent mixtures of MeCN-water, decreases when water is added to the aprotic solvent (MeCN), as shown in Figure 5.36.

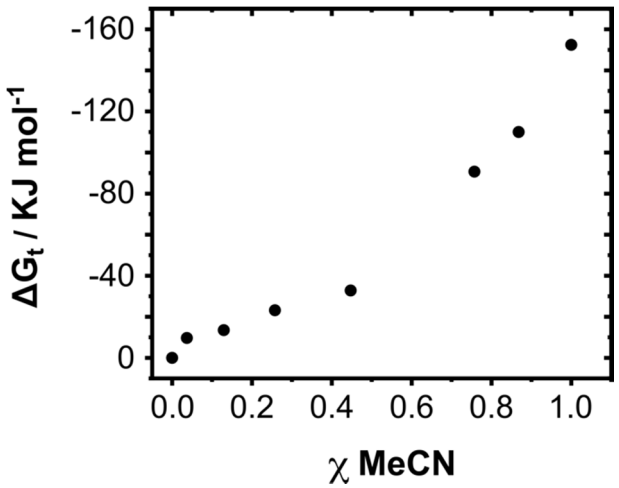

Figure 5.36: Free energy of transfer of Pd^{2+} in mixed solvent (MeCN: water) at 25 °C.

This behaviour reflects the preferential solvation of Pd^{2+} with MeCN molecules. On the other hand, IR spectroscopic data show that water addition causes strong interaction of MeCN with water, as seen in Figures 5.27-5.32.

Pd ions are indeed expected to be solvated primarily with MeCN when acetate groups undergo hydrolysis process. However, due to the strong interaction of MeCN molecules with water molecules, water molecules can replace MeCN molecules from the inner shell of Pd ions, because MeCN molecules will be coordinated with water molecules. Thus, strong solvent-solvent interactions overcome ion-solvent interactions and hence water can solvate Pd ions, specifically when χwater exceed 0.658.

5.4.7 Chronoamperometric and microscopy studies of electrodeposition

Electrodeposition of Pd was further explored by applying a driving potential that corresponds to η = -1 V for t_{dep} = 3600 s using 1 cm × 1 cm stationary BDD electrode (note a large electrode was used to get an initial idea about the effectiveness of Pd recovery with varying χwater). The chronoamperometric profile of Pd electrodeposition and the corresponding XEDS spectra for solutions, which are made of χwater = 0.132, 0.243, 0.553, 0.743, 0.871, and 0.963 are shown in Figure 5.37.

The *i-t* curve of Pd electrodeposition can be described as follow, for all χwater, first the current drops due to electrode charging, followed by a current serge due to Pd^{2+} reduction to Pd^0, however reduction of other Pd^{2+}-acetate species and free water molecules (see IR, NMR and UV-Vis discussion, sections 5.4.3 – 5.4.5) can't be ignored at this driving potential, Equation 5.9.

$$H_2O + e^- \rightarrow \frac{1}{2} H_2 + OH^- \quad Equation\ 5.9$$

For χwater = 0.132, after 700 s, the current started to decrease reaching an almost constant current at 2900 s, which can result from slow mass transport of Pd^{2+} to the electrode from the bulk and / or almost consumption of any solvated Pd^{2+} cations at the interface. The current maxima then shift to a lower t_{dep} as the water percentage increases (from χwater = 0.132 to χwater = 0.243, and 0.553). However, it appears at longer t_{dep} when χwater = 0.743. As water percentage increases the current maxima shift again to shorter deposition times χwater = 0.871 and 0.963. The current at 3600 s however shows a systematic increase with increasing χwater.

Examining the surface post electrodeposition using XEDS (Figure 5.37 (b)), generally shows that the deposited layer is made of Pd only except for the case when the

deposition was carried from the lowest water percentage (χwater = 0.132), where the spectrum demonstrates the formation of Pd and an oxide layer.

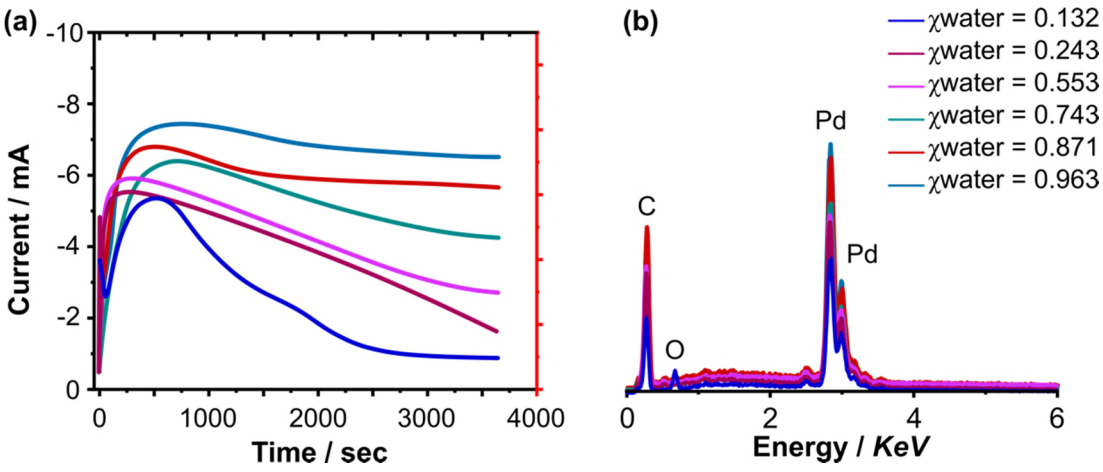

Figure 5.37: Investigation of Pd electrodeposition from 1×10^{-3} M Pd-acetate + 0.1 M $TBABF_4$ in various MeCN:water mixtures. (a) Plot of the current during chronoamperometry study of Pd electrodeposition. (b) XEDS fingerprint of the Pd deposit on BDD.

The electrodeposited material was then visualised using FE-SEM, Figure 5.38. SEM images of Pd deposition from Figure 5.38(ai) show that a solid layer has been formed on top of the electrodeposited Pd layer. In line with the XEDS spectrum, the solid layer can be attributed to the formation of a passivation layer mostly composed of Pd and an oxide layer,[567, 581] which can be described by the following Equation 5.10

$$Pd^{2+} + H_2O + 2e^- \rightarrow PdOH_{(s)} + H^+ \quad Equation\ 5.10$$

Below the electrodeposited passivation layer, Figure 5.38(aii), SEM image shows the formation of metallic Pd phase. Pd deposit appears as a high density of Pd NPs. Thus, water addition has facilitated the electrodeposition of Pd from its Pd-acetate salt in MeCN, nevertheless the passivation layer (it could be PdOH and solvent layer) has been formed, which may halt electrodeposition of metallic Pd or impact negatively the recovery process.

SEM images in Figure 5.38(bi to fii) show that by increasing water percentage, only Pd was deposited and formation of a passivation layer was not observed. Although the reason for its absence is not clear, one can postulate that the environment surrounding the Pd centres (*i.e.* either MeCN or water or BF_4^- that occupy the inner shell of Pd^{2+} ions) may impact the deposition. Also, the structure of the solution can influence the

reduction process of Pd to Pd covered with an oxides containing layer, for example in solutions that contain low percentage of water (*i.e.* χwater < 0.243) formation of timer and dimer Pd-acetate is the most dominant (Figure 5.14).

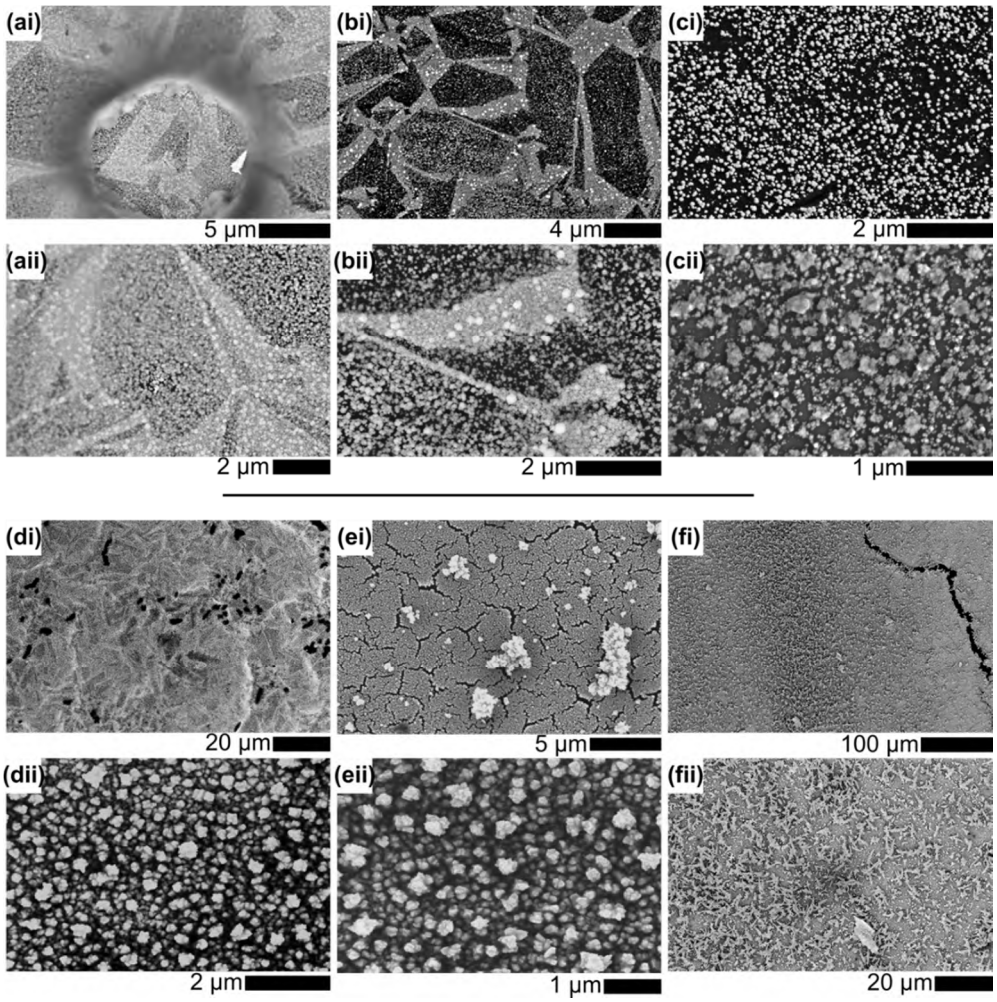

Figure 5.38: Representative FE-SEM images of Pd deposit on BDD from a solution containing 1×10^{-3} M Pd-acetate in solution made of (a) χMeCN = 0.868 and χwater = 0.132 (95%: 5% MeCN: water, v/v), (b) χMeCN = 0.757 and χwater = 0.243 (90%: 10% MeCN: water, v/v), (c) χMeCN = 0.447 and χwater = 0.553 (70%: 30% MeCN: water, v/v), (d) χMeCN = 0.257 and χwater = 0.743 (50%: 50% MeCN: water, v/v), (e) χMeCN = 0.129 and χwater = 0.871 (30%: 70% MeCN: water, v/v), and (f) χMeCN = 0.037 and χwater = 0.963 (10%: 90% MeCN: water, v/v). (i) lower and (ii) higher magnification.

On the other hand, by increasing water percentage, micro-heterogeneities domains start to form. The effect of electrodeposition from various MeCN:water mixtures is apparent, SEM images depict how the Pd morphology changes as function of χwater.

For χwater = 0.243 solution, Figure 5.38(bi and bii), Pd deposit appears as spherical NPs. When χwater reaches 0.553, Figure 5.38(ci and cii), Pd NPs start to coarsen with large variation in sizes. As χwater becomes 0.743 and 0.871, Figure 5.38(di, dii, ei and eii), the substrate is almost covered with a fractal like Pd deposit. When χwater = 0.963, Figure 5.38(fi and fii), a layer of Pd covers the surface and dendritic Pd grows on top of this layer.

5.4.8 Mechanism of electrodeposition by imaging early stage of nucleation and growth and examining the influence of the nature of the solvation shell

The growth morphologies of the Pd electrodeposits shown in Figure 5.38 are of considerable interest in terms of making electrocatalytic structures. Consequently, an understanding of how these structures can form and grow is important. Additionally, the preceding SEM images of the Pd electrodeposition (achieved after a long deposition time, 3600 s), dynamic electrochemistry studies, and spectroscopic data suggest that the environment around the Pd^{2+} ions can govern the structure of the electrodeposited material. Thus, in this section, we explore if solution structure and the nature of the solvation shell of Pd centres may indeed influence any morphology change by examining the nucleation and growth over various short electrodeposition times (50 s, 150 s, and 300s).

To achieve this, the ADF-STEM images of Pd electrodeposited on a BDD TEM plate (*Chapter 4*) shown in Figures 5.39, 5.40 and 5.41 provides high spatial resolution imaging (2 Å limit) and information about electrodeposition of Pd from three different MeCN:water mixtures. Pd structures were electrodeposited from solutions made of (i) 1×10^{-3} M Pd-acetate + 0.1 M $TBABF_4$ in χMeCN = 0.757 + χwater = 0.243 (90%:10% v/v), (solution 1, Table 5.5) (ii) 1×10^{-3} M Pd-acetate + 0.1 M $TBABF_4$ in χMeCN = 0.257 + χwater = 0.743 (50%:50% v/v), (solution 7, Table 5.5) and (iii) 1×10^{-3} M Pd-acetate + 0.02 M $TBABF_4$ + 0.08 KCl in χMeCN = 0.037 + χwater = 0.963 (10%:90% v/v), (solution 11, Table 5.5). These MeCN-water mixtures represent electrodeposition from low, moderate, and high-water content, where the inner shell of Pd ions is different for each case. A series of electrodepositions were recorded employing the same η used in this Chapter (η = -1), for t_{dep} = 50 s, 150 s, and 300 s, respectively.

In Figure 5.39(a-c), after t_{dep} = 50 s, electrodeposition yields Pd nanoclusters and monocrystalline Pd NPs (3-5 nm in diameter); the latter dominating and appearing circular. Nonetheless, a few Pd NPs look as if they have merged together (see the red arrows in Figure 5.40(a and d)). After t_{dep} = 150 s, Figure 5.39(d-f), similar features exist, but the density of Pd NPs has increased and most Pd NPs appear to be free from surface defects such as twin boundaries. They subsequently develop into large Pd nano columns at a longer electrodeposition time, t_{dep} = 300 s, as shown by the SEM images in Figure 5.39(g).

Qualitatively, the growth of the Pd nanostructures is mainly in the vertical direction and few tiny Pd NPs are observed in the background. We postulate from the previous observations that fusion of the Pd NPs centres due to surface diffusion (*i.e.* for example by surface mediated Ostwald ripening)[378] or surface aggregation and coalescence is greatly limited.[278] Most probably, Pd NPs of variable sizes nucleate and grow (progressive model) on the BDD TEM surface first. These then grow via direct attachment with minimal change in their diameter or perimeter, but considerable increase of their height is observed (*i.e.* Volmer-Weber growth).

When the water percentage increases to χwater = 0.743 (solution 7), Figure 5.40(a-c), t_{dep} = 50 s results in the formation of two features, monocrystalline circular Pd NPs (3-4 nm in diameter) and rod-like (or elongated) Pd nanostructures (10-17 nm in perimeter). Both of which can be considered as a thin deposit, evident from the mass thickness contrast (see *Chapter 2*, Section 2.3.1). After t_{dep} = 150 s, Figure 5.40(d-f), the growth of both Pd NPs and rod-like Pd nanostructures is two-dimensional* across the BDD TEM plate surface via coalescence with their nearest neighbour (*i.e.* there is not any obvious change in the image contrast).

---

* Note: the growth of Pd on BDD is a growth of a metal on a foreign substrate (see *chapter 1*), where all nanostructures or NPs are three-dimensional despite that TEM or SEM images are two-dimensional. For the current case, we refer to fusion of two or more neighbours within 1-2 nm distance as 2D growth, but the growing phase is in fact 3D.

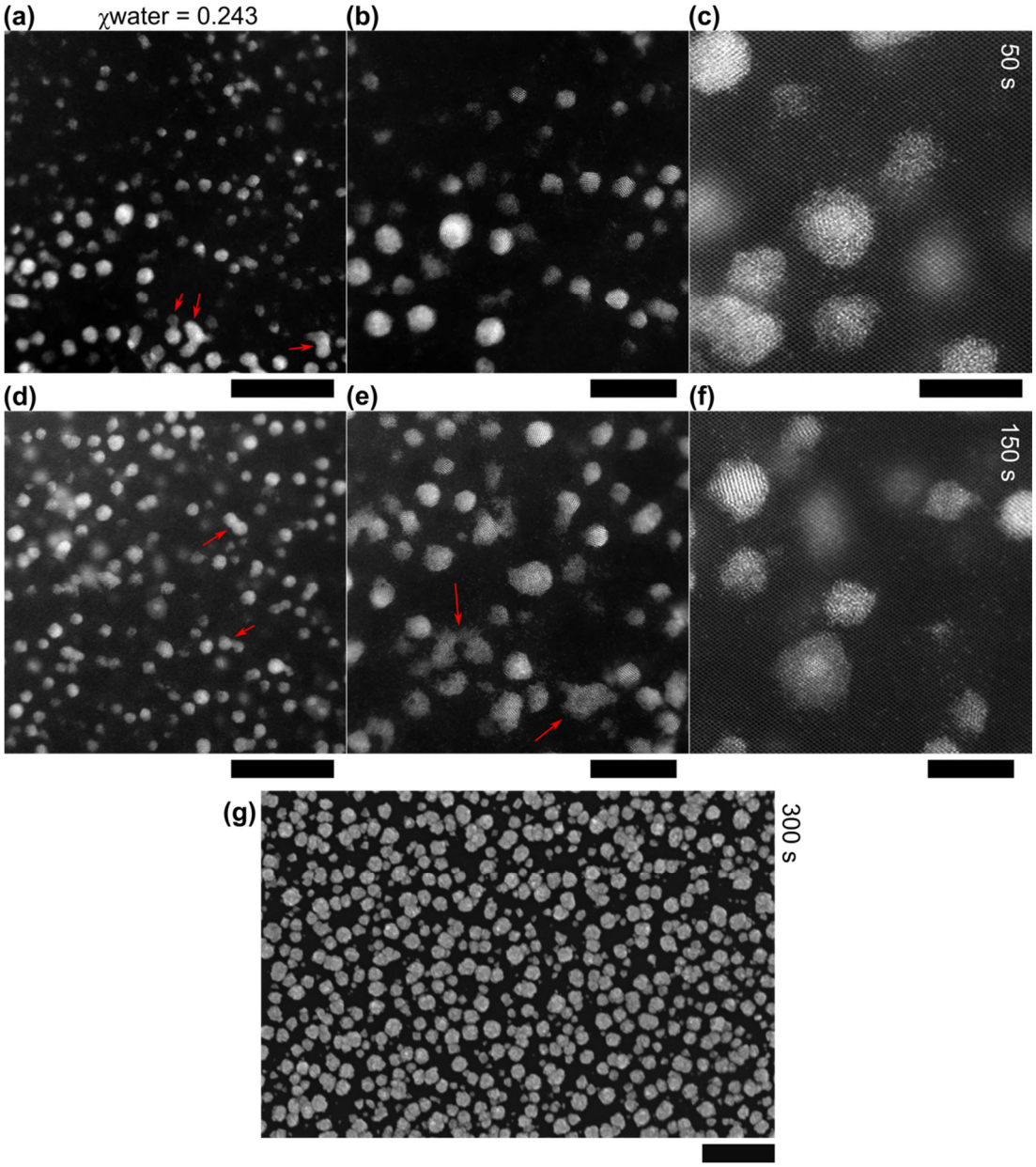

Figure 5.39: (a – f) ADF-STEM and (g) FE-SEM images of Pd NPs electrodeposition from 1×10^{-3} M Pd-acetate + 0.1 M $TBABF_4$ in χMeCN = 0.757 + χwater = 0.243 (90%:10% v/v) at an electrodeposition potential of η = -1 for t_{dep} = 50 s (a-c), 150 s (d-f) and 300 s (g). Scale bars = (a) 20 nm, (b) 10 nm, (c) 5 nm, (d) 20 nm, (e) 10 nm, (f) 5 nm, and (g) 400 nm.

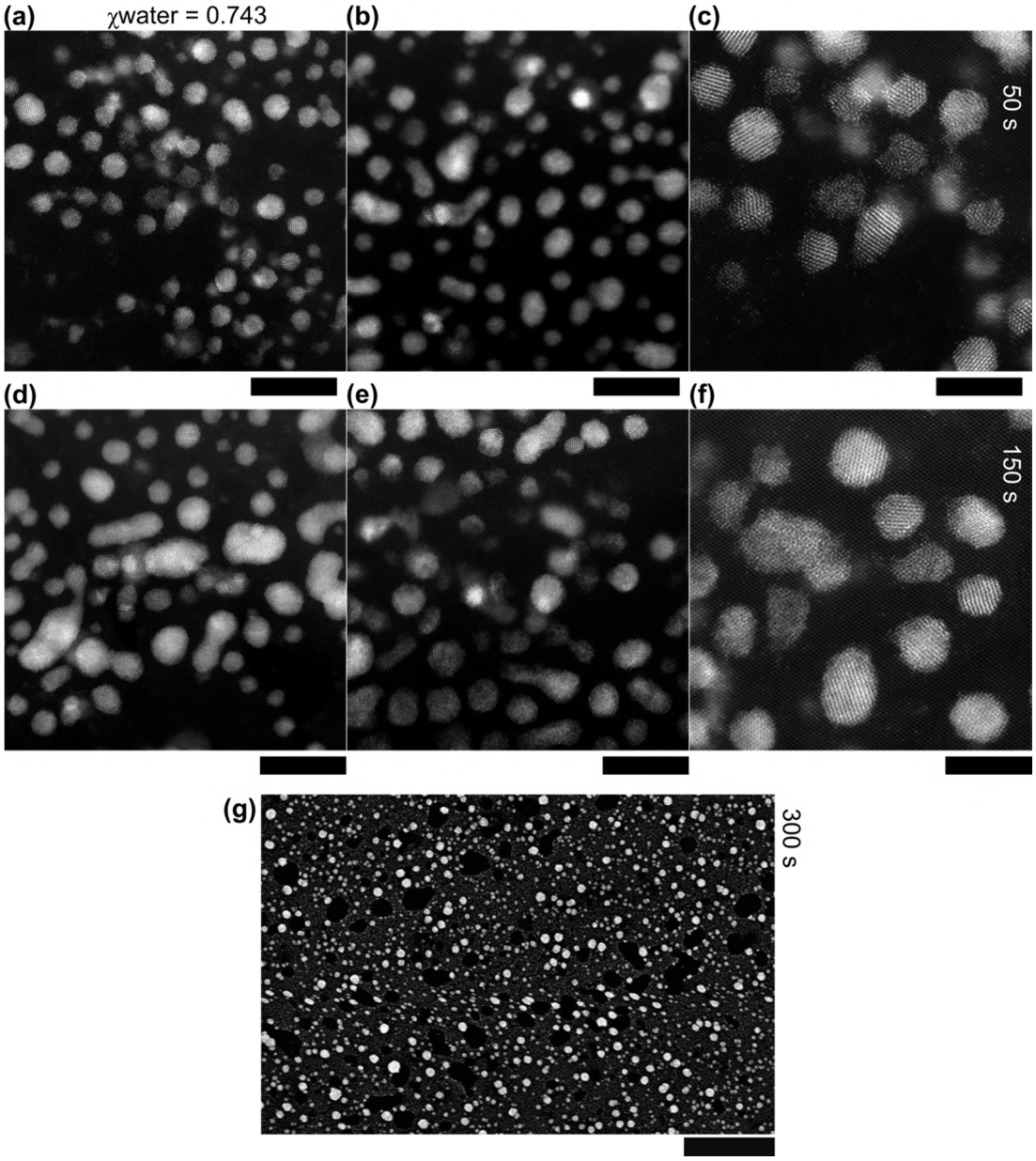

Figure 5.40: (a-f) ADF-STEM and (g) FE-SEM images of Pd NPs electrodeposition from 1×10^{-3} M Pd-acetate + 0.1 M $TBABF_4$ in χMeCN = 0.257 + χwater = 0.743 (50%:50% v/v) at an electrodeposition potential of η = -1 for t_{dep} = 50 c (a-c), 150 s (d-f) and 300 s (g). Scale bars = (a) 10 nm, (b) 10 nm, (c) 5 nm, (d) 10 nm, (e) 10 nm, (f) 5 nm, and (g) 2μm.

This implies that reduction of ions from the solution and direct attachment of the ad-atoms to the pre-existing Pd layer, or what is known as Volmer-Weber growth, is not the dominant mechanism though vertical growth is observed for some nanostructures. Such an observation can be attributed to the change in the ions' diffusion as a function of changing both the medium viscosity and the environment around the Pd^{2+} ions by

increasing the water percentage, which may influence the formation of thin elongated nanostructures (*i.e.* for χwater = 0.743, water molecules replace MeCN ones in the inner shell of Pd). Surprisingly, a longer electrodeposition time (t_{dep} = 300 s) displayed in Figure 5.40(g), leads to progressive formation of almost spherical Pd NPs.

Electrodeposition of Pd nanostructures from high water content media (χwater = 0.963, solution 11), is shown in Figure 5.41. After t_{dep} = 50 s, two distinguishable structures exist; branched defected Pd nanostructures (*i.e.* fractal nanodendrite) and monocrystalline Pd NPs with variable sizes in the range of 3 nm to 7 nm (Figure 5.41(a-c)). After t_{dep} = 150 s, Figure 5.41(d-f), the density of the spherical Pd NPs on the surface has increased, but the most prominent feature is the growth of the nano-dendritic branches in all directions (*i.e.* growth directions are not well defined). These fractal porous morphologies exhibit large perimeters and are thicker in comparison to Pd deposits from a shorter deposition time (as seen from the image contrast) and can be described as a "seaweed" growth. These structures may have been formed due to coalescence and aggregation as well as direct attachment (Volmer-Weber growth mechanism).

When the electrodeposition was driven for a longer period, t_{dep} = 300 s, large micro dendritic Pd nanostructures (note that any nanostructure which has at least one dimension greater than a μm is described as a large feature), Pd NPs (20-500 nm in diameter), and Pd nanodendrite (100-700 nm in perimeter) were formed as depicted in Figure 5.41(g).

In this study, we apply relatively high η, which means we investigate the mechanism of the deposition under diffusion limited circumstances. Since increasing water content leads to an increase of the solution viscosity,[582] we expect a decrease of the diffusional flux of Pd ions during electrodeposition from high water content solutions (*i.e.* χwater > 0.553). This means, diffusion will be enhanced at the growing Pd phase. Furthermore, η is sufficiently high and when χwater exceeds 0.743 (solutions 7 and 11), more Pd centres become free as almost they are surrounded by water and MeCN and are not bound to any acetate group. Consequently, the supersaturation is sufficiently large, and ions are being consumed in the vicinity of the growing nanostructures, which lead to the formation of dendrite morphology.[583]

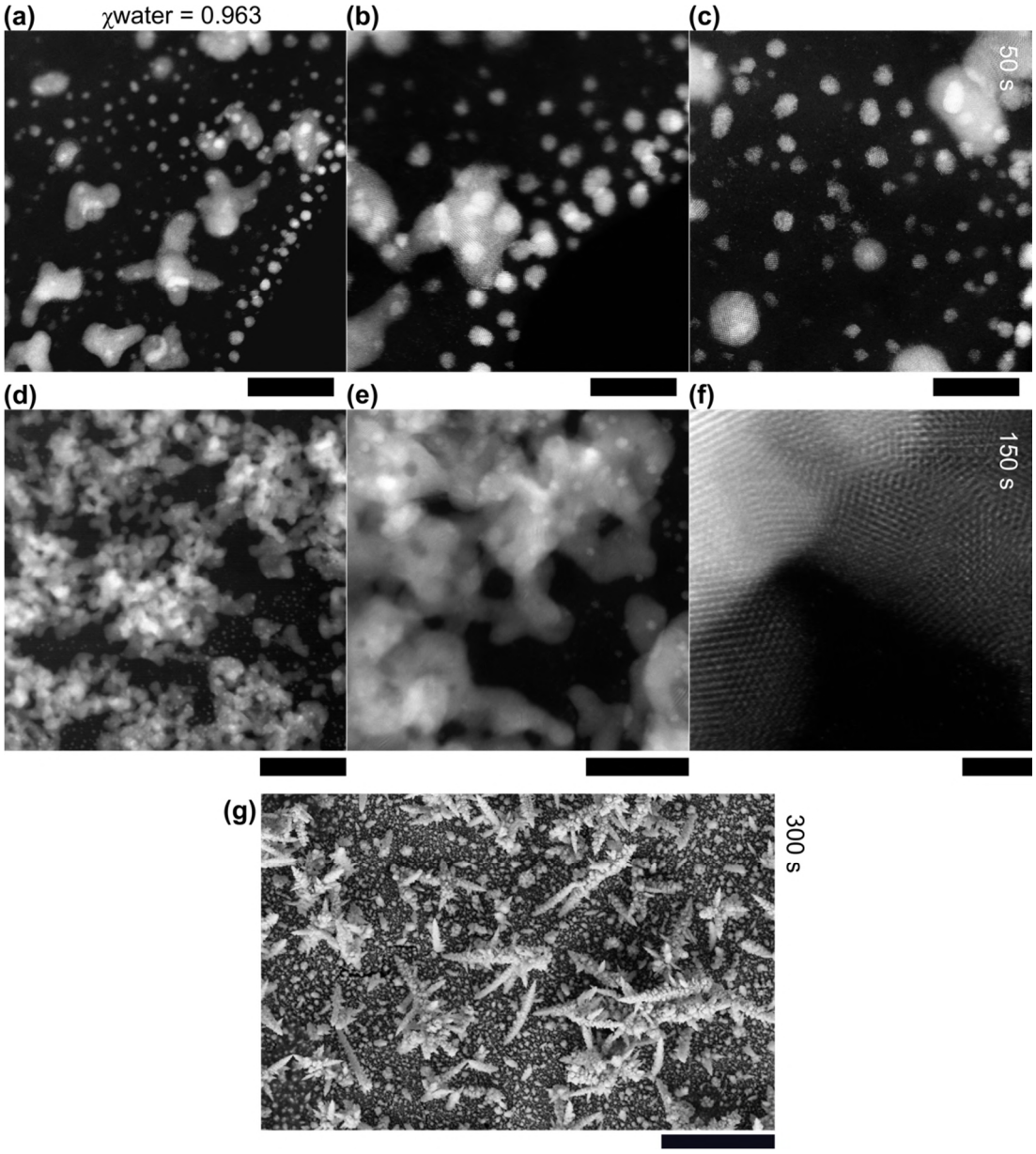

Figure 5.41: (a-f) ADF-STEM and (g) FE-SM images of Pd NPs and Pd dendritic nanostructure electrodeposition from 1 × 10^{-3} M Pd-acetate + 0.1 M $TBABF_4$ in χMeCN = 0.037 + χwater = 0.963 (10%:90% v/v) at an electrodeposition potential of η = -1 for t_{dep} = 50 s (a-c), 150 s (d-f) and 300 s (g). Scale bars = (a) 20 nm, (b) 10 nm, (c) 10nm, (d) 50 nm, (e) 20 nm, (f) 2 nm, and (g) 5 μm.

On the other hand, adding water does indeed facilitate Pd deposition but many Pd centres remain associated with the acetate groups or at least competition between ligands (*i.e.* acetate, BF_4^-, MeCN, and water) to bind to Pd ions takes place in low water contents solutions (*i.e.* χwater < 0.243). In addition to the undergoing dynamic ion-ion and ion-solvent interactions, surface wettability will be different as mostly the

surface is covered by MeCN, whereas generally water molecules occupy the surface when χwater is greater than 0.553. Thus, surface electrification will be different and surface energy may be lower for low content water studies, hence formation of spherical or hemispherical NPs is more likely.[10, 12, 583-585]

5.4.9 Conclusion

In this Section of the Chapter we demonstrate the complexity of the Pd-acetate structure both in solid form and in solution. In the solid form, Pd acetate exists as trimeric palladium acetate ($Pd_3(OAc)_6$). In MeCN solution only, the Pd ions are strongly coordinated to the acetate groups as well in a cyclic trimeric structure (*i.e.* the inner sheath of Pd is occupied by the acetate groups), whilst MeCN molecules are co-ordinated to the acetate groups (*i.e.* the outer shell). During electrochemical reduction, the Pd ions remain complexed to the acetate groups. Hence, whilst the Pd centres change their oxidation state from 2+ to 0. The reduction process does not lead to phase changes (*i.e.* formation of metallic Pd), as the Pd (0) acetate complexes remain dissolved in solution.

By adding water, structural changes occur, first due to the hydrolysis of the acetate group, which then allows solvation of Pd by MeCN molecules, resulting in a change in the inner shell co-ordination / structure of the Pd acetate complex. When χwater exceeds 0.743, the strong interactions between water and MeCN molecules overcomes the interaction between Pd and MeCN molecules. As a result, MeCN molecules, which occupy the inner shell of Pd are replaced with water molecules. Pd electrodeposition was possible from all solutions, which contain various amount of water employed in this study (χwater = 0.132-0.963).

However, χwater clearly impacts the morphology of the electrodeposited Pd. Whilst the majority of electrodeposition studies in the literature focus on investigating the impact of the driving potential, and time on the growth mechanism, here we show that the nature of the solvation shell around the Pd ions and double layer structure can also influence the morphology, for example more water leads to the formation of dendritic structures. By controlling the structure of the solvent, we might be able to control ions' diffusion and surface energy, which then can be utilised either to make spherical Pd NPs or dendritic Pd structures.

5.5 Recovery of Pd from ideal scenario solutions and synthesis solutions (industrial scenario)

5.5.1 Recovery from ideal scenario solutions

From our knowledge of Pd voltammetry in MeCN, water and mixed MeCN-water solutions, it is evident water must be present in order for electrodeposition to be possible. However, electrodeposition from low water levels solutions is possible as shown by the chronoamperometry and SEM data in Section 5.4.7 (Figures 5.37 and 5.38). To investigate the most favourable conditions for electrochemical recovery, studies were first carried out from two solutions containing (i) acidified water (pH = 1.8) and (ii) MeCN-water mixture, that contains χMeCN = 0.757 and χwater = 0.243 (*i.e.* 90%: 10% MeCN: water, v/v). A BDD RDE electrode was used to enhance the rate of mass transfer (1000 rpm). Using solutions containing χwater = 0.243 can be acceptable from both the synthesis and the industrial point of views. During synthesis, it is recommended to avoid high water content (χwater > 0.743), because water can reduce the product yield. However, some reports use water as an alternative green solvent. At the industrial level, MeCN will always contain water traces, which can be within the 10% v/v range.

The electrodeposition of Pd was then achieved by applying first a high overpotential for a shorter time, η = -1 V, for t_{dep} = 800 s, followed by lower overpotential over a longer deposition time, η = - 0.35 V, for t_{dep} = 10000 s. This is because once Pd covers the surface, other processes such as H adsorption and H_2 evolution or water electrolysis can impact the recovery process. Also, any side processes may impact the deposition *i.e.* adhesion and appearance as an example.

Figure 5.42 shows the electrodeposition of Pd from acidified water (pH = 1.8) that contains 250 ppm Pd. Both FE-SEM (Figure 5.42(a-b) and XEDS (Figure 5.42(c)) were used to characterise the Pd deposit. Pd recovered from the acidified water was electrodeposited as a continuous film on the BDD electrode. The film tore during transfer for imaging, Figure 5.42(a-b). XEDS shows that the film is made of Pd only; Pd with an oxide layer formation was not evident. Deposition from the acidified water results in a metallic reflecting layer. But the deposition layer was cracked, and the surface is not fully covered. The reason for layer cracking is not obvious (may be

during sample transfer or washing), however applying such high η, will always be accompanied with H_2 evolution that can induce such effects as well.

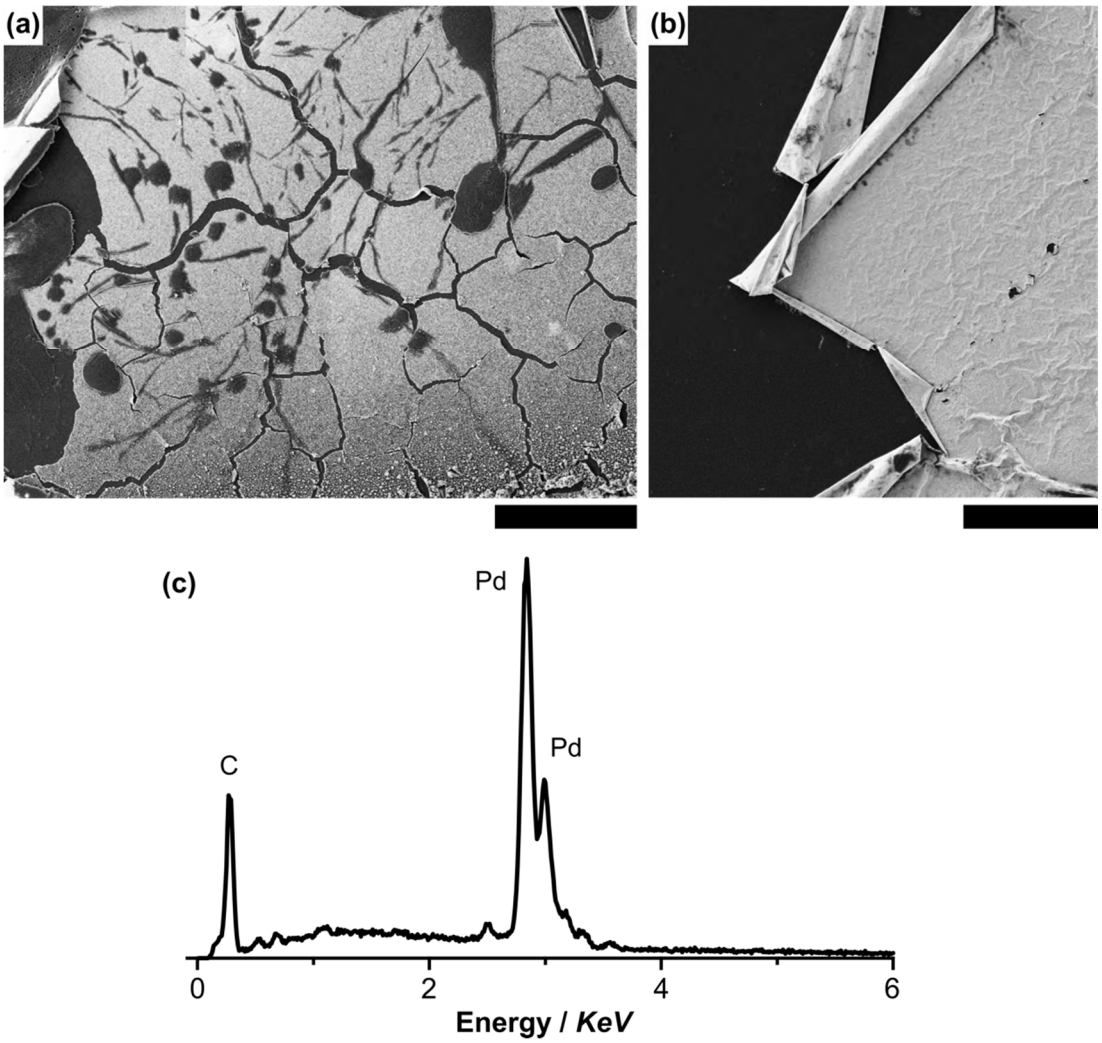

Figure 5.42: Electrochemical recovery of Pd from solution containing 250 ppm Pd as Pd-acetate + 0.1 M HCl + 0.05 M KCl in water. FE-SEM images of Pd metallic layer electrodeposited using double pulse potential steps at η = -1 V for t_{dep} = 800 s then at η = -0.35 V for t_{dep} = 10000 s, using a 25 mm diameter BDD RDE (1000 rpm). (a) In-Lens SEM image and (b) SE2 SEM image, scale bars = 200µm. (c) XEDS spectrum of Pd post the electrodeposition process.

Similarly, electrodeposition of Pd was carried out using the same electrodeposition parameters and experimental set-up but this time from a mixed solvent solution *i.e.* (χMeCN = 0.757 and χwater = 0.243), Figure 5.43. Both SEM images Figure 5.43(a and b) and XEDS spectrum Figure 5.43(c) show Pd film is deposited from solutions containing χwater = 0.243, also the film is free of oxygen. The adhesion of the

electrodeposited Pd is better than deposition from acidified aqueous solutions and the film covers the surface and is metallic but semi-reflective.

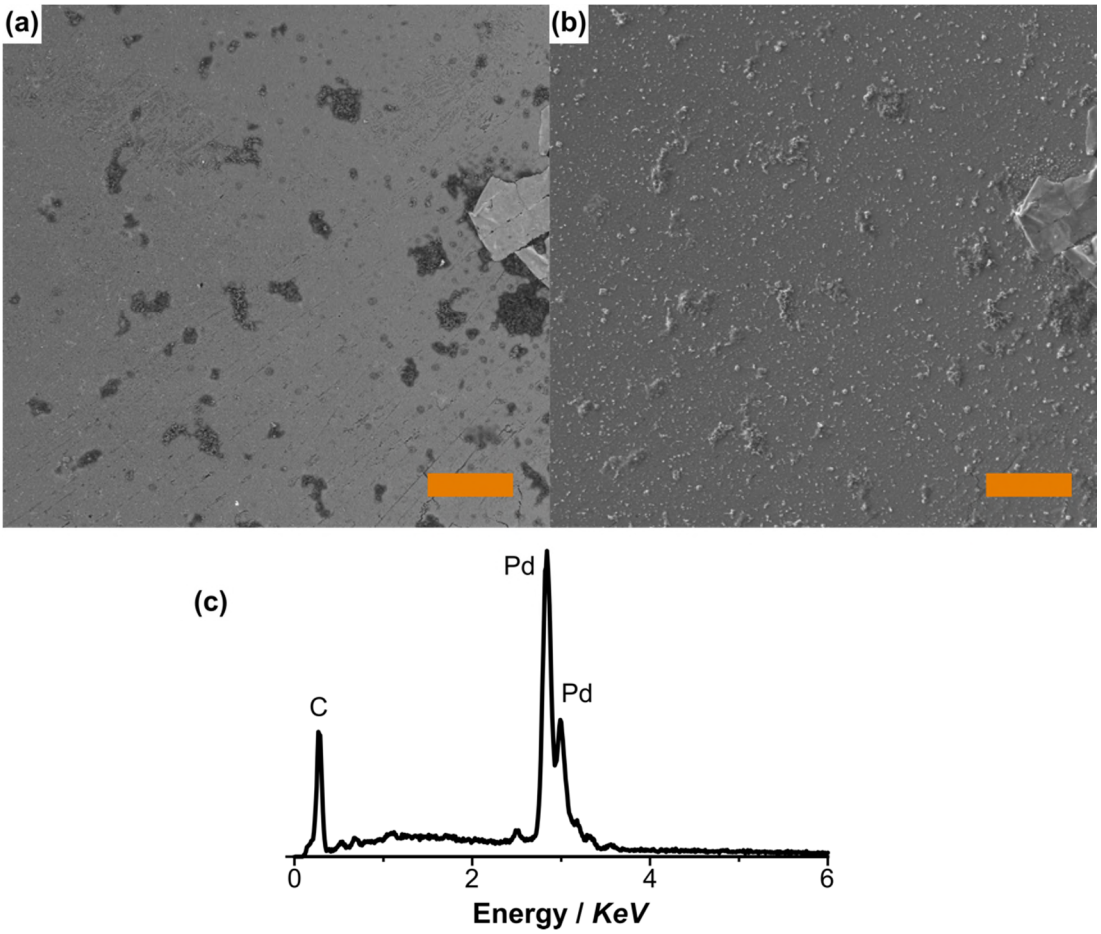

Figure 5.43: Ideal scenario case for electrochemical recovery of Pd from solution containing 250 ppm Pd as Pd-acetate + 0.1 M $TBABF_4$ in MeCN:water mixed solvent, χMeCN = 0.757 + χwater = 0.243 (90%:10% v/v) using a 25 mm diameter BDD RDE (1000 rpm). FE-SEM images of Pd metallic layer electrodeposited using double pulse potential steps at η = -1 V for t_{dep} = 800 s then at η = -0.35 V for t_{dep} = 10000 s. (a) In-Lens SEM image, and (b) SE2 SEM image. Scale bars = (a) 50 µm, and (b) 50 µm. (d) XEDS spectrum of Pd post the electrodeposition process.

5.5.2 Recovery from synthesis (industrial scenario)

Accordingly, we now examine Pd electrodeposition (*i.e.* removal) from synthesis solutions containing organic molecules by addition of just 10% water (χwater = 0.243) to the reaction mixture. In order to investigate Pd recovery from a synthetically relevant solution, the Suzuki cross-coupling reaction between 4'-bromoacetophenone and phenylboronic acid (Figure 5.44(a)) in a MeCN solvent system using the catalyst

Pd acetate and potassium carbonate as a base was chosen. Experimentally, the reaction was first carried according to the procedure outlined in the Experimental Section 5.3.2 to compare the reproducibility of the reaction to previous reports.[586, 587]

We find the reaction results in 89.8% yield of 4-acetylbiphenyl, which has the MS fingerprint shown in Figure 5.44(b) and is in a good agreement with literature.[588, 589] Figure 5.45 shows the ^{1}H NMR of the coupling product 4-acetylbiphenyl, along with the MS spectrum, both data show that the product has been made in a high purity yield. The process was then repeated but the last stage, which involves product purification using column chromatography was avoided to mimic industrial procedures as purification involves removal of the Pd catalyst.

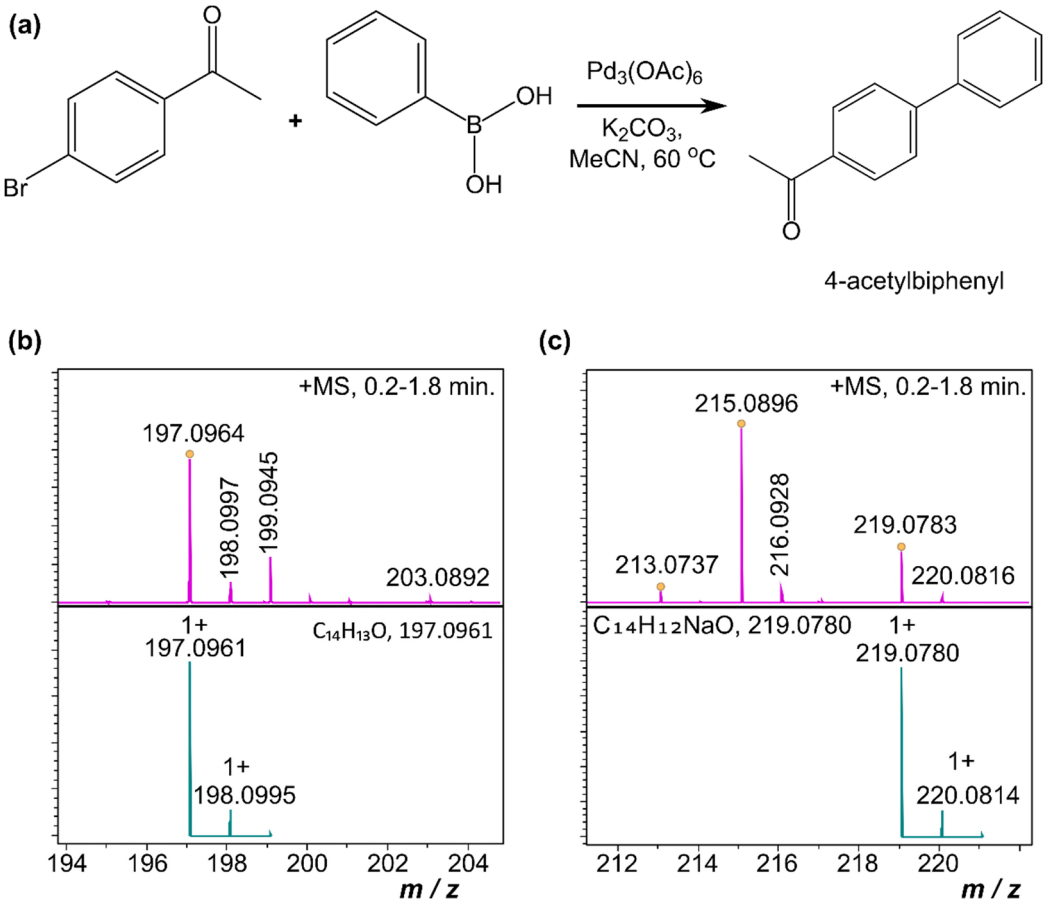

Figure 5.44: (a) The Suzuki coupling reaction of 4'-bromoacetophenone with phenylboronic acid catalyzed by Pd-acetate in MeCN. (b and c) ESI-TOF-MS analysis of crude 4-acetylbiphenyl showing the molecule and its sodiated structure, respectively.

There is a possibility that the Pd-acetate catalyst can have an oxidation state of zero at the end of the synthesis process as suggested before in different reports, see references

84, 590-593. We therefore investigated the presence of Pd^0 species by polarising the electrode anodically using BDD RDE at E_{app} = +2.0 V for t_{ox} = 10^4 s. The recorded chronoamperometry is shown in Figure 5.46(a). The linear region of the data (t_{ox} = 0 - 6 × 10^3 s) was plotted as $\ln((i_{lim}-i)/i_{lim}) = \ln(([Pd^0]l_{im}-[Pd^0])/[Pd^0]_{lim})$ *vs.* the oxidation time (t_{ox}), where i_{lim} is the current at infinite time and i is the current at t, Figure 5.46(b).

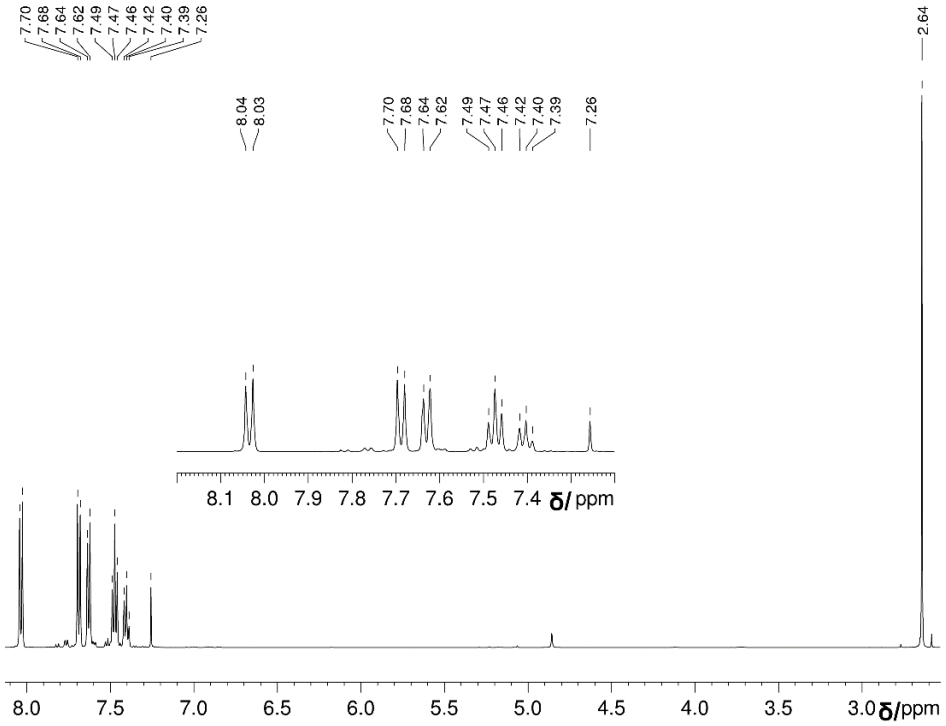

Figure 5.45: 1H NMR spectrum of crude 4-acetylbiphenyl.

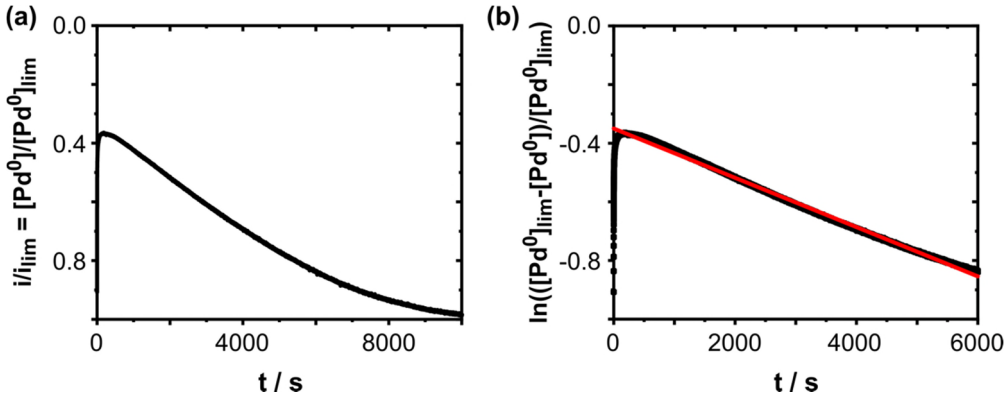

Figure 5.46: Kinetics of the in-situ formation of Pd^0 via reduction of Pd^{2+}-acetate complex. (a) Oxidation polarisation i-t curve monitored at E_{app} = +2.0 V for t_{ox} = 10^4 s in air using BDD RDE (3 mm and 500 rad s^{-1}) and (b) variation of $\ln((i_{lim}-i)/i_{lim})$ as function of time in the linear region (experimental data are in black and fitting data are in red).

The chronoamperometry plot in Figure 5.46(a) shows an increase of the oxidation current as function of time, which may be interpreted as a generation of Pd^0-acetate complexes. The plot of $\ln((([Pd^0]_{lim}-[Pd^0])/[Pd^0]_{lim})$ as function of time is linear, characteristic of a first reaction order. The rate constant (k) of Pd^0 formation was calculated from the slope of the regression line ($\ln((([Pd^0]_{lim}-[Pd^0])/[Pd^0]_{lim}) = -k*t$), with $k = 8.4 \times 10^{-5}$ s^{-1} at 25 °C. This value suggests slow formation of Pd^0-acetate complexes *in-situ* via reaction with solvent molecules and dissolved species (such as phenylboronic acid).[594] It is also important to note that the solution contains the background electrolyte, which is made of tetrabutyl ammonium (NBu_4^+) and tetrafluoroborate (BF_4^-), where NBu_4^+ ions are suggested to improve the stability of Pd^0 species in solution.[83] On contrary, the oxidation current of Pd-acetate species in binary solvent mixtures (MeCN-water) decreases over time, Figure 5.47. Consequently, *in-situ* Pd^0-acetate formation is less feasible in MeCN-water mixtures only. However, presence of organic compounds and the synthesis cycle may influence the oxidation status of Pd.

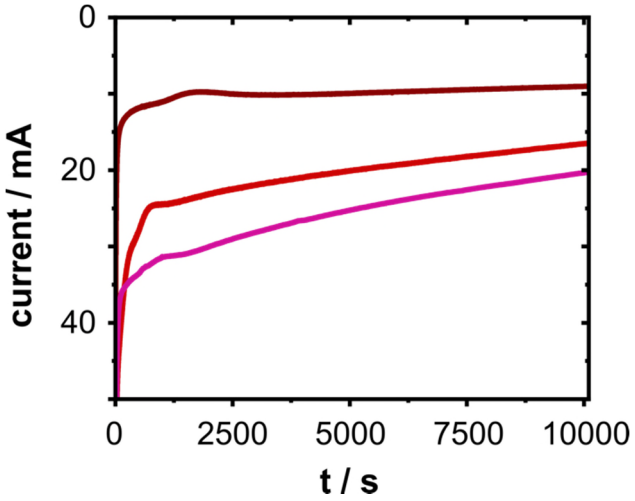

Figure 5.47: Oxidation polarisation *i-t* curve monitored at E_{app} = +2.0 V for $t_{ox} = 10^4$ s using BDD RDE (3 mm and 500 rad s^{-1}), from solutions containing 1×10^{-3} M Pd-acetate + 0.1 M $TBABF_4$ in χMeCN = 0.757 + χwater = 0.243 (wine red), χMeCN = 0.447 + χwater = 0.553 (red) and χMeCN = 0.257 + χwater = 0.743 (pink).

Therefore, an anodic polrisation was established prior the electrodepsotion by applying η = + 0.3 V for 1.8×10^{10} s. At this η, oxidation of other organic molecules does not occur. This process will then aid in converting Pd^0 species in the reaction

mixture to Pd^{2+} (*i.e.* CVs were ran before and after this process to get insights about the presence of Pd^{2+}, but these data are not shown here).

Electrodeposition of Pd from the synthesis solution (Figures 5.48 – 5.50) was then explored by applying the same recovery parametrs used earlier in Section 5.5.1. First electrochemical recovery was investigated from the Suzuki reaction solution prior to the separation and extraction of the final product 4-acetylbiphenyl (*i.e.* in the presence of the final product or crude solution, we call it here recovery 1, Figure 5.48, using a BDD RDE (25 mm diameter) at a rotation speed of 1000 rpm. In the second case, the final product (4-acetylbiphenyl) was first separated from the crude solution but no column purification was carried out. Therefore, two solutions result, one contains the product and the other solution contains all the remaining organic and Pd-acetate catalyst. The later was used for the electrochemical recovery as shown in Figure 5.49 (recovery 2, in the absence of the final product). Finally, recovery from the crude reaction solution was investigated but under stationary conditions using a higher surface area (1 cm × 10 cm) as grown BDD electrode, while employing the same electrochemical recovery parameters utilised in the first two cases, Figure 5.50 (recovery 3).

In all cases electrodeposition of Pd was evident as shown by the SEM images and the XEDS spectra, the Pd deposit in Figure 5.48 (a-d) appears as a brittle/fractal dendritic film, whereas the Pd deposit in Figure 5.59 (a-d) is a continuous textured film with the presence of large particles on top of the film. Electrodeposition using a large surface area as grown BDD electrode, Figure 5.50 (a-d), results in a different morphology in comparison to the previous two cases. The Pd deposition appears as irregular large cauliflower particles that have aggregated to form a very rough film. For all cases, the deposited layer is made of Pd only, and Pd with an oxide layer was absent as shown by the XEDS spectra, Figures 5.48 (e), 5.49 (e) and 5.50 (e).

The effectiveness of the electrochemical recovery procedure was measured by evaluating the concentration of Pd in the solution, before and after electrodeposition, using ICP-MS, Table 5.7. Current efficiencies were calculated by measuring the weight increase of the BDD as function of electrodeposition, Table 5.7.[526] Obviously, enhanced mass transport is expected when BDD RDE is used, hence we notice better recovery in terms of Pd concentration and current efficiency. However, the as grown BDD, which has a rougher surface may provide a better avenue for Pd deposition,

because adhesion to the surface is improved. Thus, leaching any metallic Pd deposit back to the solution is less possible. The current values of Pd after recovery are promising and suggest the possibility of using electrodeposition as a technique for Pd removal after the synthesis.

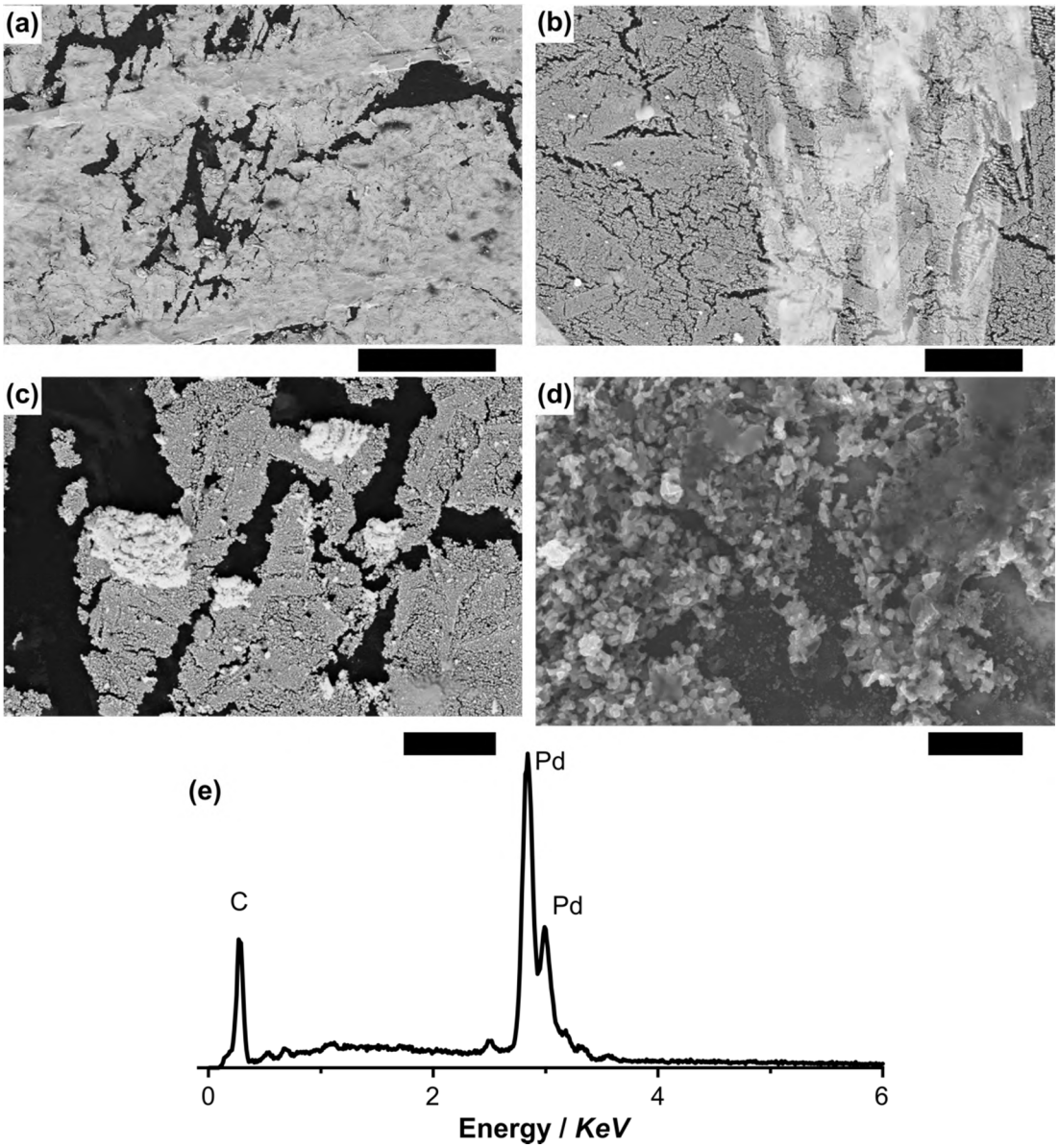

Figure 5.48: Industrial scenario case for electrochemical recovery of Pd from the Suzuki coupling reaction solution containing 210 ppm Pd as Pd-acetate + 0.1 M $TBABF_4$ in MeCN:water mixed solvent, χMeCN = 0.757 + χwater = 0.243 (90%:10% v/v) using a 25 mm diameter BDD RDE (1000 rpm). (a-d) In-Lens FE-SEM images of Pd metallic layer electrodeposited using double pulse potential steps at η = -1 V for t_{dep} = 800 s then at η = -0.35 V for t_{dep} = 10000 s. Scale bar = (a) 20 µm, (b) 6 µm, (c) 4 µm, and (d) 1µm. (e) XEDS spectrum of Pd post the electrodeposition process.

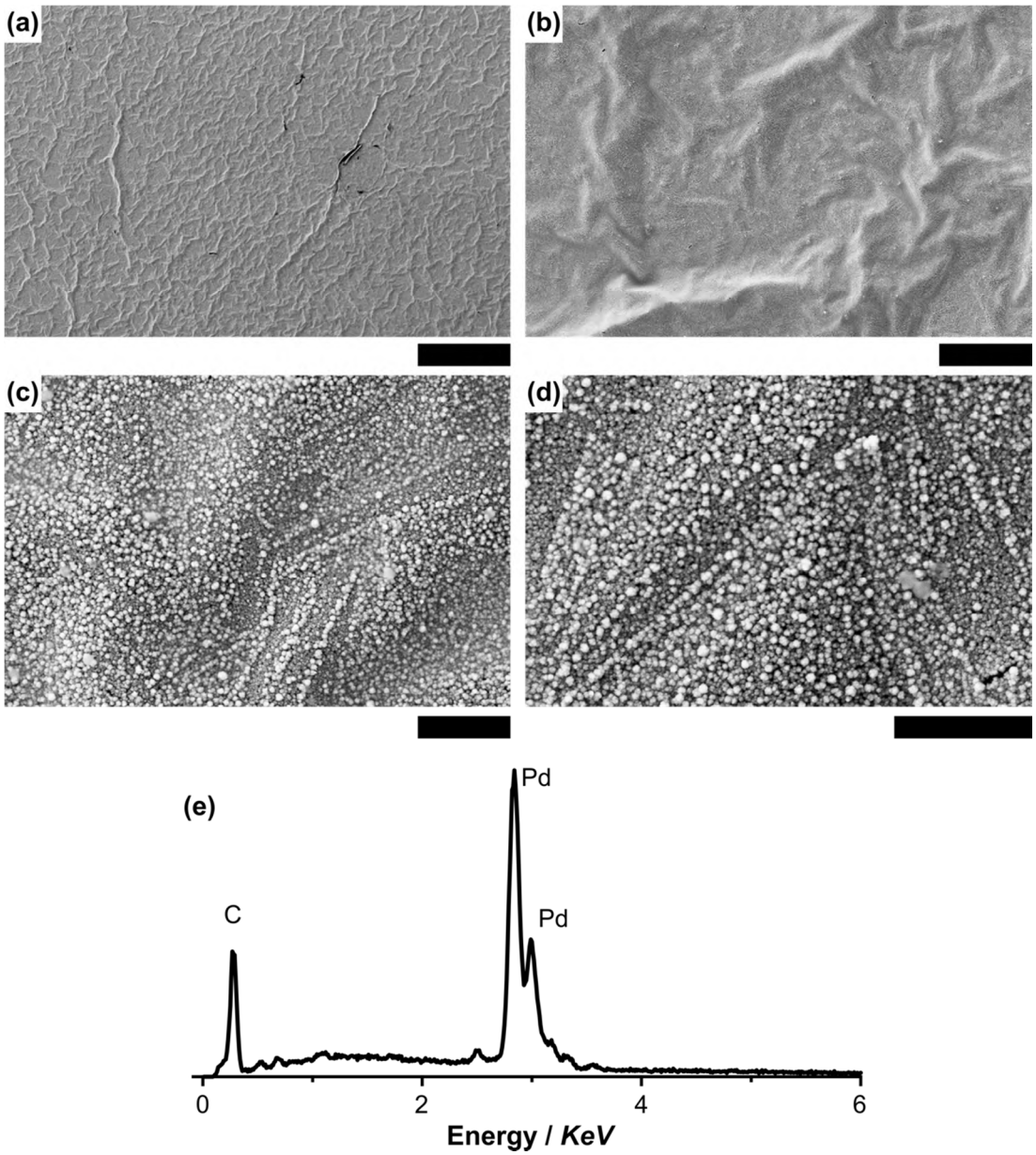

Figure 5.49: Industrial scenario case for electrochemical recovery of Pd from the Suzuki coupling reaction solution containing 193 ppm Pd as Pd-acetate + 0.1 M $TBABF_4$ in MeCN:water mixed solvent, χMeCN = 0.757 + χwater = 0.243 (90%:10% v/v) using a 25 mm diameter BDD RDE (1000 rpm). (a-d) In-Lens FE-SEM images of Pd metallic layer electrodeposited using double pulse potential steps at η = -1 V for t_{dep} = 800 s then at η = -0.35 V for t_{dep} = 10000 s. Scale bar = (a) 200µm, (b) 20 µm, (c) 2µm, and (d) 2 µm. (e) XEDS spectrum of Pd post the electrodeposition process.

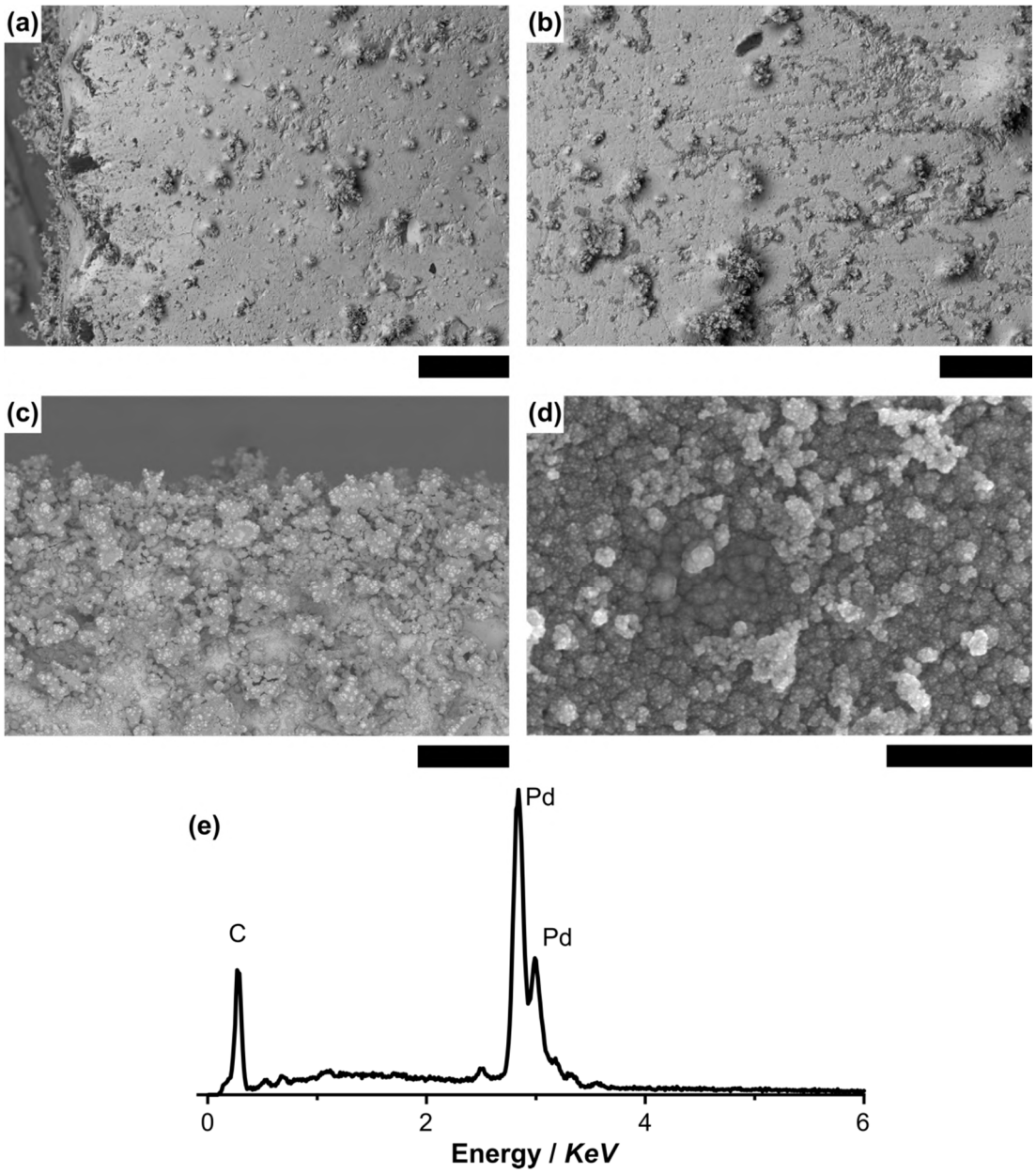

Figure 5.50: Industrial scenario case for electrochemical recovery of Pd from the Suzuki coupling reaction solution containing 205 ppm Pd as Pd-acetate + 0.1 M $TBABF_4$ in MeCN:water mixed solvent, χMeCN = 0.757 + χwater = 0.243 (90%:10% v/v) using a 1 cm × 10 cm BDD electrode. (a-d) In-Lens FE-SEM images of Pd metallic layer electrodeposited using double pulse potential steps at η = -1 V for t_{dep} = 800 s then at η = -0.35 V for t_{dep} = 10000 s. Scale bar = (a) 100 µm, (b) 100 µm, (c) 100µm, and (d) 400 nm. (e) XEDS spectrum of Pd post the electrodeposition process.

5.5.3 Conclusion

The aforementioned results o Pd recovery from organic synthesis represent a guide for further electrochemical studies, which can investigate electrodeposition of other Pd catalysts from mixed solvent systems at the industrial level. This certainly requires using different techniques such as spectroscopy, dynamic electrochemistry, analytical and physical tools, and microscopy to develop knowledge about the feasibility of Pd electrodeposition, its effectiveness and robustness. Also, future work could consider designing a recovery cell for effective recovery over shorter period of deposition and for better effective Pd removal.

In general, we show that the structure of catalysts such as Pd-acetate is complicated either in the solid form or upon dissolution. Ion-solvent and solvent-solvent interaction influence the environment surrounding the Pd cations. Based on the water content (here we refer to in terms of mole fractions or v/v), the inner shell of Pd will be either occupied with MeCN or water or both of them. Though the bond between the acetate groups and Pd is relatively strong, water addition can alter the association between Pd and the acetate groups. Thus, Pd cations can be solvated by solvent molecules, and hence they can be electrodeposited on the surface. Finally, electrodeposition can be applied to a solution of a complex nature such as organic synthesis solution that contain a diverse organic and inorganic compound.

Table 5.7: Concentration of Pd prior and post electrodeposition and the current efficiency of the electrochemical recovery process using BDD electrodes.

Recovery method	**1**			**2**			**3**		
	Conc.(start) / ppm	**Conc.(final) / ppm**	**CE* %**	**Conc.(start) / ppm**	**Conc.(final) / ppm**	**CE* %**	**Conc.(start) / ppm**	**Conc.(final) / ppm**	**CE* %**
	210 ± 5	4.1725 ± 0.1011	78.3	193 ± 1	1.215 ± 0.302	88.1	211 ± 3	6.9335 ± 0.4013	75.1
Appearance	High area coverage, metallic, reflecting but layer cracked			Complete coverage, metallic and thick			Complete coverage, metallic but non-reflective, rough		
Adhesion	Fairly good			Good			Very good		

*current efficiency is estimated from the weight increase of the BDD

Chapter 6

Conclusions and future outlook

Despite the fact that electrodeposition has been an extensively studied subject, there is plenty of work still required to understand the basic fundamentals of metal nucleation and growth. This is partly because to date we lack the proper control over the nanostructures which grow under potential driving forces. Some attempts have used template electrodeposition to direct the growth path, or utilised a catalytic property to make a monolayer film.[595, 596] Other literature has shown how the presence of additives may lead to the formation of unique nanostructures, which have exceptional catalytic properties.[447] Nevertheless, many studies to date have relied on a trial-and-error approach or have used analogy arguments to describe electrodeposition. In this work, we demonstrate how the applied deposition potential and temperature are crucial parameters towards influencing the structure, particle size, density number and shape of the electrodeposited Pt material on BDD. From this work it became apparent that, to be able to understand nucleation and growth, as well as associated structural changes, it is necessary to visualise the system at the atomic level. Through making electron transparent BDD, as demonstrated in this work, we can provide new insights into Au nucleation and record growth mechanisms by depositing Au at different time intervals. A more complex system, the electrodeposition of Pd from its Pd-acetate salt in organic solutions and mixed solvents (*i.e.* acetonitrile) was then studied.

In *Chapter 3*, under both room temperature and pulse heating conditions, we show that increasing the deposition potential while fixing the deposition time (t_{dep} = 5 s) leads to a reduction in the size of Pt NPs. At room temperature, and for electrodepositions that employed low driving potentials (E_{dep} = +0.1 V and 0.0 V), we obtained randomly formed and relatively large Pt NPs (mostly hemispherical or spherical in shape). By increasing the deposition potential (E_{dep} = -0.1 V), smaller Pt NPs start to form as well as large ones. When E_{dep} = -0.2 V, the BDD surface is almost covered with small Pt NPs. When, laser pulse heating was applied in tandem with the chronoamperometric deposition, both small and large Pt NPs were formed at E_{dep} = +0.1 V. A similar observation is recorded for deposition at E_{dep} = 0.0 V, but the NPs density was higher. By increasing E_{dep} to -0.1 V, the BDD surface was covered by small Pt NPs, with a

much narrower size distribution. However, some large Pt NPs were observed. Approaching E_{dep} = -0.2 V, the surface is almost covered with monodispersed tiny Pt NPs. The electrocatalytic activity of the Pt NPs made using pulse heating for $H_{ads/des}$ was higher in comparison to those made at room temperature. This was further investigated by examining methanol oxidation. This test study showed that each deposition condition leads to distinct electrocatalytic properties. Indeed, the mechanism of methanol oxidation and its conversion pathways are yet to be resolved. However, we can infer about structure-activity relationships from both methanol oxidation and $H_{ads/des}$ studies. From this, we transferred the Pt NPs to a carbon grid, suitable for TEM imaging and noticed that room temperature electrodeposition results in compact Pt NPs, whereas electrodeposition from the laser pulse heated baths result in nanoporous Pt NPs. The enhanced electrocatalytic activity can then be correlated not only to size, loading and distribution, but also to the structure (*i.e.* the NPs morphology). In future work, it will be possible to study the stability and structural changes of the Pt NPs during cycling, either in methanol containing solutions, or in acid. In doing so, we can then explore the suitability of using such materials for long period catalysis.

In *Chapter 4*, we use electron transparent BDD in combination with IL-STEM to track Au nucleation and growth. A fixed overpotential is employed for different growth time (5 ms, 10 ms, and 30 ms) to probe the initial stages of Au electrodeposition. By driving the electrodeposition at a high η, and for a short time scale (t_{dep} = 5 ms), we observed the formation of Au atoms, atomic clusters and Au NPs (1-3 nm in diameter). By increasing the deposition time, amorphous clusters were transformed into crystalline Au NPs. Also, Au NPs or Au clusters and NPs start to fuse together. Since TEM can be a quantitative technique, atom counting has helped us visualise that Au NPs grow both by a Volmer-Weber growth mechanism, and also through the fusion of two or more neighbouring Au NPs, and clusters. The process by which nanostructures fuse can be described as a surface mediated Ostwald ripening or in terms of coalescence and aggregation. Future work will include exploring the effect of varying η, in the absence of any electroactive species in the solution, on the surface movement of atoms, clusters and NPs. Also, the impact of the electron beam during TEM data acquisition on the stability of the nanostructures can be considered. Further work will

include a more theoretical treatment of nucleation and growth, with an aim to better understand of the intricacies of electrodeposition mechanisms.

In *Chapter 5*, we provide a proof of concept study about how we can electrodeposit Pd from its Pd-acetate salt in organic solvents. Pd-acetate is the most notably used catalyst in pharmaceutical industries, however its structure as solid and in solution is complex, hence its behavior is non-trivial and the current recovery approaches fail to remove Pd from the synthesis solution. The challenge in this work was to find an approach to recover Pd without impacting the other chemicals exist in the solution (*i.e.* active pharmaceutical ingredient, organic molecules), thus harsh digestion methods were not an option. This is achieved by the controlled addition of water to MeCN, resulting in a mixed solvent media. Through this approach, we show that the bond between the Pd and the acetate group is altered. From the addition of small amounts of water (χwater < 0.553), water microdomains form, which aid Pd-acetate hydrolysis. As a consequence, Pd is no longer bound to the acetate group and MeCN starts to occupy the inner shell of Pd *i.e.* Pd ions have become solvated with MeCN molecules. By increasing the water content, a competition between MeCN and water molecules establishes over the occupancy of the inner shells of Pd. Though thermodynamically Pd prefers to be solvated with MeCN molecules, MeCN-water interactions were strong enough to overcome Pd-MeCN interaction. Thus, Pd ions in a high-water content mixture (χwater > 0.812), are assumed to be solvated with water molecules.

In general, the work presented in this thesis represents an attempt to enhance understanding of the nucleation and growth of Pt, Au, and Pd on BDD. Parameters such as electrodeposition potential, deposition time, temperature, and the nature of the solution were investigated. Though electrodeposition may appear to be a simple process, control of the deposition parameters, and understanding how they impact the process of phase growth are crucial. No doubt more experimental and theoretical work are still required. The current theoretical treatment of *i-t* curves can benefit greatly from attaining new insights about early stages of nucleation. This may help in reformulating some of the commonly used equations to better predict how a NP can form. Finally, with the introduction of an electron transparent BDD, that works as both an electrode and a plate for TEM imaging, new insights about materials formation and behaviour during catalysis or energy storage can be explored.

Bibliography and references

1. Sawyer, D. T.; Sobkowiak, A.; Roberts, J. L., *Electrochemistry for Chemists*. John Wiley & Sons, Inc.: New York, **1995**.
2. Galvani; Volta, A. *Philosophical Transactions of the Royal Society of London* **1793,** 83, 10-44.
3. Volta, A. *The Philosophical Magazine* **1799,** 4, (13), 59-68.
4. Nicholson, W.; Carlisle, A. *Journal of Natural Philosophy, Chemistry, and the Arts* **1800,** 4, 272.
5. Breitkopf, C.; Swider-Lyons, K., Electrochemical Science — Historical Review. In *Springer Handbook of Electrochemical Energy*, Breitkopf, C.; Swider-Lyons, K., Eds. Springer: Berlin, Heidelberg, 2017; pp 1-9.
6. Faraday, M. *Philosophical Transactions of the Royal Society of London* **1834,** 124, 77-122.
7. Bard, A. J.; Faulkner, L. R., *Electrochemical Methods: Fundamentals and Applications*. John Wiley & Sons, Inc.: New York, **2001**.
8. Schmickler, W.; Santos, E., A few basic concepts. In *Interfacial Electrochemistry*, Springer: Berlin, Heidelberg, 2010; pp 29-37.
9. Milchev, A., *Electrocrystallization: Fundamentals of Nucleation and Growth*. Kluwer Academic Publishers: New York, **2002**.
10. Paunovic, M.; Schlesinger, M., *Fundamentals of Electrochemical Deposition*. John Wiley & Sons: Hoboken, New Jersey, **2006**.
11. Toth, P. S.; Dryfe, R. A. *The Analyst* **2015,** 140, (6), 1947-54.
12. Budevski, E.; Staikov, G.; Lorenz, W. J., *Electrochemical Phase Formation and Growth*. Wiley-VCH Verlag GmbH: Weinheim, **2007**.
13. Fink, C. G. *Science* **1950,** 112, (2897), 12.
14. Milchev, A.; Malinowski, J. *Surface Science* **1985,** 156, 36-43.
15. Milchev, A.; Stoyanov, S.; Kaischev, R. *Thin Solid Films* **1974,** 22, (3), 267-274.
16. Milchev, A.; Stoyanov, S.; Kaischev, R. *Thin Solid Films* **1974,** 22, (3), 255-265.
17. Gunawardena, G.; Hills, G.; Montenegro, I.; Scharifker, B. *Journal of Electroanalytical Chemistry and Interfacial Electrochemistry* **1982,** 138, (2), 225-239.
18. Venables, J. A.; Spiller, G. D. T.; Hanbucken, M. *Reports on Progress in Physics* **1984,** 47, (4), 399.
19. Phillips, W. M. *Transactions of the American Electrochemical Society* **1930,** 58, (1), 387-401.
20. Audrieth, L. F.; Nelson, H. W. *Chemical Reviews* **1931,** 8, (2), 335-352.
21. Mele, C.; Rondinini, S.; D'Urzo, L.; Romanello, V.; Tondo, E.; Minguzzi, A.; Vertova, A.; Bozzini, B. *Journal of Solid State Electrochemistry* **2009,** 13, (10), 1577-1584.
22. Plieth, W., *Electrochemistry for Materials Science*. 1st ed.; Elsevier: Amsterdam, Boston, **2008**.
23. Bockris, J. O.; Devanathan, M. A. V.; Muller, K. *Proceedings of the Royal Society A: Mathematical, Physical and Engineering Sciences* **1963,** 274, (1356), 55-79.
24. Mehl, W.; Bockris, J. O. M. *The Journal of Chemical Physics* **1957,** 27, (3), 818-819.

25. Suni, I. I. *Journal of Applied Electrochemistry* **1997,** 27, (11), 1219-1231.
26. Scharifker, B. R.; Mostany, J., Electrochemical Nucleation and Growth. In *Encyclopedia of Electrochemistry*, Bard, A. J.; Stratmann, M., Eds. Wiley-VCH: Germany, 2007; Vol. 1, pp 512-534.
27. Pangarov, N. *Electrochimica Acta* **1962,** 7, (1), 139-146.
28. Nasirpouri, F., Fundamentals and Principles of Electrodeposition. In *Electrodeposition of Nanostructured Materials*, Springer International Publishing: Switzerland, 2017; pp 75-121.
29. Kissinger, P.; Heineman, W. R., *Laboratory Techniques in Electroanalytical Chemistry*. Marcel Dekker: New York, **1996**.
30. Finklea, H. O.; Bard, A. J.; Rubinstein, I., *Electroanalytical Chemistry: A Series of Advances*. **1996**; p 109.
31. Jerkiewicz, G., From electrochemistry to molecular-level the solid-liquid electrochemical interface - An overview. In *Solid-Liquid Electrochemical Interfaces*, Jerkiewicz, G.; Soriaga, M. P.; Uosaki, K.; Wieckowski, A., Eds. American Chemical Society: Washington, 1997; Vol. 656, pp 1-12.
32. Ritchie, I. M.; Bailey, S.; Woods, R. *Adv. Colloid Interface Sci.* **1999,** 80, (3), 183-231.
33. Compton, R. G.; Laborda, E.; Ward, K. R., *Understanding Voltammetry: Simulation of Electrode Processes*. Imperial College Press: London, **2013**.
34. Reichardt, C., *Handbook of Solvents*. 2nd ed.; ChemTec Publishing: Oxford, **2014**.
35. Brett, C. M. A.; Brett, A. M. O., *Electrochemistry Principles, Methods, and Applications*. Oxford University Press: Oxford, **1993**.
36. O'M Bockris, J.; Reddy, A., *Modern Electrochemistry 1: Ionics*. Kluwer Academic Publishing: New York, **1998**.
37. Newman, J.; Thomas-Alyea, K. E., *Electrochemical Systems*. 3 ed.; John Wiley & Sons: Hoboken, New Jersey, **2012**.
38. Franks, F., *Water : a Comprehensive Treatise*. Plenum: New York ; London, **1972**.
39. Jessop, P. G. *Green Chemistry* **2011,** 13, (6), 1391-1398.
40. Némethy, G.; Scheraga, H. A. *The Journal of Chemical Physics* **1962,** 36, (12), 3382-3400.
41. Eisenberg, D.; Kauzmann, W., *The Structure and Properties of Water*. Oxford University Press: Oxford, **1969**.
42. Hasted, J., *Water: A Comprehensive Treatise*. Plenum Press: New York, **1972**; Vol. 1.
43. Ben-Naim, A., *Water and Aqueous Solutions: Introduction to a Molecular Theory*. Springer US: New York, **1974**.
44. Henderson, M. A. *Surface Science Reports* **2002,** 46, (1), 1-308.
45. Sigala, P. A.; Ruben, E. A.; Liu, C. W.; Piccoli, P. M. B.; Hohenstein, E. G.; Martínez, T. J.; Schultz, A. J.; Herschlag, D. *Journal of the American Chemical Society* **2015,** 137, (17), 5730-5740.
46. Barrette, W. C.; Johnson, H. W.; Sawyer, D. T. *Analytical chemistry* **2002,** 56, (11), 1890-1898.
47. Wells, C. F. *Journal of the Chemical Society, Faraday Transactions 1: Physical Chemistry in Condensed Phases* **1974,** 70, (0), 694-704.
48. Smallwood, I. M., *Handbook of Organic Solvent Properties*. Butterworth-Heinemann: Oxford, **1996**; p 289-305.

49. Zhu, X.-Q.; Hao, W.-F.; Tang, H.; Wang, C.-H.; Cheng, J.-P. *Journal of the American Chemical Society* **2005,** 127, (8), 2696-2708.
50. Cox, B. G.; Parker, A. J. *Journal of the American Chemical Society* **1973,** 95, (2), 402-407.
51. Cox, B. G.; Parker, A. J. *Journal of the American Chemical Society* **1973,** 95, (2), 408-410.
52. Cox, B. G.; Hedwig, G. R.; Parker, A. J.; Watts, D. W. *Australian Journal of Chemistry* **1974,** 27, (3), 477-501.
53. Cox, B. G.; Parker, A. J.; Waghorne, W. E. *The Journal of Physical Chemistry* **1974,** 78, (17), 1731-1740.
54. Cox, B. G.; Natarajan, R.; Waghorne, W. E. *Journal of the Chemical Society, Faraday Transactions 1: Physical Chemistry in Condensed Phases* **1979,** 75, (0), 86-95.
55. Kolthoff, I. M.; Coetzee, J. F. *Journal of the American Chemical Society* **1957,** 79, (8), 1852-1858.
56. Coetzee, J. F.; Kolthoff, I. M. *Journal of the American Chemical Society* **1957,** 79, (23), 6110-6115.
57. Kolthoff, I. M.; Coetzee, J. F. *Journal of the American Chemical Society* **1957,** 79, (4), 870-874.
58. Coetzee, J. F.; Padmanabhan, G. R. *The Journal of Physical Chemistry* **1962,** 66, (9), 1708-1713.
59. Coetzee, J. F.; McGuire, D. K. *The Journal of Physical Chemistry* **1963,** 67, (9), 1810-1814.
60. Coetzee, J. F.; Padmanabhan, G. R.; Cunningham, G. P. *Talanta* **1964,** 11, (2), 93-103.
61. Reimers, J. R.; Hall, L. E. *Journal of the American Chemical Society* **1999,** 121, (15), 3730-3744.
62. Eaton, G.; Pena-Nuñez, A. S.; Symons, M. C. R. *Journal of the Chemical Society, Faraday Transactions 1: Physical Chemistry in Condensed Phases* **1988,** 84, (6), 2181-2193.
63. Moreau, C.; Douhéret, G. *Thermochimica Acta* **1975,** 13, (4), 385-392.
64. Aurbach, D., *Nonaqueous Electrochemistry*. Marcel Dekker, Inc.: New York, **1999**.
65. Cobble, J. W.; Murray, R. C. *Faraday Discussions of the Chemical Society* **1977,** 64, (0), 144-149.
66. Linert, W., *Highlights in Solute-Solvent Interactions*. Springer-Verlag Wien GmbH: New York, **2002**.
67. Buckingham, A. D. *Discussions of the Faraday Society* **1957,** 24, (0), 151-157.
68. Jensen, W. B. *Chemical Reviews* **1978,** 78, (1), 1-22.
69. Krygowski, T. M.; Fawcett, W. R. *Journal of the American Chemical Society* **1975,** 97, (8), 2143-2148.
70. Krygowski, T. M.; Radomski, J. P.; Rzeszowiak, A.; Wrona, P. K.; Reichardt, C. *Tetrahedron* **1981,** 37, (1), 119-125.
71. Ohtaki, H. *Monatshefte fuer Chemie/Chemical Monthly* **2001,** 132, (11), 1237-1268.
72. Koneshan, S.; Rasaiah, J. C.; Lynden-Bell, R. M.; Lee, S. H. *The Journal of Physical Chemistry B* **1998,** 102, (21), 4193-4204.
73. Mukerjee, P. *The Journal of Physical Chemistry* **1961,** 65, (5), 740-744.

74. Frank, H. S.; Wen, W.-Y. *Discussions of the Faraday Society* **1957,** 24, (0), 133-140.
75. Parker, A. J. *Chemical Reviews* **1969,** 69, (1), 1-32.
76. Tomasi, J.; Persico, M. *Chemical Reviews* **1994,** 94, (7), 2027-2094.
77. Singh, P.; MacLeod, I. D.; Parker, A. J. *Journal of Solution Chemistry* **1982,** 11, (7), 495-508.
78. Takei, T. *Surface Technology* **1979,** 8, (6), 543-552.
79. Huppert, D.; Kolodney, E.; Gutman, M.; Nachliel, E. *Journal of the American Chemical Society* **1982,** 104, (25), 6949-6953.
80. Schmid, R. *Journal of Solution Chemistry* **1983,** 12, (2), 135-152.
81. Leo, A.; Hansch, C.; Elkins, D. *Chemical Reviews* **1971,** 71, (6), 525-616.
82. Hummer, G.; Pratt, L. R.; García, A. E. *The Journal of Physical Chemistry* **1996,** 100, (4), 1206-1215.
83. Amatore, C.; Jutand, A.; Thuilliez, A. *Organometallics* **2001,** 20, (15), 3241-3249.
84. Amatore, C.; Jutand, A. *Accounts of Chemical Research* **2000,** 33, (5), 314-321.
85. Amatore, C.; Carre, E.; Jutand, A.; M'Barki, M. A.; Meyer, G. *Organometallics* **1995,** 14, (12), 5605-5614.
86. Ohtaki, H.; Radnai, T. *Chemical Reviews* **1993,** 93, (3), 1157-1204.
87. Parker, A. J. *Quarterly Reviews, Chemical Society* **1962,** 16, (2), 163-187.
88. Bockris, J. O. M.; Khan, S. U. M., *Surface Electrochemistry: A Molecular Level Approach*. 1 ed.; Springer Science+Business Media: New York, **1993**.
89. Conway, B. E., *Theory and Principles of Electrode Processes*. **1965**.
90. Conway, B. E. *Progress in Surface Science* **1984,** 16, (1), 1-137.
91. Adzic, R.; Bockris, J. O. M.; Conway, B. E.; White, R. E., *Modern Aspects of Electrochemistry*. **1990**; p 163.
92. Lukaszewski, M.; Soszko, M.; Czerwinski, A. *Int. J. Electrochem. Sci.* **2016,** 11, (6), 4442-4469.
93. Jaaf-Golze, K. A.; Kolb, D. M.; Scherson, D. *Journal of Electroanalytical Chemistry and Interfacial Electrochemistry* **1986,** 200, (1), 353-362.
94. Nichols, R. J.; Magnussen, O. M.; Hotlos, J.; Twomey, T.; Behm, R. J.; Kolb, D. M. *Journal of Electroanalytical Chemistry and Interfacial Electrochemistry* **1990,** 290, (1), 21-31.
95. Stimming, U.; Vogel, R.; Kolb, D. M.; Will, T. *Journal of Power Sources* **1993,** 43, (1), 169-180.
96. Kolb, D. M. *Angewandte Chemie International Edition* **2001,** 40, (7), 1162-1181.
97. Kolb, D. M. *Surface Science* **2002,** 500, (1), 722-740.
98. Marković, N. M.; Marinković, N. S.; Adžić, R. R. *Journal of Electroanalytical Chemistry and Interfacial Electrochemistry* **1988,** 241, (1), 309-328.
99. Furuya, N.; Koide, S. *Surface Science* **1989,** 220, (1), 18-28.
100. Faguy, P. W.; Markovic, N.; Adzic, R. R.; Fierro, C. A.; Yeager, E. B. *Journal of Electroanalytical Chemistry and Interfacial Electrochemistry* **1990,** 289, (1), 245-262.
101. Marković, N. M.; Marinković, N. S.; Adžić, R. R. *Journal of Electroanalytical Chemistry and Interfacial Electrochemistry* **1991,** 314, (1), 289-306.

102. Parsons, R.; Ritzoulis, G. *Journal of Electroanalytical Chemistry and Interfacial Electrochemistry* **1991,** 318, (1), 1-24.
103. Nart, F. C.; Iwasita, T.; Weber, M. *Electrochimica Acta* **1994,** 39, (13), 2093-2096.
104. Funtikov, A. M.; Linke, U.; Stimming, U.; Vogel, R. *Surface Science* **1995,** 324, (1), L343-L348.
105. Markovic, N. M.; Gasteiger, H. A.; Ross, P. N. *The Journal of Physical Chemistry* **1995,** 99, (11), 3411-3415.
106. Iwasita, T.; Nart, F. C.; Rodes, A.; Pastor, E.; Weber, M. *Electrochimica Acta* **1995,** 40, (1), 53-59.
107. Hoshi, N.; Suzuki, T.; Hori, Y. *Journal of Electroanalytical Chemistry* **1996,** 416, (1), 61-65.
108. Xia, X. H.; Iwasita, T.; Ge, F.; Vielstich, W. *Electrochim. Acta* **1996,** 41, 711.
109. Grgur, B.; Marković, N.; Ross, P. *Canadian Journal of Chemistry* **1997,** 75, (11), 1465-1471.
110. Markovic, N.; Grgur, B.; Ross, P. *The Journal of Physical Chemistry B* **1997,** 101, (27), 5405-5413.
111. Funtikov, A. M.; Stimming, U.; Vogel, R. *Journal of Electroanalytical Chemistry* **1997,** 428, (1), 147-153.
112. Gomez, R.; Orts, J. M.; Feliu, J. M., *Anion Adsorption and Charge Transfer on Single-Crystal Electrodes*. **1997**.
113. Giesen, M.; Dietterle, M.; Stapel, D.; Ibach, H.; Kolb, D. M. *Surface Science* **1997,** 384, (1), 168-178.
114. Martin, H. B.; Argoitia, A.; Angus, J. C.; Landau, U. *Journal of The Electrochemical Society* **1999,** 146, (8), 2959-2964.
115. Climent, V.; Coles, B. A.; Compton, R. G. *The Journal of Physical Chemistry B* **2002,** 106, (20), 5258-5265.
116. Climent, V.; Coles, B. A.; Compton, R. G. *The Journal of Physical Chemistry B* **2002,** 106, (23), 5988-5996.
117. Ross, J. W.; DeMars, R. D.; Shain, I. *Analytical chemistry* **1956,** 28, (11), 1768-1771.
118. Tokuda, K.; Enomoto, N.; Matsuda, H.; Koizumi, N. *Journal of Electroanalytical Chemistry and Interfacial Electrochemistry* **1983,** 159, (1), 23-32.
119. McCreery, R. L. *Chemical Reviews* **2008,** 108, (7), 2646-2687.
120. Alkire, R. C.; Bartlett, P. N.; Lipkowski, J., *Electrochemistry of Carbon Electrodes*. Wiley VCH Verlag GmbH & Co. KGaA: Weinheim, Germany, **2015**.
121. Unwin, P. R.; Güell, A. G.; Zhang, G. *Accounts of Chemical Research* **2016,** 49, (9), 2041-2048.
122. Macpherson, J. V. *Physical Chemistry Chemical Physics* **2015,** 17, (5), 2935-2949.
123. Macpherson, J. V., The Use of Conducting Diamond in Electrochemistry. In *Electrochemistry of Carbon Electrodes*, Alkire, R. C.; Bartlett, P. N.; Lipkowski, J., Eds. WileyVCH Verlag GmbH & Co. KGaA: Weinheim, Germany, 2016; pp 163-210.
124. Masood, A.; Aslam, M.; Tamor, M. A.; Potter, T. J. *Applied Physics Letters* **1992,** 61, (15), 1832-1834.
125. Swain, G. M.; Ramesham, R. *Analytical chemistry* **1993,** 65, (4), 345-351.
126. Xu, J.; Granger, M. C.; Chen, Q.; Strojek, J. W.; Lister, T. E.; Swain, G. M. *Analytical chemistry* **1997,** 69, (19), 591A-597A.

127. Cvacˇka, J.; Quaiserova, V.; Park, J.; Show, Y.; Muck, A.; Swain, G. M. *Analytical chemistry* **2003,** 75, (11), 2678-2687.
128. Thomas, A. V.; Patel, H. H.; Reif, L. A.; Chemburkar, S. R.; Sawick, D. P.; Shelat, B.; Balmer, M. K.; Patel, R. R. *Organic Process Research & Development* **1997,** 1, (4), 294-299.
129. Newland, J. C. The Fabrication and Application of Diamond Sensors for Electrochemical Analysis in Single and Multiple Phase Systems. Ph. D. thesis, University of Warwick, **2014**.
130. Meng, L. Thermo-Electrochemistry of Boron Doped Diamond from Fundamentals to Application. Ph. D. thesis, University of Warwick, **2016**.
131. Yang, N., *Novel Aspects of Diamond*. Springer: Berlin, Germany, **2015**; Vol. 121.
132. Bundy, F. P.; Hall, H. T.; Strong, H. M.; Wentorf Jun, R. H. *Nature* **1955,** 176, 51.
133. Bundy, F. P. *The Journal of Chemical Physics* **1963,** 38, (3), 631-643.
134. Amotz, D. B.; Lee, M. R.; Cho, S. Y.; List, D. J. *The Journal of Chemical Physics* **1992,** 96, (12), 8781-8792.
135. Gutmann, V., *Coordination Chemistry in Non-Aqueous Solutions*. Springer-Verlag: Vienna, **2012**.
136. Gutmann, V. *Coordination Chemistry Reviews* **1976,** 18, (2), 225-255.
137. Haggerty, S. E. *Earth and Planetary Science Letters* **1994,** 122, (1), 57-69.
138. Seiichiro, M.; Yoichiro, S.; Mutsukazu, K.; Nobuo, S. *Japanese Journal of Applied Physics* **1982,** 21, (4A), L183.
139. Kamo, M.; Sato, Y.; Matsumoto, S.; Setaka, N. *Journal of Crystal Growth* **1983,** 62, (3), 642-644.
140. Spitsyn, B. V.; Bouilov, L. L.; Derjaguin, B. V. *Journal of Crystal Growth* **1981,** 52, 219-226.
141. Matsumoto, S.; Sato, Y.; Tsutsumi, M.; Setaka, N. *Journal of Materials Science* **1982,** 17, (11), 3106-3112.
142. Bachmann, P. K.; Leers, D.; Lydtin, H. *Diamond and Related Materials* **1991,** 1, (1), 1-12.
143. Kobashi, K.; Nishimura, K.; Kawate, Y.; Horiuchi, T. *Physical Review B* **1988,** 38, (6), 4067-4084.
144. Chang, C. P.; Flamm, D. L.; Ibbotson, D. E.; Mucha, J. A. *Journal of Applied Physics* **1988,** 63, (5), 1744-1748.
145. Karasawa, S.; Kobayashi, K.; Watanabe, T.; Togashi, F. *Surface and Coatings Technology* **1990,** 43-44, 41-52.
146. Celii, F. G.; Butler, J. E. *Annual Review of Physical Chemistry* **1991,** 42, (1), 643-684.
147. Butler, J. E.; Woodin, R. L. *Philosophical Transactions of the Royal Society of London. Series A: Physical and Engineering Sciences* **1993,** 342, (1664), 209-224.
148. Angus, J. C.; Argoitia, A.; Gat, R.; Li, Z.; Sunkara, M.; Wang, L.; Wang, Y. *Philosophical Transactions of the Royal Society of London. Series A: Physical and Engineering Sciences* **1993,** 342, (1664), 195-208.
149. Butler, J. E.; Mankelevich, Y. A.; Cheesman, A.; Jie, M.; Ashfold, M. N. R. *Journal of Physics: Condensed Matter* **2009,** 21, (36), 364201.
150. Balmer, R. S.; Brandon, J. R.; Clewes, S. L.; Dhillon, H. K.; Dodson, J. M.; Friel, I.; Inglis, P. N.; Madgwick, T. D.; Markham, M. L.; Mollart, T. P.; Perkins, N.; Scarsbrook, G. A.; Twitchen, D. J.; Whitehead, A. J.; Wilman, J. J.; Woollard, S. M. *Journal of Physics: Condensed Matter* **2009,** 21, (36), 364221.

151. Janssen, G.; van Enckevort, W. J. P.; Vollenberg, W.; Giling, L. J. *Diamond and Related Materials* **1992,** 1, (7), 789-800.
152. Tallaire, A.; Achard, J.; Silva, F.; Sussmann, R. S.; Gicquel, A. *Diamond and Related Materials* **2005,** 14, (3), 249-254.
153. Tallaire, A.; Collins, A. T.; Charles, D.; Achard, J.; Sussmann, R.; Gicquel, A.; Newton, M. E.; Edmonds, A. M.; Cruddace, R. J. *Diamond and Related Materials* **2006,** 15, (10), 1700-1707.
154. Djemia, P.; Tallaire, A.; Achard, J.; Silva, F.; Gicquel, A. *Diamond and Related Materials* **2007,** 16, (4), 962-965.
155. elementsix Electrochemical boron doped diamond. https://www.e6.com/en/home/materials+and+products/polycrystalline+cvd+diamond/electrochemical+boron+doped+diamond/bdd+diamond (19 November 2018),
156. Ostrovskaya, L.; Perevertailo, V.; Ralchenko, V.; Dementjev, A.; Loginova, O. *Diamond and Related Materials* **2002,** 11, (3), 845-850.
157. Salazar-Banda, G. R.; Andrade, L. S.; Nascente, P. A. P.; Pizani, P. S.; Rocha-Filho, R. C.; Avaca, L. A. *Electrochimica Acta* **2006,** 51, (22), 4612-4619.
158. Wang, S.; Swope, V. M.; Butler, J. E.; Feygelson, T.; Swain, G. M. *Diamond and Related Materials* **2009,** 18, (4), 669-677.
159. May, P. W. *Endeavour* **1995,** 19, (3), 101-106.
160. Bundy, F. P. *Journal of Geophysical Research: Solid Earth* **1980,** 85, (B12), 6930-6936.
161. Spear, K. E.; Dismukes, J. P., *Synthetic diamond: emerging CVD science and technology*. John Wiley & Sons: **1994**; Vol. 25.
162. Vandersande, J. W.; Zoltan, L. D. *Diamond and Related Materials* **1995,** 4, (5-6), 641-644.
163. Spicka, H.; Griesser, M.; Hutter, H.; Grasserbauer, M.; Bohr, S.; Haubner, R.; Lux, B. *Diamond and Related Materials* **1996,** 5, (3), 383-387.
164. Gheeraert, E.; Deneuville, A.; Mambou, J. *Diamond and Related Materials* **1998,** 7, (10), 1509-1512.
165. Lagrange, J. P.; Deneuville, A.; Gheeraert, E. *Diamond and Related Materials* **1998,** 7, (9), 1390-1393.
166. Inushima, T.; Matsushita, T.; Ohya, S.; Shiomi, H. *Diamond and Related Materials* **2000,** 9, (3), 1066-1070.
167. Williams, A. W. S.; Lightowlers, E. C.; Collins, A. T. *Journal of Physics C: Solid State Physics* **1970,** 3, (8), 1727.
168. Blase, X.; Bustarret, E.; Chapelier, C.; Klein, T.; Marcenat, C. *Nature Materials* **2009,** 8, 375.
169. Lee, B.-J.; Ahn, B.-T.; Baik, Y.-J. *Diamond and Related Materials* **1999,** 8, (2), 251-256.
170. Ushizawa, K.; Watanabe, K.; Ando, T.; Sakaguchi, I.; Nishitani-Gamo, M.; Sato, Y.; Kanda, H. *Diamond and Related Materials* **1998,** 7, (11), 1719-1722.
171. Patten, H. V.; Meadows, K. E.; Hutton, L. A.; Iacobini, J. G.; Battistel, D.; McKelvey, K.; Colburn, A. W.; Newton, M. E.; Macpherson, J. V.; Unwin, P. R. *Angewandte Chemie International Edition* **2012,** 51, (28), 7002-6.
172. Tomlinson, L. I.; Patten, H. V.; Green, B. L.; Iacobini, J.; Meadows, K. E.; McKelvey, K.; Unwin, P. R.; Newton, M. E.; Macpherson, J. V. *Electroanalysis* **2016,** 28, (10), 2297-2302.
173. Iwaki, M.; Sato, S.; Takahashi, K.; Sakairi, H. *Nuclear Instruments and Methods in Physics Research* **1983,** 209-210, 1129-1133.

174. Alehashem, S.; Chambers, F.; Strojek, J. W.; Swain, G. M.; Ramesham, R. *Analytical chemistry* **1995,** 67, (17), 2812-2821.
175. Ulrich, G.; Winfried, V.; Jens, Z. *Measurement Science and Technology* **2009,** 20, (4), 042002.
176. elementsix Synthetic Diamond Properties. https://www.e6.com/en/Home/The+power+of+supermaterials/Synthetic+diamonds+extreme+properties/ (19 November 2018),
177. Etzel, K. D.; Bickel, K. R.; Schuster, R. *Chemphyschem : a European journal of chemical physics and physical chemistry* **2010,** 11, (7), 1416-24.
178. Ferro-García, M. A.; Rivera-Utrilla, J.; Rodríguez-Gordillo, J.; Bautista-Toledo, I. *Carbon* **1988,** 26, (3), 363-373.
179. Niu, J.; Conway, B. E. *Journal of Electroanalytical Chemistry* **2003,** 546, 59-72.
180. Oren, Y.; Soffer, A. *Electrochimica Acta* **1983,** 28, (11), 1649-1654.
181. Tricoli, V.; Vatistas, N.; Marconi, P. F. *Journal of Applied Electrochemistry* **1993,** 23, (4), 390-392.
182. Chailapakul, O.; Popa, E.; Tai, H.; Sarada, B.; Tryk, D.; Fujishima, A. *Electrochemistry communications* **2000,** 2, (6), 422-426.
183. Gandini, D.; Mahé, E.; Michaud, P. A.; Haenni, W.; Perret, A.; Comninellis, C. *Journal of Applied Electrochemistry* **2000,** 30, (12), 1345-1350.
184. Sarada, B. V.; Rao, T. N.; Tryk, D. A.; Fujishima, A. *Analytical chemistry* **2000,** 72, (7), 1632-1638.
185. Read, T. L.; Macpherson, J. V. *Journal of Visualized Experiments* **2016**, (107), e53484.
186. Kim, J.; Chun, Y.-S.; Lee, S.-K.; Lim, D.-S. *RSC Advances* **2015,** 5, (2), 1103-1108.
187. Bron, M.; Roth, C., Carbon Materials in Low-Temperature Polymer Electrolyte Membrane Fuel Cells. In *Electrochemistry of Carbon Electrodes*, Alkire, R. C.; Bartlett, P. N.; Lipkowski, J., Eds. Wiley VCH Verlag GmbH & Co. KGaA: Weinheim, Germany, 2016; pp 241-284.
188. Helmholtz, H. *Annalen der Physik und Chemie* **1879,** 243, (7), 337-382.
189. Gurney, R. W. *Physical Review* **1935,** 47, (6), 479-482.
190. Parsons, R. *Chemical Reviews* **1990,** 90, (5), 813-826.
191. Grahame, D. C. *Chemical Reviews* **1947,** 41, (3), 441-501.
192. Zaera, F. *Chemical Reviews* **2012,** 112, (5), 2920-2986.
193. Devanathan, M. A. V.; Tilak, B. V. K. S. R. A. *Chemical Reviews* **1965,** 65, (6), 635-684.
194. Breitkopf, C.; Swider-Lyons, K., Modern Electrochemistry. In *Springer Handbook of Electrochemical Energy*, Breitkopf, C.; Swider-Lyons, K., Eds. Springer: Berlin, Heidelberg, 2017; pp 11-30.
195. Atkins, P.; De Paula, J., *Atkins' physical chemistry*. 9 ed.; W. H. Freeman and Company: New York, **2010**.
196. Gouy, M. *Journal of Theoretical and Applied Physics* **1910,** 9, (1), 457-468.
197. Chapman, D. L. *The London, Edinburgh, and Dublin Philosophical Magazine and Journal of Science* **1913,** 25, (148), 475-481.
198. Stern, O. *Z. Elektrochem* **1924,** 30, (508), 1014-1020.
199. Grahame, D. C. *Zeitschrift für Elektrochemie, Berichte der Bunsengesellschaft für physikalische Chemie* **1958,** 62, (3), 264-274.
200. Mott, N. F.; Watts-Tobin, R. J. *Electrochimica Acta* **1961,** 4, (2), 79-107.

201. Bedzyk, M.; Bommarito, G.; Caffrey, M.; Penner, T. *Science* **1990,** 248, (4951), 52-56.
202. Oldham, K. B. *Journal of Electroanalytical Chemistry* **2008,** 613, (2), 131-138.
203. Pavaskar, G.; Ramakrishnasubramanian, K.; Kandagal, V. S.; Kumar, P. *Frontiers in Energy Research* **2018,** 5, (36).
204. Schmickler, W.; Santos, E., Thermodynamics of ideal polarizable interfaces. In *Interfacial Electrochemistry*, Springer: Berlin, Heidelberg, 2010; pp 77-89.
205. Grahame, D. C. *Annual Review of Physical Chemistry* **1955,** 6, (1), 337-358.
206. Grahame, D. C. *Journal of the American Chemical Society* **1958,** 80, (16), 4201-4210.
207. Grahame, D. C.; Parsons, R. *Journal of the American Chemical Society* **1961,** 83, (6), 1291-1296.
208. Levine, S. *Journal of Colloid and Interface Science* **1971,** 37, (3), 619-634.
209. Levine, S.; Mingins, J.; Bell, G. M. *Journal of Electroanalytical Chemistry and Interfacial Electrochemistry* **1967,** 13, (3), 280-329.
210. Barradas, R. G.; Hamilton, P. G.; Conway, B. E. *The Journal of Physical Chemistry* **1965,** 69, (10), 3411-3417.
211. Bockris, J. O. M.; Khan, S. U., *Quantum Electrochemistry*. Plenum Press: New York and London, **1979**.
212. Bockris, J. O. M., *Comprehensive Treatise Of Electrochemistry*. Plenum Press: New York, **1980**.
213. Conway, B. E., *Thermodynamic and Transport Properties of Aqueous and Molten Electrolytes*. Plenum press: New York ; London, **1983**.
214. Landstorfer, M.; Guhlke, C.; Dreyer, W. *Electrochimica Acta* **2016,** 201, 187-219.
215. You, H.; Liu, Y.; Ulvestad, A.; Pierce, M. S.; Komanicky, V. *Current Opinion in Electrochemistry* **2017,** 4, (1), 89-94.
216. Yan, J.-W.; Tian, Z.-Q.; Mao, B.-W. *Current Opinion in Electrochemistry* **2017,** 4, (1), 105-111.
217. Pajkossy, T.; Jurczakowski, R. *Current Opinion in Electrochemistry* **2017,** 1, (1), 53-58.
218. Lin, Z.; Taberna, P.-L.; Simon, P. *Current Opinion in Electrochemistry* **2017,** 6, (1), 115-119.
219. Favaro, M.; Jeong, B.; Ross, P. N.; Yano, J.; Hussain, Z.; Liu, Z.; Crumlin, E. J. *Nature Communications* **2016,** 7, 12695.
220. Page, A.; Perry, D.; Unwin, P. R. *Proceedings of the Royal Society A: Mathematical, Physical & Engineering Sciences* **2017,** 473, (2200), 20160889.
221. Chen, S., Practical Electrochemical Cells. In *Handbook of Electrochemistry*, Zoski, C. G., Ed. Elsevier: Amsterdam, 2007; pp 33-56.
222. Nasirpouri, F., An Overview to Electrochemistry. In *Electrodeposition of Nanostructured Materials*, Springer International Publishing: Switzerland, 2017; pp 43-73.
223. Ciobanu, M.; Wilburn, J. P.; Krim, M. L.; Cliffel, D. E., Fundamentals. In *Handbook of Electrochemistry*, Zoski, C. G., Ed. Elsevier: Amsterdam, 2007; pp 3-29.
224. Arning, M. D.; Minteer, S. D., Electrode Potentials. In *Handbook of Electrochemistry*, Zoski, C. G., Ed. Elsevier: Amsterdam, 2007; pp 813-827.
225. Pletcher, D., *A First Course In Electrode Processes*. Royal Society of Chemistry: London, **2009**.

226. Lyons, E. H. *Journal of The Electrochemical Society* **1954,** 101, (7), 363-375.
227. Lyons, E. H. *Journal of The Electrochemical Society* **1954,** 101, (7), 376-381.
228. Harrison, J. A.; Thompson, J. *Electrochimica Acta* **1973,** 18, (11), 829-834.
229. Turner, D. R.; Whitfield, M. *Journal of Electroanalytical Chemistry and Interfacial Electrochemistry* **1979,** 103, (1), 43-60.
230. Dini, J. W., *Electrodeposition: The Material Science of Coatings and Substrates*. Noyes Publications: New Jersey, **1993**.
231. Stoyanov, S. *Thin Solid Films* **1973,** 18, (1), 91-98.
232. Milchev, A.; Stoyanov, S. *Journal of Electroanalytical Chemistry and Interfacial Electrochemistry* **1976,** 72, (1), 33-43.
233. Mostany, J.; Mozota, J.; Scharifker, B. R. *Journal of Electroanalytical Chemistry and Interfacial Electrochemistry* **1984,** 177, (1), 25-37.
234. Zhang, Z.; Lagally, M. G. *Science* **1997,** 276, (5311), 377-383.
235. Becker, R.; Doring, W. *Annalen der Physik* **1954**.
236. Walton, D. *The Journal of Chemical Physics* **1962,** 37, (10), 2182-2188.
237. Budevski, E.; Staikov, G.; Lorenz, W. J. *Electrochimica Acta* **2000,** 45, (15–16), 2559-2574.
238. Ustarroz, J. New insights into nanoparticle electrodeposition: an electrochemical aggregative growth mechanism. Ph. D. thesis, Vrije Universiteit Brussel, Brussel, **2013**.
239. Murray, C. B.; Kagan, C. R.; Bawendi, M. G. *Annual Review of Materials Science* **2000,** 30, (1), 545-610.
240. Teng, X.; Liang, X.; Maksimuk, S.; Yang, H. *Small* **2006,** 2, (2), 249-253.
241. Woehl, T. J.; Evans, J. E.; Arslan, I.; Ristenpart, W. D.; Browning, N. D. *ACS Nano* **2012,** 6, (10), 8599-8610.
242. Bicelli, L. P.; Bozzini, B.; Mele, C.; D'Urzo, L. *Int. J. Electrochem. Sci.* **2008,** 3, (4), 356-408.
243. Budevski, E. B.; Staikov, G. T.; Lorenz, W. J., *Electrochemical phase formation and growth: an introduction to the initial stages of metal deposition*. John Wiley & Sons: **2008**.
244. Petrii, O. A. *Russian Chemical Reviews* **2015,** 84, (2), 159-193.
245. Staikov, G. *Nanoscale* **2016,** 8, (29), 13880-13892.
246. Kelaidopoulou, A.; Kokkinidis, G.; Milchev, A. *Journal of Electroanalytical Chemistry* **1998,** 444, (2), 195-201.
247. Staikov, G.; Milchev, A., The Impact of Electrocrystallization on Nanotechnology. In *Electrocrystallization in Nanotechnology*, Wiley-vch Verlag GmbH & Co. KGaA: Weinheim, 2007; pp 1-29.
248. Valov, I.; Sapezanskaia, I.; Nayak, A.; Tsuruoka, T.; Bredow, T.; Hasegawa, T.; Staikov, G.; Aono, M.; Waser, R. *Nature Materials* **2012,** 11, 530-535.
249. Penner, R. M. *The Journal of Physical Chemistry B* **2002,** 106, (13), 3339-3353.
250. Penner, R. M., Electrodeposition of Nanostructures and Microstructures on Highly Oriented Pyrolytic Graphite (HOPG). In *Handbook of Electrochemistry*, Zoski, C. G., Ed. Elsevier: Amsterdam, 2007; pp 661-677.
251. Volmer, M.; Weber, A. *zpch* **1926,** 119U, (1), 277.
252. Burton, W. K.; Cabrera, N.; Frank, F. C. *Philosophical Transactions of the Royal Society A: Mathematical, Physical and Engineering Sciences* **1951,** 243, (866), 299-358.

253. Scharifker, B.; Hills, G. *Electrochimica Acta* **1983,** 28, (7), 879-889.
254. Scharifker, B. R.; Mostany, J. *Journal of Electroanalytical Chemistry and Interfacial Electrochemistry* **1984,** 177, (1), 13-23.
255. Lefebvre, M. C.; Conway, B. E. *Journal of Electroanalytical Chemistry* **2000,** 480, (1), 46-58.
256. Boxley, C. J.; White, H. S.; Lister, T. E.; Pinhero, P. J. *The Journal of Physical Chemistry B* **2003,** 107, (2), 451-458.
257. Rodríguez Nieto, F. J.; Andreasen, G.; Martins, M. E.; Castez, F.; Salvarezza, R. C.; Arvia, A. J. *The Journal of Physical Chemistry B* **2003,** 107, (41), 11452-11466.
258. LeBeau, J. M.; Findlay, S. D.; Allen, L. J.; Stemmer, S. *Journal of Physics: Conference Series* **2012,** 371, (1), 012053.
259. Uosaki, K. *Japanese Journal of Applied Physics* **2015,** 54, (3), 14.
260. Weber, M. L.; Wilson, A. J.; Willets, K. A. *The Journal of Physical Chemistry C* **2015,** 119, (32), 18591-18601.
261. Alloyeau, D.; Dachraoui, W.; Javed, Y.; Belkahla, H.; Wang, G.; Lecoq, H.; Ammar, S.; Ersen, O.; Wisnet, A.; Gazeau, F.; Ricolleau, C. *Nano Letters* **2015,** 15, (4), 2574-2581.
262. Hodnik, N.; Dehm, G.; Mayrhofer, K. J. J. *Accounts of Chemical Research* **2016,** 49, (9), 2015-2022.
263. Jovanovič, P.; Hodnik, N.; Ruiz-Zepeda, F.; Arcon, I.; Jozinović, B.; Zorko, M.; Bele, M.; Šala, M.; Šelih, V. S.; Hocevar, S. B.; Gaberscek, M. *Journal of the American Chemical Society* **2017**.
264. LaGrow, A. P.; Ward, M. R.; Lloyd, D. C.; Gai, P. L.; Boyes, E. D. *Journal of the American Chemical Society* **2017,** 139, (1), 179-185.
265. van den Bos, K. H. W.; Altantzis, T.; De Backer, A.; Van Aert, S.; Bals, S. *Advances in Physics: X* **2018,** 3, (1), 814-832.
266. Cruickshank, B. J.; Gewirth, A. A.; Rynders, R. M.; Alkire, R. C. *Journal of The Electrochemical Society* **1992,** 139, (10), 2829-2832.
267. Zoval, J. V.; Lee, J.; Gorer, S.; Penner, R. M. *The Journal of Physical Chemistry B* **1998,** 102, (7), 1166-1175.
268. Radisic, A.; Long, J. G.; Hoffmann, P. M.; Searson, P. C. *Journal of The Electrochemical Society* **2001,** 148, (1), C41-C46.
269. Hyde, M. E.; Banks, C. E.; Compton, R. G. *Electroanalysis* **2004,** 16, (5), 345-354.
270. Day, T. M.; Unwin, P. R.; Macpherson, J. V. *Nano Letters* **2007,** 7, (1), 51-57.
271. Dudin, P. V.; Unwin, P. R.; Macpherson, J. V. *The Journal of Physical Chemistry C* **2010,** 114, (31), 13241-13248.
272. Lai, S. C. S.; Lazenby, R. A.; Kirkman, P. M.; Unwin, P. R. *Chemical Science* **2015,** 6, (2), 1126-1138.
273. Kim, Y.-R.; Lai, S. C. S.; McKelvey, K.; Zhang, G.; Perry, D.; Miller, T. S.; Unwin, P. R. *The Journal of Physical Chemistry C* **2015,** 119, (30), 17389-17397.
274. Miller, T. S.; Sansuk, S.; E, S. P.; Lai, S. C. S.; Macpherson, J. V.; Unwin, P. R. *Catalysis Today* **2015,** 244, 136-145.
275. Bentley, C. L.; Kang, M.; Unwin, P. R. *Current Opinion in Electrochemistry* **2017,** 6, (1), 23-30.
276. Breuer, N.; Stimming, U.; Vogel, R. *Electrochimica Acta* **1995,** 40, (10), 1401-1409.

277. Allongue, P.; Maroun, F. *Curr. Opin. Solid State Mat. Sci.* **2006,** 10, (3-4), 173-181.
278. Ustarroz, J.; Hammons, J. A.; Altantzis, T.; Hubin, A.; Bals, S.; Terryn, H. *Journal of the American Chemical Society* **2013,** 135, (31), 11550-11561.
279. Harniman, R. L.; Plana, D.; Carter, G. H.; Bradley, K. A.; Miles, M. J.; Fermín, D. J. *Nature Communications* **2017,** 8, (1), 1-8.
280. Radisic, A.; Vereecken, P. M.; Hannon, J. B.; Searson, P. C.; Ross, F. M. *Nano Letters* **2006,** 6, (2), 238-242.
281. Ustarroz, J.; Gupta, U.; Hubin, A.; Bals, S.; Terryn, H. *Electrochemistry Communications* **2010,** 12, (12), 1706-1709.
282. Becker, R.; Döring, W. *Annalen der Physik* **1935,** 416, (8), 719-752.
283. Ustarroz, J.; Hammons, J. A.; Van Ingelgem, Y.; Tzedaki, M.; Hubin, A.; Terryn, H. *Electrochemistry Communications* **2011,** 13, (12), 1320-1323.
284. Ustarroz, J.; Ke, X.; Hubin, A.; Bals, S.; Terryn, H. *The Journal of Physical Chemistry C* **2012,** 116, (3), 2322-2329.
285. Scharifker, B. R.; Mostany, J.; Palomar-Pardavé, M.; González, I. *Journal of The Electrochemical Society* **1999,** 146, (3), 1005-1012.
286. Heerman, L.; Tarallo, A. *Electrochemistry Communications* **2000,** 2, (2), 85-89.
287. Grujicic, D.; Pesic, B. *Electrochimica Acta* **2002,** 47, (18), 2901-2912.
288. Palomar-Pardavé, M.; Ramírez, M. T.; González, I.; Serruya, A.; Scharifker, B. R. *Journal of The Electrochemical Society* **1996,** 143, (5), 1551-1558.
289. Heerman, L.; Tarallo, A. *Journal of Electroanalytical Chemistry* **1999,** 470, (1), 70-76.
290. Xu, X. H.; Hussey, C. L. *Journal of The Electrochemical Society* **1992,** 139, (11), 3103-3108.
291. Zouari, I.; Lapicque, F.; Calvo, M.; Cabrera, M. *Chemical Engineering Science* **1990,** 45, (8), 2467-2474.
292. Zouari, I.; Lapicque, F.; Calvo, M.; Cabrera, M. *Journal of The Electrochemical Society* **1992,** 139, (8), 2163-2170.
293. Fleischmann, M.; Hendra, P. J.; McQuillan, A. J. *Chemical Physics Letters* **1974,** 26, (2), 163-166.
294. Fleischmann, M.; Pons, S.; Sousa, J.; Ghoroghchian, J. *Journal of Electroanalytical Chemistry* **1994,** 366, (1), 171-190.
295. Pötzschke, R. T.; Gervasi, C. A.; Vinzelberg, S.; Staikov, G.; Lorenz, W. J. *Electrochimica Acta* **1995,** 40, (10), 1469-1474.
296. Miranda-Hernández, M.; Palomar-Pardavé, M.; Batina, N.; González, I. *Journal of Electroanalytical Chemistry* **1998,** 443, (1), 81-93.
297. Day, T. M.; Unwin, P. R.; Wilson, N. R.; Macpherson, J. V. *Journal of the American Chemical Society* **2005,** 127, (30), 10639-10647.
298. Jonathan, R. *Japanese Journal of Applied Physics* **2001,** 40, (4S), 2650.
299. Kim, J.; Dick, J. E.; Bard, A. J. *Accounts of Chemical Research* **2016,** 49, (11), 2587-2595.
300. Kim, J.; Bard, A. J. *Journal of the American Chemical Society* **2016,** 138, (3), 975-979.
301. Markov, I. *Thin Solid Films* **1976,** 35, (1), 11-20.
302. Moffat, T. P. *Journal of The Electrochemical Society* **1994,** 141, (11), 3059-3070.
303. Hyde, M. E.; Compton, R. G. *Journal of Electroanalytical Chemistry* **2003,** 549, 1-12.

304. Milchev, A.; Heerman, L. *Electrochimica Acta* **2003,** 48, (20), 2903-2913.
305. Mirkin, M. V.; Nilov, A. P. *Journal of Electroanalytical Chemistry and Interfacial Electrochemistry* **1990,** 283, (1), 35-51.
306. Heerman, L.; Tarallo, A. *Journal of Electroanalytical Chemistry* **1998,** 451, (1), 101-109.
307. Correia, A. N.; Machado, S. A. S.; Avaca, L. A. *Journal of Electroanalytical Chemistry* **2000,** 488, (2), 110-116.
308. Palomar-Pardavé, M.; González, I.; Soto, A. B.; Arce, E. M. *Journal of Electroanalytical Chemistry* **1998,** 443, (1), 125-136.
309. Tarallo, A. *Journal of Electroanalytical Chemistry* **1998,** 1, (451), 101-109.
310. Sluyters-Rehbach, M.; Wijenberg, J. H. O. J.; Bosco, E.; Sluyters, J. H. *Journal of Electroanalytical Chemistry and Interfacial Electrochemistry* **1987,** 236, (1-2), 1-20.
311. Milchev, A.; Zapryanova, T. *Electrochimica acta* **2006,** 51, (14), 2926-2933.
312. Milchev, A.; Zapryanova, T. *Electrochimica Acta* **2006,** 51, (23), 4916-4921.
313. Pei, A.; Zheng, G.; Shi, F.; Li, Y.; Cui, Y. *Nano Letters* **2017,** 17, (2), 1132-1139.
314. Oskam, G.; Long, J. G.; Natarajan, A.; Searson, P. C. *Journal of Physics D: Applied Physics* **1998,** 31, 1927-1949.
315. Oskam, G.; Searson, P. C. *Journal of The Electrochemical Society* **2000,** 147, (6), 2199-2205.
316. Oskam, G.; Searson, P. C. *Surface Science* **2000,** 446, (1), 103-111.
317. Grujicic, D.; Pesic, B. *Electrochimica Acta* **2006,** 51, (13), 2678-2690.
318. Abyaneh, M. Y.; Fleischmann, M.; Del Giudice, E.; Vitiello, G. *Electrochimica Acta* **2009,** 54, (3), 879-887.
319. Zapryanova, T.; Hrussanova, A.; Milchev, A. *Journal of Electroanalytical Chemistry* **2007,** 600, (2), 311-317.
320. Radisic, A.; West, A. C.; Searson, P. C. *Journal of the Electrochemical Society* **2002,** 149, (2), C94-C99.
321. Radisic, A.; Ross, F. M.; Searson, P. C. *The Journal of Physical Chemistry B* **2006,** 110, (15), 7862-7868.
322. Radisic, A.; Vereecken, P. M.; Searson, P. C.; Ross, F. M. *Surface Science* **2006,** 600, (9), 1817-1826.
323. Sheridan, E.; Hjelm, J.; Forster, R. J. *Journal of Electroanalytical Chemistry* **2007,** 608, (1), 1-7.
324. Isse, A. A.; Gottardello, S.; Maccato, C.; Gennaro, A. *Electrochemistry Communications* **2006,** 8, (11), 1707-1712.
325. Komsiyska, L.; Staikov, G. *Electrochimica Acta* **2008,** 54, (2), 168-172.
326. Zoval, J. V.; Stiger, R. M.; Biernacki, P. R.; Penner, R. M. *The Journal of Physical Chemistry* **1996,** 100, (2), 837-844.
327. Suzuki, E. **2002,** 208, (3), 153-157.
328. Zhong, W.; Overney, G.; Tománek, D. *Europhysics Letters* **1991,** 15, (1), 49-54.
329. Simm, A. O.; Ji, X.; Banks, C. E.; Hyde, M. E.; Compton, R. G. *Chemphyschem : a European journal of chemical physics and physical chemistry* **2006,** 7, (3), 704-709.
330. Toghill, K. E.; Compton, R. G. *Electroanalysis* **2010,** 22, (17-18), 1947-1956.
331. Thomas, G.; Goringe, M. J., *Transmission Electron Microscopy of Materials*. Wiley: New York, **1979**.

332. Williamson, M. J.; Tromp, R. M.; Vereecken, P. M.; Hull, R.; Ross, F. M. *Nature Materials* **2003,** 2, (8), 532-536.
333. Chen, H.; Gao, Y.; Zhang, H.; Liu, L.; Yu, H.; Tian, H.; Xie, S.; Li, J. *The Journal of Physical Chemistry B* **2004,** 108, (32), 12038-12043.
334. Ross, F. M. *Science* **2015,** 350, (6267), aaa98861-aaa98869.
335. Gloaguen, F.; Léger, J. M.; Lamy, C.; Marmann, A.; Stimming, U.; Vogel, R. *Electrochimica Acta* **1999,** 44, (11), 1805-1816.
336. Mamme, M. H.; Deconinck, J.; Ustarroz, J. *Electrochimica Acta* **2017,** 258, 662-668.
337. Mamme, M. H.; Kohn, C.; Deconinck, J.; Ustarroz, J. *Nanoscale* **2018,** 10, (15), 7194-7209.
338. Gründler, P., *In-situ Thermoelectrochemistry*. Springer: Berlin Heidelberg, **2015**.
339. Gründler, P.; Kirbs, A.; Dunsch, L. *Chemphyschem : a European journal of chemical physics and physical chemistry* **2009,** 10, (11), 1722-1746.
340. Meng, L.; Iacobini, J. G.; Joseph, M. B.; Macpherson, J. V.; Newton, M. E. *Faraday Discuss* **2014,** 172, 421-38.
341. Abbott, A. P.; Durling, N. E. *Physical Chemistry Chemical Physics* **2001,** 3, (4), 579-582.
342. Unwin, P. R., *Instrumentation and Electroanalytical Chemistry*. Wiley-VCH: Weinheim, **2003**.
343. Akkermans, R. P.; Suárez, M. F.; Roberts, S. L.; Fulian, Q.; Compton, R. G. *Electroanalysis* **1999,** 11, (16), 1191-1202.
344. Wildgoose, G. G.; Giovanelli, D.; Lawrence, N. S.; Compton, R. G. *Electroanalysis* **2004,** 16, (6), 421-433.
345. Ramírez, C.; Arce, E. M.; Romero-Romo, M.; Palomar-Pardavé, M. *Solid State Ionics* **2004,** 169, (1), 81-85.
346. Gründler, P.; Zerihun, T.; Kirbs, A.; Grabow, H. *Analytica Chimica Acta* **1995,** 305, (1), 232-240.
347. Compton, R. G.; Coles, B. A.; Marken, F. *Chemical communications* **1998**, (23), 2595-2596.
348. Marken, F.; Matthews, S. L.; Compton, R. G.; Coles, B. A. *Electroanalysis* **2000,** 12, (4), 267-273.
349. Marken, F.; Sur, U. K.; Coles, B. A.; Compton, R. G. *Electrochimica Acta* **2006,** 51, (11), 2195-2203.
350. Gründler, P.; Kirbs, A. *Electroanalysis* **1999,** 11, (4), 223-228.
351. Gründler, P.; Frank, O.; Kavan, L.; Dunsch, L. *Chemphyschem : a European journal of chemical physics and physical chemistry* **2009,** 10, (3), 559-563.
352. Gründler, P. *J Fresenius' Journal of Analytical Chemistry* **1998,** 362, (2), 180-183.
353. Miller, B. *Journal of the Electrochemical Society of India* **1983,** 130, (7), 1639-1640.
354. Gabrielli, C.; Keddam, M.; Lizee, J. F. *Journal of Electroanalytical Chemistry and Interfacial Electrochemistry* **1983,** 148, (2), 293-297.
355. Wachholz, F.; Gimsa, J.; Duwensee, H.; Grabow, H.; Gründler, P.; Flechsig, G.-U. *Electroanalysis* **2007,** 19, (5), 535-540.
356. von Gutfeld, R. J.; Budd, H. F. *Applied Physics Letters* **1979,** 34, (10), 617-619.
357. von Gutfeld, R. J.; Tynan, E. E.; Melcher, R. L.; Blum, S. E. *Applied Physics Letters* **1979,** 35, (9), 651-653.

358. Puippe, J. C.; Acosta, R. E.; von Gutfeld, R. J. *Journal of The Electrochemical Society* **1981,** 128, (12), 2539-2545.
359. von Gutfeld, R. J.; Romankiw, L. T.; Acosta, R. E. *IBM Journal of Research and Development* **1982,** 26, (2), 136-144.
360. Gómez, E.; Pollina, R.; Vallés, E. *Journal of Electroanalytical Chemistry* **1995,** 397, (1), 111-118.
361. Goux, A.; Pauporté, T.; Chivot, J.; Lincot, D. *Electrochimica Acta* **2005,** 50, (11), 2239-2248.
362. Burchardt, T. *International Journal of Hydrogen Energy* **2002,** 27, (3), 323-328.
363. Izutsu, K., *Electrochemistry in nonaqueous solutions*. Wiley-VCH Verlag GmbH & Co. KGaA: Weinheim, **2009**.
364. Titova, V. N.; Kazakov, V. A.; Petrova, N. V.; Biłłozor, S. *Journal of Electroanalytical Chemistry* **1995,** 381, (1), 227-230.
365. Hidalgo-Acosta, J. C.; Mendez, M. A.; Scanlon, M. D.; Vrubel, H.; Amstutz, V.; Adamiak, W.; Opallo, M.; Girault, H. H. *Chemical Science* **2015,** 6, (3), 1761-1769.
366. Mele, C.; Bozzini, B. *Journal of Solid State Electrochemistry* **2009,** 13, (10), 1553-1559.
367. Amatore, C.; Jutand, A. *Journal of Organometallic Chemistry* **1999,** 576, (1), 254-278.
368. Shen, C.; Shen, H.; Yang, M.; Xia, C.; Zhang, P. *Green Chemistry* **2015,** 17, (1), 225-230.
369. Wang, L.; Green, L.; Li, Z.; McCabe Dunn, J.; Bu, X.; Welch, C. J.; Li, C.; Wang, T.; Tu, Q.; Bekos, E.; Richardson, D.; Eckert, J.; Cui, J. *Organic Process Research & Development* **2011,** 15, (6), 1371-1376.
370. Yokoya, T.; Nakamura, T.; Matsushita, T.; Muro, T.; Takano, Y.; Nagao, M.; Takenouchi, T.; Kawarada, H.; Oguchi, T. *Nature* **2005,** 438, 647.
371. Bouwelen, S. E. G. a. J. E. F. a. F. M. v. *Journal of Physics D: Applied Physics* **2000,** 33, (8), 985.
372. Hutton, L.; Newton, M. E.; Unwin, P. R.; Macpherson, J. V. *Analytical chemistry* **2008,** 81, (3), 1023-1032.
373. Tachibana, T.; Williams, B. E.; Glass, J. T. *Physical Review B* **1992,** 45, (20), 11968-11974.
374. Tachibana, T.; Williams, B. E.; Glass, J. T. *Physical Review B* **1992,** 45, (20), 11975-11981.
375. Hussein, H. E. M.; Amari, H.; Macpherson, J. V. *ACS Catalysis* **2017,** 7, (10), 7388-7398.
376. Hutton, L. A.; Newton, M. E.; Unwin, P. R.; Macpherson, J. V. *Analytical chemistry* **2011,** 83, (3), 735-45.
377. Meng, L.; Ustarroz, J.; Newton, M. E.; Macpherson, J. V. *The Journal of Physical Chemistry C* **2017,** 121, (12), 6835-6843.
378. Hussein, H. E. M.; Maurer, R. J.; Amari, H.; Peters, J. J. P.; Meng, L.; Beanland, R.; Newton, M. E.; Macpherson, J. V. *ACS Nano* **2018,** 12, (7), 7388-7396.
379. Alani, R.; Swann, P. R. *MRS Proceedings* **1991,** 254, 43-63.
380. Skoog, D. A.; Holler, F. J.; Nieman, T. A., *Principles of instrumental analysis*. 5th ed.; Saunders College Publication: Philadelphia, **1998**.
381. Zouari, I.; Bellagi, A.; Lapicque, F. *Journal of Applied Electrochemistry* **1998,** 28, (1), 80-88.

382. Williams, D. B.; Carter, C. B., *Transmission Electron Microscopy: A Textbook for Materials Science*. Springer: Boston, MA, **2009**.
383. Wang, Z. L. *The Journal of Physical Chemistry B* **2000,** 104, (6), 1153-1175.
384. Pennycook, S. J. *Annual Review of Materials Science* **1992,** 22, (1), 171-195.
385. Egerton, R. F., *Electron energy-loss spectroscopy in the electron microscope*. Springer: New York, **2011**.
386. Brydson, R., *Aberration-Corrected Analytical Transmission Electron Microscopy*. A John Wiley & Sons, Ltd.: United Kingdom, **2011**.
387. McDowell, M. T.; Lee, S. W.; Harris, J. T.; Korgel, B. A.; Wang, C.; Nix, W. D.; Cui, Y. *Nano Letters* **2013,** 13, (2), 758-764.
388. Lloret, F.; Araujo, D.; Alegre, M. P.; Gonzalez-Leal, J. M.; Villar, M. P.; Eon, D.; Bustarret, E. *Physica Status Solidi A* **2015,** 212, (11), 2468-2473.
389. Martinez, G. T.; Jones, L.; De Backer, A.; Béché, A.; Verbeeck, J.; Van Aert, S.; Nellist, P. D. *Ultramicroscopy* **2015,** 159, (Part 1), 46-58.
390. Wu, J.; Shan, H.; Chen, W.; Gu, X.; Tao, P.; Song, C.; Shang, W.; Deng, T. *Advanced Materials* **2016,** 28, (44), 9686-9712.
391. Xie, Z.-H.; Jiang, Z.; Zhang, X. *Journal of The Electrochemical Society* **2017,** 164, (9), A2110-A2123.
392. Harris, P. *Journal of Carbon Research* **2018,** 4, (1), 4.
393. Zhang, D.; Zhu, Y.; Liu, L.; Ying, X.; Hsiung, C.-E.; Sougrat, R.; Li, K.; Han, Y. *Science* **2018,** 359, (6376), 675-679.
394. LeBeau, J. M.; Findlay, S. D.; Allen, L. J.; Stemmer, S. *Physical Review Letters* **2008,** 100, (20), 2061011-2061014.
395. James, E. M.; Browning, N. D. *Ultramicroscopy* **1999,** 78, (1), 125-139.
396. Hofer, F.; Schmidt, F. P.; Grogger, W.; Kothleitner, G. *IOP Conference Series: Materials Science and Engineering* **2016,** 109, (1), 012007.
397. Echlin, P., *Handbook of Sample Preparation for Scanning Electron Microscopy and X-Ray Microanalysis*. Springer US: Boston, MA, **2009**.
398. Stokes, D. J., *Principles and Practice of Variable Pressure/Environmental Scanning Electron Microscopy (VP ESEM)*. John Wiley & Sons, Ltd: West Sussex, United Kingdom, **2008**.
399. Goldstein, J. I.; Newbury, D. E.; Michael, J. R.; Ritchie, N. W. M.; Scott, J. H. J.; Joy, D. C., *Scanning Electron Microscopy and X-Ray Microanalysis*. Springer New York: New York, NY, **2018**.
400. Binnig, G.; Quate, C. F.; Gerber, C. *Physical Review Letters* **1986,** 56, (9), 930-933.
401. Voigtländer, B., Intermittent Contact Mode/Tapping Mode. In *Scanning Probe Microscopy: Atomic Force Microscopy and Scanning Tunneling Microscopy*, Springer Berlin Heidelberg: Berlin, Heidelberg, 2015; pp 205-221.
402. Voigtländer, B., *Scanning Probe Microscopy: Atomic Force Microscopy and Scanning Tunneling Microscopy*. Springer Berlin Heidelberg: Berlin, Heidelberg, **2015**.
403. Voigtländer, B., Technical Aspects of Atomic Force Microscopy (AFM). In *Scanning Probe Microscopy: Atomic Force Microscopy and Scanning Tunneling Microscopy*, Springer Berlin Heidelberg: Berlin, Heidelberg, 2015; pp 157-175.
404. Litster, S.; McLean, G. *Journal of Power Sources* **2004,** 130, (1), 61-76.
405. Liu, H.; Song, C.; Zhang, L.; Zhang, J.; Wang, H.; Wilkinson, D. P. *Journal of Power Sources* **2006,** 155, (2), 95-110.
406. Kleijn, S. E.; Lai, S. C.; Koper, M. T.; Unwin, P. R. *Angewandte Chemie International Edition* **2014,** 53, (14), 3558-86.

407. Brainina, K. Z.; Galperin, L. G.; Vikulova, E. V. *Journal of Solid State Electrochemistry* **2012,** 16, (7), 2357-2363.
408. Chen, A.; Holt-Hindle, P. *Chemical Reviews* **2010,** 110, (6), 3767-3804.
409. Gamburg, Y. D.; Zangari, G., *Theory and practice of metal electrodeposition*. Springer: New York, **2011**.
410. Aaboubi, O.; Merienne, E.; Amblard, J.; Chopart, J.-P.; Olivier, A. *Journal of The Electrochemical Society* **2002,** 149, (3), E90-E95.
411. Smalley, J. F.; Krishnan, C. V.; Goldman, M.; Feldberg, S. W.; Ruzic, I. *Journal of Electroanalytical Chemistry and Interfacial Electrochemistry* **1988,** 248, (2), 255-282.
412. Smalley, J. F.; Feldberg, S. W.; Chidsey, C. E. D.; Linford, M. R.; Newton, M. D.; Liu, Y.-P. *Journal of Physical Chemistry* **1995,** 99, (35), 13141-13149.
413. Hinoue, T.; Harui, R.; Izumi, T.; Watanabe, I.; Watarai, H. *Analytical Sciences* **1995,** 11, (1), 1-8.
414. Kraft, A. *Int. J. Electrochem. Sci.* **2007,** 2, (5), 355-385.
415. Sussmann, R. S.; Scarsbrook, G. A.; Wort, C. J. H.; Wood, R. M. *Diamond and Related Materials* **1994,** 3, (9), 1173-1177.
416. John, P.; Polwart, N.; Troupe, C. E.; Wilson, J. I. B. *Diamond and Related Materials* **2002,** 11, (3–6), 861-866.
417. Yoshida, K.; Morigami, H. *Microelectronics Reliability* **2004,** 44, (2), 303-308.
418. Natter, H.; Hempelmann, R. *The Journal of Physical Chemistry* **1996,** 100, (50), 19525-19532.
419. Sun, Y.; Xia, Y. *Science* **2002,** 298, (5601), 2176-2179.
420. Peng, Z.; Yang, H. *Nano Today* **2009,** 4, (2), 143-164.
421. Geboes, B.; Ustarroz, J.; Sentosun, K.; Vanrompay, H.; Hubin, A.; Bals, S.; Breugelmans, T. *ACS Catalysis* **2016,** 6, (9), 5856-5864.
422. Snyder, J.; McCue, I.; Livi, K.; Erlebacher, J. *Journal of the American Chemical Society* **2012,** 134, (20), 8633-8645.
423. Pasricha, R.; Bala, T.; Biradar, A. V.; Umbarkar, S.; Sastry, M. *Small* **2009,** 5, (12), 1467-1473.
424. Gund, G. S.; Dubal, D. P.; Jambure, S. B.; Shinde, S. S.; Lokhande, C. D. *Journal of Materials Chemistry A* **2013,** 1, (15), 4793-4803.
425. Sasidharan, M.; Bhanja, P.; Senthil, C.; Bhaumik, A. *RSC Advances* **2016,** 6, (14), 11370-11377.
426. González, E.; Arbiol, J.; Puntes, V. F. *Science* **2011,** 334, (6061), 1377-1380.
427. Rodríguez, J. M. D.; Melián, J. A. H.; Peña, J. P. *Journal of Chemical Education* **2000,** 77, (9), 1195.
428. Zolfaghari, A.; Conway, B. E.; Jerkiewicz, G. *Electrochimica Acta* **2002,** 47, (8), 1173-1187.
429. Thomas, J.; Gemming, T., *Analytical Transmission Electron Microscopy: An Introduction for Operators*. Springer: Netherlands, **2014**.
430. Caplovicova, M.; Danis, T.; Buc, D.; Caplovic, L.; Janik, J.; Bello, I. *Ultramicroscopy* **2007,** 107, (8), 692-697.
431. Lu, G.; Zangari, G. *Electrochimica Acta* **2006,** 51, (12), 2531-2538.
432. Simonov, A. N.; Cherstiouk, O. V.; Vassiliev, S. Y.; Zaikovskii, V. I.; Filatov, A. Y.; Rudina, N. A.; Savinova, E. R.; Tsirlina, G. A. *Electrochimica Acta* **2014,** 150, 279-289.
433. Yasin, H. M.; Denuault, G.; Pletcher, D. *Journal of Electroanalytical Chemistry* **2009,** 633, (2), 327-332.

434. Cherevko, S.; Kulyk, N.; Chung, C.-H. *Nanoscale* **2012,** 4, (2), 568-575.
435. Topalov, A. A.; Katsounaros, I.; Auinger, M.; Cherevko, S.; Meier, J. C.; Klemm, S. O.; Mayrhofer, K. J. J. *Angewandte Chemie International Edition* **2012,** 51, (50), 12613-12615.
436. Ustarroz, J.; Altantzis, T.; Hammons, J. A.; Hubin, A.; Bals, S.; Terryn, H. *Chemistry of Materials* **2014,** 26, (7), 2396-2406.
437. Biegler, T.; Rand, D. A. J.; Woods, R. *Journal of Electroanalytical Chemistry and Interfacial Electrochemistry* **1971,** 29, (2), 269-277.
438. Tranchida, D.; Piccarolo, S.; Deblieck, R. *Measurement Science and Technology* **2006,** 17, (10), 2630.
439. Wilson, N. R.; Clewes, S. L.; Newton, M. E.; Unwin, P. R.; Macpherson, J. V. *The Journal of Physical Chemistry B* **2006,** 110, (11), 5639-5646.
440. Sun, S.; Murray, C. B.; Weller, D.; Folks, L.; Moser, A. *Science* **2000,** 287, (5460), 1989-1992.
441. Feng, J.-J.; Li, A.-Q.; Wang, A.-J.; Lei, Z.; Chen, J.-R. *Microchimica Acta* **2011,** 173, (3), 383-389.
442. Gao, F.; Yang, N.; Obloh, H.; Nebel, C. E. *Electrochemistry Communications* **2013,** 30, 55-58.
443. Gao, F.; Yang, N.; Smirnov, W.; Obloh, H.; Nebel, C. E. *Electrochimica Acta* **2013,** 90, 445-451.
444. Liu, Y.; Gokcen, D.; Bertocci, U.; Moffat, T. P. *Science* **2012,** 338, (6112), 1327-1330.
445. Viet-Long, N.; Michitaka, O.; Van Nong, N.; Minh-Thi, C.; Masayuki, N. *Advances in Natural Sciences: Nanoscience and Nanotechnology* **2012,** 3, (2), 1-4.
446. Mitchell, D. R. G. *Microscopy Research and Technique* **2008,** 71, (8), 588-593.
447. Tian, N.; Zhou, Z.-Y.; Sun, S.-G.; Ding, Y.; Wang, Z. L. *Science* **2007,** 316, (5825), 732-735.
448. Quan, Z.; Wang, Y.; Fang, J. *Accounts of Chemical Research* **2013,** 46, (2), 191-202.
449. Vogt, H.; Balzer, R. J. *Electrochimica Acta* **2005,** 50, (10), 2073-2079.
450. Nikolic, N. D.; Pavlovic, L. J.; Pavlovic, M. G.; Popov, K. I. *J. Serb. Chem. Soc.* **2007,** 72, (12), 1369-1381.
451. Long, N. V.; Chien, N. D.; Hayakawa, T.; Hirata, H.; Lakshminarayana, G.; Nogami, M. *Nanotechnology* **2009,** 21, (3), 035605.
452. Koper, M. T. *Nanoscale* **2011,** 3, (5), 2054-2073.
453. Housmans, T. H. M.; Wonders, A. H.; Koper, M. T. M. *The Journal of Physical Chemistry B* **2006,** 110, (20), 10021-10031.
454. Vidal-Iglesias, F. J.; Arán-Ais, R. M.; Solla-Gullón, J.; Herrero, E.; Feliu, J. M. *ACS Catalysis* **2012,** 2, (5), 901-910.
455. Long, N. V.; Ohtaki, M.; Hien, T. D.; Jalem, R.; Nogami, M. *Journal of Nanoparticle Research* **2011,** 13, (10), 5177.
456. Rossmeisl, J.; Ferrin, P.; Tritsaris, G. A.; Nilekar, A. U.; Koh, S.; Bae, S. E.; Brankovic, S. R.; Strasser, P.; Mavrikakis, M. *Energy and Environmental Science* **2012,** 5, 8335-8342.
457. Hamnett, A. *Catalysis Today* **1997,** 38, (4), 445-457.
458. Liu, Z.; Ling, X. Y.; Su, X.; Lee, J. Y. *The Journal of Physical Chemistry B* **2004,** 108, (24), 8234-8240.
459. Mancharan, R.; Goodenough, J. B. *Journal of Materials Chemistry* **1992,** 2, (8), 875-887.

460. Hofstead-Duffy, A. M.; Chen, D.-J.; Sun, S.-G.; Tong, Y. J. *Journal of Materials Chemistry* **2012,** 22, 5205-5208.
461. Chung, D. Y.; Lee, K.-J.; Sung, Y.-E. *The Journal of Physical Chemistry C* **2016,** 120, (17), 9028-9035.
462. Zhao, D.; Xu, B.-Q. *Physical Chemistry Chemical Physics* **2006,** 8, (43), 5106-5114.
463. Solla-Gullon, J.; Vidal-Iglesias, F. J.; Lopez-Cudero, A.; Garnier, E.; Feliu, J. M.; Aldaz, A. *Physical Chemistry Chemical Physics* **2008,** 10, (25), 3689-3698.
464. Dimos, M. M.; Blanchard, G. J. *The Journal of Physical Chemistry C* **2010,** 114, (13), 6019-6026.
465. Wasmus, S.; Kuver, A. *Journal of Electroanalytical Chemistry* **1999,** 461, (1-2), 14-31.
466. Oshchepkov, A. G.; Simonov, A. N.; Simonov, P. A.; Shmakov, A. N.; Rudina, N. A.; Ishchenko, A. V.; Cherstiouk, O. V.; Parmon, V. N. *Journal of Electroanalytical Chemistry* **2014,** 729, (Supplement C), 34-42.
467. Du, B.; Tong. *The Journal of Physical Chemistry B* **2005,** 109, (38), 17775-17780.
468. Gloaguen , F.; Le´ger , J.-M.; Lamy , C. *Journal of Applied Electrochemistry* **1997,** 27, (9), 1052-1060.
469. Mariano, R. G.; McKelvey, K.; White, H. S.; Kanan, M. W. *Science* **2017,** 358, (6367), 1187-1192.
470. Kim, T. W.; Choi, K. S. *Science* **2014,** 343, (6174), 990-996.
471. Wang, C.; Waje, M.; Wang, X.; Tang, J. M.; Haddon, R. C.; Yan. *Nano Letters* **2004,** 4, (2), 345-348.
472. Zach, M. P.; Ng, K. H.; Penner, R. M. *Science* **2000,** 290, (5499), 2120-2123.
473. Li, M.; Zhao, Z.; Cheng, T.; Fortunelli, A.; Chen, C.-Y.; Yu, R.; Zhang, Q.; Gu, L.; Merinov, B. V.; Lin, Z.; Zhu, E.; Yu, T.; Jia, Q.; Guo, J.; Zhang, L.; Goddard, W. A.; Huang, Y.; Duan, X. *Science* **2016,** 354, (6318), 1414-1419.
474. Velmurugan, J.; Noël, J.-M.; Nogala, W.; Mirkin, M. V. *Chemical Science* **2012,** 3, (11), 3307-3314.
475. Matsushima, H.; Lin, S. W.; Morin, S.; Magnussen, O. M. *Faraday Discussions* **2016,** 193, (0), 171-185.
476. Li, Z. Y.; Young, N. P.; Di Vece, M.; Palomba, S.; Palmer, R. E.; Bleloch, A. L.; Curley, B. C.; Johnston, R. L.; Jiang, J.; Yuan, J. *Nature* **2007,** 451, 46.
477. Zhou, M.; Dick, J. E.; Bard, A. J. *Journal of the American Chemical Society* **2017,** 139, (48), 17677-17682.
478. Mayrhofer, K. J. J.; Meier, J. C.; Ashton, S. J.; Wiberg, G. K. H.; Kraus, F.; Hanzlik, M.; Arenz, M. *Electrochemistry Communications* **2008,** 10, (8), 1144-1147.
479. Klein, R. K.; Kephart, J. O.; Pantell, R. H.; Park, H.; Berman, B. L.; Swent, R. L.; Datz, S.; Fearick, R. W. *Physical Review B* **1985,** 31, (1), 68-92.
480. Hutton, L. A.; Iacobini, J. G.; Bitziou, E.; Channon, R. B.; Newton, M. E.; Macpherson, J. V. *Analytical chemistry* **2013,** 85, (15), 7230-7240.
481. Blum, V.; Gehrke, R.; Hanke, F.; Havu, P.; Havu, V.; Ren, X.; Reuter, K.; Scheffler, M. *Computer Physics Communications* **2009,** 180, (11), 2175-2196.
482. Perdew, J. P.; Burke, K.; Ernzerhof, M. *Physical Review Letters* **1996,** 77, (18), 3865-3868.
483. Tkatchenko, A.; Scheffler, M. *Physical Review Letters* **2009,** 102, (7), 0730051-0730054.
484. Bahn, S. R.; Jacobsen, K. W. *Computing in Science & Engineering* **2002,** 4, (3), 56-66.

485. Henkelman, G.; Uberuaga, B. P.; Jónsson, H. *The Journal of Chemical Physics* **2000,** 113, (22), 9901-9904.
486. Goedecker, S. *The Journal of Chemical Physics* **2004,** 120, (21), 9911-9917.
487. Peterson, A. A. *Topics in Catalysis* **2014,** 57, (1), 40-53.
488. Meijering, E.; Dzyubachyk, O.; Smal, I., Chapter nine - Methods for Cell and Particle Tracking. In *Methods in Enzymology*, conn, P. M., Ed. Academic Press: 2012; Vol. 504, pp 183-200.
489. Frenkel, D.; Smit, B., *Understanding Molecular Simulation: From Algorithms To Applications*. 2nd ed.; Academic Press: San Diego, **2002**; Vol. 1, p 97-115.
490. Shinotsuka, H.; Tanuma, S.; Powell, C. J.; Penn, D. R. *Surface and Interface Analysis* **2015,** 47, (9), 871-888.
491. Lomax, D. J.; Dryfe, R. A. W. *Journal of Electroanalytical Chemistry* **2018,** 819, 374-383.
492. Wild, C.; Herres, N.; Koidl, P. *Journal of Applied Physics* **1990,** 68, (3), 973-978.
493. Fujita, T.; Guan, P.; McKenna, K.; Lang, X.; Hirata, A.; Zhang, L.; Tokunaga, T.; Arai, S.; Yamamoto, Y.; Tanaka, N.; Ishikawa, Y.; Asao, N.; Yamamoto, Y.; Erlebacher, J.; Chen, M. *Nature Materials* **2012,** 11, (9), 775-780.
494. Redmond, P. L.; Hallock, A. J.; Brus, L. E. *Nano Letters* **2005,** 5, (1), 131-135.
495. Ouyang, R.; Liu, J.-X.; Li, W.-X. *Journal of the American Chemical Society* **2013,** 135, (5), 1760-1771.
496. Xue, Y.; Huang, B.; Yi, Y.; Guo, Y.; Zuo, Z.; Li, Y.; Jia, Z.; Liu, H.; Li, Y. *Nature Communications* **2018,** 9, (1), 1460.
497. Gambardella, P.; Rusponi, S.; Veronese, M.; Dhesi, S. S.; Grazioli, C.; Dallmeyer, A.; Cabria, I.; Zeller, R.; Dederichs, P. H.; Kern, K.; Carbone, C.; Brune, H. *Science* **2003,** 300, (5622), 1130-1133.
498. Seh, Z. W.; Kibsgaard, J.; Dickens, C. F.; Chorkendorff, I.; Norskov, J. K.; Jaramillo, T. F. *Science* **2017,** 355, (6321), 1-12.
499. Anastas, P. T.; Kirchhoff, M. M. *Accounts of Chemical Research* **2002,** 35, (9), 686-694.
500. Fu, F.; Wang, Q. *Journal of Environmental Management* **2011,** 92, (3), 407-418.
501. Sousa, S.; Jimenez-Guerrero, P.; Ruiz, A.; Ratola, N.; Alves, A. *Environmental technology* **2011,** 32, (5-6), 673-83.
502. Binns, C. W.; Lee, M. K.; Lee, A. H. *Annual Review of Public Health* **2018,** 39, (1), 403-420.
503. Biswas, J. K.; Rai, M.; Mondal, M.; Ingle, A. P., The flop side of using heavy metal(oids) s in the traditional medicine: toxic insults and injury to human health. In *Biomedical Applications of Metals*, Rai, M.; Mondal, M.; Ingle, A. P., Eds. Springer International Publishing AG: Cham, 2018; pp 257-276.
504. Garrett, C. E.; Prasad, K. *Advanced Synthesis & Catalysis* **2004,** 346, (8), 889-900.
505. Gutmann, B.; Cantillo, D.; Kappe, C. O. *Angewandte Chemie International Edition* **2015,** 54, (23), 6688-6728.
506. Busacca, C. A.; Fandrick, D. R.; Song, J. J.; Senanayake, C. H. *Advanced Synthesis and Catalysis* **2011,** 353, 1825-1864.
507. Martin, R.; Buchwald, S. L. *Accounts of Chemical Research* **2008,** 41, (11), 1461-1473.

508. Jiang, X.; Lee, G. T.; Prasad, K.; Repič, O. *Organic Process Research & Development* **2008,** 12, (6), 1137-1141.
509. Manley, P. W.; Acemoglu, M.; Marterer, W.; Pachinger, W. *Organic Process Research & Development* **2003,** 7, (3), 436-445.
510. Amatore, C.; Carre, E.; Jutand, A.; M'Barki, M. A. *Organometallics* **1995,** 14, (4), 1818-1826.
511. Roshchin, A. V.; Veselov, V. G.; Panova, A. I. *J Hyg Epidemiol Microbiol Immunol* **1984,** 28, (1), 17-24.
512. Marguí, E.; Van Meel, K.; Van Grieken, R.; Buendía, A.; Fontàs, C.; Hidalgo, M.; Queralt, I. *Analytical chemistry* **2009,** 81, (4), 1404-1410.
513. Marguí, E.; Queralt, I.; Hidalgo, M. *Spectrochimica Acta Part B: Atomic Spectroscopy* **2013,** 86, 50-54.
514. Hough, W. L.; Smiglak, M.; Rodríguez, H.; Swatloski, R. P.; Spear, S. K.; Daly, D. T.; Pernak, J.; Grisel, J. E.; Carliss, R. D.; Soutullo, M. D.; Davis, J. J. H.; Rogers, R. D. *New Journal of Chemistry* **2007,** 31, (8), 1429-1436.
515. Qin, C.; Granger, A.; Papov, V.; McCaffrey, J.; Norwood, D. L. *Journal of Pharmaceutical and Biomedical Analysis* **2010,** 51, (1), 107-113.
516. Forfar, L. C.; Murray, P. M., Meeting Metal Limits in Pharmaceutical Processes. In *Topics in Organometallic Chemistry*, Springer: Berlin, Heidelberg, 2018.
517. Bien, J. T.; Lane, G. C.; Oberholzer, M. R., Removal of Metals from Process Streams: Methodologies and Applications. In *Organometallics in Process Chemistry*, Springer: Berlin, Heidelberg, 2004; pp 263-283.
518. Prashad, M.; Hu, B.; Har, D.; Repic, O.; Blacklock, Thomas J.; Acemoglu, M. *Advanced Synthesis & Catalysis* **2001,** 343, (5), 461-472.
519. Barbaro, P.; Liguori, F. *Chemical Reviews* **2009,** 109, (2), 515-529.
520. Rosso, V. W.; Lust, D. A.; Bernot, P. J.; Grosso, J. A.; Modi, S. P.; Rusowicz, A.; Sedergran, T. C.; Simpson, J. H.; Srivastava, S. K.; Humora, M. J.; Anderson, N. G. *Organic Process Research & Development* **1997,** 1, (4), 311-314.
521. S. Anson, M.; P. Leese, M.; Tonks, L.; M. J. Williams, J. *Journal of the Chemical Society, Dalton Transactions* **1998**, (21), 3529-3538.
522. Phillips, S.; Kauppinen, P. *Platinum Metals Review* **2010,** 54, (1), 69-70.
523. Slater, C. S.; Savelski, M. J.; Ruiz-Felix, M. N. *Journal of Environmental Science and Health, Part A* **2013,** 48, (13), 1602-1608.
524. Schwartz, D. *Interface-Electrochemical Society* **2006,** 15, (1), 32-35.
525. Chen, G. *Separation and Purification Technology* **2004,** 38, (1), 11-41.
526. Basirun, W. J.; Pletcher, D.; Saraby-Reintjes, A. *Journal of Applied Electrochemistry* **1996,** 26, (8), 873-880.
527. Hutton, L. A.; O'Neil, G. D.; Read, T. L.; Ayres, Z. J.; Newton, M. E.; Macpherson, J. V. *Analytical chemistry* **2014,** 86, (9), 4566-4572.
528. Barakat, M. A. *Arabian Journal of Chemistry* **2011,** 4, (4), 361-377.
529. Gniewek, A. *Journal of Organometallic Chemistry* **2016,** 823, 90-96.
530. Amatore, C.; Jutand, A.; M'Barki, M. A. *Organometallics* **1992,** 11, (9), 3009-3013.
531. Swathirajan, S. *Journal of The Electrochemical Society* **1986,** 133, (4), 671-680.
532. Walsh, F. C.; Herron, M. E. *Journal of Physics D: Applied Physics* **1991,** 24, (2), 217.
533. Conway, B. E.; Bockris, J. O. M. *Electrochimica Acta* **1961,** 3, (4), 340-366.

534. Mehl, W.; Bockris, J. O. M. *Canadian Journal of Chemistry* **1959,** 37, (1), 190-204.
535. Rumble, J., *CRC Handbook of Chemistry and Physics*. 99 ed.; CRC press: New York, **2018**.
536. Emsley, J., *Nature's building blocks: an AZ guide to the elements*. Oxford University Press: **2011**.
537. Andersen, J. E. T.; Bech-Nielsen, G.; Møller, P.; Reeve, J. C. *Journal of Applied Electrochemistry* **1996,** 26, (2), 161-170.
538. Liu, Q. X.; El Abedin, S. Z.; Endres, F. *Surface and Coatings Technology* **2006,** 201, (3–4), 1352-1356.
539. Ito, Y.; Nohira, T. *Electrochimica Acta* **2000,** 45, (15-16), 2611-2622.
540. Yuguang Zhao; VanderNoot, T. J. *Electrochimica Acta* **1997,** 42, (1), 3-13.
541. Cui, C. Q.; Jiang, S. P.; Tseung, A. C. C. *Journal of The Electrochemical Society* **1991,** 138, (4), 1001-1006.
542. Hubin, A.; Gonnissen, D.; Simons, W.; Vereecken, J. *Journal of Electroanalytical Chemistry* **2007,** 600, (1), 142-150.
543. Mecucci, A.; Scott, K. *Journal of Chemical Technology and Biotechnology* **2002,** 77, (4), 449-457.
544. Touabi, N.; Martinez, S.; Bounoughaz, M. *J International Journal of Electrochemical Science* **2015,** 10, 7227.
545. Frenking, G.; Fröhlich, N. *Chemical Reviews* **2000,** 100, (2), 717-774.
546. Dedieu, A. *Chemical Reviews* **2000,** 100, (2), 543-600.
547. Amatore, C.; Azzabi, M.; Jutand, A. *Journal of the American Chemical Society* **1991,** 113, (22), 8375-8384.
548. Amatore, C.; Jutand, A.; Khalil, F.; M'Barki, M. A.; Mottier, L. *Organometallics* **1993,** 12, (8), 3168-3178.
549. Amatore, C.; Blart, E.; Genet, J. P.; Jutand, A.; Lemaire-Audoire, S.; Savignac, M. *The Journal of Organic Chemistry* **1995,** 60, (21), 6829-6839.
550. van Asselt, R.; Elsevier, C. J.; Amatore, C.; Jutand, A. *Organometallics* **1997,** 16, (3), 317-328.
551. Amatore, C.; Jutand, A. *Coordination Chemistry Reviews* **1998,** 178, 511-528.
552. Amatore, C.; Jutand, A.; Meyer, G. *Inorganica Chimica Acta* **1998,** 273, (1), 76-84.
553. Amatore, C.; Jutand, A.; Lemaıˆtre, F.; Luc Ricard, J.; Kozuch, S.; Shaik, S. *Journal of Organometallic Chemistry* **2004,** 689, (23), 3728-3734.
554. Bakhmutov, V. I.; Berry, J. F.; Cotton, F. A.; Ibragimov, S.; Murillo, C. A. *Dalton transactions* **2005**, (11), 1989-92.
555. Carole, W. A.; Colacot, T. J. *Chemistry* **2016,** 22, (23), 7686-95.
556. Carole, W. A.; Bradley, J.; Sarwar, M.; Colacot, T. J. *Organic Letters* **2015,** 17, (21), 5472-5475.
557. Kirik, S. D.; Mulagaleev, R. F.; Blokhin, A. I. *Acta Crystallographica Section C* **2004,** 60, (9), m449-m450.
558. Skapski, A. C.; Smart, M. L. *Journal of the Chemical Society D: Chemical Communications* **1970**, (11), 658b-659.
559. Mulagaleev, R. F.; Kirik, S. D. *Russian Journal of Applied Chemistry* **2011,** 83, (12), 2065-2075.
560. Nosova, V. M.; Ustynyuk, Y. A.; Bruk, L. G.; Temkin, O. N.; Kisin, A. V.; Storozhenko, P. A. *Inorganic chemistry* **2011,** 50, (19), 9300-9310.
561. Schneider, H. *Electrochimica Acta* **1976,** 21, (9), 711-718.

562. McDonald, R. S. *Analytical chemistry* **1986,** 58, (9), 1906-1925.
563. Jamroz, D.; Stangret, J.; Lindgren, J. *Journal of the American Chemical Society* **1993,** 115, (14), 6165-6168.
564. Stoyanov, E. S. *Journal of Structural Chemistry* **2000,** 41, (3), 440-445.
565. Kragten, D. D.; van Santen, R. A.; Crawford, M. K.; Provine, W. D.; Lerou, J. J. *Inorganic chemistry* **1999,** 38, (2), 331-339.
566. Kunkely, H.; Vogler, A. *Chemical Physics Letters* **1999,** 308, (3), 169-172.
567. Rand, D. A. J.; Woods, R. *Journal of Electroanalytical Chemistry and Interfacial Electrochemistry* **1972,** 35, (1), 209-218.
568. Polcaro, A. M.; Palmas, S. *Electrochimica Acta* **1991,** 36, (5), 921-926.
569. Pluntke, Y.; Kibler, L. A.; Kolb, D. M. *Physical Chemistry Chemical Physics* **2008,** 10, (25), 3684-3688.
570. Grennberg, H.; Foot, J. S.; Banwell, M. G.; Roman, D. S., Palladium(II) Acetate. In *Encyclopedia of Reagents for Organic Synthesis*, 2001; pp 1-35.
571. Rahman, H. M. A.; Hefter, G.; Buchner, R. *The Journal of Physical Chemistry B* **2012,** 116, (1), 314-323.
572. Abdelrahman, A. I.; Mohammad, A. M.; Okajima, T.; Ohsaka, T. *The Journal of Physical Chemistry B* **2006,** 110, (6), 2798-2803.
573. Bertie, J. E.; Lan, Z. *The Journal of Physical Chemistry B* **1997,** 101, (20), 4111-4119.
574. Bedford, R. B.; Bowen, J. G.; Davidson, R. B.; Haddow, M. F.; Seymour-Julen, A. E.; Sparkes, H. A.; Webster, R. L. *Angewandte Chemie International Edition* **2015,** 54, (22), 6591-4.
575. Freire, M. G.; Neves, C. M.; Marrucho, I. M.; Coutinho, J. A.; Fernandes, A. M. *The Journal of Physical Chemistry A* **2010,** 114, (11), 3744-3749.
576. Pandey, R. N.; Henry, P. M. *Canadian Journal of Chemistry* **1974,** 52, (8), 1241-1247.
577. Takamuku, T.; Tabata, M.; Yamaguchi, A.; Nishimoto, J.; Kumamoto, M.; Wakita, H.; Yamaguchi, T. *The Journal of Physical Chemistry B* **1998,** 102, (44), 8880-8888.
578. Loring, J. S.; Fawcett, W. R. *The Journal of Physical Chemistry A* **1999,** 103, (19), 3608-3617.
579. Mollner, A. K.; Brooksby, P. A.; Loring, J. S.; Bako, I.; Palinkas, G.; Fawcett, W. R. *The Journal of Physical Chemistry A* **2004,** 108, (16), 3344-3349.
580. Case, B.; Parsons, R. *Transactions of the Faraday Society* **1967,** 63, (0), 1224-1239.
581. Dubouis, N.; Serva, A.; Salager, E.; Deschamps, M.; Salanne, M.; Grimaud, A. *The Journal of Physical Chemistry Letters* **2018,** 9, (23), 6683-6688.
582. Thompson, J. W.; Kaiser, T. J.; Jorgenson, J. W. *Journal of Chromatography A* **2006,** 1134, (1), 201-209.
583. Hauwiller, M. R.; Zhang, X.; Liang, W. I.; Chiu, C. H.; Zhang, Q.; Zheng, W.; Ophus, C.; Chan, E. M.; Czarnik, C.; Pan, M.; Ross, F. M.; Wu, W. W.; Chu, Y. H.; Asta, M.; Voorhees, P. W.; Alivisatos, A. P.; Zheng, H. *Nano Letters* **2018,** 18, (10), 6427-6433.
584. Ihle, T.; Müller-Krumbhaar, H. *Physical Review Letters* **1993,** 70, (20), 3083-3086.
585. Müller-Krumbhaar, H.; Zimmer, M.; Ihle, T.; Saito, Y. *Physica A: Statistical Mechanics and its Applications* **1996,** 224, (1), 322-337.
586. Feng, X.; Yan, M.; Zhang, T.; Liu, Y.; Bao, M. *Green Chemistry* **2010,** 12, (10), 1758-1766.

587. Narayanan, R.; El-Sayed, M. A. *Journal of the American Chemical Society* **2003,** 125, (27), 8340-8347.
588. Colacot, T. J.; Qian, H.; Cea-Olivares, R.; Hernandez-Ortega, S. *Journal of Organometallic Chemistry* **2001,** 637-639, 691-697.
589. Jiang, N.; Ragauskas, A. J. *Tetrahedron Letters* **2006,** 47, (2), 197-200.
590. de Vries, J. G. *Dalton transactions* **2006**, (3), 421-429.
591. Herrmann, W. A.; Böhm, V. P. W.; Reisinger, C.-P. *Journal of Organometallic Chemistry* **1999,** 576, (1), 23-41.
592. Herrmann, W. A. *Angewandte Chemie International Edition English* **2002,** 41, (8), 1290-309.
593. Miyaura, N.; Suzuki, A. *Chemical Reviews* **1995,** 95, (7), 2457-2483.
594. Molina de la Torre, J. A.; Espinet, P.; Albéniz, A. C. *Organometallics* **2013,** 32, (19), 5428-5434.
595. Schwarzacher, W.; Kasyutich, O. I.; Evans, P. R.; Darbyshire, M. G.; Yi, G.; Fedosyuk, V. M.; Rousseaux, F.; Cambril, E.; Decanini, D. *Journal of Magnetism and Magnetic Materials* **1999,** 198-199, 185-190.
596. Ahn, S. H.; Tan, H.; Haensch, M.; Liu, Y.; Bendersky, L. A.; Moffat, T. P. *Energy & Environmental Science* **2015,** 8, (12), 3557-3562.